Diss. ETH No. 17714

# Challenges in Operational Numerical Weather Prediction at High Resolution in Complex Terrain

A dissertation submitted to the
SWISS FEDERAL INSTITUTE OF TECHNOLOGY (ETH)
Zürich

for the degree of
DOCTOR OF SCIENCES

presented by
MATTEO BUZZI
Dipl. Umw.-Natw. ETH
born on 22 May 1975
citizen of Porza (TI)

accepted on the recommendation of

Prof. Dr. Atsumu Ohmura, examiner
PD Dr. M. W. Rotach, co-examiner
Prof. Dr. C. Schär, co-examiner
Prof. Dr. A. A. Holtslag, co-examiner

2008

Matteo Buzzi
Altwiesenstr. 89
CH-8051 Zürich - Swizerland
matteo.buzzi@meteoswiss.ch

# Abstract

Numerical Weather Prediction (NWP) in complex terrain is a challeging task. The experience collected with the COSMO model - a limited area NWP non-hydrostatic model operated by MeteoSwiss in the Alpine region - indicates that several meteorological aspects mainly at local scale are still not well reproduced. The present study focuses on some challenging aspects of NWP at high resolution in complex terrain. This work explores the topographic effects on radiation, tests the performance of the turbulence scheme in a semi-idealized set-up using the single column version of COSMO at high vertical resolution, evaluates its ability to reproduce a realistic diurnal cycle and analyses the deficiencies of the COSMO 2 m temperature diagnostics in the alpine region.

Radiation is known as the primary forcing of the planetary boundary layer and its balance is significantly influenced by topography. Local slope aspect (slope orientation) and slope angle (slope inclination) considerably modify the amount and daily course of down-welling short wave radiation. Shading effects in case of horizon angles higher than sun elevation angles generate significant differences in sunrise and sunset times. In addition, reduced skyview has a significant impact as well, causing a complex spatial variability of the downward longwave and downward diffuse radiation components. In order to resolve more of the important details of the complex topography, NWP models are or will be operated in the near future at fine grid resolution close to 1 km. At this grid spacing, topographic effects become important also for weather modelling, because the impact of slope aspect, slope angle or slope inclination, skyview factor as well as shadowing effects significantly modify radiation fluxes at the Earth's surface.

A comprehensive and relatively simple parameterization scheme for topographic effects on radiation taken from the literature has been modified and implemented in the COSMO model. The approach is based on correction factors for surface radiation components. In Chapter 2 the impact of this parameterisation scheme at different horizontal resolutions (7 and 2.2 km) is investigated. The performance is evaluated using topography-adapted satellite data (global radiation) and ground based stations (longwave radiation). The radiation performance with the new radiation correction scheme is significantly improved both for direct solar radiation and for longwave radiation. Secondary benefits can also be observed in the near surface temperature.

A prerequisite for any validation and detailed investigation of model performance is a test of its components under idealised conditions. In Chapter 3 the performance of the COSMO-SC ("single column") turbulence scheme (a TKE scheme with a 1.5 order turbulence closure at the hierarchy level 2.5) is investigated in the framework of the first GABLS intercomparison case (GEWEX Atmospheric Boundary Layer Study).

The model performs well as compared to the other participating models and to LES (Large Eddy Simulation). The modification of some model parameters combined with the high vertical resolution has permitted to discover and highlight an important stability aspect of the COSMO turbulence scheme. In a shear-driven stable boundary layer, the vertical diffusivities show spurious oscillations. This problematic model deficiency has been explored and possible solutions have been proposed. The unrealistic oscillations are eliminated by introducing a vertical filtering of the vertical wind gradient functions before evaluating the stability functions. The simulations

additionally show that the use of a too large minimum diffusion coefficient leads to the loss of important structures within the planetary boundary layer, such as the low level jet.

In Chapter 4 a small step in direction of more complexity was performed. A real diurnal cycle is simulated with the same one-dimensional modelling system of the previous chapter. The case is that chosen by the second GABLS intercomparison case, which is again a single column model intercomparison project in the framework of GEWEX. This case has been taken from the CASES-99 experiment and covers two full diurnal cycles.

The results highlight some important limitations of one-dimensional modelling (single column approach) in cases with a significant dynamical variability such as geostrophic wind changes in time and space, or horizontal advection. Additionally, the typical morning transition in the wind speed and in the friction velocity are not well captured by the model.

One of the standard verifications for the NWP performance is to compare model results with in-situ observations. For near-surface temperature and relative humidity (or dew point) observational data are usually available at 2 m above surface. Because the first atmospheric level in most of the NWP models such as COSMO is located higher, these variables have to be diagnosed from prognostic variables both at the surface and at the first atmospheric layer using interpolation formulas. Deficiencies in the diagnostics can strongly influence the evaluated quality of a model. Chapter 5 explores the typical problems of the 2 m diagnostics of temperature and dew point in the COSMO model in the Alpine region (complex terrain).

The COSMO diagnostics produces 2 m values which are too close to the surface value, leading, e.g., to an enhanced cold bias in stable conditions and a phase error of the maximum 2 m temperature. This deficiency is caused by the use of an unrealistic effective canopy height, which discriminates between exponential and logarithmic profile. The effective canopy height is determined from the total roughness length, that includes also an orographic part. A new formulation based on the characteristics of the Roughness Sublayer in combination with the introduction of the local roughness length is presented (considering only the surface coverage) and compared to the current diagnostics. The verification on the basis of some case studies indicates a significant improvement in the 2 m temperature and dew point diagnostics.

# Zusammenfassung

Die numerische Wettervorhersage in komplexer Topographie ist eine herausfordernde Aufgabe. Die Erfahrungen mit dem COSMO Modell - ein nicht-hydrostatisches Modell für bregrenzte Gebiete, das bei MeteoSchweiz für den alpinen Raum betrieben wird, zeigen, dass verschiedene meteorologische Aspekte vor allem auf der lokalen Skala noch nicht gut reproduziert werden. Diese Studie fokussiert auf einige spezielle Aspekte der numerischen Wettervorhersage mit hoher horizontaler Auflösung in komplexem Gelände. In dieser Arbeit werden die topographischen Effekte auf die Strahlung untersucht, die Leistung des Turbulenzschema in einem semi-idealisierten Fall mit der eindimensionalen Version von COSMO mit sehr hohen vertikalen Auflösung getestet und es wird die Fähigkeit des Modells evaluiert, den realen Tagesgang der planetaren Grenzschicht zu reproduzieren. Schliesslich werden die Mängeln der 2 m Temperaturdiagnose in der alpinen Region analysiert.

Die Strahlung ist als der wichtigste Antrieb der planetaren Grenzschicht bekannt und ihre Bilanz wird stark von der Topographie beeinflusst. Hangorientierung und Hangneigung modifizieren die Menge und den Tagesgang der kurzwelligen Strahlung sehr stark. Abschattungseffekte im Fall vom höheren Horizontwinkel als die Elevationswinkel der Sonne generieren bedeutsame Zeitdifferenzen in dem Sonnenaufgang und -untergang. Ausserdem hat eine reduzierte Sichtbarkeit des Himmels (skyview) auch einen bedeutsamen Einfluss, weil sie eine komplexe Variabilität der langwellingen und diffusen Strahlung nach unten verursacht. Um mehr Details der komplexen Topographie zu beschreiben, sind oder werden numerische Wettermodelle mit einer horizontalen Auflösung nahe 1 km betrieben. Bei dieser Gitterauflösung sind topographische Effekte wichtig, weil der Einfluss von Hangneigung, Hangexposition, Skyviewfaktor und Abschattung die Strahlungsflüsse an der Oberfläche deutlich modifizieren.

In dieser Arbeit wurde eine einfache und übersichtliche Parameterisierung aus der Literatur modifiziert und in COSMO implementiert, um topographische Effekte auf die Strahlung zu untersuchen. Die Methode basiert auf Korrekturfaktoren für die Strahlungskomponenten an der Oberfläche. Im Kapitel 2 werden die Auswirkungen dieser Parametrisierung bei verschiedenen horizontalen Aufösungen untersucht. Als Vergleich dienten topographieadaptierte Satellitendaten (Globalstrahlung) und Bodenstationen (langwellige Strahlung). Die Qualität der Strahlungsvorhersage ist mit dem neuen Korrekturschema sowohl für kurzwellige als auch für langwellige Strahlung deutlich verbessert worden. Die positiven Effekte können auch in der oberflächennahen Temperatur beobachtet werden.

Eine Vorbedingung für jede Validierung und Untersuchung der Qualität eines numerischen Wettermodells ist das Testen seiner Komponenten unter idealisierten Bedingungen. Im Kapitel 3 wird das COSMO-SC ("single column") Turbulenzschema (ein TKE Schema mit einer Schliessung der Ordung 1.5 bzw. des Hierarchieniveaus 2.5) im Rahmen der ersten GABLS Vergleichsstudie (GEWEX Atmospheric Boundary Layer Study) untersucht. Das Modell erreicht eine gute Leistung im Vergleich mit den anderen teilnehmenden Modellen und LES (Large Eddy Simulation). Die Modifikation von einigen Modellparametern, kombiniert mit einer hohen vertikalen Auflösung, hat zur Entdeckung eines wichtigen Stabilitätsaspekts des Turbulenzschemas geführt. In einer von der

Windscherung bestimmten Grenzschicht zeigen die vertikalen Diffusionskoeffizienten unerwartete Oszillationen. Dieser problematische Modellmangel wurde untersucht und verschiedene Lösungen vorgeschlagen. Die unrealistischen Oszillationen konnten durch das Filtern der Windgradienten vor der Evaluation der Stabilitätsfunktionen eliminiert werden. Ausserdem zeigen die Simulationen, dass die Wahl von einem zu hohen minimalen Diffusionskoeffizient zu einem Verlust von wichtigen Grenzschichtstrukturen, wie z.B. dem "low level jet", führen kann.

Im Kapitel 4 wurde ein kleiner Schritt in Richtung grössere Komplexität gemacht. Mit dem gleichen idealisierten ein-dimensionalen Modellsystem des vohergehenden Kapitels wurde ein realer Tagesgang simuliert. Derjenige Fall ist der, welcher bei der zweiten GABLS Vergleichstudie im Rahmen von GEWEX ausgewählt wurde und stammt vom CASES-99 Experiment (zwei volle Tagesgänge).

Die Ergebnisse zeigen einige wichtige Limitierungen der eindimensionalen Modellierung in Fällen mit signifikanter dynamischer Variabilität in Form von räumlichen und zeitlichen Änderungen des geostrophischen Windes. Zusätzlich wurde eine mangelhafte Reproduktion des morgigen Überganges in Termen von Windgeschwindigkeit und Reibungsgeschwindigkeit festgestellt.

Die Verifikation von numerischen Wettervohersagemodellen erfolgt üblicherweise anhand von Vergleichen der Modellresultaten mit lokalen Beobachtungen. Für oberflächennahen Grössen sind Beaobachtungen meist auf 2 m verfügbar. Weil die erste atmosphärische Schicht in den meisten Wettervohersagemodellen wie COSMO höher als 2 m positioniert ist, müssen diese Variablen aus anderen prognostischen Variablen an der Oberfläche und von der ersten atmosphärischen Schicht mit Hilfe von Interpolationsformeln diagnostiziert werden. Fehler in der Diagnose können die Qualitätsevaluation eines Modelles stark beinflussen. Kapitel 5 untersucht die typischen Probleme der 2 m Temperatur- und Taupunkt Diagnose im COSMO Modell in der alpinen Region.

Die COSMO-Diagnose produziert Werte, die zu nahe an den Oberflächenwerten liegen, was z.B. zu einer verstärkten negativen Temperaturabweichung im Winter und einen Phasenfehler der Maximumtemperatur führt. Diese mangelhafte Leistung ergibt sich aus einer unrealistischen Bestand-Höhe, welche die Wahl zwischen exponentiellem und logarithmischem Interpolationsprofil bestimmt. Die effektive Bestandeshöhe wird in COSMO indirekt ahand der Rauhigkeitslänge berechnet, welche wiederum aus einer lokalen plus einer orographischen Komponente zusammengesetzt ist. Ein neue Ansatz, der auf der physikalische Charakteristika des "Roughness Sublayer" basiert, und zusätzlich die lokale von der orographischen Rauhigkeit trennt, wird vorgestellt und mit der aktuellen operationellen Diagnose verglichen. Die Verifikation anhand von einigen Fallstudien zeigt eine signifikante Verbesserung der 2 m Temperatur und 2 m Taupunkt mit dem neuen Verfahren.

# Contents

# Chapter 1

# Introduction

## 1.1 The planetary boundary layer in complex terrain

The planetary boundary layer (PBL) is the part of the atmosphere that is directly influenced by the underlying surface (Stull, 1988). A detailed understanding and modelling of the PBL can in fact allow to better describe and forecast the atmospheric environment, where people live. In the PBL temperature and humidity are affected by the transfer of heat and moisture to and from the surface of the Earth, which are driven by turbulent transport processes. Friction at the surface leading to shear stress slows the wind, generating a vertical wind gradient and a consequent downward turbulent transport of momentum. Heat, moisture and momentum fluxes from or to the surface modify the state of the boundary layer. The surface energy balance is the central engine of the PBL, influencing the availability of energy at the surface. The PBL is usually warmed by an upward transfer of heat from Earth's surface during the day and cooled by a downward transfer of heat from the atmosphere to the Earth's surface during the night (Whiteman, 2000). A correct simulation of the diurnal cycle, for instance the change from stable to unstable situations and vice-versa, is a very important issue in order to properly describe the PBL. For the unstable or convective boundary layer (CBL) during daytime one of the important challenges is the proper description of the interactions between the different scales of turbulent eddies, spacing from the very small eddies related to turbulent dissipation up to the large scale eddies leading to convection. For the stable boundary layer (SBL) several aspects play an important role, because different physical processes are involved (Nieuwstadt, 1984a,b): topographical slope effects (Whiteman, 2000; Whiteman et al., 2004), intermittent turbulence, internal gravity waves and meandering motions as well as surface heterogeneities can play an important role (Mahrt, 1999). Different physical approaches for each of these processes are necessary.

PBL meteorology faces a challenging task: it should be able to understand and explain PBL processes over flat and horizontally homogenous terrain, over surfaces with large roughness elements and over inhomogenous and complex terrain. The smaller degree of complexity has favoured the knowledge and understanding over flat and horizontally homogenous terrain. In fact, through the pioneer work of Monin and Obukhov (1954), Willis and Deardoff (1974) and Nieuwstadt (1984a,b) on similarity theory, Kolmogorov (1941) or Kaimal et al. (1972) on spectral characteristics of turbulence, PBL meteorology has focussed most of the research on the flows over flat and horizontally homogenous terrain. The detailed investigation of the vertical turbulence structure of the PBL in field campaigns over flat and generally homogenous terrain as in Kansas (e.g. Haugen et al., 1971; Businger et al., 1971) or large eddy simulations (e.g. Deardoff, 1972; for a review see Nieuwstadt et al., 1993) led to the development of Local, Surface Layer and Mixed Layer similarity and scaling approaches for SBL and CBL (see, e.g., the review in Holtslag and Nieuwstadt, 1986).

The first step towards more complexity is the detailed description of the surface layer, the region at the bottom of the PBL, which extends up to some 10% of the PBL height (Stull, 1988). In the surface layer, wind and stress exhibit negligible rotation with height and turbulence is one of the main processes influencing the local meteorological situation. The roughness elements strongly influence the turbulent flow and have to be considered in order to properly describe the lower part of the surface layer. Generally, two main sublayers can be identified in the surface layer: (i) the inertial sublayer (ISL) and (ii) the roughness sublayer (RSL) (Garratt, 1992; Raupach et al., 1991). In the ISL the turbulent fluxes vary less than 10% and for this reason is also known as constant flux layer. It is also the region within which the wind velocity profile in neutrally buoyant conditions is logarithmic and where the Monin-Obukhov similarity theory ("Surface layer scaling") can be applied in order to describe the turbulence processes. The RSL is directly influenced by the three-dimensional distribution of the roughness elements at the surface in form of canopy elements (vegetation, buildings, small topography structures): the constant flux assumption is no more valid and deviations from the logarithmic profile are observed (Garratt, 1992; Raupach et al., 1980; Garratt, 1980). Turbulence in canopies is augmented by the presence of foliage and buildings, because additional drag force is exerted (Garratt, 1992). Inside the canopy, heat and other scalar properties - like water vapour - are exchanged between the flow and the canopy elements. The elements in the canopy generate turbulent wakes, transforming mean kinetic energy into turbulent kinetic energy (Raupach and Thom, 1981). For the special conditions within the RSL urban and vegetation canopy single-layer and multi-layers models have been developed (e.g. Martilli et al., 2002; Yamada, 1982; Wilson and Shaw, 1977; Wilson, 1988; Pinard and Wilson, 2001).

No large experimental and modelling evidence is presently available on the turbulence structure and scaling approaches in a complex terrain - such as mountainous areas - either in stable or convective boundary layer situations (Weigel and Rotach, 2004). However, several studies have been carried out on additional single complications (to the homogenous and flat conditions) such as gentle hills or idealized slopes (e.g. Taylor and Teunissen, 1987; Vosper and Mobbs, 1997, 2002), and on more "global" aspects of the boundary layer over steep and mountainous terrain. In particular, the nature and the properties of the mountain wind systems have been considered and well documented. These can generally be mechanically or thermally driven. Mechanically forced and terrain forced flows have their origin from the interaction between large scale synoptic winds and the complex topography. Typically observed are accelerated air flows, channelling effects, blocking effects, flow separation effects, creation of vortices, wakes or mountain waves, as well as special situations with mountain overflow. Because diurnal mountain winds are driven by horizontal temperature differences, the regular evolution of the winds in a given valley is closely tied to the thermal structure of the atmospheric boundary layer within the valley, which is caracterized by a cycle of buildup and breakdown of temperature inversions (Whiteman, 2000, 1982, 1990; Whiteman et al., 1999b,a; Colette et al., 2003). A comprehensive overview of the mountain wind systems can be found in Whiteman (2000) and Barry (1992) as well as in Blumen (1990).

One of the first research attempts performed in very complex terrain in the Alps and realized in the framework of the Mesoscale Alpine Programme MAP (Bougeault et al., 2001) in the Riviera Valley (Weigel et al., 2007a,b) shows that traditional scaling relationships based on the Monin-Obukhov similarity theory (Monin and Obukhov, 1954) are not directly valid in an alpine valley (Rotach et al., 2004; Rotach and Zardi, 2007). The typical PBL key processes such as exchange of momentum, heat and moisture, are not only affected by the complex turbulence structure mentioned above, but also by several topographical effects on radiation and by mesoscale (meso-$\gamma$ and meso-$\beta$) thermally and mechanically driven mountain wind systems. Also very special local topographic situations like sinkholes or basins can have complex temperature evolutions during

the wintertime (Whiteman et al., 2003).
The complexity of the boundary layer processes and wind systems normally interact also with the synoptic weather situation creating a broader range of different situations. Large scale synoptic systems and associated winds, clouds or precipitation can enhance, modify or even inhibit these local processes in the mountainous boundary layer (Whiteman and Doran, 1993; Whiteman, 2000).

## 1.2 Numerical weather prediction in complex terrain

MeteoSwiss (Federal Office of Meteorology and Climatology, Switzerland) operationally uses for numerical weather prediction (NWP) the COSMO model at present at 7 km and very soon also at 2.2 km horizontal resolution. The COSMO model is a non-hydrostatic NWP model (formerly known as "Lokal-Modell" LM in Germany or "Alpine Model" aLMo in Switzerland) initially developed at the "Deutscher Wetterdienst" (DWD) (Steppeler et al., 2003) and later in the framework of the COSMO consortium (COnsortium for Small-scale MOdelling).

The general desire of the meteorological forecaster community for a reliable point or postal code NWP over highly complex topography in the Alps is still an extremely challenging task. Beyond the aspects related to the predictability of some important meteorological situations like local convection - even using high resolution simulations (e.g. Hohenegger and Schär, 2007; Walser et al., 2004) - operational verifications in the PBL over the Swiss Alps clearly show that a state-of-the-art limited area mesoscale model such as COSMO has pronounced model deficiencies (e.g. Schubiger, 2002, 2003; Walker, 2005; Pflüger, 2003, 2004; Arpagaus et al., 2006).

Two reasons can generally explain this common verification experience. First, the coarse horizontal resolution has as unavoidable consequence that the model topography and the surface description are very different from the real one. Dependent on the horizontal grid resolution, height differences of several 100 m are usual (even at 2.2 km horizontal resolution). In addition, nearly all the main alpine valleys are not fully resolved. All the unresolved processes have to be parameterized and simplifications are unavoidable. For example, the observed subgrid scale surface heterogeneity over an area covered by a model gridbox can be large. Nevertheless, the majority of NWP models employ an averaged land use for the entire grid cell. This strongly influences the ability of the NWP model to reproducing the correct surface turbulent fluxes (Mölders and Raabe, 1996), having consequences also in the vertical caracteristics of the PBL (Molod et al., 2003). Ament and Simmer (2006) have shown that an improved representation of the land-surface heterogeneity with a subgridscale mosaic approach better reproduces the observed turbulent fluxes at the surface.
Second, the used boundary layer parameterizations, which should represent all the unresolvable or sub-grid scale processes, are generally inappropriate for highly complex terrain, because they have originally been developed for flat environments (Rotach, 1995; Rotach and Zardi, 2007). Additionally, further topographical effects and special local conditions (e.g. snow coverage), have to be accurately reproduced. All these aspects strongly limit the range of potential use of direct model output.

Mesoscale limited area NWP models used until the beginning of the 1990ies have generally been hydrostatic and showed generally pronounced deficiencies over very complex topography mainly due to the coarse resolution. The improvement of the available computing resources allowed for using also grid spacing below 10 km. Because at resolutions less than 10 km the hydrostatic approximation is not any more justified and non-hydrostatic effects have to be considered, some NWP models have been reformulated without this simplification and some necessary techniques have been developed to deal with wanted and unwanted hydrostatic effects. In the beginning of the 1990ies the time of the non-hydrostatic models started and several ones emerged. Examples are the Pennsylvania State University-NCAR fifth generation model MM5 (Dudhia, 1993; Grell et al., 1995), the Regional Atmospheric Modelling System RAMS (Pielke et al., 1992), the Canadian

Mesoscale Compressible Community NWP Model MC2 (Benoit et al., 1997) and the Advanced Regonal Prediction System ARPS (Xue et al., 2000, 2001). In the recent years several new non-hydrostatic models such as AROME (MeteoFrance) have been developed.

Experience gained in the last 10-15 years in the United States with the non-hydrostatic modelling approach is currently being used in the further developement of the new non-hydrostatic mesoscale Model NMM from NCEP (National Center for Environmental Prediction) (Janjic, 2003), that can be used with a resolution down to 100 m. Since 2004, NMM is part of the Weather Research and Forecasting system together with the WRF (Weather Research Forecasting Model) from NCAR (National Center for Atmospheric Research).

At the end of the 1990ies the "Lokal Modell" (LM) (Steppeler et al., 2003) and later its Swiss version (aLMo), both now called COSMO, became operational with a 7 km horizontal resolution. COSMO was one of the first non-hydrostatic models used operationally by an European weather forecast service.

The new generation of NWP hydrostatic models is or will be soon operated at horizontal resolution near 1 km. At this grid spacing additional physical aspects have to be considered. Coarse resolution models compute for example the radiation fluxes on horizontal surfaces (e.g. Ritter and Geleyn, 1992). At very high resolution topographic effects become important also for weather modelling, because the impact of slope aspect, slope angle or slope inclination, skyview factor as well as shadowing effects significantly modify radiation fluxes at the Earth's surface.

In the framework of MAP many experiments with high-resolution NWP models have been carried out in the Swiss Alps. Operational limited-area NWP models or research models have been used at high resolution. Some experiments have been carried out with the NWP Model MC2 with a resolution of 3 km to study predictability aspects of precipitation events (Walser and Schär, 2003). Zängl et al. (2004a) carried out numerical simulations for the lower Rhine valley with the MM5 using mesh sizes of 27, 9, 3, 1 km respectively. The observed flow evolution could essentially be reproduced correctly. Discrepancies to observations were mainly restricted to errors in the time of Föhn breakthrough and in the time of the cold front passage. Gohm et al. (2004) simulated a Föhn episode with the MM5 at several resolutions with an iteratively nesting procedure down to 267 m (with 5 intermediary nesting steps) and compared them with remote or in situ observations. The simulations were able to reproduce qualitatively well the observed patterns except for a shallow Föhn phase. This latter was not reproduced, because of a significant inaccuracy in the physical process forming a stable inversion layer as the flow approached the main Alpine crest. The results also showed the importance of a proper resolution of the model topography to capture narrow gaps and stressed the need for improvements of boundary layer parameterizations to include the effect of the surrounding topography. Zängl et al. (2004b) also performed numerical simulations with the MM5 at 800m and 1.4 km horizontal resolution for a southern Föhn episode in the Wipp Valley (Innsbruck region). An encouragingly large part of the observed flow features could be well reproduced by the simulations. Except for a small region to the east of Innsbruck, the Föhn breakthrough was correctly predicted to within an hour. As expected reduction of the horizontal resolution from 800 m to 1.4 km deteriorated the model performance mainly in marginally resolved side valleys, but not in the larger Wipp Valley. DeWekker et al. (2005) applied RAMS on a 333 m grid in the Riviera Valley. They were quite successful in reproducing temperature profiles, but some deficiencies in the flow structure have been observed.

Another perspective for high resolution simulations is given by the concept of Large Eddy Simulation (LES). Here, in contrast to the commonly used Reynolds averaging approach (in RANS models), the Navier-Stokes equations are spatially filtered on a well defined length scale, i.e. the larger scale of the turbulence spectrum is explicitly resolved. For the smaller scales a subgrid-scale turbulence model is used (e.g. Smagorinsky, 1963; Deardoff, 1980; Moeng, 1984). The method of LES was applied with the ARPS model in the Riviera Valley in the Swiss Alps (Weigel et al.,

2007b,a; Chow et al., 2006). Weigel et al. (2007a) initialised ARPS (Xue et al., 2001, 2000) with initial and boundary conditions from the ECMWF model (European Centre for Medium Range Forecast) with a resolution of 60 km, for simulations of the boundary layer structure in the Riviera Valley. The model setup was based on iteratively nesting from 9 km down to 150 m with 3 intermediary steps. ARPS was adapted to the Riviera Valley conditions and specially initialised using additional information provided by a hydrological model to properly describe the distribution of soil moisture. The simulation results showed that the model could accurately reproduce the wind patterns observed under convective conditions in this highly complex terrain.

## 1.3 The COSMO model

The COSMO model is a limited area atmospheric prediction model initially developed at the DWD and later in the framework of the COSMO consortium (Consortium for Small-scale Modelling). A 7 km (since 2001) and a 2.2 km version (since 2008) are used operationally by MeteoSwiss for NWP purposes. The NWP system of MeteoSwiss, with corresponding forecast domains at 7 km and 2.2 km is presented in Fig. 1.1.

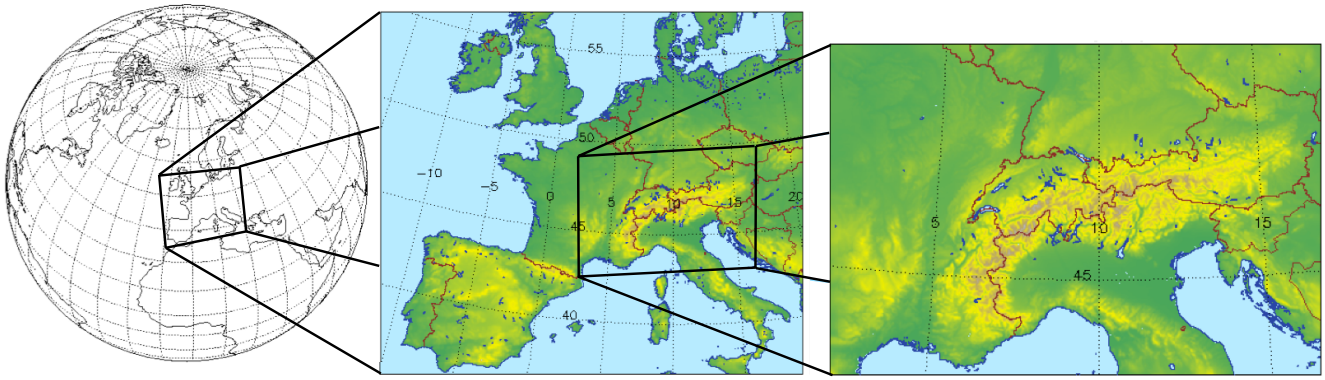


Figure 1.1: Setup of the MeteoSwiss NWP system based on the global model IFS for boundary conditions and initialisation of COSMO-7, COSMO-7 with 7 km horizontal resolution and COSMO-2 with 2.2 km resolution. COSMO-2 and COSMO-7 are one way nested.

In the COSMO model the three-dimensional fully elastic and non-hydrostatic atmospheric equations are solved numerically with second or third order finite difference methods on a Arakawa-C/Lorenz grid (Arakawa and Lamb, 1977) based on a rotated geographical (lat/lon) coordinate system. No scale approximations are performed. Vertically a stretched terrain-following grid after Gal-Ghen et al. (1975) is used and an option for the SLEVE vertical grid is available (Schär et al., 2002). The prognostic variables include pressure perturbation, Cartesian wind components, temperature, specific humidity, cloud liquid water, cloud ice, rain, snow and turbulent kinetic energy.

In the recent past the commonly used numerical solver was based on the Leapfrog time integration scheme (three-time-level scheme with centered differences, horizontally explicit), which is a variant of the numerical scheme proposed by Klemp and Wilhelmson (1978) with the extensions proposed by Skamarock and Klemp (1992). In 2004 a new numerical solver has been added as an option and this is used since 2007 for operational purposes, mainly for high resolution simulations. The new numerical core is based on a Runge-Kutta time integration scheme (Wicker and Skamarock, 1998; Förstner and Doms, 2003), which considers two time levels. The original Runge-Kutta integration scheme has been modified to a third-order upwind formulation and a

fifth-order horizontal advection formulation, as suggested by Wicker and Skamarock (2002). In the near future this new numerical solver will fully substitute the Leapfrog scheme. The three-dimensional precipitation transport is considered through the introduction of advection for the mixing ratios (liquid water, snow and ice). The lateral boundaries are treated with a one-way nesting from a driving model using the lateral boundary formulation according to Davies (1976). At the boundaries and for initialisations purposes the global model IFS of the European Centre for Medium Range Forecast (ECMWF) is used.

The physics package of COSMO considers 6 main components: radiation, precipitation microphysics, convection, soil and surface processes, turbulence in the atmosphere and turbulent transport at the surface. Radiation is computed on horizontal surfaces with a $\delta$-two stream radiation scheme (Ritter and Geleyn, 1992). The grid-scale cloud and precipitation scheme is based on a bulk microphysics parameterization including water vapour, cloud water, rain, snow, ice and optionally graupel (Reinhardt and Seifert, 2006; Kessler, 1969). A mass-flux convection scheme after Tiedke (1989) with a closure based on moisture convergence parameterizes subgridscale deep convection. At 2.2 km horizontal resolution deep convection is supposed to be explicitly resolved and the deep convection scheme is switched off leaving only the shallow convection part to be active. Two different soil models can optionally be used: a two layers model after Jacobsen and Heise (1982) and a multi-layer model after Schrodin and Heise (2001). The vertical turbulent transport is formulated with a TKE scheme following the 1.5 oder turbulence closure at the hierarchy level 2.5 proposed by Mellor and Yamada (1982) in the framework of their hierarchical model (Mellor and Yamada, 1974), considering also subgrid scale humidity fluctuations (Doms et al., 2001; Raschendorfer, 2007a, 2001). The surface transfer scheme based on the framework of the same turbulence scheme (Raschendorfer, 2007a) permits to compute the turbulent fluxes between the rigid surface and the lowest atmospheric layer delivering the transfer coefficients, which are based on transfer resistances for momentum and scalars (temperature and moisture) along three sub-layers of the transfer layer.

The COSMO model at MeteoSwiss uses a data assimilation system based on a nudging technique (Schraff, 1997). For high resolution simulations (e.g. at 2.2 km) also the assimilation of radar reflectivity is possible with the latent heat nudging technique revisited by Leuenberger and Rossa (2007).

Since 2007 a single column version of the COSMO model is available. The single column COSMO-SC model works in a hydrostatic environment and uses terrain following hybrid pressure levels. The same physical parameterizations of the NWP model are available and several forcings such as the geostrophic forcing or large scale subsidence (vertical advection) can be applied (Raschendorfer, 2007b).

## 1.4 Objectives and outline

In a NWP limited area model such as COSMO three main model components can be distinguished:

- Numerics: numerical solution of the model equations, horizontal and vertical advection.
- Physical parameterizations: radiation, turbulence, surface/soil, convection and precipitation microphysics.
- Diagnostics: additional non-prognostic variables are diagnosed as function of prognostic variables. The diagnostics calculations are often based on physical parameterizations.

This study focuses the attention on some special parts of the second and third component: the parameterization of radiation in complex terrain, the parameterization of the vertical turbulent diffusion and the 2 m diagnostics for temperature and dew point. The structure of this work covers these three main topics with four chapters, which have the following main research questions:

1. How large is the impact of the topographic effects on radiation in the COSMO model at 7 and 2.2 km horizontal resolution, respectively? Chapter 2 explores the topographic effects on radiation presenting a parameterization scheme based on correction factors.

2. How does the COSMO turbulence scheme perform in a semi-ideal shear driven and stable boundary layer? Chapter 3 assesses the performance of the COSMO turbulence scheme for a semi-ideal case of stable boundary layer simulated with the one-dimensional version of the COSMO model (COSMO-SC) using very high vertical resolution.

3. How well can the COSMO-SC model reproduce a real diurnal cycle? Chapter 4 deals with the simulation of the diurnal cycle for a real case using the one-dimensional version of the COSMO model.

4. Which are the problems in the 2 m temperature and dew point diagnostics in the surface layer over the alpine region? Chapter 5 focuses the attention on the deficiencies of the COSMO 2 m temperature and dew point diagnostics in complex terrain over the Alps.

In the following, the outline of each chapter is briefly presented.

**Chapter 2: Grid and subgrid scale topographic correction of radiation**

Radiation is known as the most important surface forcing factor, because it is both the source and the sink of energy and its balance is significantly influenced by topography. Local slope aspect (slope orientation) and slope angle (slope inclination) considerably modify the amount and daily course of down-welling short wave radiation (e.g. Whiteman et al., 1989; Whiteman, 2000; Barry, 1992; Oke, 1978; Garnier and Ohmura, 1968, 1969; Matzinger et al., 2003). Shading effects in case of higher horizon angle than sun elevation angle generate significant differences in sunrise and sunset times (Whiteman, 1990). In addition, reduced skyview has a significant impact as well, causing a complex spatial variability of the downward longwave radiation and diffuse downward radiation (e.g. Whiteman, 1990; Dubayah and Loechel, 1997).

In order to resolve more important details of the complex topography, NWP models will be operated at finer grid resolution close to 1 km in the near future. At this grid spacing, topographic effects become important also for weather modelling, because the impact of slope aspect, slope angle or slope inclination, skyview factor as well as shadowing effects significantly modify radiation fluxes at the Earth's surface. Müller and Scherrer (2005) have proposed a comprehensive and relatively simple parameterization scheme for mesoscale models, which can either be used in a gridscale or in a subgridscale mode, depending on whether the correction factors are computed on the model topography or in a finer grid and then aggregated on the target model grid.

The aim of Chapter 2 is to investigate the impact and the forecast performance in the COSMO model of both the grid scale and the subgrid scale version of this parameterization scheme at different horizontal resolutions (7 and 2.2 km), introduce improvements where necessary and directly verify the results with radiation measurements.

**Chapter 3: Performance of the COSMO-SC turbulence scheme for a stably stratified boundary layer**

NWP models often show too weak mixing in very stable situations what can lead to run-away characteristics near the ground (Viterbo et al., 1999), i.e. forecasts with extreme cold bias near the surface. This feature is regularly observed in the COSMO model in the Alpine region (mainly over snow surfaces).

A prerequisite for any validation and detailed investigation of model performance is a test of its components under idealised conditions. Horizontally homogenous boundary layers over flat

terrain can easily be investigated with numerical single column models, because the magnitude of the vertical turbulent transport processes characterising the PBL is much larger than in each horizontal direction. The COSMO-SC uses the same physical parameterizations as used for NWP, but in a hydrostatic one-dimensional environment.

In Chapter 3 the physical parameterization of the vertical turbulent diffusion following the 1.5 order turbulence closure at the hierarchy level 2.5 proposed by Mellor and Yamada (1982), implemented in COSMO by Raschendorfer (2007a), and the surface transfer scheme (Raschendorfer, 2007a) are tested in the framework of the first GABLS intercomparison case (GEWEX Atmospheric Boundary Layer Study, Holtslag et al., 2003; Cuxart et al., 2006). This intercomparison study between several turbulence models (including LES models) has already been completed some time ago without the participation of the COSMO-SC model. Still this shear-driven horizontally homogenous stable boundary layer case is used to benchmark the COSMO-SC turbulence scheme. This study investigates the model performance of the COSMO-SC model and tries to identify any peculiarities of the COSMO turbulence parameterizations, using very high vertical resolution.

**Chapter 4: Performance of the COSMO-SC moldel simulating a diurnal cycle**

Besides the aspects and the challenges related with the stable boundary layer presented for the first GABLS intercomparison study (Cuxart et al., 2006) in the previous chapter, the simulation of the diurnal cycle is an important issue for evaluating the performance of a turbulence scheme. The transition between stable and unstable boundary layers and vice-versa, as well as the processes leading to the formation of the nocturnal boundary layer at sunset, are an interesting issue to be investigated.

The component testing of the previous chapter is extended to a non-steady-state situation, namely a real diurnal cycle in the framework of the second GABLS intercomparison project (Svensson and Holtslag, 2007). This case has been taken from the CASES-99 experiment (Poulos et al., 2002) and covers two diurnal cycles. The final evaluation of the second GABALS case is still ongoing and this time the COSMO-SC model is among the participants.

The purpose of Chapter 4 is to detect more details about the performance of the COSMO-SC turbulence parameterizations using observations taken from the CASES-99 experiment. Additionally, the limits and the sensitivities of the COSMO-SC model in real conditions are investigated.

**Chapter 5: On the 2 m temperature and dew point diagnostics in the COSMO model**

One of the standard verification approaches to evaluate NWP model performance is to compare model results with in-situ observations. For near surface temperature and relative humidity (or dew point) this is done according to the WMO (World Meteorological Organisation) Standards at 2 m.

Because the first atmospheric level in most NWP models, such as COSMO is at about 10 m or higher, these variables have to be diagnosed from prognostic variables both at the surface and at the first atmospheric layer using interpolation formulas. The interpolation is often based on the parameterization scheme of the surface transfer in the surface layer. Deficiencies in the diagnostics can strongly influence the interpretation of the model performance.

Chapter 5 explores the typical problems of the 2 m diagnostics of temperature and dew point in the COSMO model complex topography over the alpine region. The role of the subgridscale roughness length is investigated. In the framework of the surface layer and its sublayers (Inertial Sublayer, ISL and Roughness Sublayer, RSL) a new diagnostic procedure is presented and compared to the operational one. Additionally, two other interpolation formulae are tested and compared to the currently used one.

# Chapter 2

# Grid and subgrid scale topographic correction of radiation

## 2.1 Introduction

### 2.1.1 Topographic effects

Radiation is known as the most important surface forcing factor, because it is both the source and the sink of energy and its balance is significantly influenced by topography. Local slope aspect (slope orientation) and slope angle (slope inclination) considerably modify the amount and daily course of down-welling short wave radiation (Whiteman et al., 1989; Whiteman, 2000; Barry, 1992; Oke, 1978; Garnier and Ohmura, 1968, 1969). Shading effects in case of higher horizon angle than sun elevation angle generate significant differences in sunrise and sunset times (Whiteman, 1990). In addition, reduced skyview has a significant impact as well, causing a complex spatial variability of the downward longwave radiation and diffuse downward radiation (Whiteman, 1990; Dubayah and Loechel, 1997). The work of Whiteman et al. (2004) even suggests that the amount of skyview is the most important topographic parameter controlling minimum temperatures in sinkholes.

Observations in the Riviera Valley during MAP show strong site-to-site contrasts in the amount of the solar downward radiation fluxes. Site-to-site differences in the solar radiation are dependent on the orientation of the valley surfaces relative to the direct solar beam component and on shading from surrounding topography. The diurnal cycle is strongly dependent on orientation: a time lag of about 2 hours and intensity differences between parallel-to-slope and normal-to-slope frames of reference of about 200 $W/m^2$ were observed on inclined surfaces (Matzinger et al., 2003). This important site-to-site variability of the available radiation amount in complex topography is confirmed by simulations combined with observations in the regions of the Lake Tekapo in New Zealand (Oliphant et al., 2003). Skyview restrictions increase the amount of longwave downward radiation and generate variability in the diffuse radiation (Matzinger et al., 2003) and sites with reduced skyview receive a part of the downward longwave and diffuse radiation directly from neighbouring areas (Plüss and Ohmura, 1996).

All these terrain induced modifications of the short and longwave balance have a strong impact on the surface energy budget, affecting also processes like snow melt (Scherer and Parlow, 1994; Zgraggen, 2001). These strong differences also modify sensible and latent heat fluxes (Whiteman, 1990). Finally, the caused differential heating can have a further significant influence on the local cross valley winds like upslope and downslope winds (Whiteman, 2000).

The coarse horizontal resolution of the most commonly used mesoscale NWP models has as unavoidable consequence that the model topography is very different from the real one. Depending on the horizontal grid spacing, height differences of several 100 m between model and real

topography are usual in very complex topography. Considering for example the Swiss Alps, the choice of a coarse resolution model leads to unresolved valleys: at 7 km horizontal resolution, even the largest alpine valleys, such as the Rhine or Rhone Valley, are completely unresolved (Fig. 2.1). This strongly reduces the range of the potential use of direct model output.

In order to capture more important details of the complex topography, the NWP models will be operated in the near future at finer grid resolutions close to 1 km. At this grid spacing, topographic effects become important also for weather modelling, because the impact of slope aspect, slope angle or slope inclination, skyview factor as well as shadowing effects significantly modifies radiation fluxes at the Earth's surface. Only few NWP models, such as MM5, UK Unified Model, HIRLAM and Meso-NH, already consider topographic effects. Shadowing effects are considered in ARPS (Colette et al., 2003; Chow et al., 2006; Chow, 2004; Weigel et al., 2006; Weigel, 2005), in NMM (Müller and Scherrer, 2005; Janjic, 2003) and HIRLAM (Senkova et al., 2007). The other models describe the solar radiation amount depending on the topography only using slope angle and slope aspect, neglecting shadowing effects and processes related to a reduced skyview.

The COSMO NWP model (Steppeler et al., 2003; Doms and Schättler, 2003a; Doms et al., 2005; Doms and Schättler, 2005) is operated at 2.2 km resolution since 2008 at MeteoSwiss. The COSMO-radiation scheme was developed by Ritter and Geleyn (1992) for coarse mesoscale NWP models computes all the surface radiation components as well as all other radiation fluxes on horizontal surfaces. Only the height of the atmospheric column above a grid point takes into account to some extent topographic aspects. If the atmospheric path of the solar and longwave radiation is longer, further scattering, reflection and absorption effects can occur. In addition, all the radiation fluxes are computed in a vertical column without considering effects coming from neighbouring grid points such as cloud shadowing. These approximations of the radiation flux problem allow to save computational resources, while still maintaining a considerably high forecast quality. Before considering a complicated wide reformulation of this scheme in a complex topography and a complete three-dimensional environment, a concept based on the correction of the surface radiation components only can help to investigate the impact of topographic effects at the chosen horizontal resolution. Müller and Scherrer (2005) have proposed a comprehensive and relatively simple parameterization scheme for mesoscale models. This scheme can be either used in a gridscale or in a subgridscale version, depending on whether the correction factors are computed on the model topography or in a finer resolved grid and then aggregated on the target model grid.

The aim of this study is to investigate the impact and the forecast performance in the COSMO model of both the grid scale and the subgrid scale version of this parameterization scheme at different horizontal resolutions. First, the parameterization scheme itself and the needed topographical parameters will be presented, including also the introduced modifications compared to the work of Müller and Scherrer (2005). Then, the attention will be focussed on the observed impact and on the verification results. Finally, an outlook and conclusion with also some practical considerations for an operational use will be outlined.

### 2.1.2 The parameterization scheme

The flux arriving to a sloping surface is given by the formula of Kondratiev et al. (1978), widely used in meteorology (e.g. in Whiteman et al., 1989; Nunez, 1980):

$$\downarrow SW^{*}_{\mathrm{dir}} = \downarrow SW_{\perp \mathrm{dir}} \cdot \cos\alpha = \frac{\downarrow SW_{\mathrm{dir}}}{\sin\theta_S} \cdot \cos\alpha \tag{2.1}$$

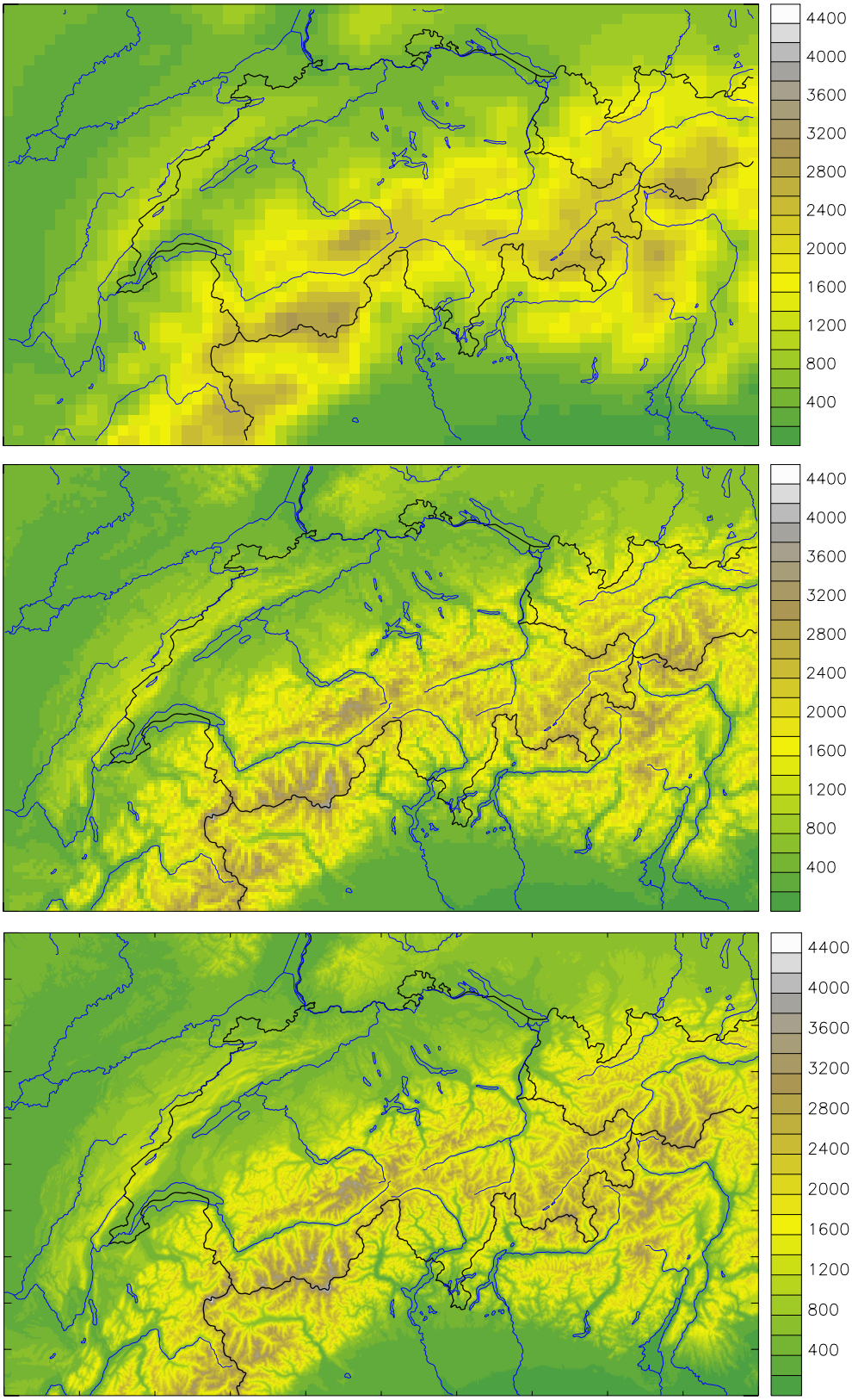


Figure 2.1: COSMO model topography and real topography over Switzerland in m above see level: upper panel 7 km resolution, middle panel 2.2 km resolution, bottom panel real topography with a 200 m resolution. The coarser the resolution the lower is the ability to resolve Alpine valleys such as Rhine and Rhone Valley.

$\downarrow SW_{\perp \mathrm{dir}}$ is the shortwave direct radiation flux on a surface perpendicular to the sun rays and $\downarrow SW_{\mathrm{dir}}$ is the corresponding flux on a horizontal surface. $\cos\alpha$ is the geometry factor, $\alpha$ is the angle between the direction of the solar beam and the normal of the sloping surface, and $\theta_S$ is the sun elevation angle ($\theta_S = 90° -$ azimuth angle). The dependence of the geometry factor from the sunshine and topographic conditions has been described by Kondratiev (1977):

$$\cos\alpha = \cos\theta_N \cdot \sin\theta_S + \sin\theta_N \cdot cos\theta_S \cdot cos(\phi_S - \phi_N). \tag{2.2}$$

See the list of symbols (page 183) and Figure 2.2 for the definition of the involved angles. Inserting Eq. 2.2 in Eq. 2.1 and introducing also shadowing effects with a shadow mask, we are able to correct the radiation component (computed on a horizontal surface) with respect to the inclined surface.

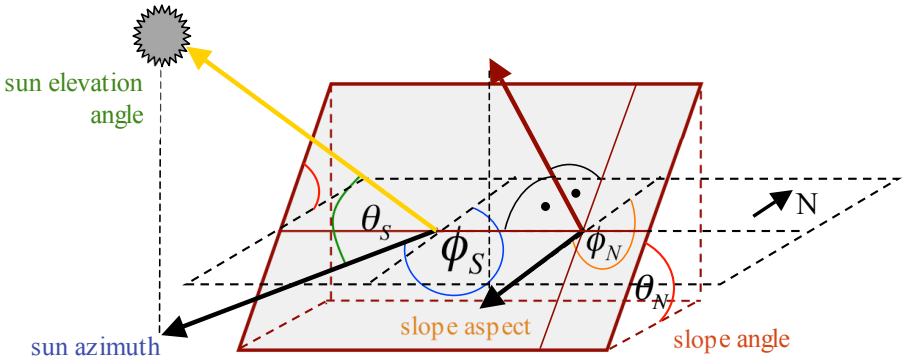


Figure 2.2: Definition of the angles used for the computation of the correction factors for direct radiation. The north direction is the reference for the sun azimuth (blue) and slope aspect (orange), which are defined as the projection on the horizontal plane of the yellow (direct solar beam) and brown vector (normal vector to the sloping surface), respectively.

$$\downarrow SW^*_{\mathrm{dir}} = \downarrow SW_{\mathrm{dir}} \cdot mask_{\mathrm{shawow}} \cdot \left[\cos\theta_N + \frac{\sin\theta_N}{\tan\theta_S}\cos(\phi_S - \phi_N)\right] \tag{2.3}$$

The term in the brackets in Eq. 2.3 corresponds to the correction factor for direct solar radiation in absence of shadowing effects. Multiplying it with the shadow mask gives the correction factor $f_{cor}$:

$$f_{cor} = mask_{\mathrm{shawow}} \cdot \left[\cos\theta_N + \frac{\sin\theta_N}{\tan\theta_S}\cos(\phi_S - \phi_N)\right]. \tag{2.4}$$

Notice that a negative value of $f_{cor}$ is considered as a shadowing effect: no direct radiation reaches the sloping surface. The correction factor allows to convert the direct solar radiation computed on a horizontal surface to that on a sloping surface. All the used symbols are explained in the list of symbols (page 183).

Some idealised daily cycles of the correction factor $f_{cor}$ are presented in the Figure 2.3 for different slope angles and slope aspects. Clearly the correction factors reach the largest values just after sunrise and just before sunset. In addition the values are larger for larger slope angles. Even values larger than 10 for selected times and slope angles can be reached. Finally, notice also the important role of the slope aspect, which defines the daily cycle asymmetry of the correction factors.

A sloping surface in a model grid box denotes a larger area than a horizontal surface in the same gridbox. All the surface fluxes are generally expressed in terms of energy per unit of gridbox surface area. A change in the surface area due to a sloping surface has to be taken into account and the correction factor (Eq. 2.4) has to further be divided by $\cos\theta_N$. By introducing this further step

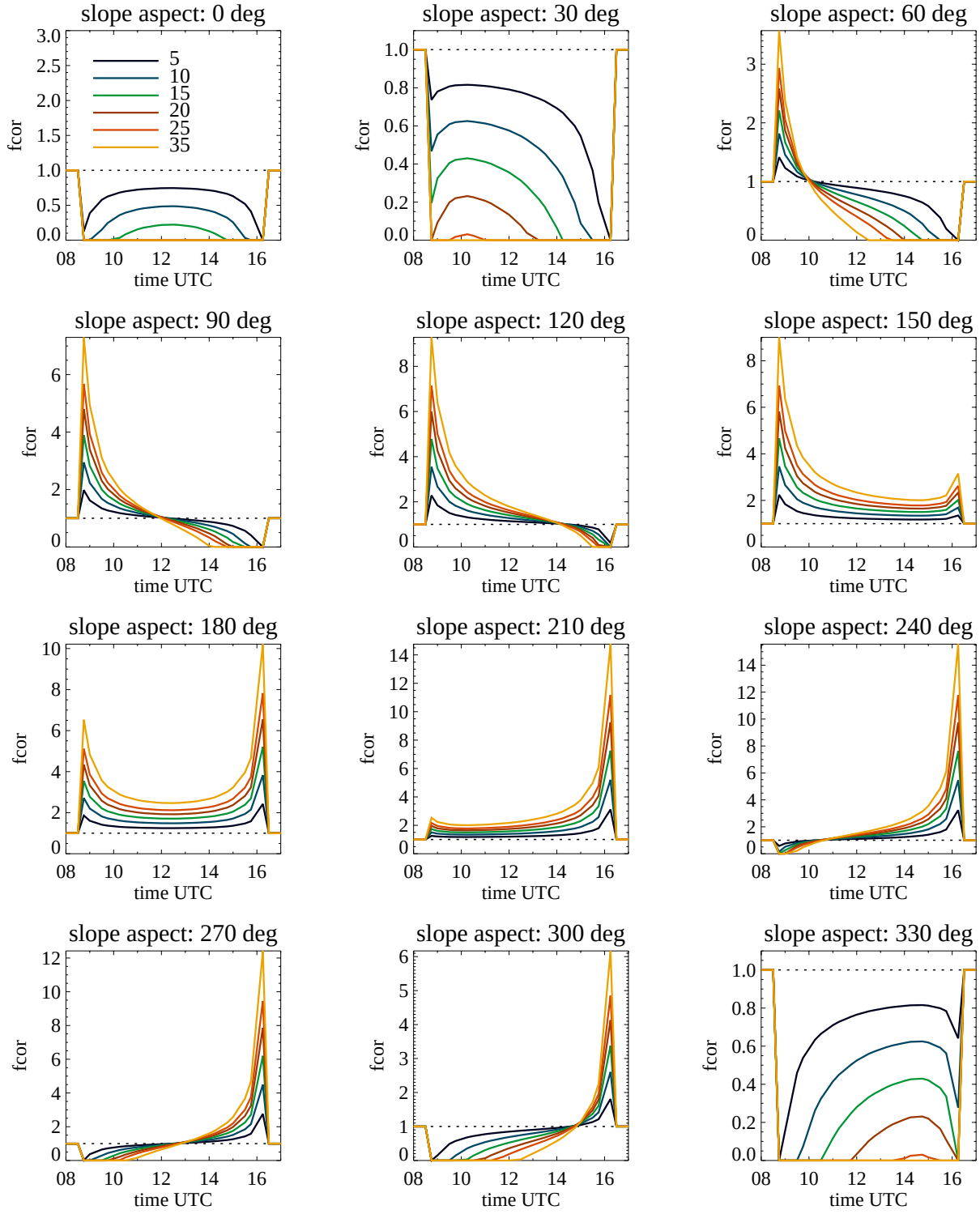


Figure 2.3: Idealized daily cycle of the correction factor $f_{cor}$ for the $21^{th}$ December 2006: each panel corresponds to an hypothetic slope with the indicated orientation (slope aspect, starting from the North and increasing clockwise), each color indicates a possible slope angle from 5 to 35° as described in the first panel. A $f_{cor}$ value of one means that the radiation on the slope corresponds to that on a horizontal surface. If the sun is below the horizon (earlier than sunrise and later than sunset) the $f_{cor}$ value is automatically set to one. Self shading effects due to the tilted plane are considered, while shadowing effects due to surrounding topography are not taken into account.

we arrive to the formula proposed by Müller and Scherrer (2005), which is the correct correction factor formulation for direct solar radiation on inclined surfaces in a model squaregrid (Eq. 2.5 and Eq. 2.6).

$$\downarrow SW^{*}_{\mathrm{dir}} = \downarrow SW_{\mathrm{dir}} \cdot mask_{\mathrm{shawow}} \cdot \left[1 + \frac{\tan\theta_N}{\tan\theta_S}\cos(\phi_S - \phi_N)\right] \tag{2.5}$$

$$f_{cor} = mask_{\mathrm{shawow}} \cdot \left[1 + \frac{\tan\theta_N}{\tan\theta_S}\cos(\phi_S - \phi_N)\right] \tag{2.6}$$

However, this additional step has to be considered with particular attention. In fact, in order to avoid inconsistencies in the surface energy balance, the other components also should be adapted to an effective larger surface area: diffuse shortwave radiation, longwave energy balance, sensible heat flux, latent heat flux and ground flux have to be scaled considering the increased surface area. Applying the surface enlargement to all the surface fluxes in the surface energy balance is equivalent to use for direct solar radiation directly Eq. 2.3 instead of Eq. 2.5, leaving the other fluxes unchanged. For this important reason, the correction factor formulation for the direct shortwave radiation used in this study (Eq. 2.4) differs from that in the work of Müller and Scherrer (2005)(Eq. 2.6). In comparison to our results Müller and Scherrer (2005) obtain higher correction factors, whether they receive more (values above one) or less radiation than an horizontal surface (values below one). The quantitative difference reaches values up to 20%. An example of the observed quantitative differences in the correction factors is given in Fig. 2.4.

The shadow mask is part of the correction factors for direct solar radiation (Eq. 2.4) and is defined as follows comparing the sun elevation and the horizon angle evaluated in the direction of the sun azimuth:

$$mask_{shadow} = \begin{cases} 0, & \theta_S < \theta_{h,\phi_S} \\ 1, & else \end{cases} . \tag{2.7}$$

The topographic effects on diffuse radiation are caused by the reduced skyview. Effective diffuse down-welling shorwave radiation can be approximated, neglecting anisotropy effects as proposed by Müller and Scherrer (2005):

$$\downarrow SW^{*}_{\mathrm{diff}} = \downarrow SW_{\mathrm{diff}} \cdot f_{\mathrm{sky}} + \uparrow SW_{\mathrm{diff}} \cdot (1 - f_{\mathrm{sky}}) \tag{2.8}$$

where $f_{\mathrm{sky}}$ is the skyview factor. The second term of Eq. 2.8 is the part of down-welling shortwave radiation reflected by adjacent areas. This contribution to the total diffuse downward radiation assumes, beside neglecting anisotropy effects, also homogeneous albedo in the neighbouring grid-points.

The longwave radiation may be modified by radiation emitted by adjacent areas and reduced by the skyview. In analogy to the diffuse solar radiation, the downward longwave radiation can be computed as follows:

$$\downarrow LW^{*} = \downarrow LW_{\mathrm{diff}} \cdot f_{\mathrm{sky}} + \uparrow LW \cdot (1 - f_{\mathrm{sky}}). \tag{2.9}$$

The skyview factor $f_{sky}$ measures the degree of site sky visibility and was widely used in many energy exchange studies in different fields such as forestry (Karlsson, 2000), mountain meteorology (Whiteman et al., 2004), urban canyon modelling (Johnson and Watson, 1984) as well as in photometrical applications (Chapman and Thornes, 2004). In mountainous regions the highest skyview factors are found on the mountain crests (Blumen, 1990), while descending into the valleys the visibility of the sky decreases. The smaller the valley cross-section the lower is the skyview factor. Blumen (1990) has proposed the following formulation for the skyview factor $f_{sky}$:

$$f_{\mathrm{sky}} = \frac{1}{n}\sum_{i=0}^{n-1}\left(1 - sin(h_i)\right). \tag{2.10}$$

This formula does not exactly correspond to that published by Müller and Scherrer (2005), which contains an editing error in the position of the summation operator. The formulation proposed by Blumen (1990) seems to have two important disadvantages. First, the skyview factor $f_{sky}$ for a point surrounded with a non-negligible horizon has also to take into account the slope angle. A tilted plane has in fact a smaller skyview factor compared to an horizontal plane. Eq. 2.10 avoids to consider this aspect. Second, it seems to produce unrealistically low skyview factor values, which cause a too strong effect of the surroundings in the radiation correction. The unrealistic skyview factor can simply be illustrated for an idealised site having an homogenous horizon of 45° for each considered sector. In these conditions one would expect a skyview factor of 0.5, because the half of the maximum possible horizon is occupied by topography. However, the above presented formula gives a value of 0.29.

For these two important reasons the computation of the skyview factor has been modified following an integration algorithm developed at MeteoSwiss (Zelenka, pers. communication). This is outlined in the following.
The slope aspect angle $\phi_N$ (azimuth of the tilted plane) defines the azimuth region for the integration leading to the skyview factor: $\phi_N - \frac{\pi}{2} \geq \psi_i \leq \frac{3}{2}\pi + \phi_N$. The entire region is subdivided in n discrete sectors $\psi_0, .., \psi_i, ..., \psi_n$ having an angle of $\Delta\psi$. For each of them, a component $sk_i$ of the whole skyview factor is computed considering inside a constant horizon angle $h_i$. All the skyview factors components are then summed up:

$$f_{\text{sky}} = \frac{1}{\pi} \sum_{i=0}^{n-1} sk_i. \tag{2.11}$$

Defining the height angle of the tilted plane or the horizon limitation due to the surface inclination as

$$hpl_i = atan\left(-sin\psi_i \frac{\sin\theta_N}{\cos\theta_N}\right)$$

it is possible to outline two cases: (1) when the horizon angle $h_i$ is larger and (2) when it is smaller than the plane height angle. In the first $\pi$ radiants of integration ($\phi_N - \frac{\pi}{2} \leq \psi_i \geq \frac{\pi}{2} + \phi_N$), the plane height angle is always smaller than the horizon even in presence of an horizontal plane, therefore the first case represented by Eq. 2.12 is used:

$$sk_i = \left(\frac{\cos\theta_N}{2}(\cos h_i)^2 \Delta\psi - \frac{\sin\theta_N}{2}\left(h_i + \sin h_i \cdot \cos h_i\right)\left(-\cos\psi_{i+1} + \cos\psi_i\right).\right). \tag{2.12}$$

Equation 2.12 is applied also in the second $\pi$ radiants sector of integration ($\phi_N - \frac{\pi}{2} \geq \psi_i \geq \frac{\pi}{2} + \phi_N$) if the plane height angle $hpl_i$ is smaller than the horizon angle $h_i$. In presence of a tilted plane the plane height angle is always greater than zero in this region. On the other hand, if the plane height angle is greater than the horizon angle (second case), equation 2.13 is used:

$$sk_i = \frac{\sin\theta_N}{2}\left(hpl_{i+1}\cos\psi_{i+1} - hpl_i\cos\psi_i\right) + \frac{1}{2}\left(\arctan\left(\frac{\psi_{i+1}}{\cos\theta_N}\right) - \arctan\left(\frac{\psi_i}{\cos\theta_N}\right)\right). \tag{2.13}$$

The other symbols not mentioned in the text have the same meaning as given in the list of symbols (page 183). Figure 2.5 compares the new formulation with that proposed by Müller and Scherrer (2005) for some idealised conditions with a constant horizon. Note the lower values obtained by Müller and Scherrer (2005) and the significant impact of the slope angle on the skyview factor.

In Fig. 2.4 an example of the difference between the new formulation and that of Müller and Scherrer (2005) is given. The differences between the two formulations reach values up to 18%.

Two concluding considerations about the presented parameterization scheme can be made. First, the parameterization of topographic effects on radiation generally follows the procedure

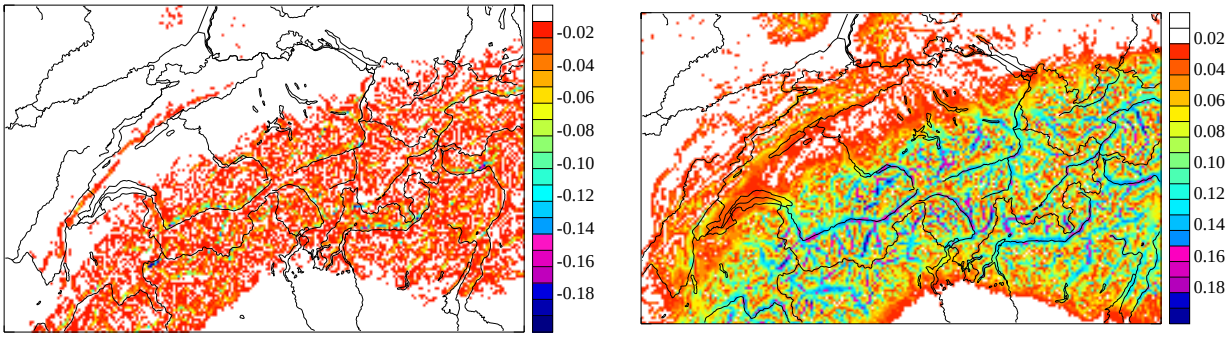


Figure 2.4: Difference in the correction factor for direct solar radiation on 20 December 2006 at 10 UTC (left) and in the sky view factors (right) between the formulation used in this study and that of Müller and Scherrer (2005) for an digital elevation model with horizontal resolution of 2.2 km. The correction factors used in this study present lower values up to 20% (difference is negative) and higher skyview factors up to 18% (positive difference).

proposed by Müller and Scherrer (2005) based on correction factors for direct solar radiation and skyview factors for longwave radiation and diffuse shortwave radiation. Second, the computation of the correction factors and skyview factors has been significantly modified in order to avoid inconsistencies in the surface energy balance and to avoid unrealistic low skyview factors.

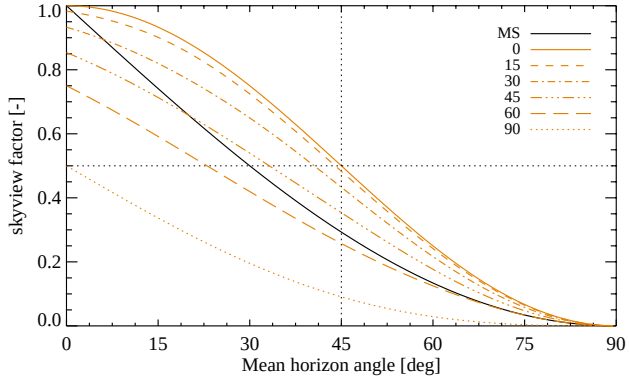


Figure 2.5: Skyview factor as function of an idealised constant horizon angle for all considered sectors: comparison of results obtained with the formulation proposed by Müller and Scherrer (2005) (MS, black line, does not consider slope angles) and that presented in this study (red lines) for different slope angles (in degrees as given in the legend).

In general, two possible implementation variants of this parameterization scheme can be considered. If the topographical parameters (slope aspect, slope angle, horizon and skyview) are computed directly on the NWP model topography we are using the grid-scale option. On the other hand, in the subgrid scale version, they are calculated on a finer grid and then aggregated on the target model grid. Because the topographical adaptation process is highly non-linear, significant differences between the two approaches are expected (this is investigated in Sections 2.5 and 2.6).

## 2.2 Topographical parameters

In order to describe the surface radiation components in a complex topography environment four topographical parameters are necessary: the slope aspect, the slope angle, the horizon and the

skyview factor. They have been calculated for three horizontal resolutions: 7 km, 2.2 km and 0.3 km. The finer resolution was only used for aggregation of the skyview factors or the correction factors for solar radiation on the 2.2 km target grid in order to study the sub-grid scale version of the parameterization scheme.

Necessary base for the computation of the topographical parameters is a Digital Elevation Model (DEM). The COSMO model topography at 7 and 2.2 km is generated starting from the GTOPO30 data set having at the equator 1 km horizontal resolution[1]. For the finer computations at 0.3 km mesh size resolution, the freely available SRTM data set covering the entire planet at about 90 m resolution[2] has been used. The data originally provided by the NASA Shuttle Radar Topographic Mission, has been corrected in order to fill missing values in mountainous areas. The validation of the resulting corrected DEM is promising (Jarvis et al., 2004). The DEM has additionally been carefully validated over the alpine region and corrected using another DEM covering only Switzerland (RITAF) having a 200 m horizontal resolution. The slope exposition, the slope angle and the height values at high altitudes denote a systematic small error which has empirically been corrected (Dürr, pers. communication).

The slope aspect considers the orientation of the model surfaces and has all possible orientation directions from 0 to 360° (Fig. 2.6). At least at 2.2 km horizontal resolution the main alpine valleys can easily be identified, because the main rivers are often the boarder of sharp slope aspect changes.

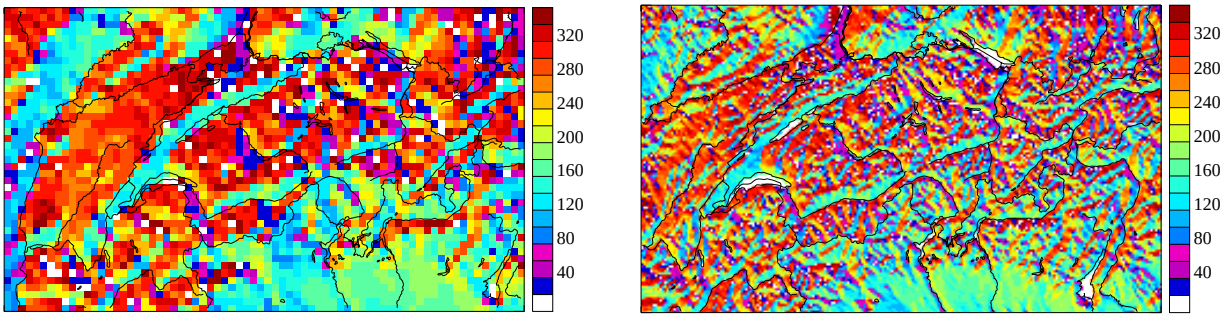


Figure 2.6: Topographical parameters: slope aspect (in degrees) at 7 km horizontal resolution (left) and at 2.2 km resolution (right).

The slope angle varies significantly depending on the horizontal grid space resolution (Fig. 2.7). At 7 km the steepest surface has a slope angle close to 8°, while a maximum value of 30° are found at 2.2 km over the relative COSMO domain. The 0.3 km resolution calculation yields a maximum slope angle of 62°. The common Swiss alpine experience highlights here the important distance between reality and modelled world, giving additional motivation on the way to high-resolution NWP modelling.

The skyview factor is a sort of integrated horizon. Also the horizon values vary considerably with the variation in the horizontal resolution. The horizon is computed every 15° (24 values for each gridpoint) and considers the maximum angle of the topography in a domain of 40 km around the gridpoint. At 7 km no horizon values exceed 13°, while at 2.2 km a maximum of 34° is found. These larger values contrast with those computed at 300 m, where horizon angles reach values up to 57°.
At 7 km resolution the skyview factor assumes only values between 0.98 and 1. For this reason, the effects on thermal and diffuse radiation are expected to probably be negligible or very small. At 2 km the minimum values decrease to 0.82 (Fig. 2.8). By computing the skyview factor on

[1]http://edc.usgs.gov/products/elevation/gtopo30/gtopo30.html
[2]http://srtm.csi.cgiar.org/index.asp

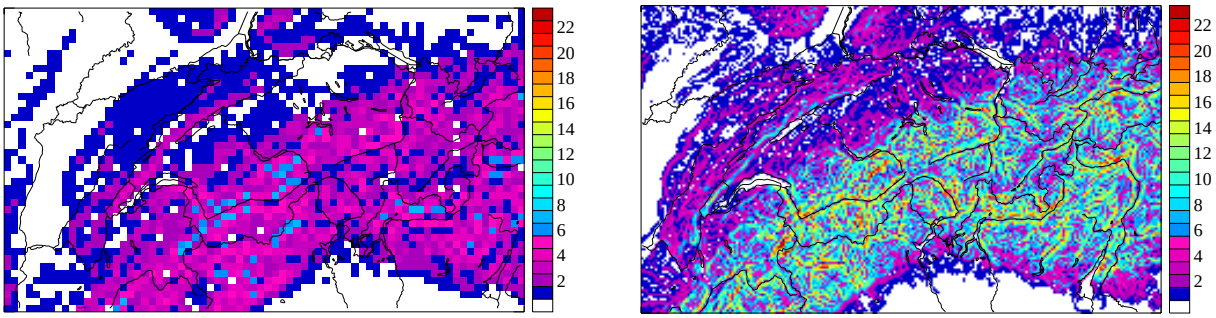


Figure 2.7: Topographical parameters: slope angle (in degrees) at 7 km horizontal resolution (left) and at 2.2 km resolution (right).

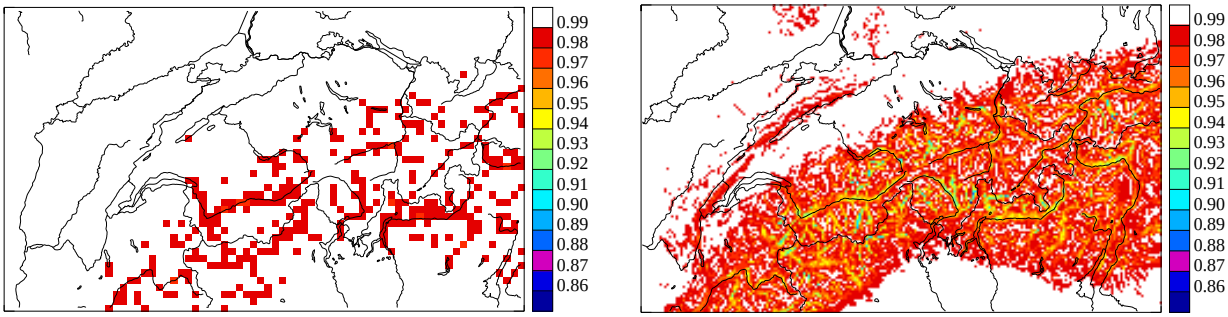


Figure 2.8: Topographical parameters: skyview factor at 7 km horizontal resolution (left) and at 2.2 km resolution (right) computed on the model grid.

a grid with 300 m mesh-size we obtain, as expected, smaller skyview factors: the minimum is close to 0.45. Aggregating the skyview factors computed on a 2.2 km resolution grid, we observe clearly smaller skyview factors compared to the grid-scale computation presented before. This fact highlights considerable non-linear effects between the two scales considered (Fig. 2.9): the aggregation yields generally clearly lower values.

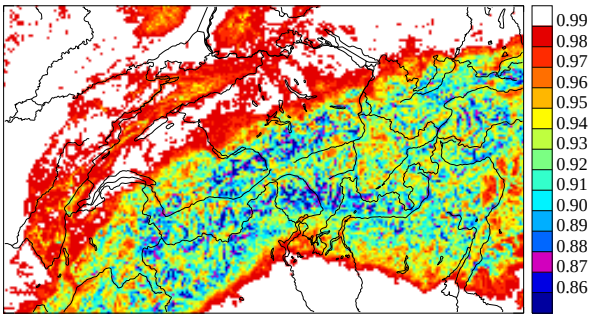


Figure 2.9: Topographical parameters: skyview factor calculated on a 300 m mesh-size grid and aggregated on the 2.2 km grid. Compare to Fig. 2.8 right panel.

## 2.3 Case studies and model settings

The parameterization scheme described in the previous sections was introduced into the COSMO model and evaluated for ten case studies: five in summer and five in winter. For each chosen day, a forecast cascade starting from the European Centre for Medium Range Forecast (ECMWF) analysis has been performed with three necessary steps. First, a COSMO 7 km and 2 km analysis

has been produced and used as initial condition: the 2.2 km analysis run has been nested into the respective 7 km analysis run. Second, a 24 hours 7 km forecast, nested directly into the ECMWF analysis (boundary conditions) has been produced. Finally, a 24 hours 2.2 km forecast nested into the respective 7 km forecast has been performed. The initialisation with an analysis and the use of ECMWF analysis as boundary conditions is expected to have forced the runs at least to a synoptically correct state. The model domain at 7 km extends over western and central Europe with a grid of 385x325 grid points. The 2.2 km model domain covers the entire Alpine region with a grid of 520x350 gridpoints. These are also the operational COSMO 7 km and the pre-operational COSMO 2.2 km domains at MeteoSwiss, respectively. For all the model integrations the COSMO version 3.20 has been used. A multilayer soil model and the new Runge Kutta numerical solver have been used. For more details about the COSMO model see the Introduction 1.3 or the Appendix A. For the 2.2 km runs the convection scheme is switched off and only the shallow convection is parameterized. At this horizontal resolution the model should be able to resolve the deep convection.

Table 2.1 presents the list of the case studies with some key descriptors. The choice of the case studies followed two principles. First, clear sky situations are those in which the direct solar radiation correction is expected to be most important. Second, locally and regionally unstable situations, in which locally induced convection is observed, could help to see if the modified radiation distribution induced by the topography can also influence the triggering mechanisms of local convection. By each model integration, the radiation code and the respective correction

| **Nr.** | **Date** | **Description** |
|---|---|---|
| 1 | 2004.12.11 | Winter, clear sky (above all in the morning) |
| 2 | 2006.12.20 | Winter, clear sky/fog (above all in the morning) |
| 3 | 2006.12.22 | Winter, clear sky/fog (above all in the morning) |
| 4 | 2006.12.24 | Winter, clear sky/fog (above all in the morning) |
| 5 | 2006.12.26 | Winter, clear sky/fog (above all in the morning) |
| 6 | 2003.08.03 | Summer mostly clear sky, some cumulus clouds in the afternoon |
| 7 | 2003.08.07 | Summer mostly clear sky, some cumulus clouds in the afternoon |
| 8 | 2005.06.19 | Summer mostly clear sky, many cumulus clouds in the afternoon |
| 9 | 2006.06.08 | Summer mostly clear sky, some cumulus clouds in the afternoon |
| 10 | 2006.06.18 | Summer local/regional convective case, with precipitation |

Table 2.1: Cases studies: the chosen cases for testing the correction parameterizations.

of the surface radiation components have been called every 15 minutes at 2.2 km horizontal resolution and every hour at 7 km resolution. A higher call frequency is not suitable due to the high computational costs of the radiation scheme. All the model results have been evaluated from an hourly direct model output.

## 2.4 Correction factors for direct solar radiation

From the computed topographical parameters (slope angle and slope aspect) and considering the shadowing effects (comparing horizon and sun elevation angle in the direction of the sun azimuth), it is possible to calculate the corrected direct solar radiation components. The components computed by the radiation scheme (Ritter and Geleyn, 1992) on horizontal surfaces are corrected applying the correction factors for direct solar radiation (Eq. 2.3). Gridpoints that receive less radiation compared with a horizontal surface yield values below one. On the contrary, gridpoints which are more exposed to the solar beam have values above one. Correction factors with value

zero mean that the grid-point is shadowed by the surrounding topography or the combination of slope aspect and slope angle leads to a self shading effect. In the gridscale option, the correction factors are determined using the topographical parameters computed on the model grid (on model topography), while in the subgrid scale option, they are the result of an aggregation of correction factors computed on a finer grid. In the finer grid the correction factors are themselves calculated from the topographical parameters at 300 m. The correction factors as well as the skyview factors are applied every time that the radiation scheme is called (every hour at 7 km and every 15 minutes at 2.2 km).

Generally, the extreme values of the correction factors were observed in the morning (after sunrise) and in the evening (before sunset), where also shadowing effects appear. Shadowing effects are remarkably stronger in the finer grid used for aggregation in the subgrid option, where many gridpoints in the wintertime never have values above zero and are for this reason continuously shadowed. The aggregation on the coarser grid often leads to a mean value above zero, giving in some regions the impression of less shadowing effects. Nevertheless, the correction is globally observed to be significantly larger than those applied in the grid-scale option. The diurnal variation of the sun azimuth leads to a daily cycle in the correction factors: depending on the slope aspect, slopes that have low correction factors or are shadowed in the morning, often experience big correction factors in the evening. The lowest values are found obviously on flat terrain and during the mid-day hours. This confirms the ideal daily cycle of the correction factors presented in Fig. 2.3.

The difference between gridscale and subgrid scale version is relatively important, and can allow us to postulate a significant impact difference between the two parameterization options. Some examples of the spacial correction factor distribution are given in Figure 2.10 (summer day) and Figure 2.11 (winter day). The figures show clearly that on summer days (like the example in June, Fig. 2.10), the correction factors near mid-day are relatively small, compared to those at the same time in winter (Fig. 2.11). In fact, the sun elevation plays an important role.

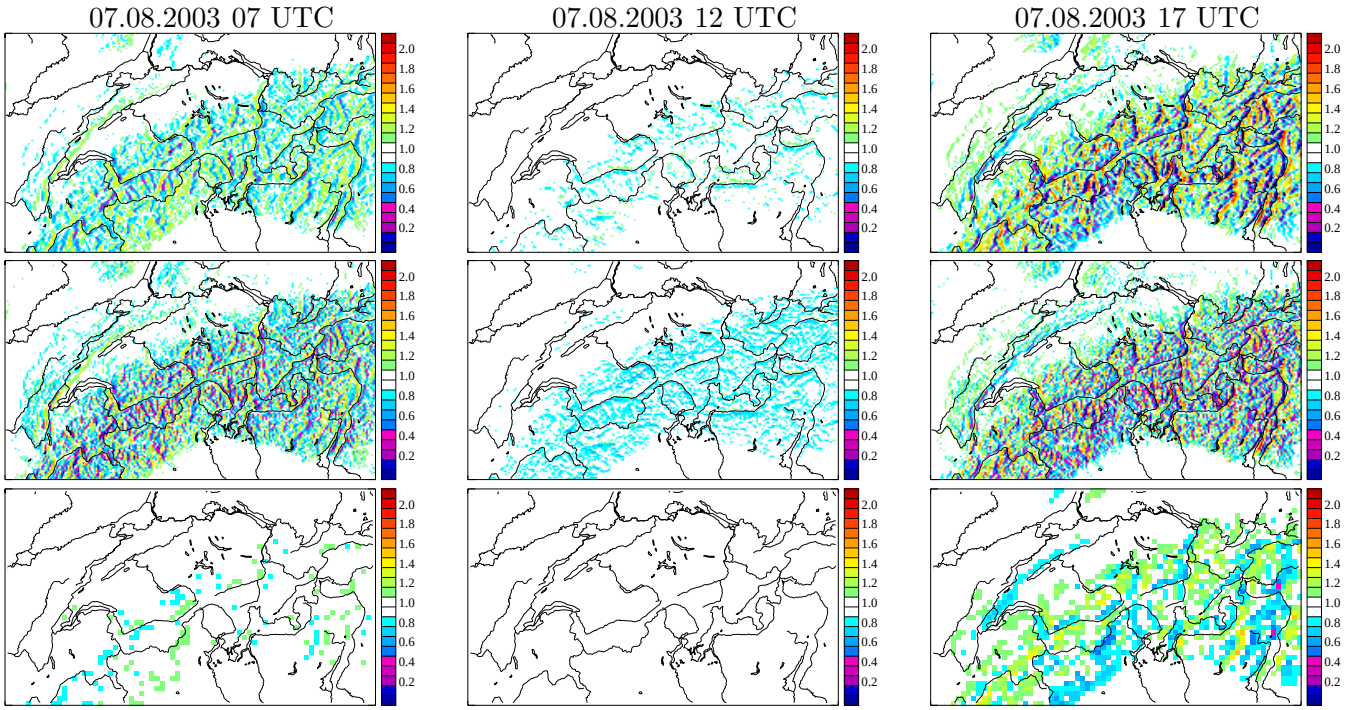


Figure 2.10: Correction factors for direct solar radiation for a summer day (07.08.2003) at 07 (left), 12 (middle) and 17 UTC (right): upper row grid-scale option COSMO-2 (2.2 km), middle row subgrid-scale option COSMO-2 (2.2 km) and lower row grid scale option COSMO 7 km.

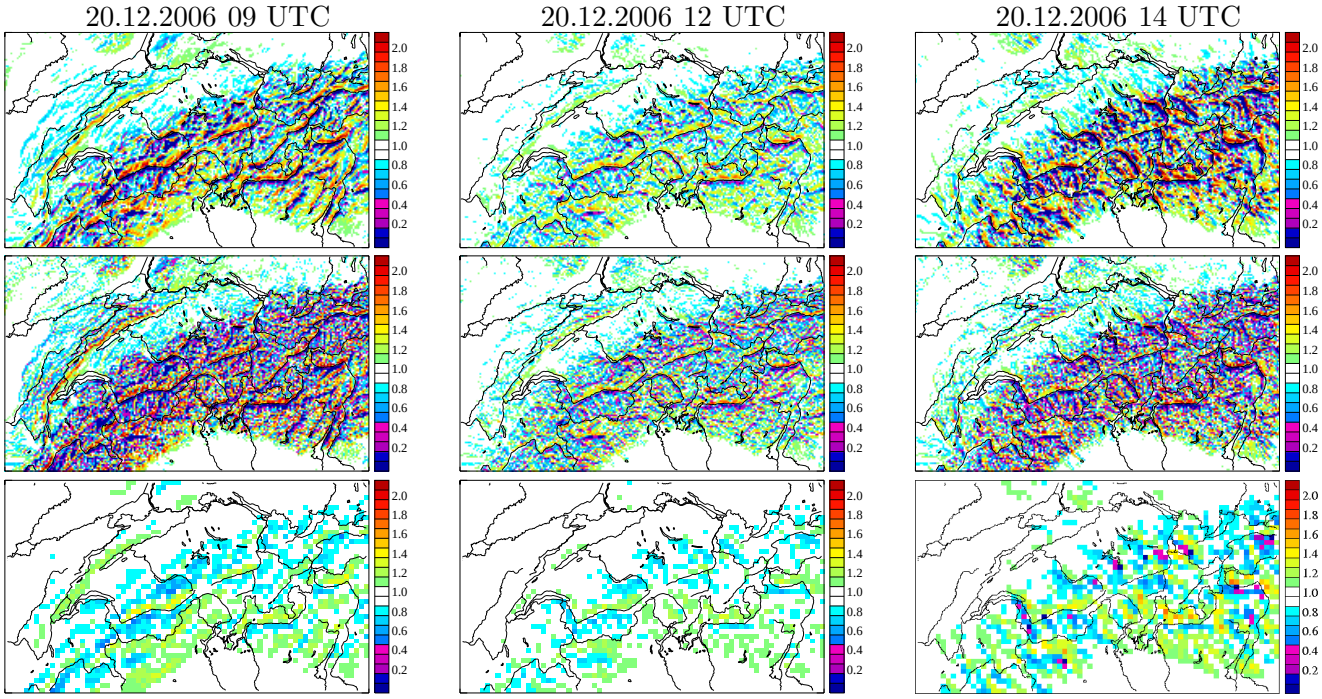


Figure 2.11: Correction factors for direct solar radiation for a winter day (20.12.2006) at 09 (left), 12 (middle) and 14 UTC (right): upper row grid-scale option COSMO-2 (2.2 km), middle row subgrid-scale option COSMO-2 (2.2 km) and lower row grid scale option COSMO 7 km.

## 2.5 Results

The impact of the new radiation correction scheme introduced in COSMO was initially evaluated and compared with the reference run (without radiation correction), and in a second step verified with surface measurements, such as ANETZ/ENET (2 m temperature, 2 m dew point, wind and global radiation), SYNOP meteorological stations(2 m temperature, 2 m dew point and wind) or ASRB weather stations (downward radiation components) as well as satellite data (global radiation). Additionally, a qualitative precipitation verification of a convective case with radar measurements has been performed.

The 113 automatic ANETZ/ENET ("Automatisches Messnetz der Schweiz, MeteoSwiss") surface stations give a wide range of validation data in the area over Switzerland, from the Swiss Highland to the complex mountain environment. In this monitoring network the global radiation is horizontally measured.

The Alpine Surface Radiation Budget (ASRB) network is a joint venture of the Institute for Atmospheric and Climate Science ETH Zurich (IACETH), the Federal Office for Metorology and Climatology (MeteoSwiss) and the Swiss Federal Institute for Snow and Avalanche Research Davos (SLF). The monitoring network has been created in order to measure accurate data of the Earth's surface radiation budget and to improve the understanding of the internal atmospheric forcing transfer down to the surface, where the radiation budget determines the energy and evaporation budget and thus the energy flux into the atmosphere. The surface radiation budget depends on the elevation, which can influence the dynamics of the atmosphere in regions with mountain chains such as the Alps (Marty et al., 2002). For this study a total of 10 remote stations of the ASRB network between 400 and 3500 m a.s.l. were chosen. At these selected sites shortwave and longwave atmospheric radiation are routinely and horizontally measured. In order to compare the observation with the model results the nearest grid-point of the model grid has been chosen.

Satellite data are very useful for validation of numerical weather prediction models because their values are representative for an entire image pixel or grid cell and not for a single specific

surface location. In addition, they cover the entire area of the model domain, allowing a better spacial verification. The observed global radiation from the satellite (METEOSAT second generation, directly derived from the high resolution visible channel) has been adapted by Dürr and Zelenka (2007) to an hypothetical topography corresponding with the horizontal resolution of the satellite data (1.1 km x 1.8 km). In fact, the satellite retrieval algorithm determines the radiation channels also on horizontal surfaces like the original radiation scheme of COSMO. A conversion for inclined surfaces is for this reason necessary. In this study we only verified a domain covering entire Switzerland and the border regions of the neighbouring countries (see Figures 2.12 and 2.13). This limitation permits the direct use of already processed data provided by MeteoSwiss. Only the available time slots having a sufficient accuracy (sun elevation greater than 5°) have been considered. The processed satellite data have been finally interpolated to the COSMO model grid using a simple aggregation algorithm (more than one satellite gridpoint is available for each model gridpoint).

### 2.5.1 The impact of the radiation correction (corrected vs. uncorrected)

The application of the computed correction and skyview factors has its first impact in the surface radiation components. Differences between runs with and without topographical radiation correction clearly depend on the model horizontal resolution, the season and the time of the day. The impact at 7 km resolution is as expected clearly smaller than at 2.2 km because the correction amount is smaller. The impact assessment on the surface radiation balance has to be done by distinguishing situations with direct influence of correction factors and situations in which the relatively small corrections induce secondary changes or a feedback in the model (for example changes in the cloud coverage or changes in the surface albedo due to a local increase of snow melt in gridpoints having already small snow amounts at the model initialisation).

The shortwave radiation amount shows a direct effect depending on the time of the day and clearly also on the correction factors, which have an impact mainly in the early morning and in the late afternoon in summer, and during the entire day in winter. An example of a winter day is illustrated in Fig. 2.12 for the 2.2 km case and in Fig. 2.13 for the 7 km case, respectively. The exposition effect of the different partially resolved alpine valley slopes can clearly be identified at 2.2 km, while at 7 km only the main reduced exposition has a small contribution due to the very moderate slope angles. Differences up to 120 $Wm^{-2}$ can be observed in the morning and in the evening at 2.2 km horizontal resolution (Fig. 2.12 d, for the morning). Complete shadowing effects can be seen in the first or last sunshine hours (Fig. 2.12 b and c). Despite the larger impact using the subgridscale correction, due to averaging reasons, in this case we generally find less gridpoints which are completely in the shade (Fig. 2.12 c). In fact, non-zero factors of subgrid points often contribute to differentiate from zero the value of the resulting aggregated correction factor. At 7 km resolution the impact on radiation is clearly smaller: only very few gridpoints are influenced by shadowing effects.

The variations in the longwave radiation balance at 7 km horizontal resolution are insignificant (Fig. 2.14 c), while at 2.2 km an impact up to 15 $Wm^{-2}$ (Fig. 2.14 a) and even up to 25 $Wm^{-2}$ in the subgridscale version can be observed (Fig. 2.14 b). The difference between the two options can be explained with the lower skyview factors of the subgridscale option.

The impact at 7 km horizontal resolution can be important only in few situations in winter, when the small radiation change can modify the snow cover amount or the local surface layer stability (allowing for increased downward sensible heat flux). Exposed gridpoints having nearly no snow are candidates for the first process, which substantially modifiesthe surface albedo and as consequence the surface radiation budget. For this reason the 7 km resolution runs will be not further analysed and investigated. The following results regard only the COSMO 2.2 km model.

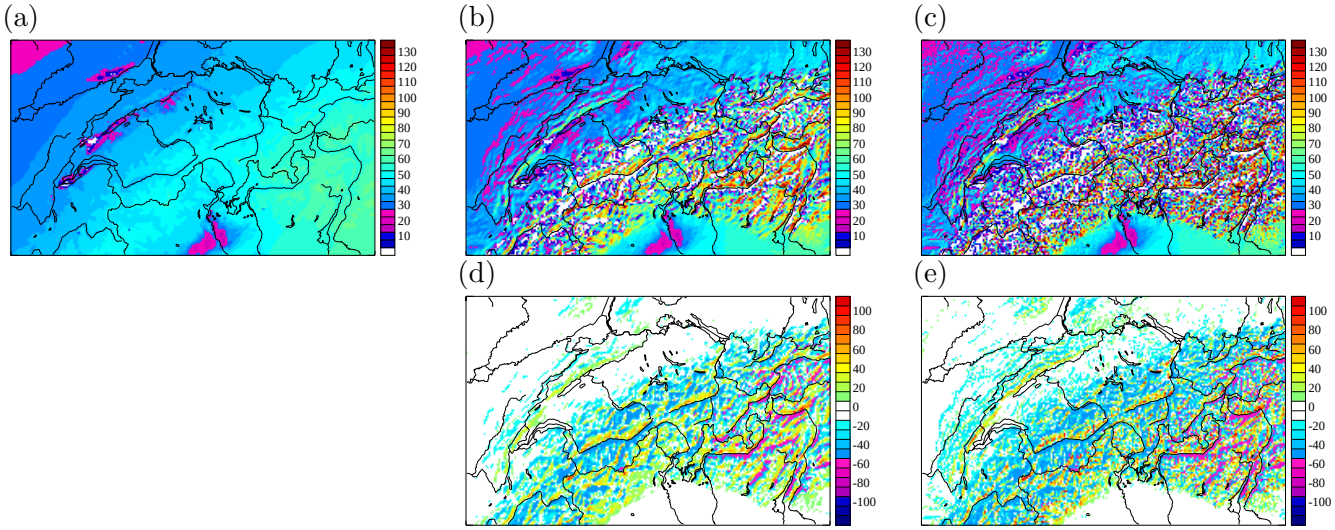


Figure 2.12: Direct shortwave incoming radiation at the surface for COSMO at 2.2 km horizontal resolution in a winter day (20.12.2006 09 UTC): (a) control run (no correction), (b) gridscale correction and (c) subgridscale correction; (d) difference between gridscale parameterization version and control run, (e) difference between subgridscale version and control run.

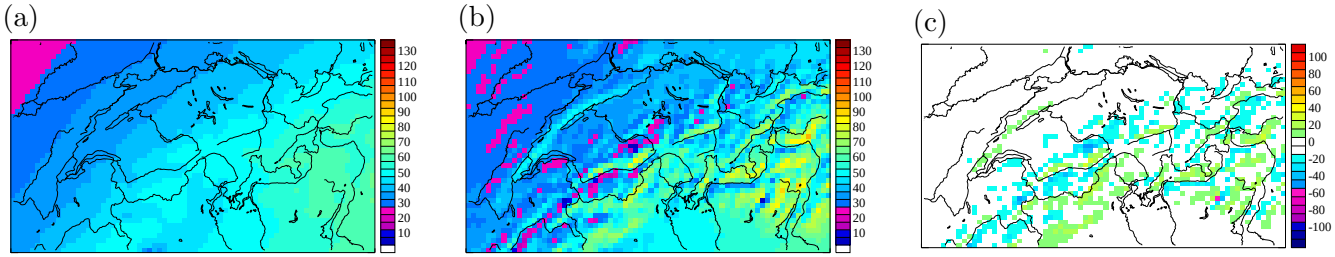


Figure 2.13: Direct shortwave radiation for COSMO at 7 km horizontal resolution in a winter day (20.12.2006 09 UTC). (a) control run (no correction), (b) with gridscale radiation correction and (c) difference between gridscale option and control run.

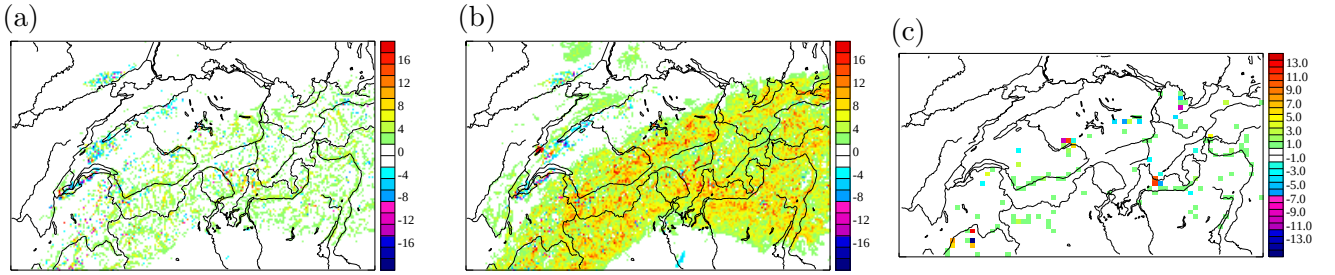


Figure 2.14: Differences in the longwawe downward radiation at the surface for COSMO at 2.2 km and 7 km for a winter day (20.12.2006 09 UTC): (a) between gridscale version and control at 2.2 km, (b) between subgrid scale version and control at 2.2 km , (c) between gridscale version and control at 7 km.

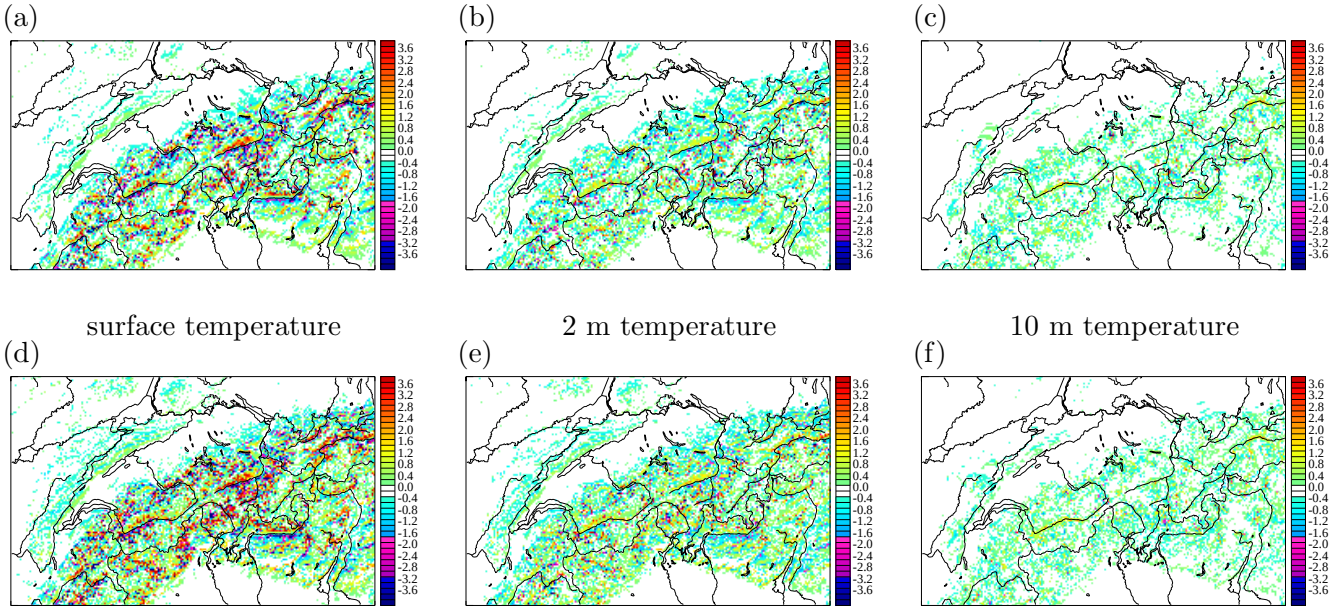


Figure 2.15: Temperature difference between runs with modified radiation scheme and control run for a winter day (20.12.2006 11 UTC): (a), (b) and (c) gridscale computed correction factors at 2.2 km resolution. (d), (e) and (f) subgridscale version. Left surface temperature, middle 2 m temperature and right temperature at the first atmospheric layer (about 10 m). Notice that some few gridpoints show larger or lower values than indicated in the colour key: these are associated with the same maximum or minimum colour indicated.

Modifications in the solar and downward longwave radiation induce a modified warming of the surface and for this reason influence the surface temperature through the surface energy balance. During the winter days, characterised by a strong surface temperature inversion, the direct impact on surface temperature reaches in the alpine region mean absolute values of $1.5° - 2.5°$C. In some few gridpoints extremely large differences up to 25°C can be observed. This important maximum variation is possible because the most gridpoints at the surface (mainly those covered with snow) are located in a very strong surface inversion. The inversion between surface and first model atmospheric layer at about 10 m can reach values up to 35°C degrees (on average $4 - 5°$C). These extremely large gradients are not realistic and illustrates the problems of the turbulence scheme in very stable situations. Generally, due to the effect of increased downward longwave radiation (Figure 2.15) a clear supremacy of gridpoints with warmer temperatures has been detected.

On the contrary, in summer the difference reaches values up to 4°C degrees. This can be explained by the direct effect of the radiation correction. Stronger effects can be seen in case of changes in the cloud coverage, where the temperature change can reach 15°C at single gridpoints.

The temperature difference propagates into the atmosphere and can clearly be detected in the diagnosed 2 m temperature and at the first atmospheric layer (at about 10 m). At all mentioned levels and for all cases evaluated, the impact of the subgridscale version is more important. The amplitude of the simulated differences decreases with the height above ground (Figure 2.15). Interesting is the mechanism observed in winter. A warmer surface temperature can even cause a lower temperature in the first atmospheric layer. In fact, a warmer temperature at the surface decreases the inversion strength allowing for a larger mixing and a larger thermal transport from the atmosphere to the ground, which induces a cooling in the first atmospheric layers. The mechanism can also happen in the opposite direction in case of lower surface temperatures: here the mixing is further reduced and the first atmospheric layer remains relatively warmer.

The thermal differences created with the topographic correction of radiation influence also the thermal circulation near surface and have an impact also on the wind direction and speed. Wind speed modifications at 10 m up to 4 m/s are observed (Figure 2.16). Nevertheless most of the

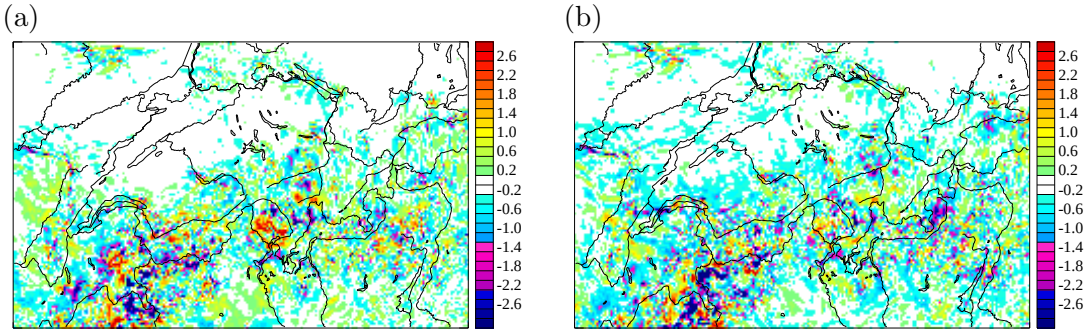


Figure 2.16: Wind speed differences at 10 m between modified versions and the control run (no correction) for a summer day (07.08.2003 14 UTC): (a) gridscale version (b) subgridscale version for the 2.2 km resolution.

gridpoints show changes smaller than 1 m/s.

As already mentioned in the beginning of this section, mainly the summer cases show a significant change in the cloud coverage. The sensitivity of the cloud coverage to the introduced radiation modifications is quite large. This secondary feedback effect considerably increases the radiation correction impact. The clouds are not only shifted horizontally between gridpoints; they are also added or reduced: the growth of an isolated and new cumulus clouds can be e.g. observed in Figure 2.17 over western Graubünden. Quite large changes are observed in Ticino, Valtellina and southern Graubünden. The significant change of the cloud coverage can for example be also associated to the variation of the thermal winds (horizontal and vertical changes), which modifies the local convection situation and the formation of the cumulus clouds. In the COSMO 2.2 km model the deep convection is expected to be resolved and only the shallow convection is still parameterized.

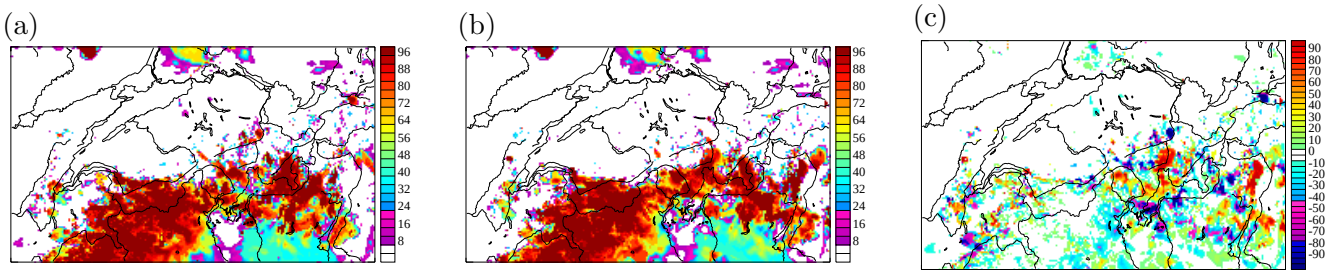


Figure 2.17: Cloud coverage and differences in the cloud coverage during a summer day (07.08.2003, 12 UTC): (a) control run, (b) gridscale version and (c) the difference (gridscale-control).

The strongly convective case (18.06.2006) shows in the afternoon some convective precipitation. The introduction of the radiation modifications induces also some differences in the precipitation patterns. The main structures do not change, but in some regions the total precipitation amount is significantly modified or shifted. The quantitative precipitation difference reaches values up to 18 mm in 24 hours. Figure 2.18 shows the total precipitation during the 24 hours of model integration and the difference with the control run.
The observed changes in the cloud cover and in the precipitation cannot be directly associated with the introduced changes in the surface radiation components due to non-linear chaotic effects of the weather system.

All the aspects presented in this section clearly show that the introduction of a topographical coherent radiation correction at the surface has a significant impact on the main model variables. The model is sensitive to the introduced radiation correction. Besides the expected effects on the

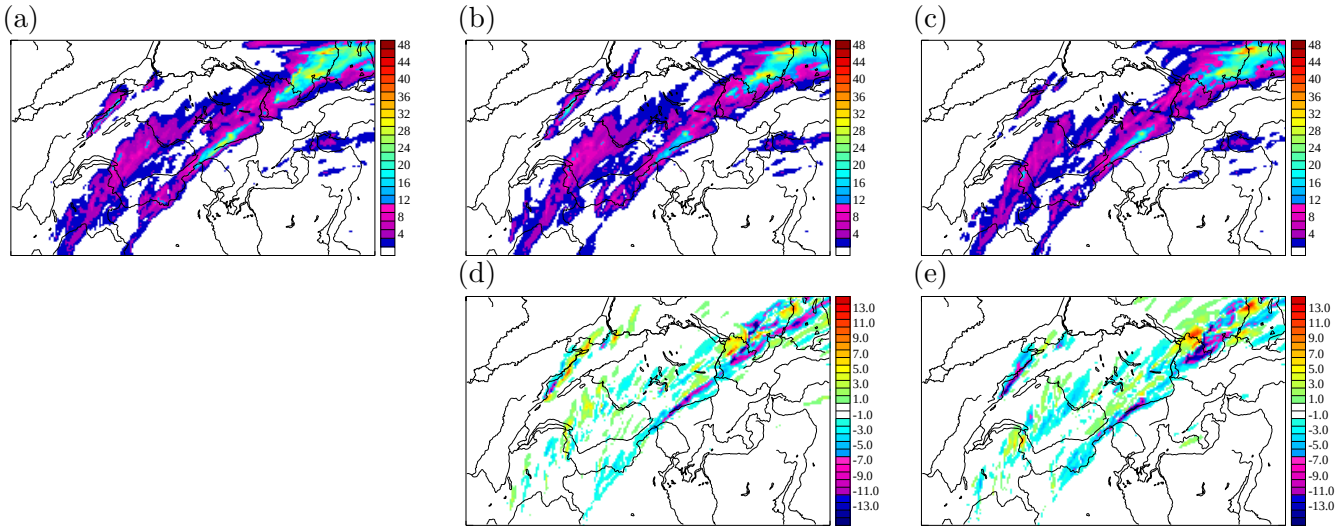


Figure 2.18: 24 hours precipitation sum for a convective case (18.06.2006): control run (a), gridscale version (b), subgrid scale version (c), difference plot between the gridscale version and control run (d), difference plot between the subgrid gridscale version and control run (d).

near surface temperature distribution (as reported by Müller and Scherrer, 2005), also significant changes in the thermal circulation, in the cloud coverage and in the precipitation amount could be seen.

### 2.5.2 Verification with observations

The model performance concerning global radiation and the impact of the correction schemes at 2.2 km resolution is presented for the winter days in Fig. 2.19 and for the summer days in Fig. 2.20. The plotted mean square error (RMSE) to the satellite data corresponds to the mean values of five cases, each one computed considering all the model grid-points in the considered satellite domain. Each figure presents three curves: the reference run with a green line, the gridscale option with the dotted red line and the subgridscale option with a dashed orange line. The verification has been repeated only for cloud free grid-points in both the model forecast and in the satellite observations.

The performance in winter shows a clear improvement of the radiation forecast using both correction schemes (Fig. 2.19). The improvements in terms of lower root mean square error (Fig. 2.19 b) are on the order of 5-10 $Wm^{-2}$. Larger improvements (10-15 $Wm^{-2}$) can be seen for cloudfree gridpoints (Fig. 2.19 a). The missing point at 15 UTC is due to a lack of classified cloud-free grid-points at low sun elevation angles. In comparison to the grid scale correction scheme, the sub-grid scale version shows a slightly worse performance. This observation has to be interpreted with caution and refers to the fact that the different horizontal resolution used in the satellite data adaptation plays an important role. In fact, for both correction schemes a significant part of the error is due to differences in the used horizontal resolution. The penalising effect is larger for the subgridscale option, because satellite data have originally a resolution closer to the 2.2 km (model resolution) than to the 300 m used for aggregation on the 2.2 km grid in the subgrid scale correction scheme. This means that the verification of the subgrid scale version is to some extent unfair. Additionally, it is important to note that the larger part of the error observed in all the compared simulations is represented by the background error of the model.

Positive effects are also seen in summer mainly in the first and last sunny hours (Fig. 2.20). The impact of the correction schemes in terms of RMSE during these time windows can clearly be seen for the cloud free grid-points (Fig. 2.20 b): the improvement can reach 15 $Wm^{-2}$. Considering

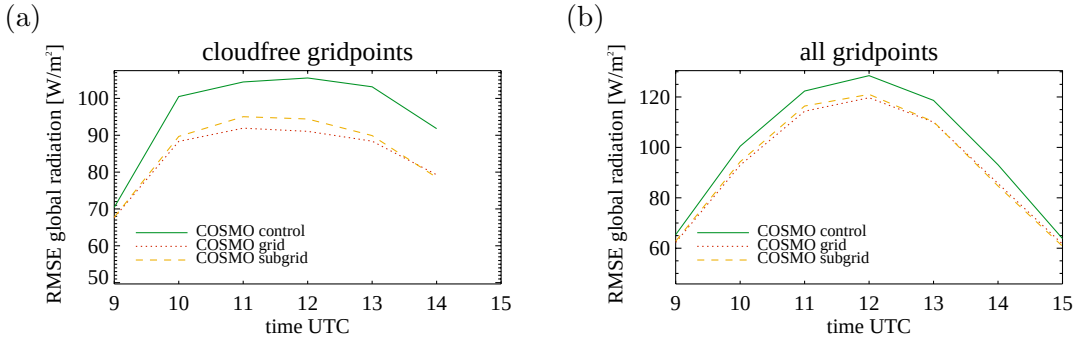


Figure 2.19: Verification of the global radiation based on adapted satellite data (Dürr and Zelenka, 2007) for five winter days: root mean square error (RMSE). (a) cloudfree gridpoints and (b) all gridpoints. The horizontal resolution is 2.2 km.

all the grid-points the RMSE improvement decreases to a few $Wm^{-2}$ (Fig. 2.20 b). The subgrid-scale scheme shows a significant degradation in performance during the central part of the day (late morning and early afternoon). The already mentioned aspect of the horizontal resolution used for verification again penalise this version.

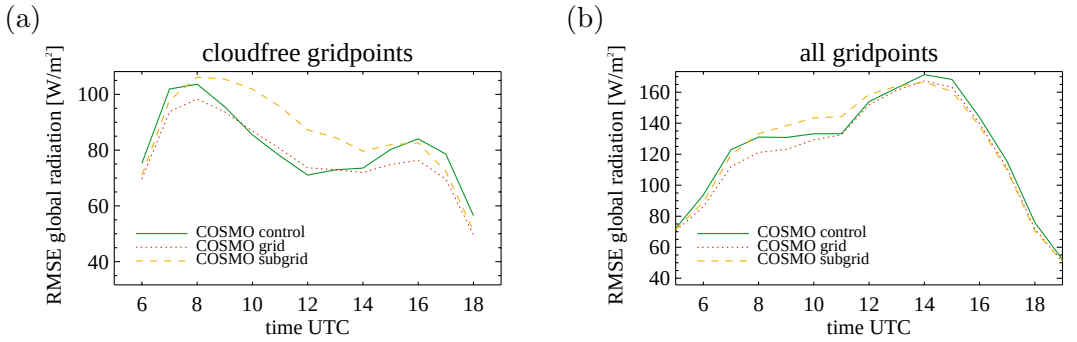


Figure 2.20: Verification of the global radiation based on adapted satellite data (Dürr and Zelenka, 2007) for five summer days: root mean square error (RMSE). (a) cloudfree gridpoints and (b) all gridpoints. The horizontal resolution is 2.2 km.

Figure 2.21 and Fig. 2.22 additionally present the results for the mean error (ME) and its standard deviation (STDEV) for the cloudfree gridpoints of the five winter cases. The ME is not really a suitable verification quantity for the global radiation in complex topography in the special situation of the chosen case studies for two reasons. First, the background error often is much larger than the sensitivity due to the introduced radiation correction. Second, the radiation correction in very complex topography together with the differences in the topography (satellite versus model topography) tend to generate a very large amount of compensating effects in the ME that significantly penalise the correction schemes compared to the uncorrected original radiation scheme. For this reason the root mean square error, presented before, gives a more objective result. The ME should at least be evaluated taking into account also its STDEV, in order to evaluate the significance of the increase or decrease in performance.

For the winter cases the negative ME is slightly reduced for the gridscale option (up to 5 $Wm^{-2}$), while the subgridscale option shows a small deterioration (Fig. 2.21) up to 5 $Wm^{-2}$. On the contrary, the standard deviation of the ME is significantly smaller for both radiation correction schemes, indicating that compensating effects are probably playing an important role in the overall result of the ME.

In summer, the deterioration in term of ME affects both options considering topographic ef-

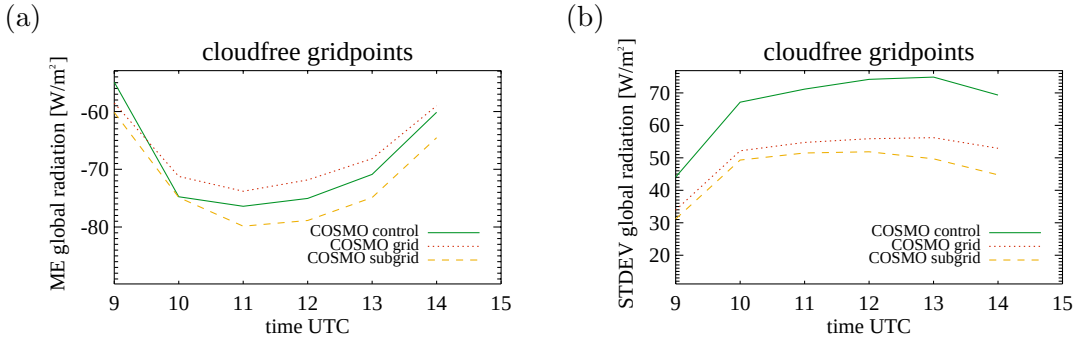


Figure 2.21: Verification of the global radiation based on adapted satellite data (Dürr and Zelenka, 2007) for 5 winter days: (a) mean error (ME) and (b) standard deviation of the mean error (STDEV) for cloudfree gridpoints. The horizontal resolution is 2.2 km.

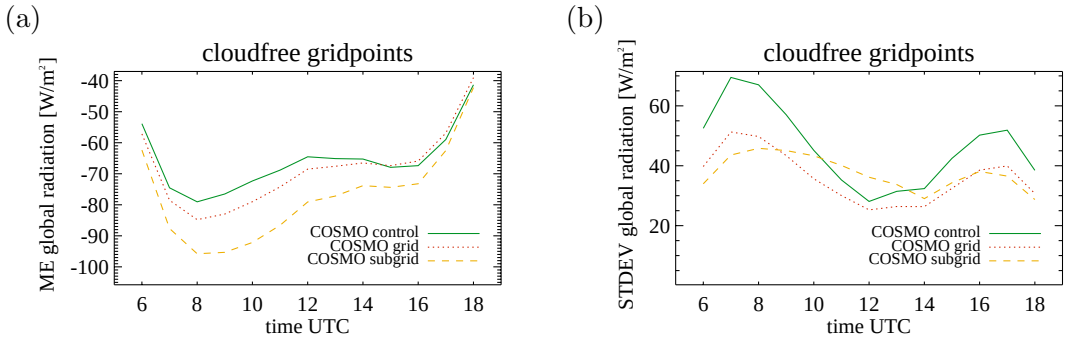


Figure 2.22: Verification of the global radiation based on adapted satellite data (Dürr and Zelenka, 2007) for 5 summer days: (a) mean error (ME) and (b) standard deviation of the mean error (STDEV) for cloudfree gridpoints. The horizontal resolution is 2.2 km.

fects leading to a slight (gridscale correction) and significant deterioration (subgridscale option), respectively (Fig. 2.22). The clear reduction of the STDEV in the morning and in the late afternoon shows that the deterioration in terms of RMS is not significant in the gridscale option. On the contrary, the deterioration during the central part of the day is significant in the subgrigscale option as already found for the RMSE.

In Fig. 2.23 the results of the long wave downward radiation verification are presented: (a) and (c) illustrate the mean error (ME) and (b) and (d) the root mean square error RSME to the ASRB surface station data, separately for winter an summer days. Note that here each value (ME and RMSE) is generated from only 5x10 values. Although nearly all the ASRB stations are located at exposed sites with generally high skyview factors (coming from the surrounding topography), which would increase the longwave downward radiation, both the mean error and the root mean square error exhibit a better performance in the corrected radiation schemes. In winter the improvement of the root mean square error can be on the order of 1 $Wm^{-2}$ in the RMSE for the grid-scale version and 3 $Wm^{-2}$ for the subgridscale version respectively (Fig. 2.23 b). The positive effect on the ME reaches 1.5 $Wm^{-2}$ for the gridscale and 6 $Wm^{-2}$ for the subgridscale version (Fig. 2.23 a). In summer the situation is similar. In the late afternoon the positive impact is reduced (Fig. 2.23 c and d) due to the high variability of the cloud coverage. The mean error improvement is up to 1 $Wm^{-2}$ for the gridscale and 2-3 $Wm^{-2}$ fore the subgrid scale version, respectively.

ASRB stations also measure the global shortwave radiation. A verification of this component of the surface radiation budget has to consider the fact that the standard radiation measurements

(ASRB as well as ANETZ/ENET stations) are taken on a horizontal surface. For this reason, mainly for the stations in very complex topography like the Swiss Alps, depending on the station a deterioration of the comparison with the two correction schemes can be expected and is also observed (not shown). This is an indirect confirmation of the quality of the correction algorithm. Compared to these standard measurements, only shadowing effects are assumed to be better captured in the adapted radiation scheme versions. Nevertheless, the shadowing effects can be better seen in the global radiation observations taken in some ANETZ station located at the valley ground (not shown).

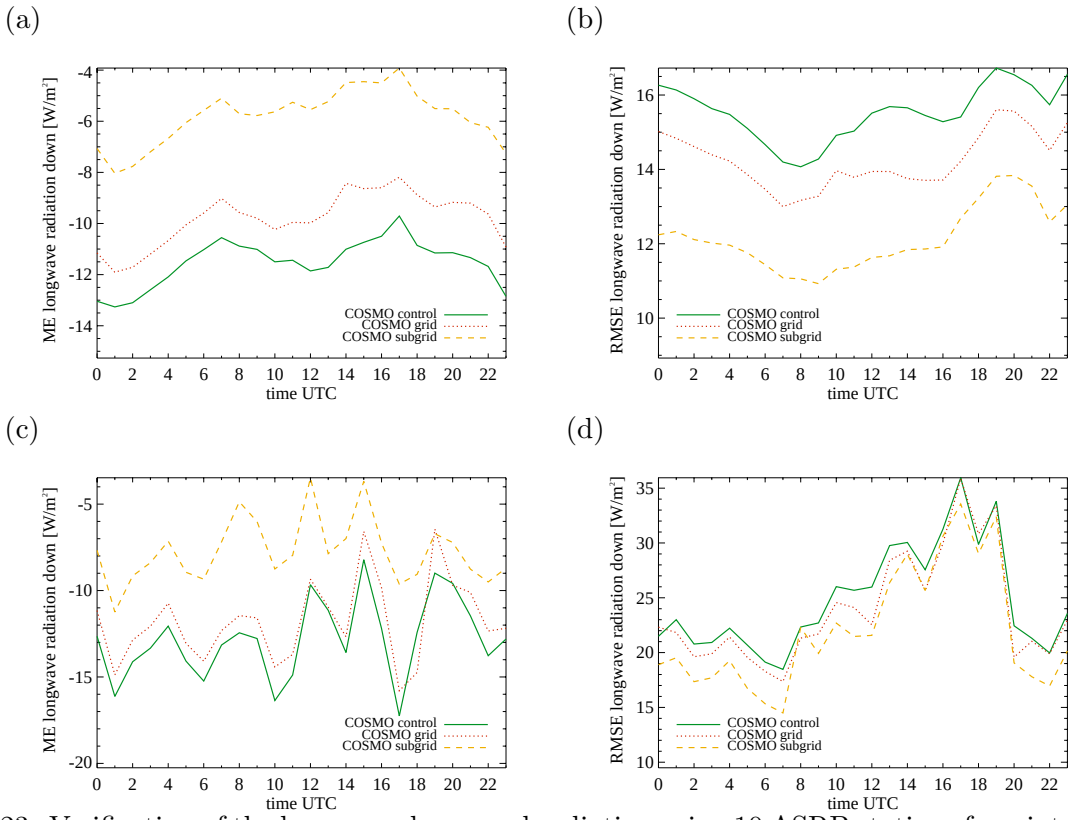


Figure 2.23: Verification of the longwave downward radiation using 10 ASRB stations for winter (top) and summer (bottom) days: (a) mean error in winter (ME), (b) root mean square error in winter (RMSE), (c) mean error in summer and (d) RMSE in summer.

The verification with SYNOP weather stations covers all the COSMO model domain and its results can be obtained for different meteorological parameters. In Figures 2.24 and 2.25 the results for 2 m temperature, 2 m dew point and wind speed are presented for the winter and the summer days, respectively. For this verification each statistical data point (ME, RMSE) considers about 5x300 pair of values. Generally, no large difference between the three versions (control run, gridscale correction and subgridscale correction) can be observed from these comparisons with meteorological observations.

In winter the 2 m temperature forecast improvement is more important than in summer. The subgridscale option generally performs better than the gridscale. The model cold bias in winter is slightly reduced and has for the subgriscale version an improvement up to 0.15°C. The quantitative improvement in terms of root mean square error can reach values in the daily cycle up to 0.1-0.2°C (Fig. 2.24 a). The root mean square error is variable (Fig. 2.24 b) and shows a singular three hour frequency; this is related to a different total number of observations, which enter into the verification. Every three hours, additional station data are available in regions, where the model

generally has a worse performance.

The verification of the wind speed for the winter cases does not really show important signals of improvement or worsening in the forecast quality (Fig. 2.24 c and f) and the performance for the dew point is for some validation times worse and for others better. The overall result is nearly neutral (Fig. 2.24 b and e).

In summer no clear signals have been observed (Fig. 2.25): the three versions are more or less similar for the three verification parameters considered. The 2 m temperature performance shows an improvement in the RMSE less than 0.05 °C in the morning hours and a worsening of about in the same order of magnitude during the central hours of the day (Fig. 2.25 a and d). The differences in the dew point are extremely small (Fig. 2.25 b and e). For the wind speed no clear trend can be identified and the overall impact can assumed to be neutral (Fig. 2.25 c and f).

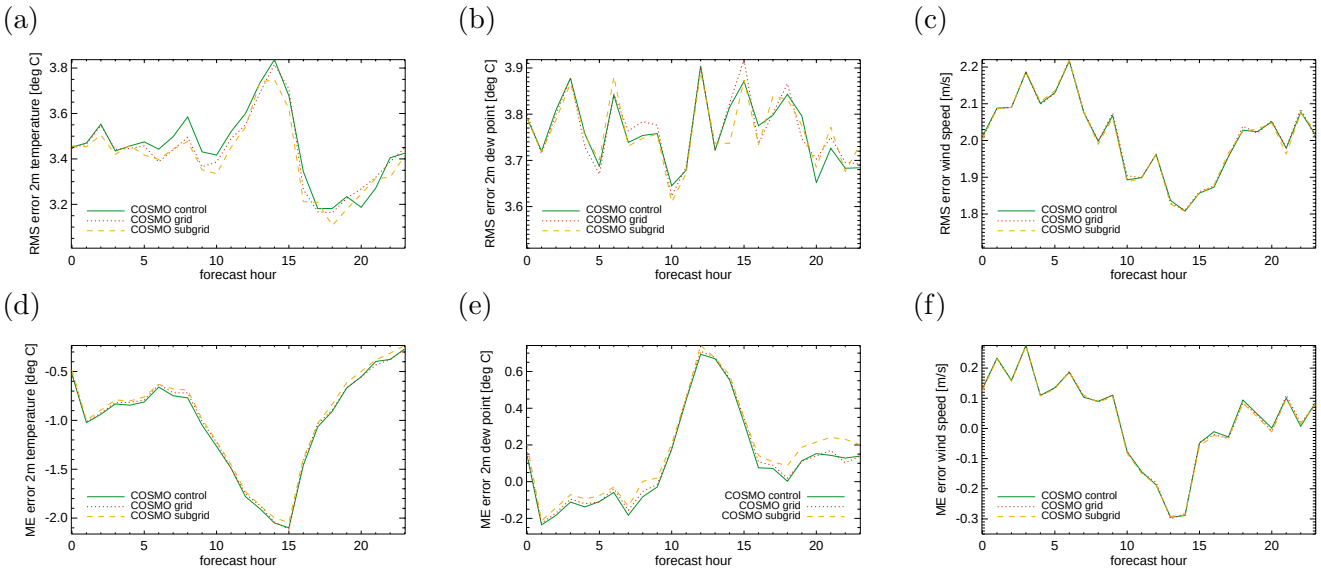


Figure 2.24: Root mean square forecast error (RMSE, top row) and mean forecast error (ME, bottom row) using SYNOP stations for all winter cases: (a) and (d) 2 m temperature, (b) and (e) 2 m dew point, (d) and (f) 10 m wind speed.

The verification at the 113 ANETZ and ENET stations covers Switzerland and its results can be obtained for different meteorological parameters. In Figures 2.26 and 2.27 the results for 2 m temperature, 2 m dew point and global radiation are presented for the winter and the summer days respectively. Additionally, also the result for the wind speed are presented in Fig. 2.27. For each meteorological parameter ME and RMSE have been computed. Each plotted value is the result of 5x113 pairs of values.

The general performance evaluation with these surface stations generally confirms the patterns observed in the SYNOP verification. In winter the 2 m temperature RMSE is reduced up to 0.15 °C (Fig. 2.26 a), while the improvement of the ME can reach 0.2 °C (Fig. 2.26 d). Nevertheless, only a slightly lower performance in terms of ME for the grid-scale version in the evening hours can be observed. The results concerning the 2 m dew point in winter are partially contradictory: they exhibit a slight decrease of the forecast quality in term of mean error and a nearly neutral effect in terms of root means square error.

As already mentioned, a direct comparison of the measured global radiation with the model forecasted values is unfortunately only possible for the control run, because the shortwave radiation component is conventionally measured horizontally. A fair comparison could be done converting the measured values with the local slope characteristics (slope angle and slope aspect), which would increase the complexity of this verification. For this reason the results concerning radiation

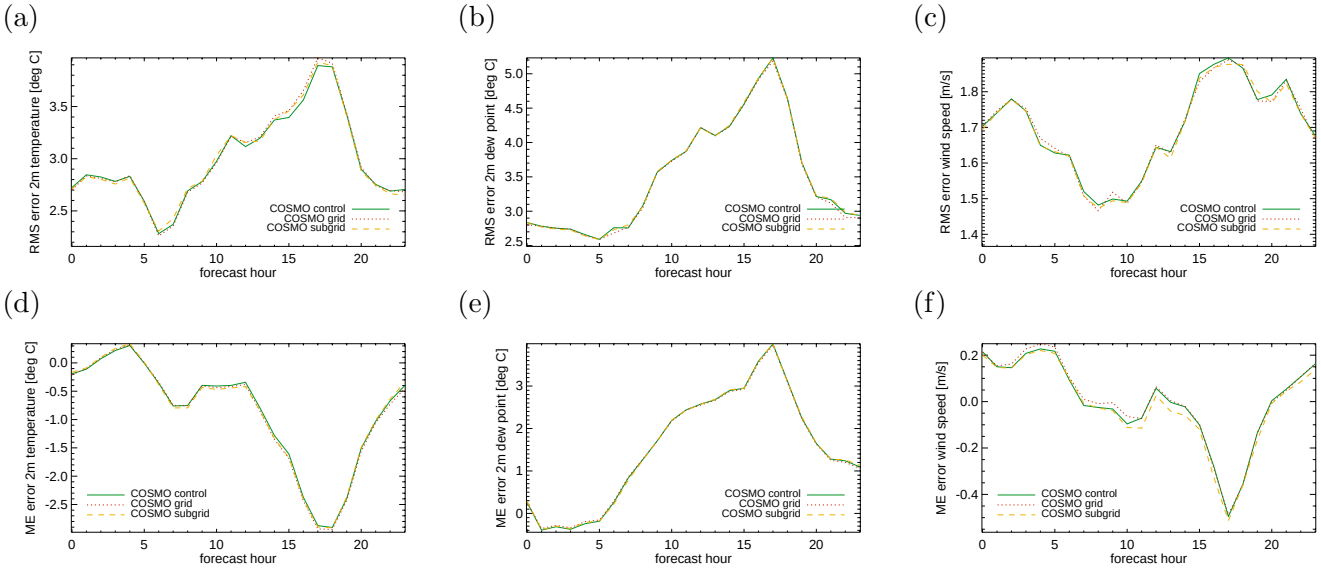


Figure 2.25: Root mean square forecast error (RMSE, top row) and mean forecast error (ME, bottom row) using SYNOP stations for all summer cases: (a) and (d) 2 m temperature, (b) and (e) 2 m dew point, (d) and (f) 10 m wind speed.

have to be interpreted with caution (Fig. 2.26 c and f). The RMSE is slightly reduced for the two versions with radiation correction (1-2 $Wm^{-2}$, Fig. 2.26 c). The ME results (Fig. 2.26 c) seem to significantly contrast with those presented in the satellite and ASRB verification, where a clear negative bias has been detected. The Swiss Plateau stations overcompensate the background error, due to the absence of fog in the model forecasts. A separate verification using only high altitude stations confirms the negative bias (not shown). From this global verification it is not possible to evaluate the better modelling of shadowing effects in the alpine valleys, because averaging of all stations masks the effect. On the contrary, a detailed observation of single stations (for example of the station Piotta) shows a clear improvement of the daily cycle of the global radiation (not shown). The verification of the wind speed components for the winter cases (Fig. 2.28 a and c) does not exhibit particular differences between the compared versions for both RSME and ME.

In summer the improvements observed in the 2 m temperature are smaller (Fig. 2.27 a) as well as those in the dew point, which exhibit for all the three options nearly identical results. In the global radiation again the already observed decrease of the forecast performance for the subgrid scale version of the correction scheme appears during the central hours (Fig. 2.27 c and f). Also for the wind components a slightly better performance of the two corrected versions can be observed (Fig. 2.27 b).

In summary, all the verification results are quantitatively presented in Tab. 2.2. The introduction of the radiation correction scheme taking into account the topographic effects on radiation, has a clear positive effect on the performance of the radiation forecast in winter for both options of the scheme (grid and subgrid). In summer the improvements are limited to the morning and in the afternoon hours. The overall performance is slightly better than the uncorrected option for the gridscale and significantly worse for the subgridscale, due to the mentioned mismatch between the verification (satellite) and model topography. For all the schemes and all the cases a significant reduction of the standard deviation of the mean error is observed, even in situations where the ME shows a deterioration. A significant improvement of the 2 m temperature mainly during winter days is observed. The other near surface variables do not show significant changes.

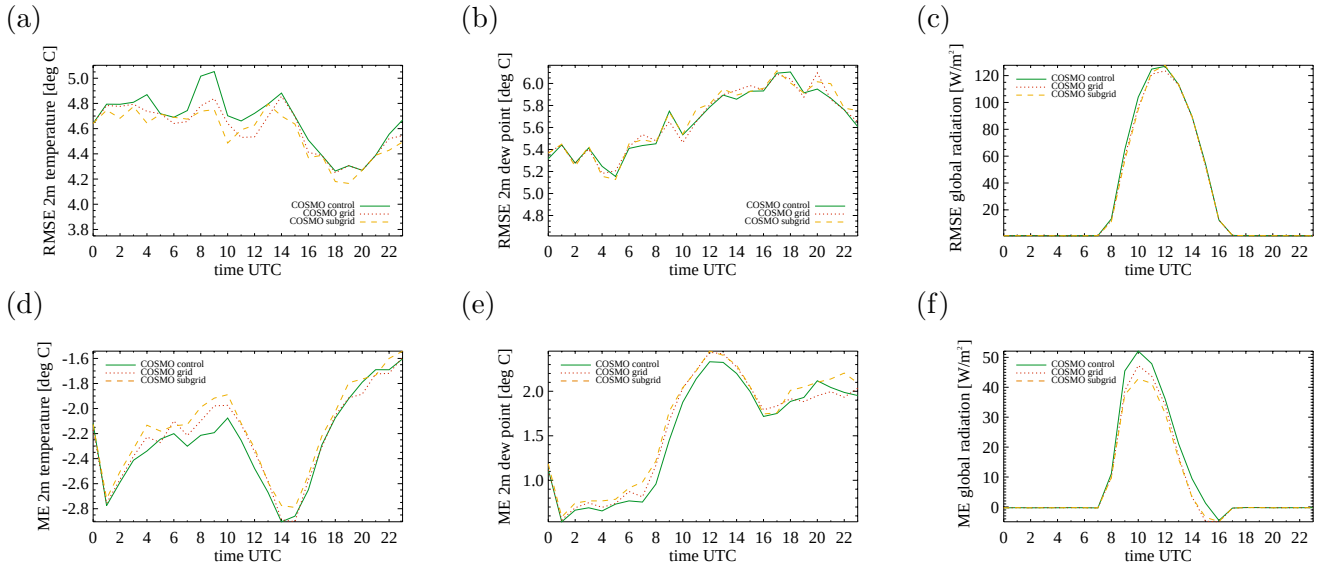


Figure 2.26: Root mean square forecast error (RMSE, top) and mean error (ME, bottom) using ANETZ and ENET stations for all winter cases: (a) and (d) 2 m temperature, (b) and (e) 2 m dew point, (c) and (f) global radiation.

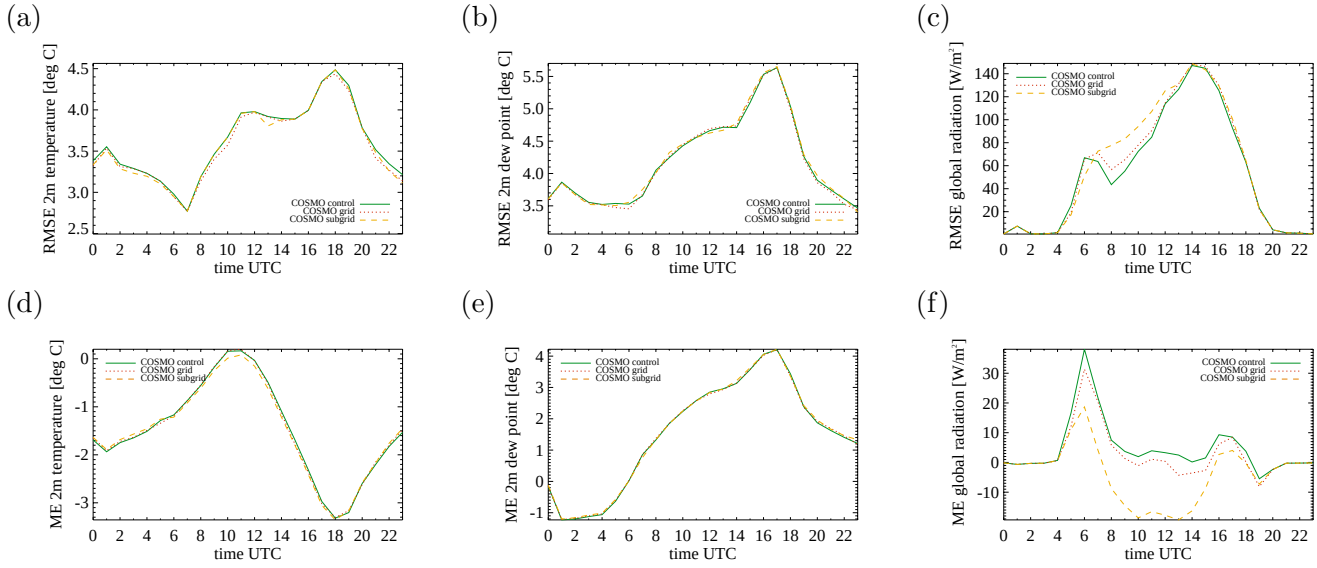


Figure 2.27: Root mean square forecast error (RMSE, top) and mean error (ME, bottom) using ANETZ and ENET stations for all summer cases: (a) and (d) 2 m temperature, (b) and (e) 2 m dew point, (c) and (f) global radiation.

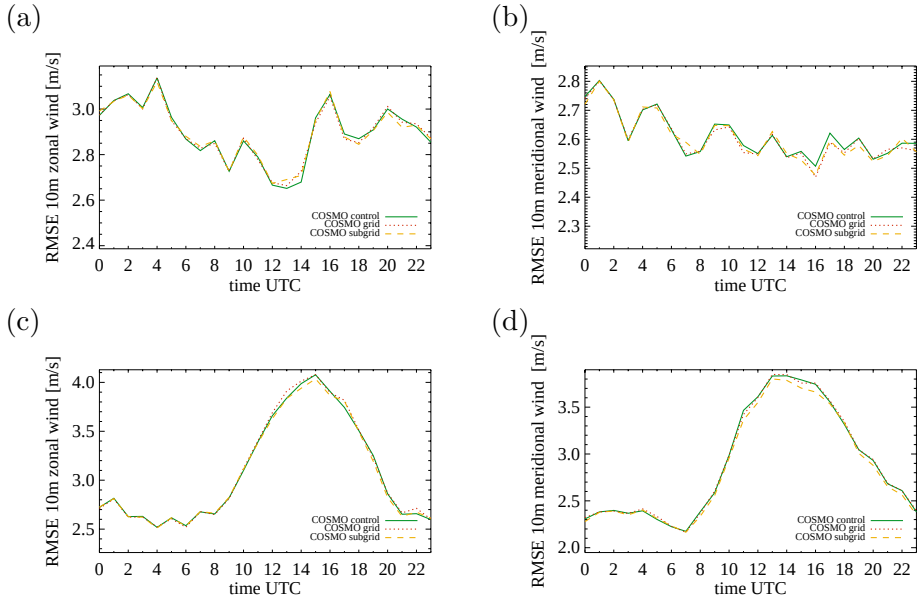


Figure 2.28: Root mean square forecast error (RMSE) for wind speed horizontal components using ANETZ and ENET stations for winter (top a, b) and summer (bottom b, c) cases: (a) and (c) zonal wind speed component, (b) and (d) meridional wind speed component.

| experiment | GLOB $[Wm^{-2}]$ | | | LWD $[Wm^{-2}]$ | | T2m $[°C]$ | | TD2m $[°C]$ | | FF10M $[m/s]$ | |
|---|---|---|---|---|---|---|---|---|---|---|---|
| | RMS | ME | SD | RMS | ME | RMS | ME | RMS | ME | RMS | ME |
| winter grid | -12.4 | -1.6 | -15.8 | -1.2 | -1.1 | -0.10 | -0.05 | 0.05 | -0.02 | -0.03 | -0.01 |
| winter subgrid | -10.2 | 2.5 | -20.4 | -3.1 | -2.9 | -0.12 | -0.08 | 0.04 | 0.04 | -0.01 | -0.01 |
| summer grid | -5.2 | 3.4 | -10.2 | -1.2 | -0.9 | -0.03 | 0.02 | -0.03 | 0.01 | 0.04 | 0.01 |
| summer subgrid | 3.5 | 11.3 | -8.7 | -2.6 | -4.5 | -0.04 | 0.03 | 0.01 | 0.01 | -0.02 | 0.02 |

Table 2.2: Summary of the quantitative improvement observed verification results using satellite observations (GLOB: global radiation), ASRB stations (LWD: long wave radiation down), ANETZ/ENET observations (T2m: 2 m temperature, TD2m: 2m dew point, FF10M: 10 m wind speed). For each statistical quantitiy a negative sign indicates an increase of performance compared to the uncorrected control simulation, while a positive sign indicates a worse result. Verification quantities: root mean square error RMS (RMSE), mean error ME and standard deviation of the mean error SD (STDEV). The values for the global radiation refer to the cloudfree gridpoints.

## 2.6 Discussion

Although the simulations with the new parameterization of topographic effects on radiation have been done only at 2.2 km horizontal resolution (large topography differences are still observed between model and reality), they show gridpoint to gridpoint differences in the shortwave downward radiation in the expected order of magnitude, as observed for example in the Riviera Valley (Matzinger et al., 2003) and other observations in complex terrain (Sturman et al., 2003).

The validation of direct short wave radiation fluxes over sloping surfaces is not a trivial task, because all the radiation measurements are conventionally taken on a reference horizontal plane. Only topography adapted satellite data (as used in this study) and topography adapted local observations (not done) give the possibility to do a fair comparison between model results and measurements. Strong differences in the slope aspect between real and 2.2 km topography can additionally lead to stronger radiation errors, compared to the results with the traditional radiation computation on horizontal surfaces. Nevertheless, the verification with adapted satellite

data gives good results. The improvement in the shortwave downward radiation is very promising and confirms that the parameterization goes in the right direction. For verification purposes the adaptation of the satellite data is crucial. In fact, the resolution of the topography used for the adaptation has to be possibly close to the model resolution. If this is not the case a false deterioration of the radiation forecast could be detected in the verification. The apparently lower performance of the subgridscale option in summer is caused by a large difference between the correction used in the satellite data (1.1x1.8 km) and the resolution used for aggregation (300x300m). The impact of the correction on the verification results can be estimated by comparing the model results with satellite data without topographical processing. Figure 2.29 presents the verification done with raw satellite data without topographical adaptation. The best performance of the reference run and the lower performance of the runs with radiation correction illustrate this aspect. The minimum error of the reference run in cloud free situations can be taken as basic indication for the model background error without any topographical effects. Note also the high RMSE in the morning and in the late afternoon for the summer cases, which demonstrates again the apparent negative impact of the topographic radiation correction if traditional global radiation data are used.

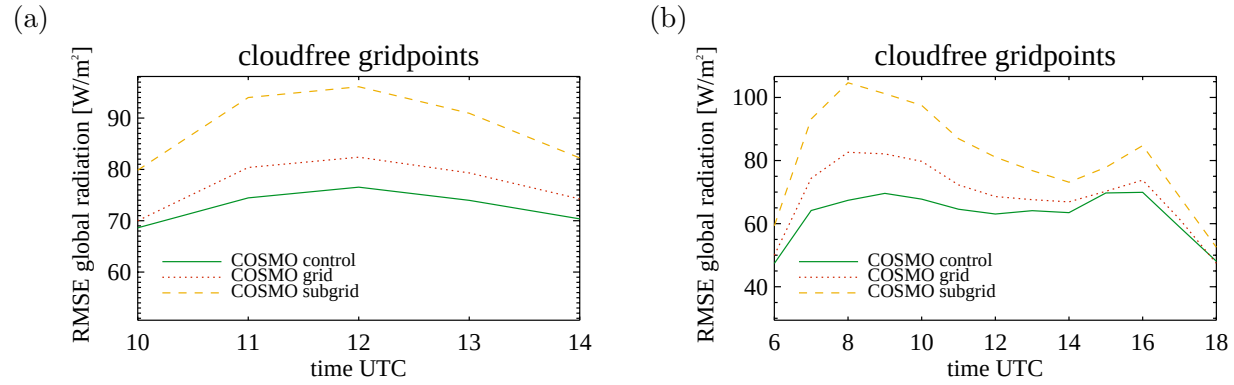


Figure 2.29: COSMO 2.2 km. Verification with satellite data without topographical adaptation for winter (a) and summer (b) cases (root mean square error, RMSE). Compare with Figures 2.19 b and 2.20 b

Besides the topographic correction and the related improvement, the shortwave radiation verification highlighted a considerable background error of the radiation scheme for the considered case study days. In winter a negative bias up to 70-90 $Wm^{-2}$ during cloud free situations can be observed. In summer the bias is slightly reduced and has a lower relative mean, considering the higher radiation fluxes, which reach the surface. As already mentioned, comparing the verification results with raw satellite data and adapted satellite data we can estimate that the background error in winter (excluding all the topographic effects) reaches some 60-70 $Wm^{-2}$ and in summer 30-40 $Wm^{-2}$. Considering the crucial forcing effect of radiation, it is important to shortly focus the attention on this aspect, in order to have an overview of the general deficiencies of the radiation scheme. Unfortunately, no complete and exhaustive verification studies of the global radiation in the COSMO model are available. Radiation verification is extremely sensitive to the amount of cloudiness. For this reason, only cloud free situations can give an objective result, even if they do not represent the majority of meteorological situations. The verification study of Gall (1998) for the meteorological station Payerne with the former model of COSMO (SM), which has the same radiation scheme (Ritter and Geleyn, 1992), confirms that in cloud free situations the model tends, especially in winter, to have a mean shortwave radiation underestimation up to 60 $Wm^{-2}$. In summer the underestimation is less pronounced. Recent comparisons of the COSMO radiation scheme with a high-quality but computationally expensive radiation model (RTX) (Bozzo, personal communication) confirms an underestimation up to 20 $Wm^{-2}$ of the shortwave radiation in

standard mid latitude clear sky winter situations (mostly dry air with low sun elevation angle). In contrast, for standard summer cloud free days with high relative humidity the mean error is strongly reduced and can also reach slightly positive values.

The order of magnitude of the shortwave radiation forecast error is comparable with what has been observed in the ECMWF model for European stations in winter (Chevallier and Morcrette, 2000). Considering the variety of meteorological situations and the better performance in summer and in cloudy situations, we can expect that the overall radiation scheme performance during an entire year is better than that observed in this study. Comparisons between radiation schemes running in different NWP models are rarely found in the literature. The variability between models is expected to be important if we assume that it could have similar patterns as found in global circulation models (GCMs). For example, Wild (2005) has found largely differing shortwave budgets in a wide range of GCMs either on a global basis or at places where observations are available.

In order to further investigate the observed background bias two entire months of 2006 forecasted by the COSMO model at 7 km horizontal resolution, operated without any topographical radiation correction, have been verified with the satellite data. The verification on a daily basis is presented in Fig. 2.30. In June we observe a positive bias, which almost completely disappears (maximum up to 10 $Wm^{-2}$) in cloud free situations (see orange points with error bars, Fig. 2.30 a). In December the mean error becomes mostly negative and reaches the highest values for cloudfree gridpoints (2.30 b). Similar pictures can be obtained if other summer or winter months are verified (not shown).

In order to gain a qualitative evaluation of the satellite data themselves, a comparison with ASRB stations has been carried out. The results can be seen in Fig. 2.31 and confirm the negative bias in winter (Fig. 2.31 a) and the better performance in summer. Compared with the entire June 2006 the chosen summer cases used in this study appear to be slightly anomalous. In fact, the observed bias for the entire June 2006 is positive, while in the case studies it is negative. In relation to that, it is interesting to point out that the difference between satellite and ASRB stations is very small in winter (daily average maximum difference up to 10 W/m2) and larger in summer, when at a few situations even the model gets better results than the satellite data. The lower quality of satellite data in summer can be related to difficulties in the detection of locally generated clouds typically observed in this season (B. Dürr 2007, personal communication). For this reason, the verification results using satellite data have to be used with some caution in summer. The COSMO radiation scheme seems to underestimate the global radiation in winterly months in cloud free situations. On the contrary, the scheme seems to systematically overestimate global radiation in cloudy situations having too opaque clouds or to underestimate the total cloud coverage.

The longwave downward radiation improvements related to the introduction of the skyview factor are quantitatively significant only in the subgridscale scheme. Normally, in clear sky situations, the model shows an underestimation of the downward longwave radiation, probably due to errors either in the vertical distribution of water vapour and the related longwave absorption (Dürr (2004), Bozzo personal comunication) or to thermal effects of neighbouring gridpoints inside valleys. It is difficult to quantify the relative weight of these two aspects. The topographic aspect is obviously expected to be significant only in complex alpine terrain. The parameterization schemes allow to significantly reduce the model error over the alpine region. The introduction of an artificial lower value of the skyview factor, as for example presented in the implementation of Müller and Scherrer (2005), could theoretically even lead to better results, because it partially compensates the model errors not related to topographic effects.
The significant sensitivity in terms of 2 m temperature differences between reference and version with topographic correction observed in this study is confirmed by the studies done with HIRLAM at 3.3 km horizontal resolution. Senkova et al. (2007) have found temperature differences due to

(a) (b)

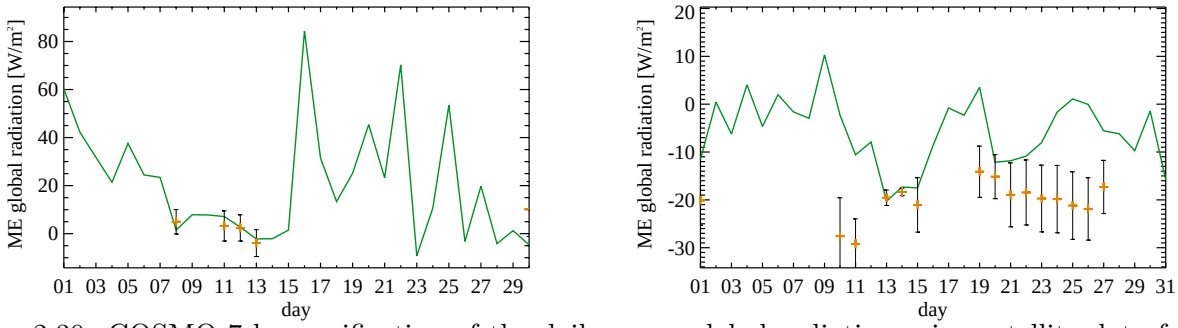


Figure 2.30: COSMO 7 km verification of the daily mean global radiation using satellite data for June 2006 (a) and December 2006 (b): the green line shows the mean error (ME) and the orange points with the error bars (standard deviation of the ME) the values for cloud-free gridpoints. The entire domain covering Switzerland is considered.

(a) (b)

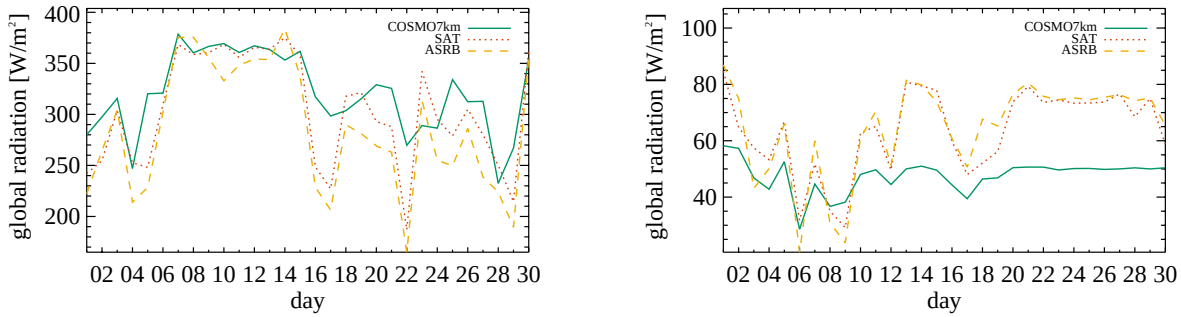


Figure 2.31: Daily mean global radiation comparison using satellite data, operational COSMO model (at 7 km resolution) and ASRB stations for June 2006 (a) December 2006 (b). For each day this comparison considers only 10 values corresponding to the 10 ASRB stations.

short wave radiation correction of 1 to 3°C.

However, the observed large sensitivity of the parameterization scheme on near surface temperature and wind speed observed in this study (sensitivity to the introduced radiation correction), contrasts with the rather small impact observed in the verification with observations. In fact, the verification results do not show large differences and indicate that on average the impact is slightly positive or neutral. This means that the used weather stations are not representative for the grid-cell they are in or that the impact is locally not always positive. The improvements have mostly local nature and the forecast quality can even deteriorate at certain sites, because even at 2.2 km horizontal resolution the local real topography is still quite different from the model topography (mainly in terms of slope angle and aspect).

The improvements in the 2 m temperature in winter are small but significant. The other meteorological parameters do not show clearly different values compared to the control run. In particular,s no systematic and significant forecast deterioration for any other parameter has been observed, except partially for the 2m dew point forecast in winter. This aspect can be explained with the introduced change in the near surface temperature without any changes in the specific humidity (at the surface and at the first atmospheric layer), which can contribute to a deterioration in the 2 m dew point forecast. It is possible that the 2 m dew point is partially better in the control run due to a double error in both the temperature and in the specific humidity.

Müller and Scherrer (2005) have performed a comparison of their original radiation correction schemes with alpine weather stations (SYNOP) and have found for a winter case study under clear

sky conditions an improvement in the 2 m temperature forecast of about 0.5-1.0 °C in RMSE during night-time and 0.1-0.3 °C during daytime. In a summer case study the positive impact during night is reduced to 0.2-0.5 °C and 0.1-0.2 ° during day. In the present study the positive impact is smaller and reduced to maximally 0.1 to 0.2 °C in winter and no significantly differences between day and night have been observed. The significantly different results during night-time compared to Müller and Scherrer (2005) can probably be explained with the higher skyview factors in our implementation (smaller correction and, therefore, less longwave radiation from neighbouring grid-points). Considered the unrealisitic low skyview factors used by Müller and Scherrer (2005), it is possible that the corrected downward longwave radiation in their simulations is larger than in reality, contributing to a compensation of other sources of error in the model (e.g. cold bias due to vanishing downward sensible heat flux). The different computation of the correction factors for direct solar radiation is probably not the cause of the slightly lower performance increase during day. The use of the Müller and Scherrer (2005) formula leads even in the cases of this study to slightly worse results (not shown).

The significant secondary effects on cloudiness are somewhat surprinsing and clearly influence the results in summer. The creation and growing mechanism of locally induced cumulus clouds, seems to be sensitive to the introduced radiation parameterization. Even locally induced convection can be slightly influenced by the correction of the radiation components at the surface, leading also to a different precipitation distribution. This aspect related to clouds should be further investigated.

The cloud parameterization in high-resolution NWP models is generally still an open issue. The COSMO radiation scheme sees only clouds located in the vertical column above the model grid cell. Figure 2.32 gives a simple sketch of the physical situation in presence of clouds. Three dimensional effects of clouds are not taken into account. In particular, in situations with low sun elevation angle, this effect can be very important. In addition, the call frequency of the radiation scheme is an important issue. Radiation schemes are very expensive in terms of computational cost. Nevertheless, higher call frequency can lead to a better representation of cloud movement effects. With the typical COSMO 2.2 km model call frequency (15 minutes) only clouds having an horizontal advection speed smaller than 8.8 km/h are well captured. For this reason the call frequency of the radiation scheme should be further increased in order to better model at least the cloud movements.

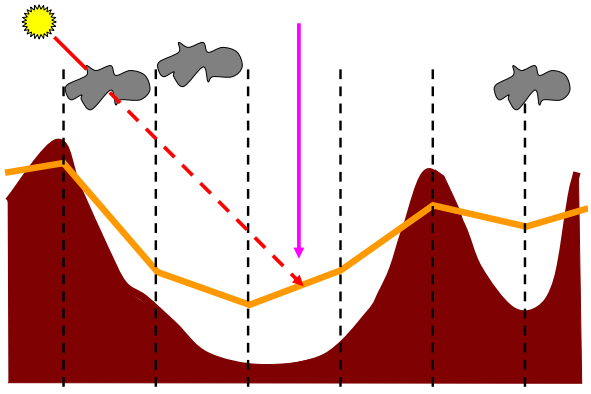

Figure 2.32: Cloud effect in high resolution NWP modelling: the radiation model sees only the clouds in the vertical column above the grid cell (pink line). In reality the sun can be partially shadowed by clouds along the non-vertical path from the top of the atmosphere and the Earth surface (red line). The brown filled area represents the real topography, while the orange line denotes the model topography.

## 2.7 Conclusions

A parameterization of topographic effects on radiation following the approach proposed by Müller and Scherrer (2005) has been implemented into the COSMO model. The topographic correction scheme for surface radiation components can be used with two possible options: gridscale and subgridscale. The first is based on a gridscale parameterization, in which the surface radiation correction factors for solar radiation and for thermal radiation have been computed using the model topography (7 km and 2.2 km horizontal resolution), whereas the second is based on a finer grid (300 m horizontal resolution) and aggregated successively on the coarser model grid (only 2.2 km).

Although the procedure of the original scheme (Müller and Scherrer, 2005) has been kept essentially unchanged, the computation of the skyview factors (for correction of longwave and diffuse shortwave radiation) and of the correction factors for direct shortwave radiation has been significantly modified in order to avoid unrealistically low skyview factors and to avoid inconsistencies in the surface energy balance. The reference surface over which all the surface energy exchanges take place in a model grid box has to be in fact the same for all considered fluxes. The effect of these modifications leads to a slightly smaller topographic correction. However, it is more realistic and consistent with the other physical parameterizations at the surface.

The model sensitivity to the introduced radiation correction and the micro-meteorological effect at 7 km resolution is significantly smaller than at 2.2 km. Nevertheless, this study has observed even at 7 km some non-negligible forecast modifications at few gridpoints due to internal feedback mechanisms such as snow melt (albedo changes). At 2.2 km the model reacts with moderately high sensitivity to the introduced change. The topography dependent modification in the radiation amount is in agreement with typical site-to-site differences observed in complex terrain regions and the sensitivity results of Senkova et al. (2007). For a convective case even a clear change in the convective precipitation distribution has been observed.

A verification against satellite data has been performed. The satellite data are also related to the inclined surfaces, i.e. the considered radiation amount represents the real available energy, in net radiation, at the orientated and inclined location of computation. This is a very important step in order to perform a fair verification of the corrected radiation components. To the knowledge of the author this is the first time that the impact of a topographic radiation correction in complex topography has directly been tested on the primary variable of interest, i.e. the radiation itself. For the global radiation an improvement forecast up to 15 $Wm^{-2}$ in the average RSME for cloud free grid-points in winter has been observed. In summer the improvement is less pronounced (5 $Wm^{-2}$) and largely determined by changes in cloud cover, induced by the local changes in the local convection.
Using high elevation permanent measurements (ASRB) the longwave downward radiation is found to be improved by some 3 $Wm^{-2}$ (RMSE) for the subgrid scale version. For the gridscale option the improvement is smaller than 1.5 $Wm^{-2}$.
All the radiation components that are directly affected by the topographic radiation correction respond as expected and give a clear signal of improvement.

The 2 m temperature RMSE based on the ANETZ-ENET and SYNOP stations is found to be better by up to 0.05-0.15°C in winter. This improvement is considerably smaller than that obtained by Müller and Scherrer (2005), where the more important improvement mainly occurs during night-time, due to the use of unrealistic low skyview factors. No significant deterioration (or even improvement) in the forecast of other meteorological fields has been observed. The spacial two-dimensional model sensitivity to the introduced radiation correction is larger than the impact observed in the station based verification.

Even if the impact on temperature and other secondary meteorological fields is, on average, relatively modest, the verification demonstrates that the topography correction of the radiation

components yields a more physically correct description of radiation in high-resolution NWP models. In the near future the further increase of the computer power could permit to operate models with higher horizontal resolution, where topographical effects on radiation are even more pronounced. Under this point of view the presented work can give an important contribution for a complex topographically consistent weather forecast in the framework of the COSMO model.

For a better evaluation of the performance of the subgrid scale version for the direct shortwave radiation satellite data adapted to an higher resolution should be used in order to avoid a penalisation of the subgrid computations. The subgrid scale option is substantially better than the gridscale version for the downward longwave radiation. This indicates that for high resolution models with steeper model topography the use of the subgrid scale version can be expected to give slightly better results. Nevertheless, this version is for practical reasons more complicated to be operated, because all the time dependent correction factors have to be computed before the model integration. The gridscale version is under this point of view simpler, because only the topographic time independent parameters (slope angle, slope aspect, skyview and horizon) have to be computed before the model integration. This can easily be done by adding these topographical parameters to the traditional external parameters. On the contrary, a strategy to compute and store the subgridscale computed correction factors in an appropriate way has to be worked out, if this option is chosen.

Further model developments toward a better performance in complex topography applications could focus their attention on the one hand on the three-dimensional cloud problem and on the other hand verify whether the assumption of isotropy (in the source of diffuse and radiation, in the albedo of the surroundings and for the thermal radiation from the surroundings) for the parameterization of shortwave diffuse and longwave radiation is really appropriate.

# Chapter 3

# Performance of the COSMO-SC turbulence scheme for a stably stratified boundary layer

## 3.1 Introduction

### 3.1.1 The stable stratified boundary layer

The planetary boundary layer is the part of the atmosphere that is directly influenced by the underlying surface (Stull, 1988). A detailed understanding and modelling of the boundary layer can in fact allow to better describe and forecast the atmospheric environment, where people live.

When the ground is colder than the overlying air the boundary layer becomes stable. The Stable Boundary Layer (SBL) forms mostly during night-time or in situations of warm air advection over cold surfaces. The treatment of SBL turbulence is a difficult subject because different physical processes can be involved (Nieuwstadt, 1984a,b): topographical slope effects can occur (Whiteman, 2000; Whiteman et al., 2004), intermittent turbulence can appear, internal gravity waves and meandering motions as well as surface heterogeneities can play an important role (Mahrt, 1999). A different approach for each of these processes could be necessary. In addition, conclusions based on an individual site may not be generally valid (Mahrt and Vickers, 2006). The SBL in flat terrain is generally driven by turbulence and longwave radiative processes. The static stability can strongly reduce turbulence and the related mixing (Beljaars and Holtslag, 1991). During clear-sky nights, in absence of solar radiation, the surface radiation balance has entirely longwave nature (Andre and Mahrt, 1982). The negative longwave energy balance causes a radiative cooling at the surface. In addition, radiation divergence in the air column can contribute to a cooling of the lowest part of the troposphere (Mahrt, 1999).

Night time observations during the Cooperative Atmosphere-Surface Exchange Study in 1999 (CASES-99, Poulos et al., 2002) show that in flat terrain SBL conditions can be simplified defining 3 different regimes depending on the relative importance of turbulence and radiation: a fully turbulent SBL, an intermittently turbulent SBL and a radiative SBL (Van de Wiel et al., 2002a,c,b). During the first regime the turbulent heat flux can reach large values due to strong radiative cooling and strong turbulent mixing induced by a strong enough vertical wind shear (Sharan et al., 2003). The large static stability is partially compensated by a moderate wind shear generating turbulence and allowing for moderately strong mixing. In the intermittent turbulent SBL periods of quiet state are alternated with turbulent perionds. This state appears mostly in very stable situations (Mahrt, 1999; Nakamura and Mahrt, 2005) and for this reason is also called very stable SBL. Nights with hardly any turbulent mixing and weak winds are associated with the radiative SBL (extremely stable SBL). In these situations the downward surface sensible heat flux after

reaching a maximum tends to decrease, failing in the attempt to compensate the radiative cooling with downward sensible heat transport. A positive feedback mechanism can take place, leading in some cases to a surface decoupling from the atmosphere (Derbyshire, 1999a). Mahrt and Vickers (2006) found that in extremely stable situations the diffusivity of momentum is significantly greater than for heat, highlighting a possible problem for modelling the SBL. The main aspects and features of the SBL are further discussed by the work of Mahrt (1999). The formation of the stable boundary layer often has also consequences on the horizontal winds: the winds above the surface layer begin to decouple from the surface friction, sometimes leading to the formation of the nocturnal low-level jet (Blackadar, 1957, 1962; Banta et al., 2003, 2006), the strength of which can be assumed to be a kind of control on the magnitude of turbulence and turbulent fluxes in the SBL (Banta et al., 2003).

In order to appropriately model the SBL more knowledge about turbulence beyond the surface layer seems to be necessary (Derbyshire, 1999a). Numerical Weather Prediction (NWP) models often show in very stable situations too weak mixing which can lead to run-away characteristics near the ground (Viterbo et al., 1999). In SBL modelling different approaches have been chosen and the stability functions of the Monin-Obukhov similarity theory often become uncertain (Mahrt, 1999). Derbyshire (1999b) gives an exaustive overview of the methods of stable boundary layer modelling.

### 3.1.2 GABLS: the first intercomparison study

The GEWEX Atmospheric Boundary layer Study (GABLS, GEWEX is the Global Energy and Water Cycle Experiment) has the objective to improve the understanding of the atmospheric boundary layer and its modelling in NWP models or climate models. A complete single column model intercomparison for a simple shear-driven SBL has been performed in the first GABLS case presented by Holtslag (2006) and reported by Cuxart et al. (2006). The basic idea of the experiment was to compare the results and the performance of many different turbulence schemes, operational and research ones, with the Large Eddy Simulations (LES) performed in a preceding comparison study conducted by Beare et al. (2006). Sixteen groups participated in the intercomparison and twenty different schemes were used (Cuxart et al., 2006). The ensemble mean obtained from the previous LES study and the standard deviation of all the LES models participating to the intercomparison have been used as reference in order to evaluate the model performances. The variability between the LES simulations was relatively small and comparisons with observations had shown generally good agreement for this weak SBL (Beare et al., 2006). Nevertheless in situations with extremely strong stratification also LES simulations seem to have limitations (Cuxart et al., 2006).

The intercomparison case is finished, published and all the model data, including the LES reference data, are freely available [1] and are an optimal data source for turbulence model validations. The COSMO-SC model did not participate to the intercomparison study. This gives us the motivation and the opportunity to evaluate its performance using the available useful validation data, provided by the first GABLS case.

### 3.1.3 Case study description

The case is a typical situation of shear driven SBL (weakly stable SBL), in which barotropic geostrophic wind is imposed and a specific prescribed surface cooling rate is applied. A minimal vertical extension domain of 400 m is used and the vertical resolution has been fixed to 6.25 m. The time step for the 9 hours time integration is set to 10 s (Cuxart et al., 2006). Figure 3.1 shows the imposed surface forcing (cooling rate 0.25 $Kh^{-1}$) and the initial potential temperature profile.

[1] http://turbulencia.uib.es/gabls

The initial wind profile is assumed to be the same as the imposed geostrophic wind (8 $ms^{-1}$ in the x- direction). The radiation scheme as well as the soil parameterizations are switched off, as prescribed by in the GABLS study in order to minimise differences between the participating models. The prescribed surface forcing limits to some extent the model and feedback mechanisms between surface and soil parameterizations. The surface-atmosphere coupling plays an important role in the simulation of the planetary boundary layer increasing the complexity of the model sensitivities (Steeneveld et al., 2006b; Holtslag et al., 2007; Marshall et al., 2003; Stökli, 2004; Schulz et al., 2001).

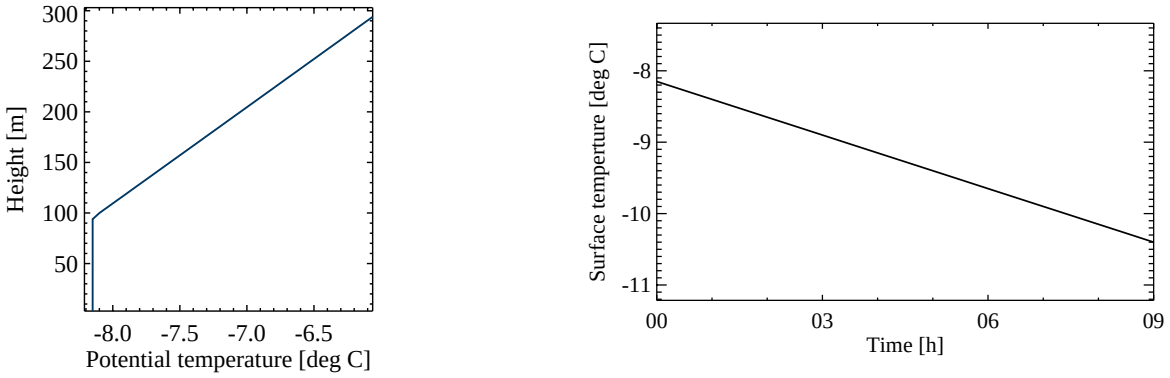


Figure 3.1: Initial potential temperature profile (left) and the prescribed surface cooling for the 9 hours simulation (right) for the first GABLS case.

### 3.1.4 The COSMO-SC model, the turbulence parameterization and the surface transfer scheme

The COSMO single column model (COSMO-SC model) works in a hydrostatic environment and uses the physical parameterizations of the NWP model COSMO (Steppeler et al., 2003; Doms et al., 2005). For this study the COSMO-SC model version 1.4 has been used. The COSMO-SC model equations for the prognostic variables wind, temperature and specific humidity are, respectively:

$$\frac{\partial U_i}{\partial t} = \epsilon_i f_c \left(U_i - U_{ig}\right) - \frac{\partial \overline{u_i' w'}}{\partial z}, \tag{3.1}$$

$$\frac{\partial \Theta}{\partial t} = -\frac{\partial \overline{\theta' w'}}{\partial z}, \tag{3.2}$$

$$\frac{\partial Q}{\partial t} = -\frac{\partial \overline{q' w'}}{\partial z}. \tag{3.3}$$

Variables denoted with capital letters are mean variables, while small letters are used for the turbulent part. $\epsilon_i$ defines the sign of the Coriolis parameter and $U_{ig}$ represents the geostrophic wind. Due to absence of the radiation scheme and the soil schemes, the single column simulation is fully driven by turbulent processes and the superposed geostrophic wind. The vertical turbulent fluxes (second order moments) are parameterized with the traditional flux-gradient approach:

$$\overline{u_i' w'} = -K_M \left(\frac{\partial U_i}{\partial z}\right) = (q \lambda_l S_M) \left(\frac{\partial U_i}{\partial z}\right), \tag{3.4}$$

$$\overline{\theta' w'} = -K_H \left(\frac{\partial \Theta}{\partial z}\right) = (q \lambda_l S_H) \left(\frac{\partial \Theta}{\partial z}\right), \tag{3.5}$$

$$\overline{q' w'} = -K_H \left(\frac{\partial Q}{\partial z}\right) = (q \lambda_l S_H) \left(\frac{\partial Q}{\partial z}\right). \tag{3.6}$$

The vertical turbulent transport, expressed in terms of turbulent exchange coefficients $K_M$ and $K_H$, is computed by the COSMO-SC turbulence scheme (TKE scheme) following the 1.5 order turbulence closure at the hierarchy level 2.5 proposed by Mellor and Yamada (1982) in the framework of their hierarchical model (Mellor and Yamada, 1974). This turbulence closure approach and its modifications have been widely used in meteorological and oceanographic applications (e.g. Galperin et al., 1988; Galperin and Kantha, 1989; Galperin and Mellor, 1991; Kantha and Clayson, 1994; Kantha, 2003; Janjic, 2001, 1990, 1994; Burk and Thompson, 1989). The closure approach solves a prognostic equation for the turbulent kinetic energy ($q^2 = 0.5 \cdot \mathrm{TKE}$), uses a turbulent master length scale and the closure stability functions $S_M$ and $S_H$, which are calculated by solving corresponding linear equations (Raschendorfer, 2001; Wacker et al., 2005). The $q^2$ equation is defined as:

$$\begin{aligned}\frac{\partial q^2}{\partial t} = \frac{1}{\bar{\rho}}\frac{\partial}{\partial z}\left[\alpha\bar{\rho}\lambda q\frac{\partial q^2}{\partial z}\right] + \frac{1}{\bar{\rho}}\frac{\partial}{\partial z}\left[2L_{pat}\bar{\rho}\left(\frac{\lambda_l g}{q\bar{\Theta}_\nu}\right)K_H\left(\frac{\partial\bar{\Theta}_\nu}{\partial z}\right)^2\right] + \\ 2K_M\left[\left(\frac{\partial U}{\partial z}\right)^2 + \left(\frac{\partial V}{\partial z}\right)^2\right] - 2K_H\frac{g}{\Theta_\nu}\left(A_{\Theta_l}\frac{\partial\Theta_l}{\partial z} + A_{Q_w}\frac{\partial Q_w}{\partial z}\right) - 2\frac{q^3}{B_1\lambda_l},\end{aligned} \tag{3.7}$$

where $\alpha$ is the constant for the turbulent transport parameterization of $q^2$ (third order moment). The second term of the right hand side of the equation is a so-called circulation term, which considers surface subgridscale heterogeneities with an horizontal length scale $L_{pat}$ as turbulence sources. This term is switched off in this study, because horizontal homogeneity is assumed. The third term on the right side of the equation is the shear production term. $\frac{\partial\Theta_\nu}{\partial z} = A_{\Theta_l}\frac{\partial\Theta_l}{\partial z} + A_{Q_w}\frac{\partial Q_w}{\partial z}$ is the gradient of potential virtual temperature, which can be expressed by the conservative variables $\Theta_l$ and $Q_w$ using the coefficients $A_{\Theta_l}$ and $A_{Q_w}$. Those coefficients again are performed with the help of a subgrid scale statistical condensation scheme according to Someria and Deardoff (1976). However, we consider only the dry case here. Thus the statistical condensation scheme is not active in our study. The last term describes the dissipation of turbulent kinetic energy (B1 is a closure constant from the Mellor and Yamada (1982) model.

The master length scale $\lambda_l$ is computed using the approach proposed by Blackadar (1962), assuming an asymptotic length scale value $\lambda_l^\infty$ of 200 m and adding the roughness length $z_0$ to the distance form the surface $z$:

$$\lambda_l = \lambda_l^\infty\frac{\kappa(z+z_0)}{\kappa(z+z_0)+\lambda_l^\infty}, \tag{3.8}$$

where $\kappa$ is the von Karman constant (set to 0.4).

For the stable case the implementation of the stability functions follows the Mellor and Yamada (1982) level-2.5 model (Eq. 3.11 and Eq. 3.12), while in unstable conditions a modified set of equations is used in order to avoid a singularity (Wacker et al., 2005; Raschendorfer, 2007a; Raschendorfer pers. communication). The stability functions in the stable case are functions of the dimensionless gradients $G_M$ and $G_H$ (Eq. 3.9 and Eq. 3.10) and are the final result of the algebraic closure of the second order moments. $G_M$ is kept free without any limitation in contrast to what Mellor and Yamada (1982) have suggested and what is used for example by Kantha and Clayson (1994):

$$G_M = \frac{\lambda_l^2}{q^2}\left[\left(\frac{\partial U}{\partial z}\right)^2 + \left(\frac{\partial V}{\partial z}\right)^2\right], \tag{3.9}$$

$$G_H = -\frac{\lambda_l^2}{q^2}\frac{g}{\Theta_\nu}\frac{\partial\Theta_\nu}{\partial z} = -\frac{\lambda_l^2}{q^2}(A_{\Theta_l}\frac{\partial\Theta_l}{\partial z} + A_{Q_w}\frac{\partial Q_w}{\partial z}). \tag{3.10}$$

$G_M$ and $G_H$ are non-dimensional functions of current shear and vertical buoyancy gradients. Negative values of $G_H$ are a sign of stable stratification. $\beta$ is the coefficient of thermal expansion.

$A_{\Theta_l}$ and $A_{Q_w}$ discussed above in connection with the $q^2$ equation. The algebraic solution for the stability functions derived according to the Mellor and Yamada (1982) 2.5 level model can be implicitly written as follows:

$$S_M = \frac{be2 \cdot a11 - be1 \cdot a21}{a11 \cdot a22 - a12 \cdot a21}, \tag{3.11}$$

$$S_H = \frac{be1 \cdot a22 - be2 \cdot a12}{a11 \cdot a22 - a12 \cdot a21} \tag{3.12}$$

where the auxiliary variables have following definition:

$$\begin{aligned} be1 &= 1 \\ be2 &= 1 - 3C1 \\ a11 &= \frac{1}{A_2} - (3B_2 - 12A_1)G_H \\ a12 &= 6A_1 G_M \\ a21 &= -(9A_2 + 12A_1)G_H \\ a22 &= \frac{1}{A_1} - 9A_2 G_H + 6A_1 G_M \end{aligned}$$

The closure constant parameters $(A_1, A_2, B_1, B_2, C_1)$ have the same numerical values of the Mellor and Yamada (1982) scheme:

$$(A_1, A_2, B_1, B_2, C_1) = (0.92, 0.74, 16.6, 10.1, 0.08). \tag{3.13}$$

The particular dependence of $S_M$ and $S_H$ from $G_M$ and $G_H$ is presented in Fig. 3.2.

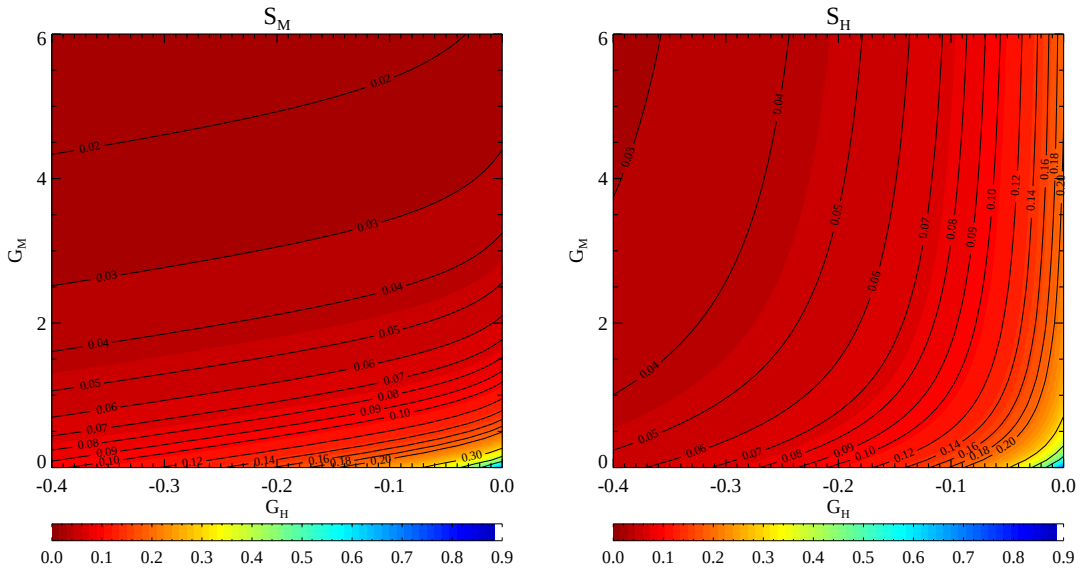


Figure 3.2: Stability functions $S_M$ (left) and $S_H$ (right) as function of $G_H$ and $G_M$ following the Mellor and Yamada (1982) turbulence closure as used in the COSMO model for the stable case. Note that no limitation for $G_M$ is active.

Other details about the turbulence scheme can be found in the Appendix B-1.

The surface transfer scheme permits to compute the turbulent fluxes between the rigid surface and the lowest atmospheric layer (transfer layer) delivering the transfer coefficients, which are

based on transfer resistances for momentum and scalars (temperature and moisture) along the three sub-layers of the transfer layer: a laminar layer, a roughness layer and the Surface Layer (or Prandtl layer). The first two layers are skin layers located below the level $l = \lambda_l/\kappa = z_0$ ($\kappa$ is the Von Karman constant and $z_0$ is the roughness length) and the third is located above it. The transfer resistances are expressed by simplified integrals of the reciprocal diffusion coefficients along the transfer layer, in which different interpolation formulae for the turbulent velocity scale are used. A necessary condition for the interpolation step is the computation of a $q^2$ value at the turbulence distance $l = \lambda_l/\kappa = z0$ and the relative turbulent diffusion coefficient following a similar approach as in the TKE scheme (Raschendorfer (2007a); Doms et al. (2001), Raschendorfer pers. communication). For momentum transfer only the resistance of the surface layer is active: laminar and roughness layer resistances are assumed to be zero. They can be activated or modified with a model parameter (rlammom $E_M$) set for the operational configuration to zero. The equivalent parameter for heat and water vapour ("rlamheat" $E_H$) is operationally set to 1.0. The transfer coefficients derived from the total transfer layer resistance directly enter into the parameterization of the surface turbulent fluxes of scalars (heat and moisture, Eq. 3.14, 3.15) and momentum (Eq. 3.16, 3.17), which are the bottom boundary condition for the simulations of the atmosphere. The surface fluxes are paremeterized using the gradients between surface and first atmospheric level ($\Delta T, \Delta QV$), the wind compontents at the first atmospheric layer ($U_{ke}, V_{ke}$) and the relative wind speed ($V_h$).

$$H_0 = -\rho \cdot C_{pd} \cdot C_\Theta \cdot V_h \cdot \Delta T \tag{3.14}$$

$$(E \cdot L_v)_0 = -\rho \cdot C_Q \cdot V_h \cdot L_v \cdot \Delta QV \tag{3.15}$$

$$(M_U)_0 = -\rho \cdot C_m \cdot V_h \cdot U_{ke} \tag{3.16}$$

$$(M_V)_0 = -\rho \cdot C_m \cdot V_h \cdot V_{ke} \tag{3.17}$$

Further details about the surface transfer scheme are presented in the Appendix B-2.

This study first presents the results obtained for the COSMO-SC operational configuration and the attempts to improve the performance reducing a key parameter for the turbulence model: the minimal vertical turbulent diffusion coefficient. The critical deterioration of the forecast quality observed with the introduction of this modification will then be analysed and several possible solutions will be proposed and compared. With help of several sensitivity experiments an optimal configuration will be defined. Finally, the performance of the obtained optimal configuration will be discussed.

## 3.2 Results and discussion

In this study the performance of the COSMO-SC turbulence scheme will be tested in the framework of the first GABLS case. For all the simulations the LES ensemble mean and its standard deviation are used as reference (Cuxart et al., 2006).

### 3.2.1 Performance of the operational configuration

The starting point of this study is the operational configuration of the COSMO-SC turbulence scheme currently used at MeteoSwiss for the daily numerical weather prediction. Compared to a normal operational COSMO run the circulation term of the TKE equation, considering subgrid scale heterogeneities, is switched off, because the simulation is assumed to happen over homogenous terrain. Additionally, the vertical resolution prescribed in the GABLS case has been used. The result for the main meteorological variables are presented in Figure 3.3 and compared with the ensemble mean of the LES simulations (dotted red line) and its standard deviation region

(yellow domain). All the figures with vertical profiles are the forecast results after nine hours of simulation. The zonal wind component shows an underestimation below the height of about 200 m and an overestimation above. Thus, the model completely misses the inversion between 150 and 200 m. On the contrary the meridional component shows an underestimation below 150 m and an overestimation above. The potential temperature profile is warmer than the LES ensemble below 150 m and colder above 200 m. The resulting profiles are a clear consequence of too strong

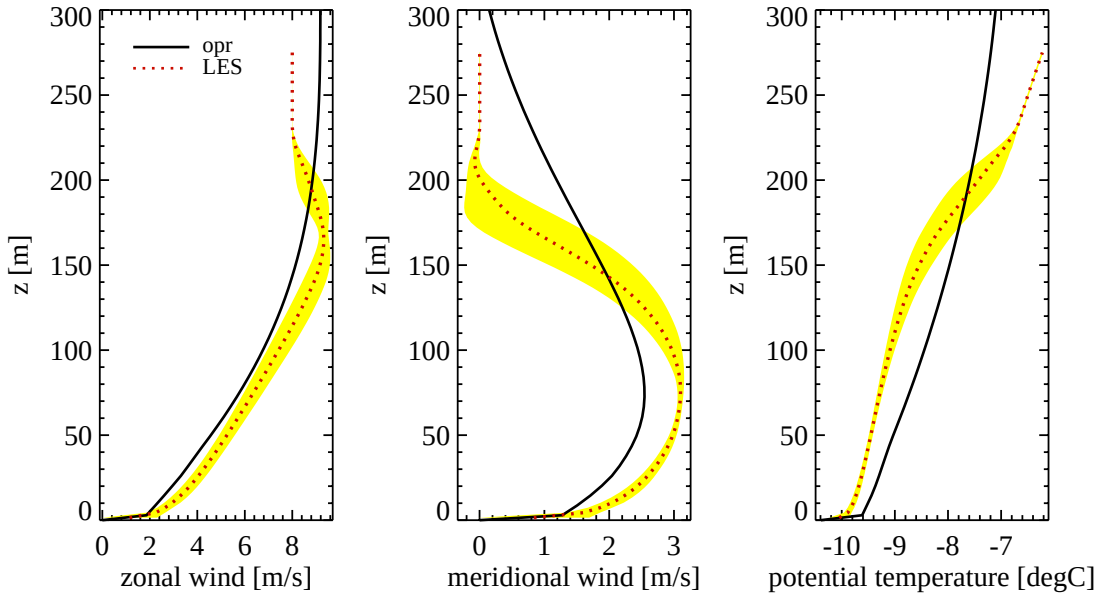


Figure 3.3: Zonal wind component (left), meridional wind component (middle) and potential temperature profile (right) after 9 hours of simulation. Black bold line for COSMO-SC operational configuration (minimum diffusion coefficient 1.0 $m^2/s$, asymptotic length scale 200 m, no laminar and roughness layer resistance for momentum), dotted red line the LES ensemble mean and its standard deviation (yellow area).

mixing, which dissolves the temperature gradient enhancement observed between 150 and 225 m. This too strong mixing is caused by the choice of a too high minimum turbulent diffusion coefficient. The turbulence scheme is controlled in stable situations by two minimum values for momentum and for scalars. These have been introduced in order to avoid a too low mixing in very stable situations, in particular because maritime boundary layer clouds were not dissolved efficiently otherwise. Further, this method assures almost always a good numerical stability of the turbulence scheme. The minimum is set operationally for both coefficients to 1 $m^2/s$. Notice that the stronger mixing in the atmosphere caused by the used higher minimum seems also to cause a non-balanced situation. The downward transport of sensible heat in the atmosphere increases the inversion between the enforced surface temperature and the temperature at the first atmospheric layer, generating a relatively strong jump of about 0.8°C in the temperature. This observation is the indirect consequence of the forced surface temperature. In a traditional model run the dynamical interaction with the soil model can probably strongly reduce such effects inducing feedback mechanisms. The evidence of a too strong mixing in the atmosphere is confirmed by the the profiles of turbulent fluxes and by the too high turbulent kinetic energy values (not shown).

### 3.2.2 Reducing the vertical mixing: the turbulence scheme instability

In order to reduce the observed excessive model diffusivity the minimum for the turbulent diffusion coefficients has been decreased. Figure 3.4 shows the model response to the progressive reduction of this value from 1.0 to 0.001 $m^2/s$. The expected reduced mixing is indeed obtained, but the

costs of this improvement in terms of profile quality are high. The smaller the chosen minimum the more the vertical profiles become unrealistic. In fact, patterns such as jumps appear in the

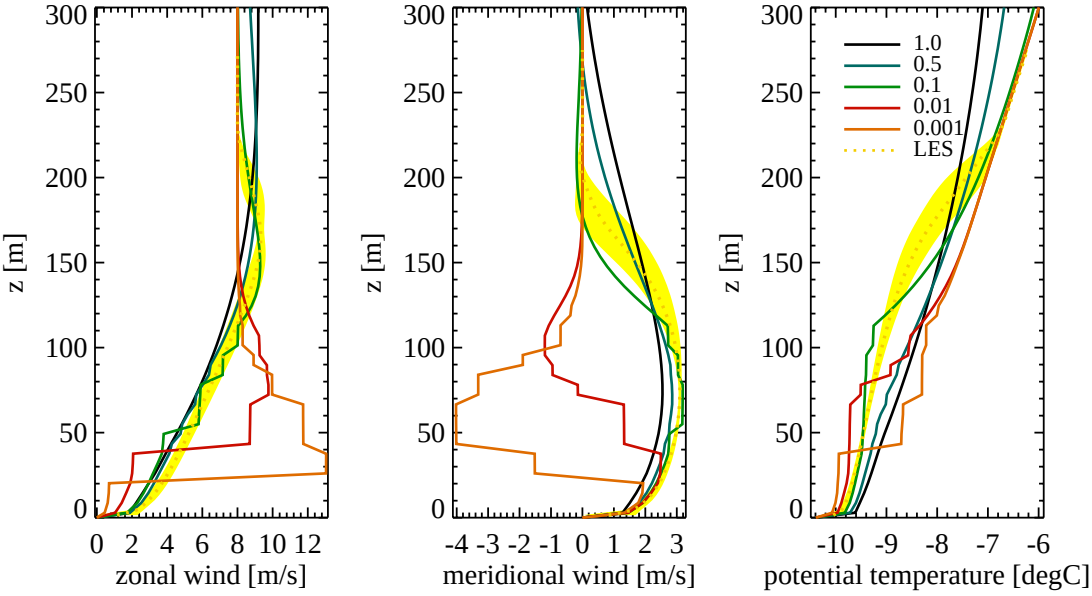


Figure 3.4: Zonal wind component (left), meridional wind component (middle) and potential temperature profile (right) after 9 hours of simulation for the GABLS 1 case. Black bold line for COSMO-SC operational configuration with the minimum value of the turbulent diffusion coefficients set to 1 $m^2/s$, the orange dotted line represents the LES ensemble mean and its standard deviation is illustrated by the yellow area. The other lines represent the experiments with reduced minimum value for the turbulent diffusion coefficient, as indicated in the legend.

vertical profiles and a further decrease of the chosen minimum even leads to a completely erratic profile, compared to the LES simulations. It seems clear that in this special SBL situation the scheme is very sensitive to the choice of this model parameter. The unrealistic jumps in the vertical profiles of wind and temperature are caused by strong oscillations in the vertical profile of the turbulent diffusion coefficients as shown in Fig. 3.5. The value of the turbulent diffusion coefficients oscillate from a certain value down to small values close to the prescribed minimum. The observed instability and related on-off oscillations additionally seem to be to some extent dependent on the vertical resolution. Figure 3.6 presents for the case with the minimum value set to 0.01 $m^2/s$ the model sensitivity to the density of vertical layers. The layer thickness has been increased from 6.25 m up to 40 m. The simulation with the coarsest vertical resolution (only 10 levels in the 400 m vertical domain) seems to remain in an acceptable result range (light red line, 40m thickness). The higher the resolution is, the more the oscillations are observed and the more steps are produced in the profiles. Note that the operational COSMO 7 km NWP model running at MeteoSwiss uses near the surface a minimum layer thickness of 20 m (first full level at about 10 m). The COSMO 2.2 km preoperational runs work with a minimum layer thickness of 20 m. Considering the fact that a minimum diffusion coefficient of 1.0 $m^2/s$ is operationally used, it is clear that at least for operational purposes, the turbulence scheme is so far not fully tested for simulations with high vertical resolutions and small minimum values of the diffusion coefficients.

### 3.2.3 Tackle the instability: some solutions

This section deals with the observed unrealistic oscillations and presents some solutions. The first step in order to tackle the instability is to localise the source of it in the turbulence scheme.
The observed stability problem is a documented and studied issue in the framework of the Mellor

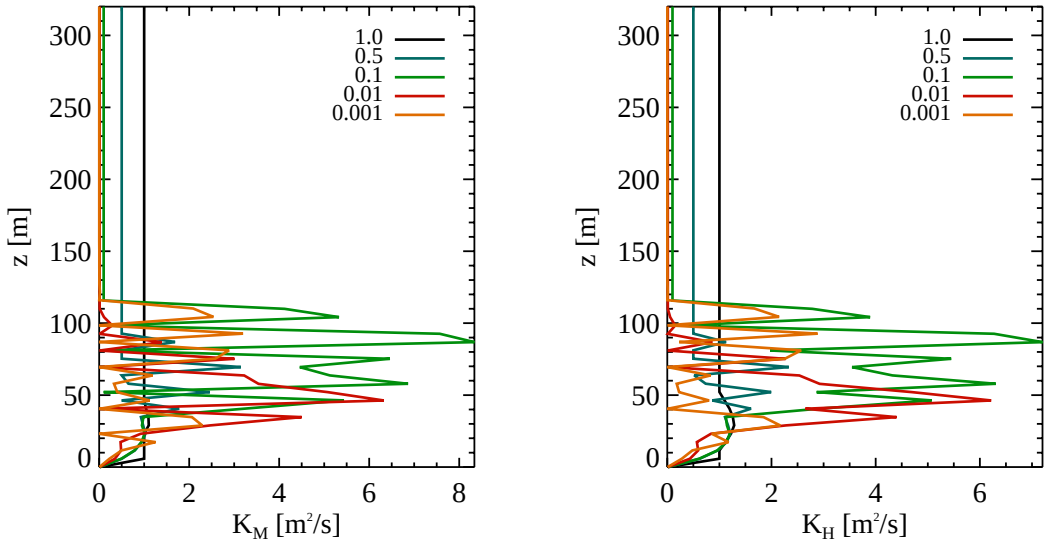


Figure 3.5: Sensitivity of the vertical profile of the turbulent diffusion coefficients for momentum (left) and for scalars as temperature and specific humidity (right) to the reduction of the minimum turbulent diffusion coefficient (after 9 hours of simulation). Notice the many unrealistic jumps, indicating the instability of the scheme, when a minimum of the turbulent diffusion coefficients smaller than 1.0 $m^2/s$ is used.

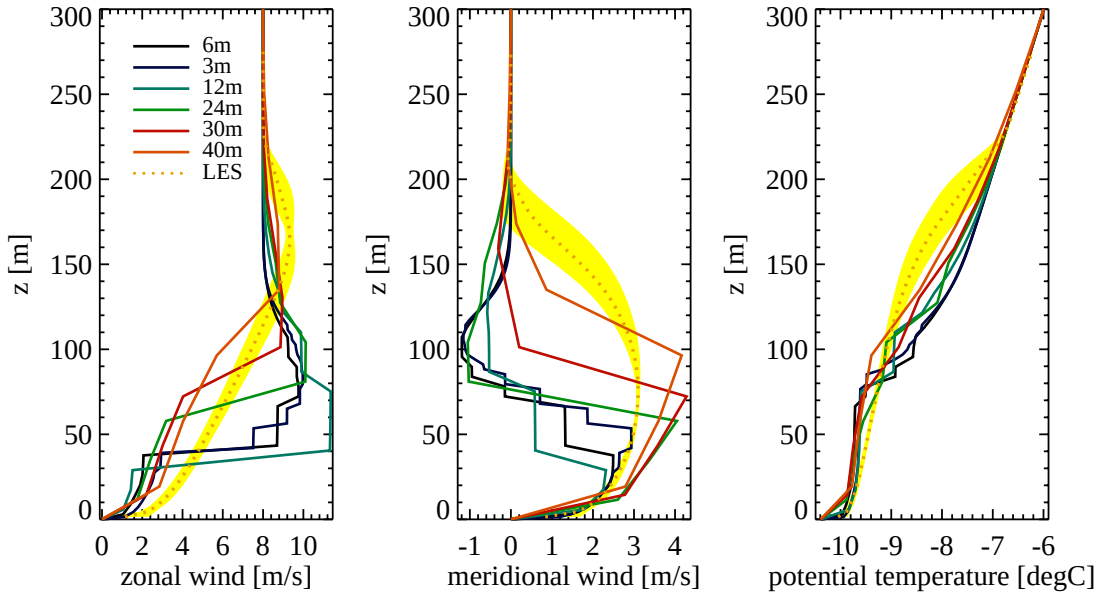


Figure 3.6: Zonal wind component (left), meridional wind component (middle) and potential temperature profile (right) after 9 hours of simulation. Sensitivity to the vertical resolution. Black bold line for COSMO-SC operational configuration with the vertical layer thickness set to 6.25m. The other lines represent the experiments with increased vertical layer thickness as indicated in the picture legend. The minimum diffusion coefficient is set to 0.01 $m^2/s$.

and Yamada (1982) turbulence model. Although such oscillations have never been mentioned in the original publications of the turbulence closure model, it seems that the problem has already been detected in a early stage of the model development (Mellor, 2003). Burchard and Deleersnijder (2001) suggest that the origin of the constraint is a physical inconsistency in the stability functions, which leads to a normalised stress function which is not monotone. The normalised stress is defined as:

$$\frac{K_M}{q^2}\left|\frac{\partial U_i}{\partial z}\right| = S_M G_M^{1/2} \tag{3.18}$$

Figure 3.7 shows for a fixed $G_H$ more than one value of $G_M$ leads to the same value for the normalized stress (Fig. 3.7 a). This either happens in the case of the original stability functions (as used in the COSMO model) or for the case with the limitation of $G_M$ (Eq. 3.21) as proposed by Mellor and Yamada (1982) in order to achieve a better forecast performance. Mellor (2003) pointed

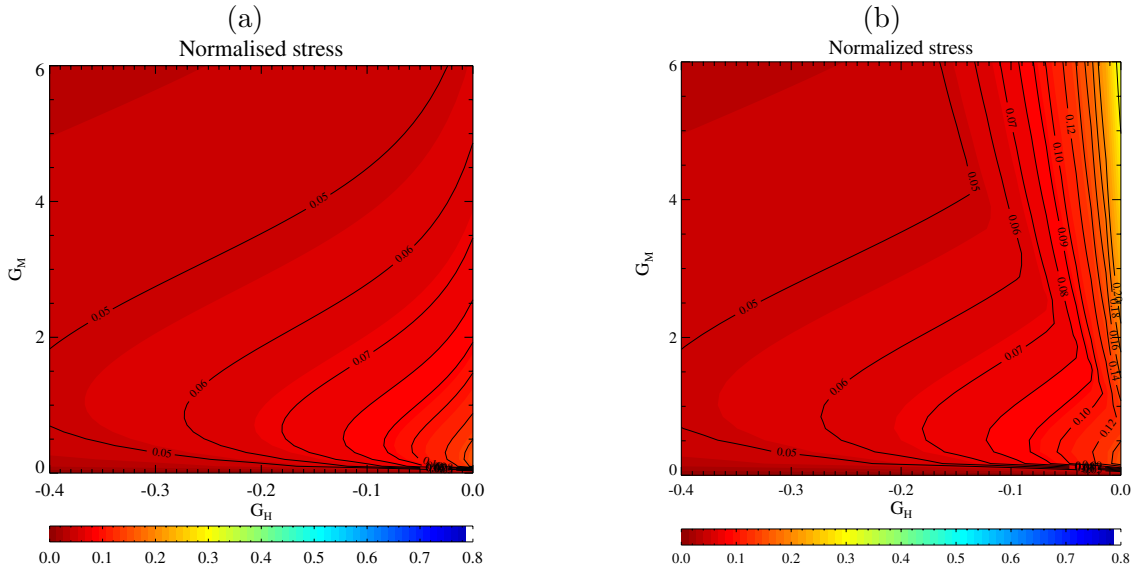


Figure 3.7: Normalized stress (Eq. 3.18) for the Mellor and Yamada (1982) stability functions without (a) and with (b) the limitation for $G_M$ (Eq. 3.21) suggested by the authors of the turbulence closure.

out that in a staggered grid (whereby the mean variables like temperature and wind components are staggered relative to the turbulence variables like q and turbulent fluxes) $G_M$ can oscillate between $k-1$ and $k+1$, where k is the vertical grid index, while in a non-staggered grid the problem does not occur. This suggests a numerical origin of the problem. The dependence on the vertical resolution can in fact be interpreted as numerical problem, which can similarly be solved as in in numerical advections schemes introducing information from neighbouring gridpoints.

These studies support the general hypothesis, that the oscillation problem in the diffusivities lies in the closure stability functions $S_H$ and $S_M$. Therefore, one may (i) directly filter the turbulent diffusion coefficients at the end of the turbulence scheme, (ii) filter the stability functions, (iii) filter the gradients or the dimensionless gradient $G_M$ going into the stability functions (Mellor, 2003), (iv) limit the range of the non-dimensional gradient function $G_M$ (Burchard and Deleersnijder, 2001), (v) use additional assumptions to simplify the stability functions or use alternative closure approaches (Galperin et al., 1988; Sukoriansky et al., 2005, 2006). In the following we present with some details each element of this list of possible solutions.

**Filtering the turbulent diffusion coefficients**

Considering the "jumping" profile of the turbulent diffusion coefficients one can try to introduce at the end of the turbulence scheme a vertical filtering of these coefficients following for example the

smoothing function presented in Eq. 3.19, where f can be substituted with the diffusion coefficients $K_M$ or $K_H$.

$$f_k^{new} = 0.5 f_k + 0.2 \left(f_{k-1} + f_{k+1}\right) + 0.05 \left(f_{k-2} + f_{k+2}\right) \tag{3.19}$$

Here the next grid-points below (k-1 and k-2) or above (k+1 and k+2) the one considered are assigned a weight of 0.2 and 0.05, respectively. Applying the smoothing in a case with a minimum value of the turbulent coefficients of 0.01 $m^2/s$ we obtain the result presented by the green line in Figure 3.8 (indicated with "K" in the legend). The instabilities represented by the temperature and wind "zig-zag" disappear and the profiles become realistic and comparable with the LES runs. The potential temperature profile falls into the range of the LES runs following the colder boarder of the LES ensemble. Compared to the ensemble mean the result is not more than 0.5 $°C$ colder and in particular the increase at around 200 m is realistically reproduced. The zonal wind speed is still slightly underestimated below 150 m, while the meridional wind is overestimated between 100 and 200 m.

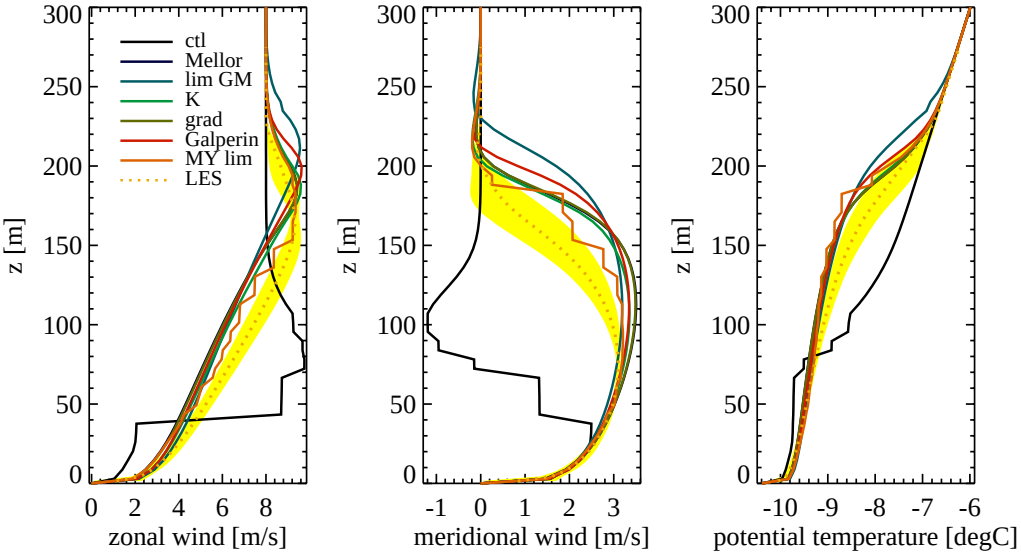


Figure 3.8: Zonal wind component (left), meridional wind component (middle) and potential temperature (right) profile after 9 simulation hours with a minimum for the turbulent diffusion coefficients set to $0.01 m^2/s$. Black line for the original COSMO-SC version (ctl), dark blue line for the version with vertical filtering of the dimensionless gradients (Mellor, 2003), light blue line for the results with the introduction of a $G_M$ limitation (lim GM, Eq. 3.23), green line for the filtering of the turbulent diffusion coefficients (K), green-yellow line for the filtering of the wind gradients (grad), red line for the quasi-equilibrium stability functions (Galperin et al., 1988) and orange line for the limitation of $G_M$ following Mellor and Yamada (1982) (MY lim, Eq. 3.21). The orange dotted line is the LES ensemble mean and its standard deviation is indicated with the yellow area.

Although the overall performance is good, this simple solution to the encountered problem is not completely satisfying under a physical point of view. In fact, it would be preferable to perform the filtering directly to the real source of the observed scheme instability, i.e. the stability functions and in particular their main dependent variables. Note that with large minimum diffusion coefficients the oscillation problem does not appear, because a kind of filtering is performed by the diffusivities themselves, which are, as mentioned, unrealistically high.

**Filtering the stability functions**

Anticipating the same filtering as presented in Eq. 3.19 to the stability functions completely solves the problem (not shown). This clearly demonstrates that the origin of the oscillations is located

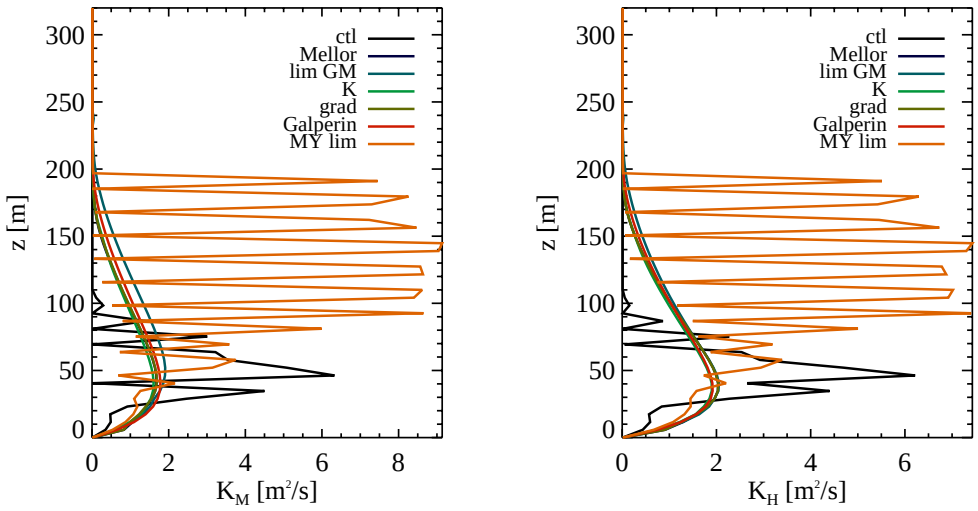


Figure 3.9: Vertical profile of the turbulent diffusion coefficients for momentum (left) and for scalars (temperature and specific humidity, right) after 9 simulation hours. A minimum of the turbulent diffusion coefficients of 0.01 $m^2/s$ is used. The line colors are the same as in Fig. 3.8. Compare with Fig. 3.5.

in the stability functions. The obtained results are nearly identical to those obtained with the next possible solution: filtering the gradients (green-yellow line in Fig. 3.9).

**Filtering the wind gradients before evaluating the stability functions**

One of the main input variables in the stability functions are wind gradients. The present shear driven atmospheric situation leads to a strong dependence of the stability functions on the local wind gradients. The sensitivity of the model to small changes of the wind gradient between neighbouring vertical gridpoints is particularly high. For that reason giving to the stability function a smoothed vertical profile as input avoids such sensitive reactions which leads to the observed oscillations. With the filtering function presented in Eq. 3.19 and applied to the gradients used for the computation of the dimensionless gradients (Eq. 3.9 and 3.10) it is possible to reach nearly the same result as for the filtering of the diffusion coefficients (Figure 3.8 light green line indicated with "grad").

**Filtering $G_M$ before evaluating the stability functions**

The filtering of the dimensionless gradient $G_M$ has been proposed by Mellor (2003) as a reply to the work of Burchard and Deleersnijder (2001). However, Mellor (2003) has proposed only a 3-point filter (Eq. 3.20) and this reduces the effect of the filter to some extent. The simulation presented in Fig. 3.8 (blue line indicated with "Mellor") performs almost exactly as the option presented before, based on the traditional gradients. This means that the impact of $\lambda^2/q^2$ on the numerical oscillations is marginal and confirms that the gradients play a central role in generating the instability. The $q^2$ values do not initiate the oscillations but only react to them.

$$f_k^{new} = 0.5 f_k + 0.25 \left( f_{k-1} + f_{k+1} \right) \tag{3.20}$$

In contrast to the present results with this case Deleersnijder and Burchard (2003) are convinced that this filtering option may not always be sufficient to prevent the unrealistic oscillations.

**Introducing a limit for $G_M$**

Already Mellor and Yamada (1982) have suggested to use a limitation of $G_M$ in order to achieve better simulation performance. They have proposed the following limitation for the dimensionless wind gradient:

$$G_M \leq 0.825 - 25.0 G_H \tag{3.21}$$

However, they did not have in mind the oscillation problem and therefore this limitation is not expected not to be a solution to this problem. It causes oscillations in the diffusivities with even larger amplitudes (Fig. 3.9). Nevertheless, the introduction of this maximum value for $G_M$ has a qualitatively positive impact. Although the oscillations in the diffusivities are still observed and the profile again shows unrealistic steps, at least the general profile shape is much closer to the reference LES runs and the other options presented bevore. Disregarding the unrealistic steps, it is interesting to note that the performance for wind speed seems to be even better than for the other options (Fig. 3.10 b, orange line). Additionally, it is encouraging that the complete failure observed with minimum diffusivities below 0.1 is clearly avoided (compare Fig. 3.8 orange line indicated with "MY lim" with red line of Fig. 3.4 indicated with "0.01").

Following the shear analysis of Burchard and Deleersnijder (2001) it is possible to derive a condition in order to obtain a monotonic function of the normalised stress. In essence this requires the dimensionless shear stress derivative to be larger than zero.

$$\frac{\partial S_M G_M^{1/2}}{\partial z} \geq 0 \tag{3.22}$$

For the stability functions in Eq. B.63 this condition is equivalent to:

$$G_M \leq \alpha_c \frac{a11(\frac{1}{A_2} - 9A_2 G_H) + be1(9A_2 - 6A_1)G_H}{a11 \cdot 6A_1} \tag{3.23}$$

Under a mathematical point of view the parameter $\alpha_c$ should be equal to one, but some empirical tests have shown for this case that its value can be increased up to 1.9 without any qualitative deterioration or commencement of oscillations. The other used variables in the limitation equation have the same meaning as presented in the introduction of the stability functions (Eq. 3.11 and 3.12). The resulting normalized stress function is presented in Fig. 3.10 a and is monotonic.

The introduction of the parameter $\alpha_c$ is the main difference to the limitation proposed by Burchard and Deleersnijder (2001) for the Mellor and Yamada (1982) stability functions in the version slightly modified by Kantha and Clayson (1994). The modified stability functions are illustrated in Fig. 3.11. The limitation of $G_M$ (Eq. 3.23) clearly reaches the goal: the oscillations in the diffusivities are eliminated. Nevertheless compared with the filtering solutions, presented above, it performs slightly worse (Fig. 3.8 blue-green line indicated with "lim GM"). The temperature inversion is vertically shifted (about 20 m) to higher altitudes. The same happens with the position of the maximum wind speed (low level jet, Fig. 3.10 b). Note that the introduction of the parameter $\alpha_c$ has significantly reduced this shift. The condition proposed by Burchard and Deleersnijder (2001) is for this reason to some extent too conservative and leads in this SBL case to a small forecast deterioration. The cost of the limitation is not zero.

**Use a quasi-equilibrium approach**

If turbulence equilibrium is assumed (shear and buoyancy turbulence production are fully compensated by the dissipation) $G_M$ can be expressed as function of $G_H$ and substituted in the $S_H$ and $S_M$ stability functions. The quasi-equilibrium condition is defined as follows:

$$G_M = \frac{1}{B_1 S_M} - \frac{S_H}{S_M} G_H \tag{3.24}$$

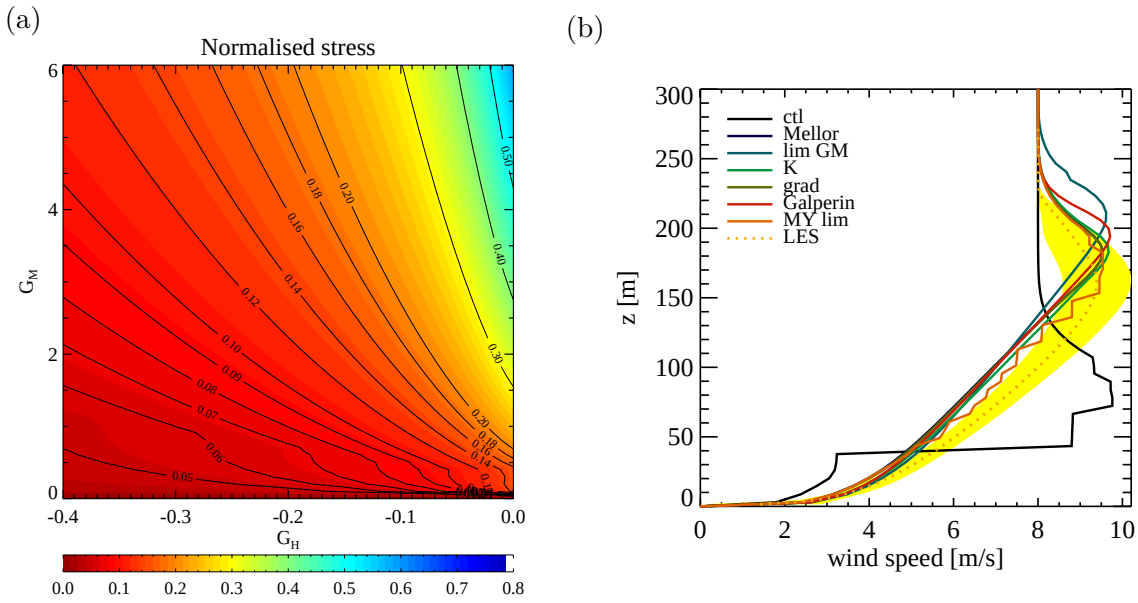


Figure 3.10: (a) Normalized stress (Eq. 3.18) for the Mellor and Yamada (1982) stability functions with the limitation for for $G_M$ (Eq. 3.23) and (b) wind speed for the case of the minimum diffusion coefficient set to 0.01 $m^2/s$. The line colors are the same as in Fig. 3.8.

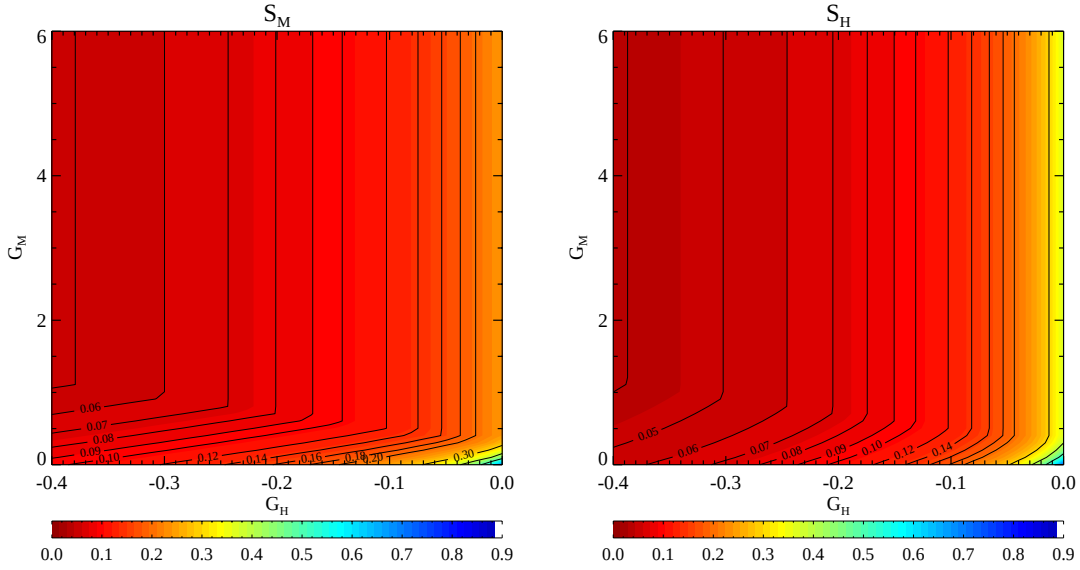


Figure 3.11: Stability functions $S_M$ (left) and $S_H$ (right) as function of $G_M$ and $G_H$ following the Mellor and Yamada (1982) turbulence closure with the introduced limitation for $G_M$(Eq. 3.23). Compare with Fig. 3.2.

The quasi-equilibrium stability functions proposed by Galperin et al. (1988) overcome the oscillation problem and perform stably. However, the performance is slightly reduced. The height of the low level jet is increased as well as the overestimation of the zonal wind above 100 m (Fig. 3.8 red line indicated with "Galperin"). One reason for this deterioration could be the fact that Galperin et al. (1988) use the quasi-equilibrium stability functions with an additional limitation of the master length scale $\lambda$. The implementation of this additional step in the COSMO model is not straightforward. Deleersnijder and Burchard (2003) argue that the physical costs of the quasi equilibrium version may not be zero, because this approach implies additional assumptions. However, in the simulated case the negative impact is moderately small.

**Use a new closure approach**

The stability functions derived from the quasi-normal scale elimination (Sukoriansky et al., 2005, 2006) also seem to work properly and do not present the oscillation problem (Perov, personal comunication). It has not explicitly been tested on the COSMO turbulence model.

The turbulent fluxes presented in Fig. 3.12 confirm that the filtering solutions, the quasi-equilibrium stability function and the limitation of $G_M$ solve the oscillation problem. The filtering options (turbulent diffusion coefficient, normal gradients and dimensionless gradients) give a stable result and are very close to the LES ensemble mean.

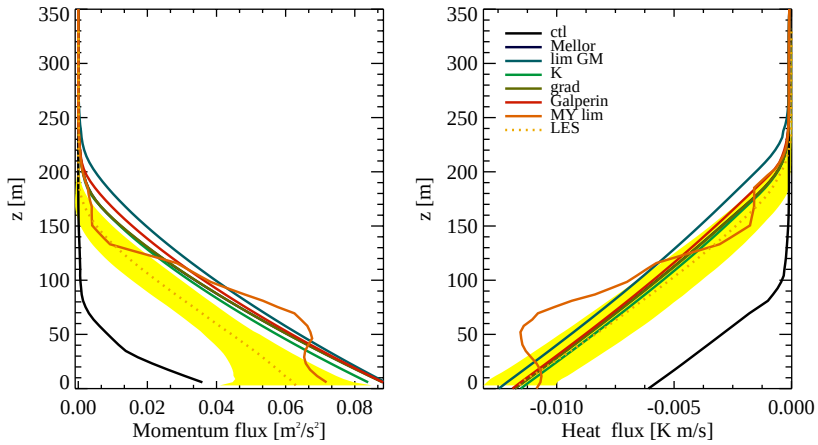


Figure 3.12: Vertical profile of the turbulent fluxes: left momentum flux and right heat flux. The line colors are the same as in Fig. 3.8.

### 3.2.4 Sensitivity study

The COSMO-SC turbulence scheme contains some parameters that have been tuned using measurement data or weather forecast experience. In order to assess the model sensitivity and to acquire an overview about the relative importance of these model parameters in the framework of this special shear driven SBL, some of them have been chosen and slightly modified. On three of them particular attention has been put: the minimum diffusion coefficient, the asymptotic mixing length and the parameter controlling the laminar resistance for momentum in the transfer scheme.

**Sensitivity to the minimum turbulent diffusion coefficient**

The minimum turbulent diffusion coefficient is a key parameter in stable situations, as already mentioned before in this work. The value of this parameter has been decreased in order to reduce the turbulent mixing. The model reacts very sensitively to changes in this parameter.

The reduction of the minimum has permitted to discover the stability problem associated with unrealistic oscillations in the diffusivities, which has been addressed in the previous section. Figure 3.13 depicts the same sensitivity experiment as in Fig. 3.4 but using the option with the wind gradients filtering, which avoids the oscillations and consequently allows for a fair comparison of all results. This experiment shows that minimum coefficients larger than 0.1 $m^2/s$ have the unavoidable consequence of a clear overestimation of the turbulent mixing. The experiment with minimum equal to 0.1 $m^2/s$ gives in the region with increased inversion (between 150 and 230 m) the best result. However, the total magnitude of wind speed related to the low level jet is better captured with lower diffusivities minima (Figure 3.20a). Notice that the low level jet as well as the increase of temperature inversion between 150 and 230 m are completely missed by the runs with minimum diffusivities higher than 0.1 $m^2/s$. Very interesting is the fact that the profiles remain stable and unchanged even if the minimum from 0.01 $m^2/s$ is further reduced: the results with 0.01 $m^2/s$ are nearly identical to those with 0.001 $m^2/s$. This means that from this point the model runs free without direct diffusivity limitations and is a good reason to take 0.01 as optimal value. Fig. 3.14 shows the turbulent fluxes, which are clearly overestimated in case of minimum diffusivities larger than 0.1 $m^2/s$. For the 0.01 and 0.001$m^2/s$ runs only a slight overestimation of the momentum fluxes is observed. For the sensible heat fluxes the runs with 0.01 and 0.001 $m^2/s$ perform better than those with higher minimum diffusivities. Compared to the case with 0.01 $m^2/s$ the forecast improvement in the sensible heat fluxes is observed above 150 m.

From this experiment we can conclude that for this special shear driven turbulence situation a minimum turbulent diffusion coefficient not larger than 0.1 $m^2/s$ is absolutely necessary (optimally it should be set to 0.01) in order to resolve the typical boundary layer structures (increased inversion and low level jet).

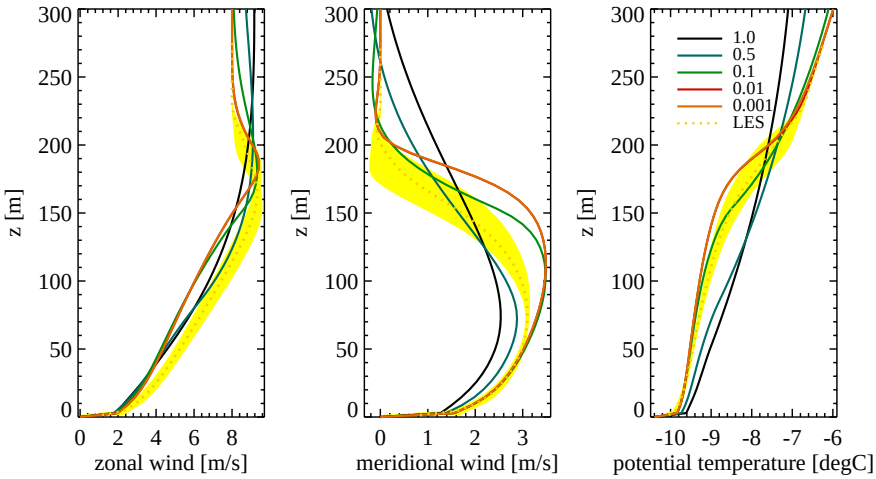


Figure 3.13: Zonal wind component (left), meridional wind component (middle) and potential temperature profile (right) after 9 hours of simulation. Black bold line for COSMO-SC operational configuration with the minimum value of the turbulent diffusion coefficients fixed to 1 $m^2/s$, the orange dotted line represents the LES ensemble mean and its standard deviation is illustrated by the yellow area. The other lines represent the experiments with reduced minimal value for the turbulent diffusion coefficients, as indicated in the legend. For this experiment the filtering of the gradients before the evaluation of the stability functions has been applied. Compare with Fig. 3.4.

**Sensitivity to asymptotic mixing length**

Reducing Blackadar's asymptotic length scale $\lambda_l^\infty$, also the mixing length or master length scale becomes smaller and vice-versa. However, the relation is not linear (Eq. B.29). Figure 3.15

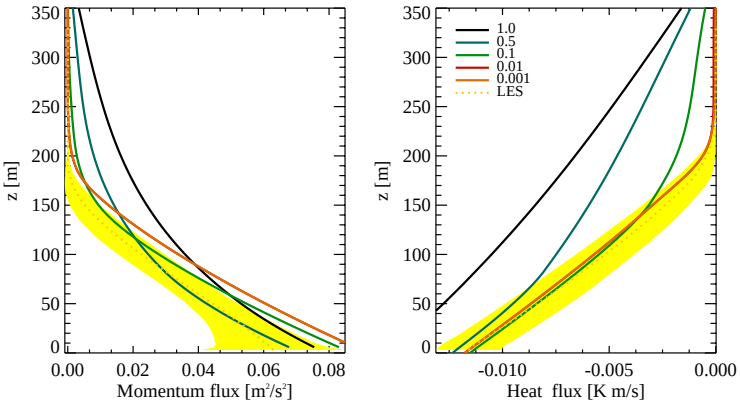


Figure 3.14: Vertical profile of the turbulent fluxes in the case of the sensitivity study for minimum diffusivity: left momentum flux and right heat flux. The line colors are the same as in Fig. 3.13.

shows the model reaction for wind and temperature to the introduction of different values of the asymptotic turbulence length scale (from 400 to 20 m). In this experiment the minimum diffusion coefficient has been set to 0.01 $m^2/s$ and the filtering of the wind gradients is active. The operational value used in the COSMO model is 200 m.

The wind and temperature profiles show a better correspondence with the LES reducing the value of this parameter, but the sensitivity is generally moderately small. Interesting are runs with an asymptotic length scale larger than 200 m: the temperature and wind profiles are nearly identical indicating that values larger than 200 m do not influence the model or are compensated by other model components. The optimal value seems to be close to 40 m. Figure 3.16 illustrates the impact on the turbulent fluxes. The reduced length scale permits to obtain better momentum flux profiles. The vertical profile of the sensible heat fluxes is already close to the LES ensemble mean and a reduction of this parameter goes slightly in the wrong direction, which is partially in contradiction to the results in the temperature profile. The TKE values surprisingly show a high sensitivity to changes in this paramenter (Fig. 3.17 b). The sensitivity is only partially observed in the tendency terms of the TKE equation, because modifications in other model components compensate the effect of the mixing length (not shown). A smaller master length scale means an higher TKE dissipation rate and lower TKE values. Lower TKE values reduce the dissipation amount. These effects are in balance. For these reasons a lower master length scale with a lower TKE value has as consequence a nearly unchanged dissipation rate (Eq. 3.7). The "external" use of the TKE values, for example for driving dispersion models, should seriously take into account this aspect. No choice of the asymptotic length scale leads to a vertical profile of TKE any close to the LES results. This contrasts with the fact that, the other variables are so close to the LES values.

Low values of the asymptotic length scale seem to have a positive effect on the position of the low level jet (Fig. 3.20 b): a small shift down to lower altitudes is observed. Finally, also the observed inverse proportionality of the stability functions has to be mentioned, that partially compensate a reduction of the mixing length: a decrease of the mixing length corresponds to a small increase of the stability functions values (not shown).

**Sensitivity to the laminar resistance for momentum**

The parameter "rlammom" controls the laminar resistance for momentum and implicitly the related roughness layer resistance in the surface transfer scheme. In the operational configuration it is set to zero. Due to this setting, the complete transfer resistance for momentum is expressed only by the effective surface layer part, assuming the roughness length z0 to be equal to the

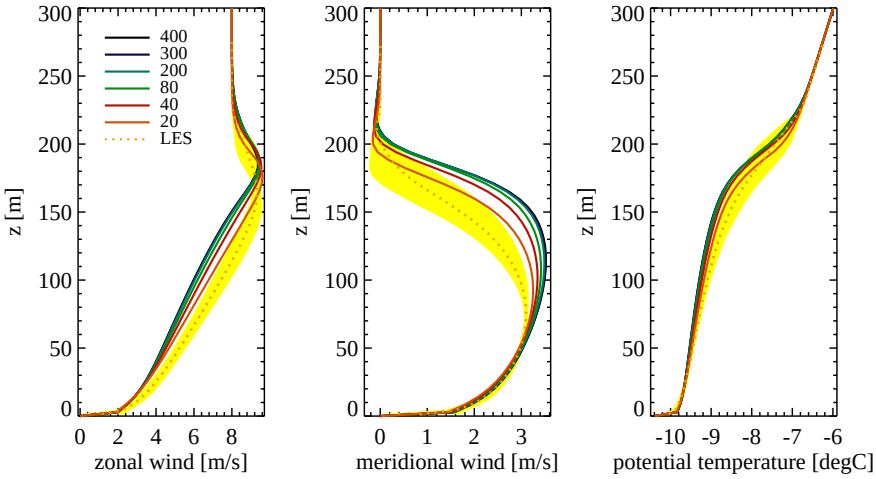


Figure 3.15: Model sensitivity to changes in the asymptotic mixing length $\lambda_l^\infty$ for the case with gradient filtering before the evaluation of the stability functions. Zonal wind component (left), meridional wind component (middle) and potential temperature (right) profile after 9 simulation hours. Blue-green line for the COSMO-SC version with vertical smoothing of the stability functions ($\lambda_l^\infty = 200m$). Orange dotted line is the LES ensemble mean and its standard deviation (yellow area). The other lines correspond to other values of $\lambda_l^\infty$.

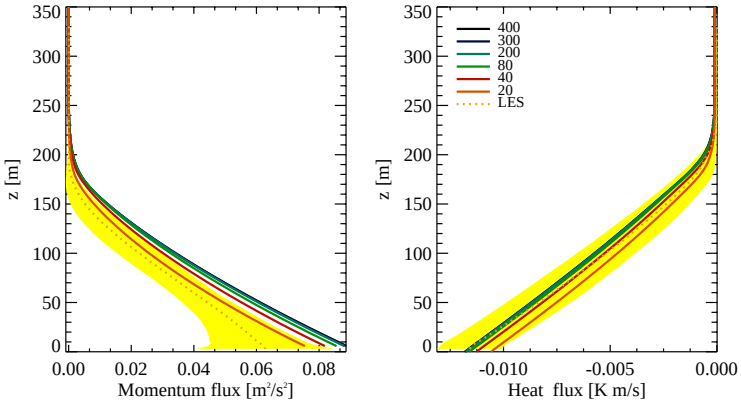


Figure 3.16: Vertical profile of the turbulent fluxes for the sensitivity tests with the asymptotic length scale: left momentum flux and right heat flux. The line colors are the same as in Fig. 3.15

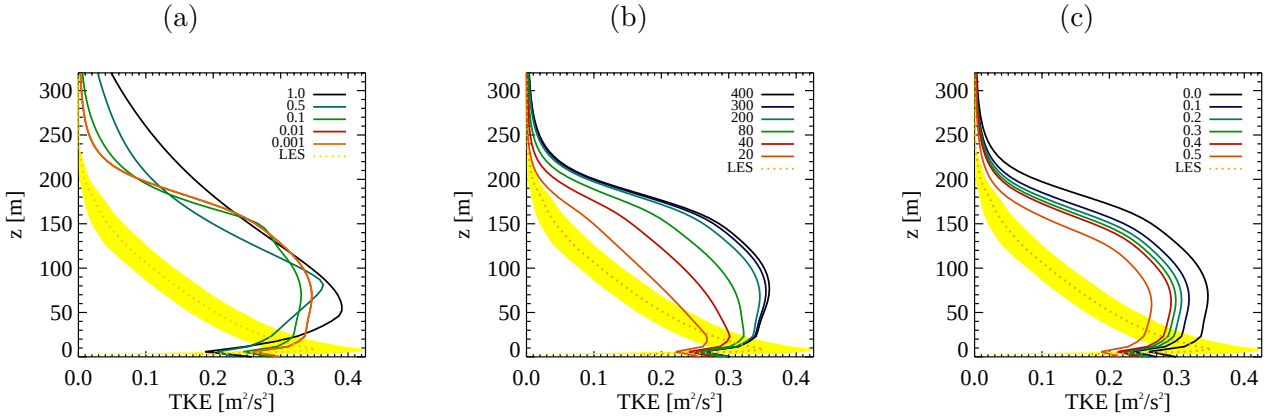


Figure 3.17: Turbulent kinetic energy (a) for the sensitivity study with the minimum diffusivity, (b) for different asymptotic length scales and (c) for the experiments with the increased laminar resistance for momentum. In each legend the chosen values of the corresponding parameter are indicated.

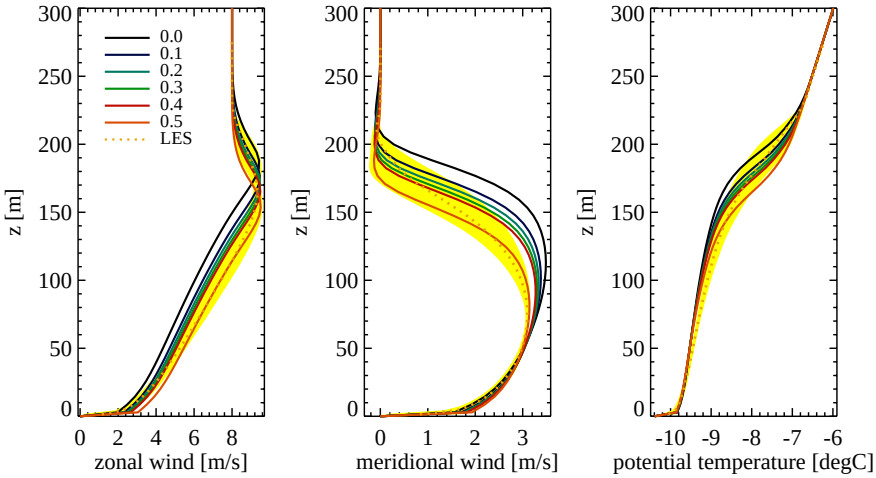


Figure 3.18: Model sensitivity to changes in the laminar resistance for momentum for the case with gradients filtering before the evaluation of the stability functions. Zonal wind component (left), meridional wind component (middle) and potential temperature (right) profile after 9 simulation hours. Black line for the COSMO-SC reference version with no resistance for momentum in the laminar layer (0.0). Orange dotted line is the LES ensemble mean and its standard deviation (yellow area).

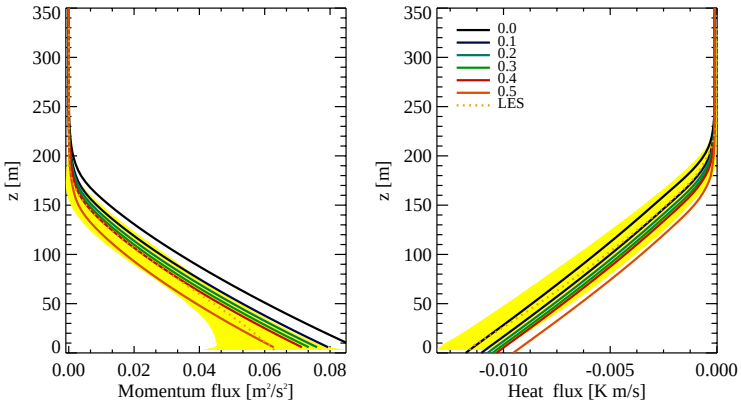


Figure 3.19: Vertical profile of the turbulent fluxes for the sensitivity study with the increased laminar resistance for momentum: left momentum flux and right heat flux. The line colors are the same as in Fig. 3.18.

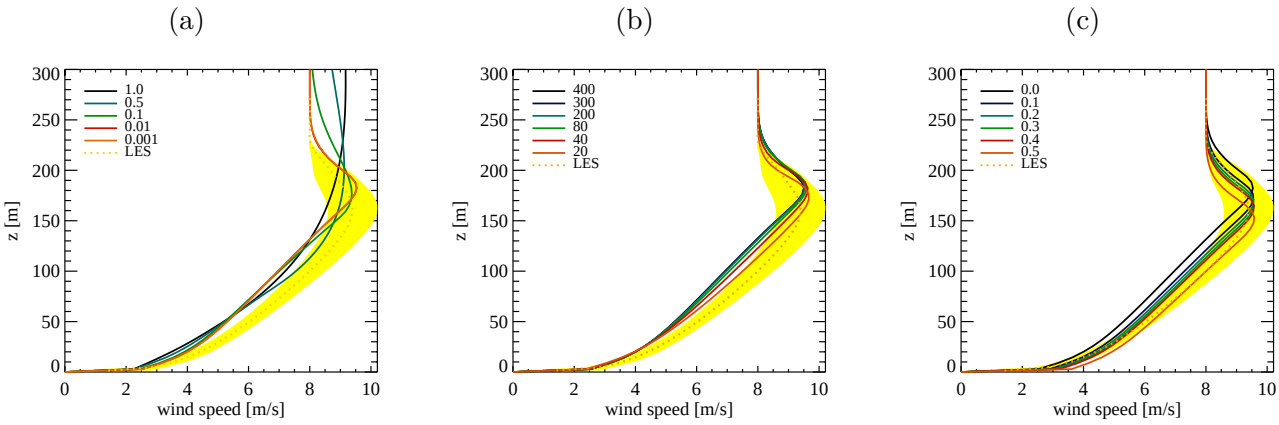


Figure 3.20: Wind speed (a) for the sensitivity study with the minimum diffusivity, (b) for simulations with different asymptotic length scales and (c) for the experiments with the increased laminar resistance for momentum. In each legend the chosen values of the corresponding parameter are indicated .

turbulent distance of the roughness layer depth (including the laminar layer). In reality z0 should be somewhat smaller than this depth, leading to accordingly smaller drag coefficients (transfer coefficients for momentum). The parameter "rlammom" controls the laminar resistance in the surface transfer scheme. For momentum only the surface layer part of the transfer scheme is active as resistance: the other two layers are considered as inexistent. The observed slight overestimation of the momentum fluxes could be related to this effect. The results of a sensitivity test with higher values of this control parameter are presented in Fig. 3.13 c for temperature and in Fig. 3.20 c for wind speed. As expected the increase of this parameter permits to get a better profile of the momentum fluxes, as well as for the wind speed. The position of the low level jet is optimal compared to the LES for a value between 0.2 and 0.3. Although we have changed only the laminar resistance for momentum we observe also a feedback in the temperature profile: values of the parameter between 0.1 and 0.2 give the best results for temperature. The equivalent parameter for heat "rlamheat", set normally to 1.0, does not influence that much the model results (not shown).

**Sensitivity to other parameters**

Related with the TKE equation the constant $\alpha$ is used (Eq. 3.7 set operationally to 0.2). The change of this model constant $\alpha$, affecting the turbulent transport of turbulent kinetic energy (parametrization of the third order moment) doesn't have any significant effect because the turbulent transport parameterization is artificially limited in order to avoid negative TKE values. The modification of the TKE weighting in time, introduced in the operational configuration in order to avoid strong variation from time step to time step, has in this case no significant effects.

Other important parameters are the closure constants A1, A2, B1, B2 and C1 (Eq. B.65) which also have a strong influence on the simulation results. However, in absence of observations it is quite dangerous to play with them. In addition the used constants seem to be widely accepted in the NWP modelling world and are considered generally optimal for semi ideal boundary layers.

The sensitivity study presented in this section has shown that there are at least three model parameters which have a significant impact on the simulations of this shear driven SBL: the minimum diffusion coefficient, the asymptotic length scale and the parameter related to the laminar resistance to momentum. In the next section we try to combine the results gained in the sensitivity study and in the solution of the oscillation problem in order to assemble an optimal configuration.

### 3.2.5 The optimal configuration

The analysis of all the proposed solutions to overcome the observed unrealistic oscillations has shown that the version with the filtering of the gradients (either fully dimensional gradients or dimensionless gradients) gives the best results. Although the filtering of the diffusion coefficients give nearly identical results, it should be avoided for three reasons. First, it is physically not really consistent to solve the problem with a filter at the end of the turbulence scheme forgetting the source of the instability. Second, it does not really make sense to introduce the filtering at the end if this work has found the source of the problem, the stability functions. Although the option with the $G_M$ limitation shows a slightly worse result it deserves to be considered as another possible optimal solution, because it solves the origin of the problem with a physically consistent limitation. In addition this option is easier to be implemented inside the turbulence model.

The minimun turbulent diffusion coefficient should be set to the maximum value which does not actively influence the model: this value has been determined to be close to 0.01 $m^2/s$. Values up to 0.1 $m^2/s$ are acceptable and do not really negatively affect the capture of important structures such as low level jets and temperature inversions.

The asymptotic mixing length should have values smaller than the value operationally used at MeteoSwiss (200 m). It is proposed to choose a value of 40 m what permits to obtain a small improvement.

The choice about the additional laminar resistance for momentum is more complicated. On the one hand for consistency reasons with the scalar resistances the laminar resistance for momentum should be larger than zero. On the other hand this probably raises some important constraints that have not be observed in this study. An overall better performance of the model is reached with values of this parameter between 0.1 and 0.2. It is set to a conservative value of 0.1.

Combining the filtering of the gradients and the three values of the respective three selected parameters we can define a kind of optimum configuration. The results of this configuration compared to our initial operational configuration are presented in Figs. 3.21 and 3.22 for the temperature and the wind components. In the same figure also the other one-dimensional turbulence models, which have participated in the GABLS intercomparison study (Cuxart et al., 2006), are plotted. In Fig. 3.21 the results collected in the first phase of the intercomparison project are illustrated, while some optimised simulations of the second phase are presented in Fig. 3.22. The COSMO operational configuration and in particular the optimal configuration performs well compared to other models. The optimal configuration reaches profile results very close to the LES ensemble mean. It may be noted that the improvement in the optimisation process (black bold to gray vs dashed lines in Fig. 3.21 and Fig. 3.22) is much more successful than for the most of the other models participating in GABLS and that the optimal configuration performs comparably well also using the coarser vertical resolution used for numerical weather prediction at MeteoSwiss (Fig. 3.22).

The vertical profile of the turbulent kinetic energy TKE, presented in Figure 3.23, shows a clear overestimation above 50 m and an underestimation below 50m for both the versions. The differences with the LES results are larger for the operational configuration. The overestimation and underestimation of the TKE values are not consistent with the observed turbulent fluxes of the optimal configuration, which are within the LES range (Fig. 3.24). The good temperature and wind profiles suggest that the overestimated mixing is avoided in the optimal configuration and does not play an important a role in the overestimation of the TKE values.

In order to eventually find the origin of the TKE differences with the LES, a look at the tendency terms of the TKE equation could give some hints. From the $q^2$ equation (Eq. 3.7) it is possible to follow the 4 main tendencies terms: shear production, buoyancy production, dissipation and transport, which are presented in Figure 3.25. Unfortunately we cannot compare the TKE term's time series in order to identify the source in time of the observed differences.

The shear production term is as expected at least two orders of magnitude greater than the

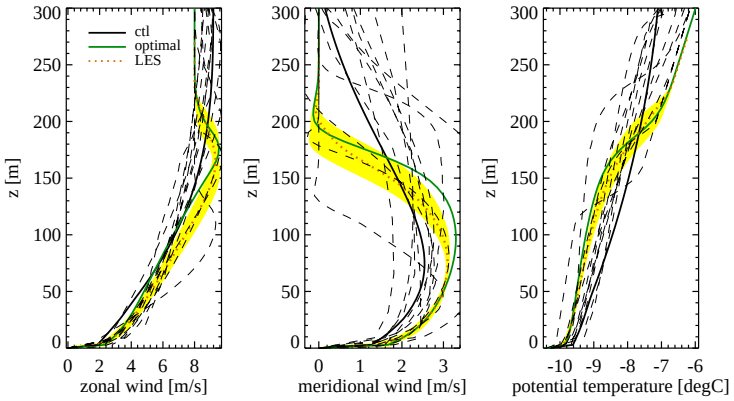


Figure 3.21: Zonal wind component (left), meridional wind component (middle) and potential temperature (right) profile after 9 simulation hours. Black line is for the COSMO-SC reference operational version (ctl). Green line is the optimal configuration. All the other lines are other models, which have participated to the first intercomparison study (pre GABLS phase). Orange dotted line is the LES ensemble mean and its standard deviation (yellow surface).

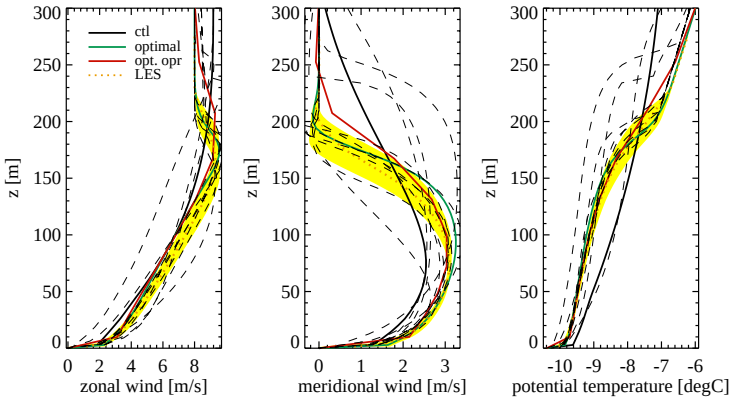


Figure 3.22: Zonal wind component (left), meridional wind component (middle) and potential temperature (right) profile after 9 simulation hours. Black line is for the COSMO-SC reference operational version (ctl). Green line is the optimal configuration. All the other lines are other models, which have participated to the first intercomparison study (post GABLS phase). Orange dotted line is the LES ensemble mean and its standard deviation (yellow surface).

buoyancy production term: the SBL under consideration is shear driven. The TKE production by the wind shear is well captured by the COSMO-SC model either for the optimal or for the operational configuration except for the peak close to the ground (at about 10 m). Although the relative significance of the buoyancy term is small, it shows generally an overestimation for the operational configuration and a good performance for the optimal configuration. The dissipation term falls in the LES range. Note that significantly different TKE values (between operational and optimal configuration) give similar values for the dissipation. Finally, for the transport term the negative peak at 10 m is underestimated. This peak is in accordance with the observed underestimation of TKE below 50 m. On the contrary, the overestimation above 50 m remains unexplained. Because the time series of the TKE terms are not available a further investigation of this aspect was not possible.

In Figure 3.26 (left) the time series of the Obuchov length scale shows a stabilisation after about 3-4 hours. At this time a steady state is reached. The time evolution of the surface stress for the optimal configuration is well in the LES range, while a underestimation is observed for the

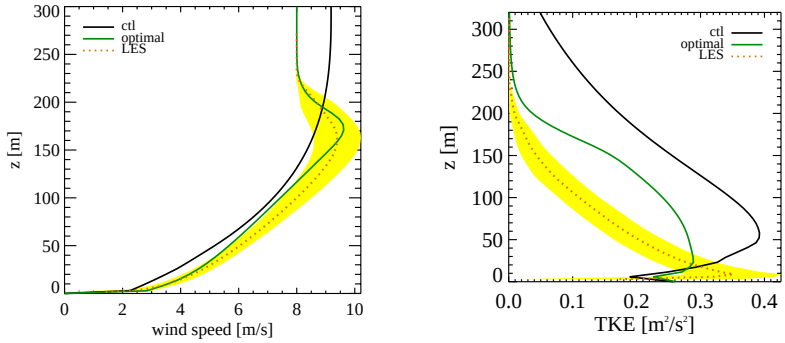


Figure 3.23: (a) Vertical wind speed profile and (b) vertical profile of the Turbulent Kinetic Energy (TKE) for the optimal configuration compared to the operational configuration.

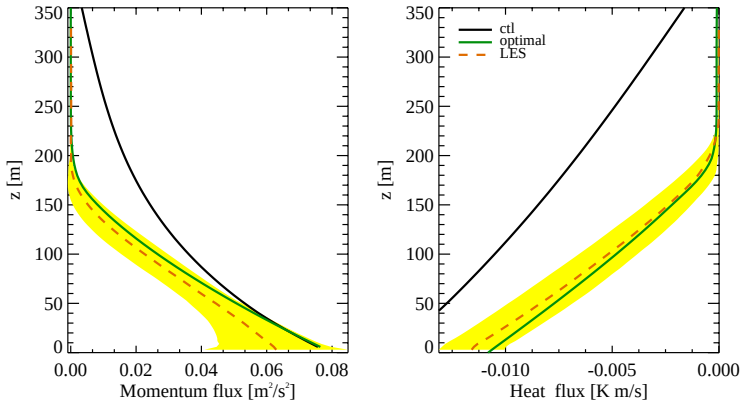


Figure 3.24: Vertical profile of the turbulent fluxes: left momentum flux and right heat flux. The line colors are the same as in Fig. 3.21

operational configuration (not shown). During the GABLS intercomparison case a boundary layer height has been diagnosed: the height at which the stress (momentum flux) falls to 5% of its surface value, divided by 0.95. After about five hours of simulation the steady state boundary layer height is reached at about 170 m (Figure 3.26 middle). The diagnosed height is in good agreement with the LES simulations for the optimal configuration. The operational configuration shows a clear overestimation of the boundary layer height due to overestimated momentum fluxes. The time series of the surface heat flux shows the expected overestimation of the downward flux for the operational configuration and a good agreement with the LES values for the optimal configuration.

The COSMO-SC turbulence scheme in the optimized version shows very good results, most of them in the range of the LES runs either for the traditional meteorological variables or for the turbulent fluxes. In order to get this good performance three main optimization steps have been necessary. First, the overestimation of the turbulent mixing has been limited, reducing the minimum value of the turbulent diffusion coefficients to 0.01 $m^2/s$. Second, in order to avoid a scheme instability a filtering function has to be applied to the vertical gradients used as input for the stability functions. Finally, two additional model parameters have been modified compared to the operational configuration.

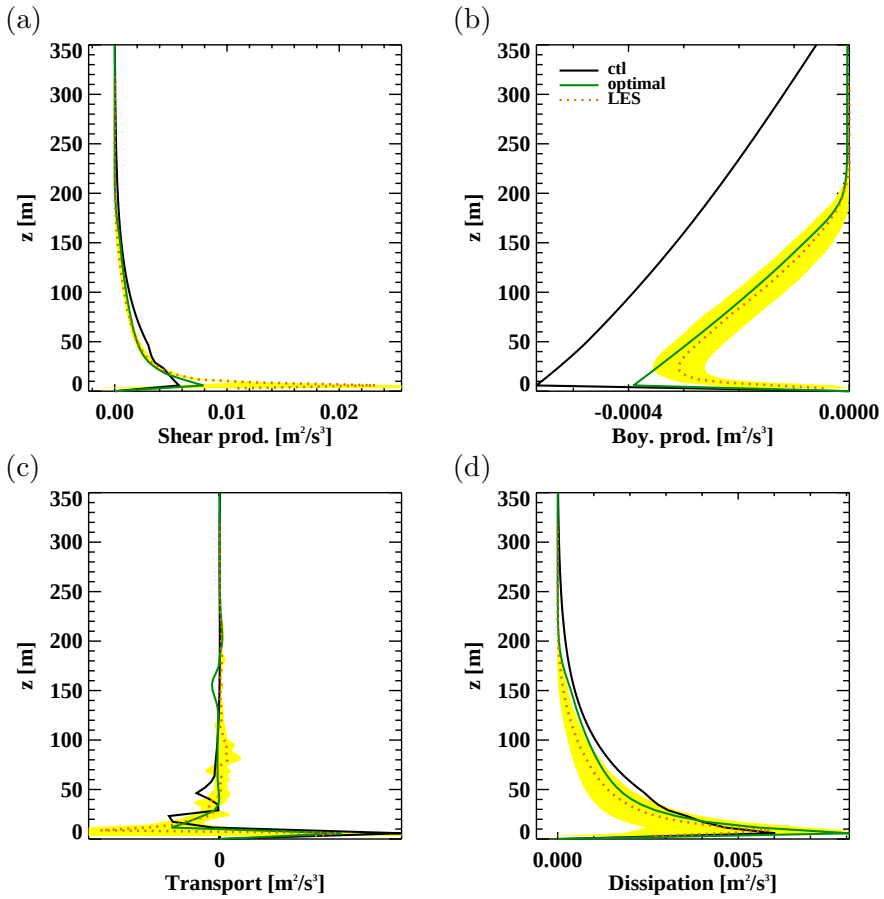


Figure 3.25: TKE production an consumption terms. (a) Shear production, (b) buoyancy production or consumption, (c) TKE turbulent transport and (d) TKE dissipation. The colour lines are the same as in Figure 3.21.

## 3.3 Summary and conclusions

The first GABLS case, characterised by a shear-driven stable boundary layer, has been simulated in this study with the COSMO-SC model, which did not participate to the international intercomparison study (Cuxart et al., 2006; Holtslag, 2006). The performance of the COSMO model has been evaluated using as reference the LES simulation made for the GABLS intercomparisons. The operational configuration of the turbulence scheme used for numerical weather forecast at MeteoSwiss or at the German Weather Service shows a too strong mixing, because the turbulent diffusion coefficients cannot reach values below 1 $m^2/s$. The performed simulations suggest that it is not justified to have a minimum value of the turbulent diffusion coefficients in this special boundary layer situation, where the wind shear is still able to produce enough turbulence. The minimum value was introduced in the operational NWP model especially in order to better capture very stable boundary layer situations with weak winds, avoiding too cold near-surface temperatures and avoiding problems with boundary layer clouds in the maritime SBL. However, in other situations with enough shear generated turbulence, this choice could lead to a significant deterioration of the forecast quality. As seen in the simulated case the overestimated mixing can dissolve important vertical structures, such as the important increase of the vertical temperature inversion at a certain height and - most important - the low level jet.

The attempt to overcome the overestimated mixing by reducing the minimum value of the turbulent diffusion coefficient has permitted to discover model instabilities and extremely high sensitivities to lower minimum values. The instability appears in terms of spurious oscillations

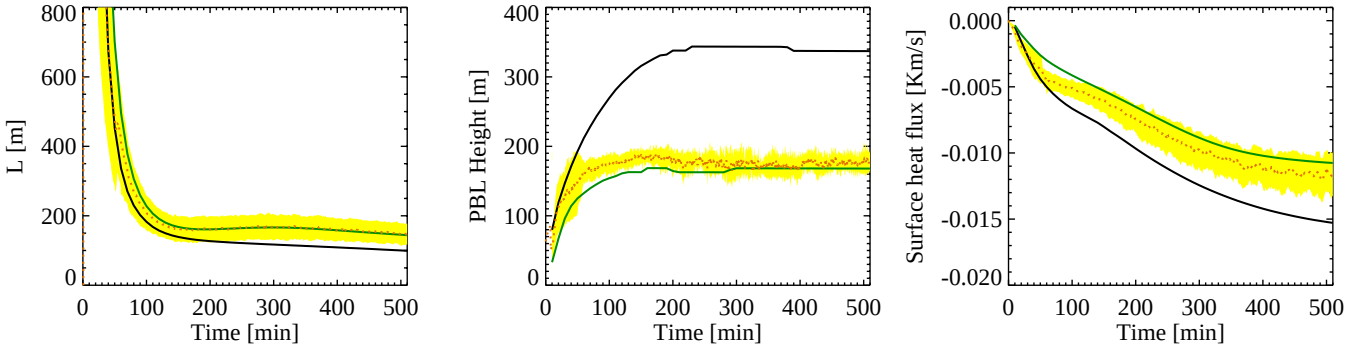


Figure 3.26: Time series for the Obuchov length (left), for the diagnosed boundary layer height (middle, which correspond to the height at which the stress (momentum fluxes) falls to 5% of its surface value, divided by 0.95) and right the surface sensible heat flux for. The line colours are the same as in Figure 3.21.

in the vertical profile of the diffusivities and has been associated to oscillations in the stability functions which react extremely sensitively to unsmoothed profiles of the vertical wind gradients. This study has demonstrated that the problem is strictly related to the properties of the used Mellor and Yamada (1982) turbulence closure model (1.5 order at the level 2.5). For minimum diffusivity values lower than 0.1 $m^2/s$ the oscillations even lead to completely unrealistic vertical profiles for temperature and wind. The oscillation problem has been analysed in depth and different solutions - proposed by the author and found in the literature - have been compared to each other for the first time. The application of a vertical filter function on the vertical wind gradients, before being used as input for the stability functions, has been found to provide the solution yielding the best results. Alternatively also a limitation of the non-dimensional wind gradient has been proposed.

The application of a smaller minimum turbulent diffusion coefficient, as used in this study in the optimised configuration (0.01 $m^2/s$) should seriously be taken into consideration for operational applications. At least a conservative reduction to 0.1 $m^2/s$ should be introduced in order to avoid the loss of special SBL structures, such as the formation of increased temperature inversions and low level jets. Further, the current problem of too rapid resolving of low stratus at boundary layer inversions over land can probably be cured by this choice.

The commonly observed negative consequence with lower minimum diffusivities represented by a too cold near surface SBL during very stable situations seems not to be a serious problem of the COSMO model, possibly due to the effect of the circulation term, already implemented in the COSMO turbulence scheme. This additional source term for TKE prevents turbulence from vanishing even in the SBL without mean vertical wind shear. The concept leading to this extension has some similarities with other approaches like the consideration of turbulent potential energy and turbulent total energy (Mauritsen and Svensson, 2007; Schumann and Gerz, 1995; Zilitinkevich, 2006) and is under further development at DWD. Since the surface transfer scheme of the COSMO model is based on the atmospheric turbulence scheme, the transfer coefficients can not drop to zero for the same reason. This is an other reason that a decoupling of the surface in a very stable SBL may be not a serious problem for the COSMO model even for considerably reduced minimum diffusion coefficients.

Besides the impact of reduced minimum diffusivities other sensitivity tests have been carried out. The model is only moderately sensitive to changes in Blackadar's asymptotic mixing length scale and significantly sensitive to an increased resistance for momentum in the transfer layer. This study proposes to reduce the asymtotic length scale from the 200 m to 40 m. An increased resistance for momentum in the transfer scheme activating the laminar and roughness layer resistances permits to reduce the overestimation of the momentum fluxes and to ameliorate the wind

profile. It has been proposed to seriously evaluate a modification of the parameter value using the value 0.1. In these two sensitivity experiments a large impact on the TKE values has been observed even if the changes in temperature or wind speed are quantitatively not that large. This indicates that the change in the $q^2$ values have partially been compensated for by changes in the stability functions. This aspect should be taken seriously into account if model forecasted TKE values are directly used for example for dispersion experiments.

The pool of data provided by the first GABLS case and used in this study has demonstrated how useful such intercomparison studies can be for testing and validating turbulence models.

## Acknowledgements

The author thanks Matthias Raschendorfer (German Weather Service, DWD) for providing us the COSMO-SC code and the related introductory information and Cuxart et al. (2006) for making available on the web the results of the GABLS first intercomparison case.

# Chapter 4

# Performance of the COSMO-SC model simulating a diurnal cycle

## 4.1 Introduction

### 4.1.1 The diurnal cycle in the planetary boundary layer

The planetary boundary layer (PBL) over land generally undergoes a significant diurnal cycle especially in clear sky situations, due to the variability of the solar forcing. The diurnal cycle of the solar radiation has strong implications on the mass, momentum and energy exchanges in the atmospheric boundary layer (ABL). After the typical stable nocturnal boundary layer (NBL), created by the surface radiative cooling and characterised by a surface temperature inversion, the daytime PBL begins when the net surface sensible heat flux is directed upward after sunrise. As more solar energy reaches the surface the more free convective eddies become active in transporting sensible heat (or moisture) upward; this warms (or moistens) the air above and increases the downward transport of momentum accelerating the flow below. The unstable boundary layer reaches its maximum extension and depth in early afternoon. Near sunset, rapid radiative processes of heat loss occur at the ground and a temperature inversion starts to grow from the bottom surface (Oke, 1978; Stull, 1988; Garratt, 1992). If the wind shear-generated turbulence is strong enough, the cooling is performed by transporting heat towards the ground (Estourel et al., 1986). The NBL depth is likely to be well defined in clear sky situations and evolves with time (Garratt, 1992). Garratt and Brost (1981) suggest that three sublayers can often be identified in the NBL, so far cooling is involved and enough turbulence is available: (i) the surface layer dominated by radiation, (ii) a layer throughout the most of the NBL where turbulent cooling dominates and (iii) a layer in the NBL upper part dominated again by radiative cooling. Radiative flux divergence plays an important role in the formation of the surface inversion mainly in the early evening (Sun et al., 2003; Ha and Mahrt, 2003; Andre and Mahrt, 1982). The formation of the stable boundary layer has as consequence that horizontal winds above the surface layer begin to decouple from the surface friction, sometimes leading to the formation of the nocturnal low-level jet (Blackadar, 1957, 1962; Banta et al., 2003, 2006).

The different behaviour of the stable and the unstable boundary layer has to be taken into account and sometimes different physical approaches are used: for example non-local turbulence closures have been developed in order to properly simulate the daytime PBL (Hong and Pan, 1996; Holtslag and Boville, 1993) or different scaling approaches are used (Garratt, 1992; Stull, 1988). Zhang and Zheng (2004) have noticed that the majority of PBL studies have been focussed on diurnal cycles of the temperature and little attention has been paid to the skills of capturing the diurnal cycle of surface and PBL winds. This lack of investigations is to some extent related to uncertainties in parameterizing the vertical momentum transport, and pressure diffusion in the

PBL; this lack is also partially related to the misconception that the development of the convective boundary layer is associated more to the transfer of sensible heat than to the momentum fluxes (Zhang and Zheng, 2004).

Besides the aspects and the challenges related with the stable boundary layer presented for the first GABLS intercomparison study (Cuxart et al., 2006) in the previous chapter, the simulation of the diurnal cycle is an important issue for evaluating the performance of a turbulence scheme. The transition between stable and unstable boundary layer and vice-versa, as well as the processes leading to the formation of the nocturnal boundary layer at sunset, are an interesting issue to be investigated. The simulation of the entire diurnal cycle and the transition between stable and unstable boundary layer is still an open research field also in large eddy simulations, which have been originally developed and used for convective situations (Kumar et al., 2006).

Aim of this study is to evaluate the performance of the single column COSMO model during a two-diurnal-cycles simulation in the framework of the second GABLS intercomparison experiment (Svensson and Holtslag, 2007), which was based on in the CASES 99 field campaign (Poulos et al., 2002).

After a short presentation of the single column model and of the special case study, this chapter will focus its attention on the performance of the model and will highlight some aspects related to the limits of the single column model and the sensitivity to two important aspects: the geostrophic forcing and the initialisation. Finally, a sensitivity study for some model parameters will be presented.

### 4.1.2 The COSMO-SC model

The single column COSMO-SC model works in a hydrostatic environment and uses the same physical parameterizations of the NWP model COSMO (Steppeler et al., 2003; Doms et al., 2005, 2001). The model equations have been presented in the second chapter 3.1.4. Optionally in this study also radiative tendencies for temperature have been added. The turbulent fluxes follow the local flux gradient approach, which implies the computation of the turbulent diffusion coefficients depending on the turbulent kinetic energy, on a master length scale and on a stability function. The vertical turbulent transport, expressed in terms of turbulent exchange coefficients, is computed by the COSMO-SC turbulence scheme (TKE scheme) following the 1.5 order turbulence closure at the hierarchy level 2.5 proposed by Mellor and Yamada (1982) in the framework of their hierarchical model (Mellor and Yamada, 1974). This Reynolds stress model and its modifications have been widely used in meteorological and oceanographic applications (e.g. Galperin et al., 1988; Galperin and Kantha, 1989; Galperin and Mellor, 1991; Kantha and Clayson, 1994; Kantha, 2003; Janjic, 2001, 1990, 1994; Burk and Thompson, 1989).

The closure approach solves a prognostic equation for the turbulent kinetic energy, uses a master length scale (dependent on an asymptotic length scale and on the height above ground) and solves an equation for each of the stability functions for momentum and scalars (Raschendorfer, 2001; Wacker et al., 2005; Raschendorfer, 2007b; Doms et al., 2001). The stability functions for unstable conditions have been modified compared to the original work of Mellor and Yamada (1982) in order to avoid singularities. For further details about the turbulence scheme see the previous chapter 3.1.4 and the Appendix B-1. The surface transfer scheme permits to compute the turbulent fluxes between the rigid surface and the lowest atmospheric layer (transfer layer) delivering the transfer coefficients, which are based on transfer resistances for momentum and scalars (temperature and moisture) along the three sub-layers of the transfer layer: a laminar layer, a roughness layer and surface layer (or Prandtl layer). The transfer coefficients are derived from the total transfer layer resistance and go directly into the parameterization of the surface turbulent fluxes of scalars (heat and moisture) and momentum, which are the bottom boundary condition for the simulations of the atmosphere. Further details about the transfer scheme are

presented in the Appendix B-2. The surface boundary condition necessary for the determination of the surface fluxes for temperature and moisture can be computed in case of coupled soil-atmosphere simulations with the combination of the COSMO radiation parameterizations (Ritter and Geleyn, 1992) and a multilayer soil model (Schrodin and Heise, 2001).

### 4.1.3 The second GABLS intercomparison case

The second GABLS one-dimensional model intercomparison project in the framework of the GEWEX Atmospheric Boundary-Layer Study (Holtslag et al., 2003) has been chosen with the purpose to study the diurnal cycle (Svensson and Holtslag, 2007). This case has been taken from the CASES-99 experiment (Poulos et al., 2002) and fully covers two diurnal cycles, which have already beensimulated by Steeneveld et al. (2006a,b). The geographical location of the experiment, Kansas US, is covered with prairie grassland and the area is relatively flat with some minor topographical features (roughness length set to 3 cm). Following the initiator of the intercomparison study, the chosen simulation period should present a textbook case of a radiation forced diurnal cycle (Svensson and Holtslag, 2007).

For the second GABLS intercomparison case the simulation has been defined to be started at 21 UTC (16 local time) on October 22 1999 and the simulation length has been fixed to 59 hours. The initialisation profiles for temperature, humidity and wind (Fig. 4.3 black line), the constant geostrophic forcing (Fig. 4.4 red line) the subsidence starting at October 23 at 21 UTC and the surface temperature forcing (Fig. 4.2) have been prescribed. The radiation parameterization as well as the surface and soil parameterizations have been prescribed to be switched off. The COSMO model results corresponding exactly to this GABLS intercomparison case have been submitted to the organisers. The results of the intercomparison are still not published. Some preliminary results have been presented in the second GABLS workshop in Stockolm in June 2007 and indicate a significantly large spread between the participating models as presented for the 2 m temperature in Fig. 4.1. The COSMO single column model, used in the present study,

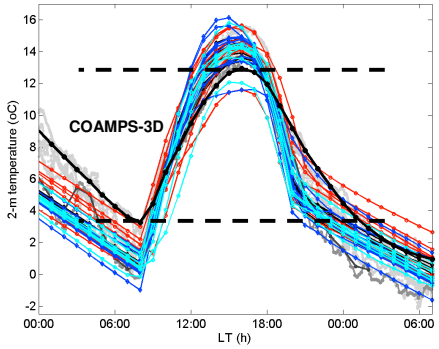


Figure 4.1: 2 m temperature results during the first day of the second GABLS intercomparison case. Each line correspond to a participating model. In the background in grey the observations and in the solid black line the simulation with the 3D model COAMPS (courtesy of Gunilla Svennsson, University of Stockolm)

is participating in this intercomparison experiment. Here, the focus is put on the investigation of the main model sensitivities and on the comparison with the observations. For the present purpose, the initialisation, the added forcings and the length of the simulation have been slightly modified compared to the prescription of the GABLS 2 intercomparison study: five important aspects have been changed. First, the simulations have been limited to the period starting on October 22 at 21 UTC or on October 23 at 01 UTC and finishing on October 25 at 05 UTC (56 or 52 hours, respectively). Second, the initialisation profiles for temperature, humidity and wind components have been taken from vertical soundings, which have previously been slightly filtered

in order to be smoother, thus allowing for a reduction in the spin-off effect at the beginning of the simulation. Third, the compared single column model has been forced with a surface temperature during night-time closer to the observations (Fig. 4.2). Forth, the prescribed geostrophic forcing has been taken as time-dependent using an estimation based on the radiosoundings (see constant geotrophic forcing and time dependent geostrophic forcing presented in Fig. 4.4 black line) or taken from a computed three-dimensional simulation done with a Coupled Ocean-Atmosphere Prediction System (COAMPS[2], Svennsson personal communication).

During the simulation, the background geostrophic wind comes from the northern sector and it is weakening somewhat in combination with some subsidence during the second day. During the second day of simulation and during night time the geostrophig wind shows a significant height dependence, which introduces an additional complexity for a one-dimensional simulation. This aspect has not been considered for this study.

The surface specific humidity is prescribed and kept constant during the entire simulation time. A detailed analysis of the radiosoundings, considering the typical temperature daily cycle in the PBL and the observed moderately strong winds during the target time window, suggests that temperature advection is not negligible. This has been estimated for this study from the radiosoundings at the top of the boundary layer. From hour 6 (October 23 at 03 UTC ) to hour 16 (October 23 13 UTC) a cold air advection in the residual layer (resulting from the formation of the stable boundary layer) can be identified. A negative temperature advection of about $-2.0 \cdot 10^{-4} K/s$ has been identified during the first night. Later, for the whole air column up to 3000 m, a positive temperature advection of about $5 \cdot 10^{-5} K/s$ has been diagnosed, similarly to the simulations performed by Steeneveld et al. (2006b). In the original GABLS 2 experiment the cold advection effect has indirectly been considered by prescribing a colder temperature profile than observed below 800-1000 m (Fig. 4.3). The temperature advection is not considered in our simulation but has to be kept in mind during the interpretation of the results.

Additionally, subsidence is considered in terms of vertical downward advection starting on October 23 at 21 UTC. It is prescribed through Eq. 4.1 as in the intercomparison study.

$$\begin{cases} w = -0.005 \frac{z}{1000} m/s, z \leq 1000m \\ w = -0.005 m/s, z \geq 1000m \end{cases} \tag{4.1}$$

The prescribed surface forcing to some extent limits the model and the feedback mechanisms between surface and soil parameterizations. The soil parameterization is in fact switched off, as prescribed in the intercomparison study for reducing model differences. The surface-atmosphere coupling plays an important role in the simulation of the PBL increasing the complexity of the model sensitivities (Steeneveld et al., 2006b; Holtslag et al., 2007; Marshall et al., 2003; Stökli, 2004; Schulz et al., 2001).

The radiation parameterization is switched on and actively influences the temperature tendencies only in the atmosphere (surface temperature is prescribed) giving mainly during night negative radiative temperature tendencies, due to longwave radiation emissions.

Although the case seems to be moderately complex due to the dynamical situation, at least during the second day, the many available observations of the CASES 99 field campaign (Poulos et al., 2002) give a good opportunity to compare many aspects of the COSMO model results and to evaluate the performance during a complete diurnal cycle, as well as to identify the limits of the single column modelling in a real situation.

### 4.1.4 COSMO single column model settings

For this study the COSMO single column model version 1.4 has been used. The 56 hours simulation has a vertical extension of 3500 m and 100 vertical layers. Near the ground the vertical resolution

[2]http://www.nrlmry.navy.mil/coamps-web/web/home

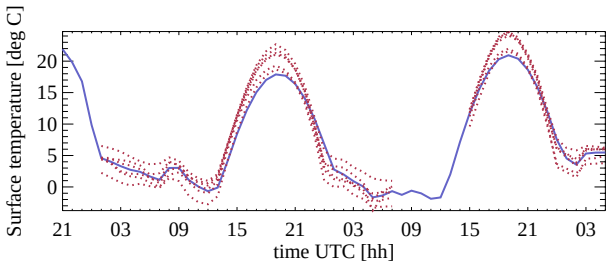


Figure 4.2: Surface temperature forcing used as boundary condition for the atmospheric single column modelling. The blue line is the complete surface forcing prescribed and the red dotted lines are the observations taken in the CASES 99 field campaign. The different lines refer to different sites over the target area of the field campaign.

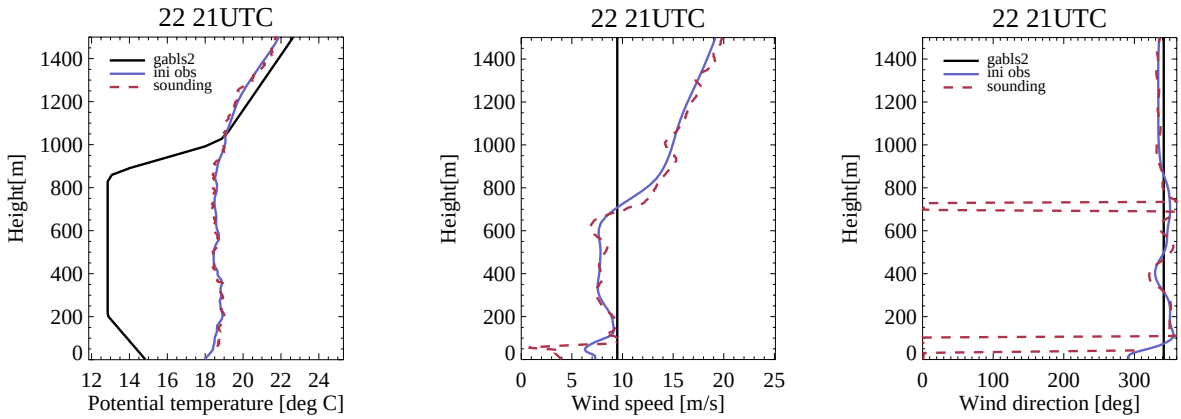


Figure 4.3: Initial profile for potential temperature (left), wind speed (middle) and wind direction (right) used for the simulations started on the October 22 at 21 UTC. The black line represents the GABLS 2 initialisation. The blue line represents the filtered sounding used as alternative initial profile. The red dashed line corresponds to the original sounding values.

is about 3 m and at the top of the vertical column about 75 m. The soil parameterizations are switched off (except for a comparison run), while the radiation parameterization is active producing in the atmosphere radiative tendencies for temperature. The time step used is 10 s. For the entire simulation a minimal diffusion coefficient of 0.01 $m^2/s$ (for momentum and scalars) and an asymptotic length scale of 100 m is applied (see previous chapter for the definitions of these two parameters). The filtering of the wind gradients before the evaluation of the stability function is active in order to avoid the unrealistic oscillations during the stable situations below 500 m (see previous chapter). The surface temperature forcing has been presented in the previous section as well as the three options for the geostrophic forcing. In the next sections besides the reference simulation of the second GABLS intercomparison several other simulations will be presented. For each one the specific modifications compared to the standard settings will be mentioned.

## 4.2 Results and discussion

### 4.2.1 Performance for the second GABLS intercomparison case

First step of this study is to evaluate the performance for the original GABLS case (except for the slightly modified surface temperature forcing) and to compare it with the simulation initialised directly from the observations. In both simulations the same constant geostrophic and

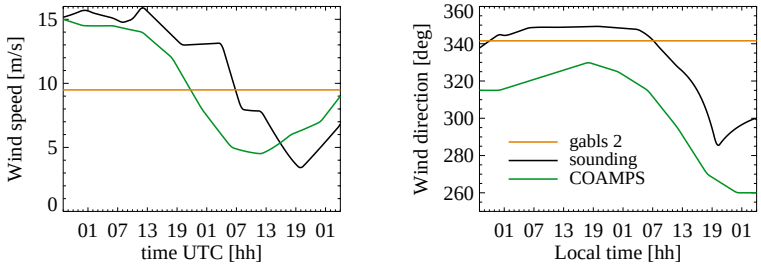


Figure 4.4: Options of geotrophic wind used for forcing the single column model: left wind speed and right wind direction. Red line as used in the GABLS 2 intercomparison study (constant in time and in space), black line time dependent and height averaged estimated from the available radiosoundings and green line time dependent and height averaged computed from a NWP model (COAMPS).

surface forcing is used. The results are presented in the Figure 4.5 for 10 m wind speed and 2 m temperature and in Figure 4.6 for the friction velocity and the sensible heat flux at the surface. For the second GABLS case (black lines) the temperature forecast at screen level is generally in the observed range during daytime, as expected in case of an observed forcing applied just 2 m below. During the first hours of cooling, colder temperatures than observed are simulated. This is due on one the hand to the colder initialisation (compare the initialisation profiles in Fig. 4.3) and on the other hand to a possible mismatch between the radiative temperature used for the forcing and the real surface temperature (or vegetation temperature). This second possible explaination is confirmed by the simulation done with a real initialisation (Fig. 4.5 blue line), where despite the better start temperature the colder bias is reached anyway. Notice the higher amplitude of the temperature for the real case, due to a warmer temperature in the first atmospheric layers, deriving from the warmer initialisation.

The performance for the wind speed at 10 m is quite poor mainly during the morning of the first day (underestimation) and during the entire second day (Fig. 4.5): overestimation of the majority of observations in the night, overestimation in the central part of the day. Considering an average of all observations, the overestimation of the wind speed reaches the maximum in the early morning of the second day. The observed daily cycle could not be well reproduced and the morning transition from a quite calm night-time regime to the daytime windier regime is nearly completely missed on the first day. Interesting is the different behaviour for the simulation with real initialisation during the afternoon of the second day, where an underestimation is observed. This difference is caused by the modified initialisation. Only during the first night, in the afternoon and evening of the first day the model performs well.

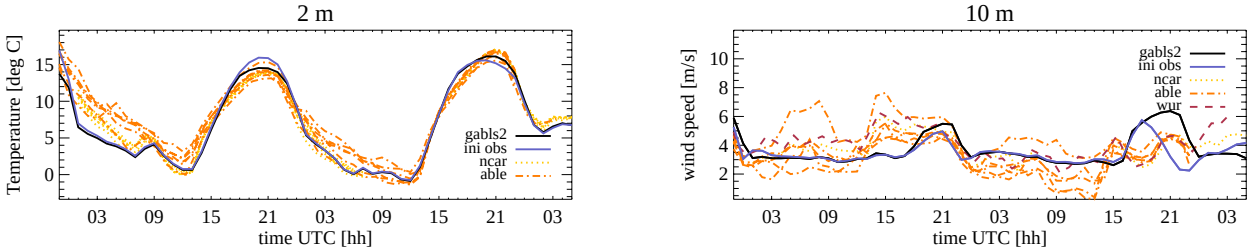


Figure 4.5: COSMO single column model results for the 2 m temperature (left) and 10 m wind speed (right) using the initialisation of the second GABLS intercomparison project (black line) and the observed initial profiles for temperature and wind (blue line). For both cases a constant geostrophic forcing is used (red line in Fig. 4.4). Yellow, orange and red dotted or dashed lines represent observations at different sites in an area of about 60 km of diameter.

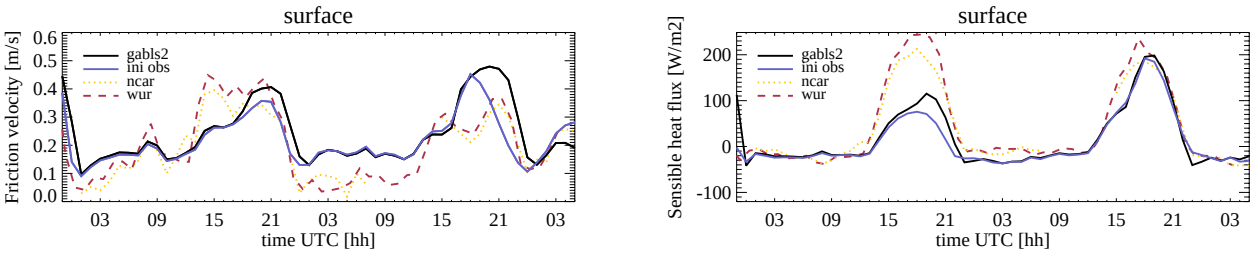


Figure 4.6: COSMO single column model results for the friction velocity (left) and for the sensible heat flux (right) using the initialisation of the second GABLS intercomparison project (black line) and the observed initial profiles for temperature and wind (blue line). For both cases a constant geostrophic forcing is used (red line in Fig. 4.4). Yellow and red dashed lines represent observations.

The momentum fluxes at the surface presented in Fig. 4.6 (left) show an underestimation of the morning transition as for the wind speed, and a clear overestimation during the second night and the second day (mainly for the original GABLS settings). The sensible heat fluxes are massively underestimated during the first daytime (Fig. 4.6 right). During night-time the results are better, even if a tendency of overestimation of the downward fluxes during the second night can be identified. The underestimation of the sensible heat fluxes can be related to three key aspects of the surface heat flux parameterization: (i) an underestimation of the temperature difference between surface and first atmospheric layer, (ii) an underestimation of the wind speed and (iii) an underestimation of the transfer coefficient (too strong resistance in the surface layer). The first aspect is probably not really important if the forced surface temperature is correct and consistent with the eddy covariance measurements. The run started from the observations (warmer) does not show a really large increase of the sensible heat flux (only in the afternoon of day one a significant increase is observed), what excludes a large influence. The underestimation of the flux is the cause of the underestimation of the wind speed. The evaluation of the third possible source of error is more difficult. It is possible that a smaller roughness length at the sites of eddy covariance measurements could have a negative impact on the validation. During the second day a better performance of the heat fluxes are obtained with at the same time an overestimation of the wind speed. The same picture is observed for both the turbulent fluxes (momentum and sensible heat) in the first 50 m of the vertical column (not shown).

The negative performances for the wind speed and the turbulent fluxes could be related to dynamical aspects or initialisation aspects. The geostrophic forcing is not constant in time and changes during the simulation. Additionally, the differences during the second day afternoon indicate that the initialisation plays a crucial role. For this reason in the next section the model sensitivity to changes in the geostrophic forcing and in the initialisation time will be investigated.

### 4.2.2 Sensitivity to the geostrophic forcing

The results for the three time series of the geostrophic forcing (Fig. 4.4) are presented in Fig. 4.7 and 4.8: geostrophic wind is constant in time (black line), estimated from the vertical soundings (green line) or taken from a 3D model simulation (blue line). During the first 16 hours both simulations with time dependent geostrophic forcing induce higher momentum fluxes and the consequent overestimation (Fig. 4.7). The source of this strong overestimation is probably related to the decoupling of the surface layer flow from the residual layer flow or to the initialisation profile of the wind speed (mismatch between used geostrophic wind and initialisation windprofile). The decoupling hypothesis over night would mean a height dependence of the geostrophic forcing. This effect cannot be simulated with a vertically constant geostrophic forcing as implemented in the COSMO single column model and used in this study. The effect of the initialisation profile will

be presented in the next section and seems to be also partially involved. Central is the difference between initialisation profile of the wind speed and direction, and the corresponding values of the geostrophic forcing. During day-time of the first day, the simulation with the model-computed geostrophic forcing shows a good correspondence to the observations of the momentum fluxes both at the surface (Fig. 4.7 left) and at higher locations (Fig. 4.7 right), while the simulation with the geostrophic wind estimated from the soundings shows an overestimation of the fluxes in the afternoon and in the following night. The quality deterioration using the sounding-forcing is significant. The estimation of the geostrophic wind from the radiosounding is probably not appropriate in this special case: a typical vertical dependence of the forcing has to be introduced or a better suitable method for estimating the geostrophic wind based on horizontal pressure gradients has to be used. The morning transition is better simulated by the two runs with time dependent geostrophic forcings. In the second night (October 23 from 00UTC to 13UTC), the overestimation is clearly reduced with the model-derived forcing. The daily cycle during the second day is well captured even if a delay in the morning transition is observed and the amplitude is slightly overestimated.

As expected the impact of a geotrophic wind change is significant also on the wind components, which have similar behaviour as the momentum fluxes: overestimation in the first night for both the time dependent forcings and a clear overestimation for the sounding-derived forcing during the afternoon of the first day (Fig. 4.8).

The impact of different geostrophic forcings is also observed in the surface sensible heat fluxes (Fig. 4.8). During the first night both simulations with the time dependent forcings cause an overestimation of the downward fluxes. During the second night only the forcing from the sounding shows the overestimation. Notice the reduced underestimation of the heat fluxes during the day-time of the first day for the simulation with dynamically derived forcing from the soundings. This can be associated with the overestimation of the wind speed mentioned before. During the second day all three simulations have similar sensible heat fluxes and are closer to the observations.

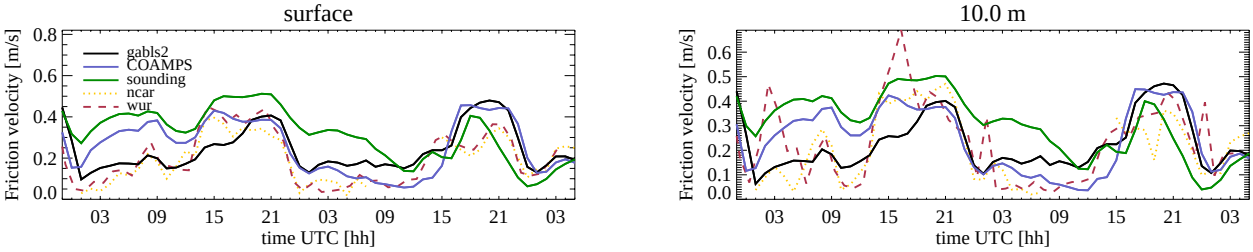


Figure 4.7: COSMO single column model results for the friction velocity at the surface (left) and the momentum flux at 10 m expressed as local friction velocity (right) for the simulations with the three timeseries of the geostrophic forcing taken vertically constant (Fig. 4.4). Black line constant geostrophic forcing, blue line forcing with COAMPS geostrophic wind and green line forcing with geostrophic wind estimated from soundings.

Concluding, as expected the model shows a high sensitivity to changes in the geostrophic forcing. The higher variability indicates that the uncertainty due to this dynamical forcing is not negligible and the introduction of a height dependent forcing is probably necessary in order to properly simulate these two days.

### 4.2.3 Sensitivity to the initial conditions

In the comparison of the results between the GABLS original case and the case with real initialisation, the importance of the initial conditions has already been mentioned. The differences in the temperature profile between GABLS prescription and observations have strong effects on the

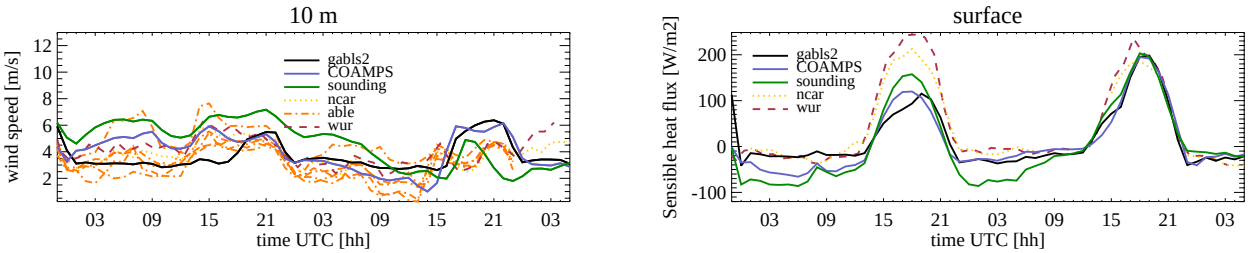


Figure 4.8: COSMO single column model results for the friction velocity (left) and for the sensible heat flux at the surface (right) for the simulations with the three timeseries of the geostrophic forcing taken vertically constant (presented in Fig. 4.4).Black line constant geostrophic forcing, blue line forcing with COAMPS geostrophic wind and green line forcing with geostrophic wind estimated from soundings.

vertical temperature profile. The simulation of the two daily cycles has been repeated for three additional initialisation times: four, five and six hours later than the original initialisation (22 October at 21 UTC), respectively. The model-derived geostrophic forcing is used for all the simulations. The results are presented in Fig. 4.9 for the turbulent momentum fluxes at the surface and at 10 m height (expressed as local friction velocity), in Fig. 4.10 for the 10 m wind speed and the sensible heat flux at the surface, and in Figure 4.11 for the vertical profile of potential temperature and wind. The impact of the initialisation time is important for all the turbulent fluxes. The run initialised on October 22 at 21 UTC seems to diverge from the other runs and gives the worst results in the vertical profiles of wind and temperature as well as in the first night and the entire second day for the friction velocity, momentum fluxes and wind speed.

The overestimation of the momentum fluxes during the first night and during the second day is strongly reduced if the simulation is initiated later both at the surface (Fig. 4.9 left) and at 10 m height (Fig. 4.9 right). This observation is in contrast to the increased overestimation during daytime of the first day for the runs started later. The shape of the diurnal cycle of the momentum fluxes is modified if the simulations start later.

Similar results can be seen in the 10 m wind speed (Fig. 4.10 left). The diminishing wind speed tendency during the second night is well captured by all the simulations. Promising is also the better simulation of the second day, even if the morning transition is delayed by about one hour.

The sensible heat flux is also affected by the different initialisation times. The overestimation of the downward flux is reduced in the first night for runs started later. On the contrary, during the second day we observe a better performance for the run started earlier.

The initialisation has also an impact on the potential temperature profile. Figure 4.11 presents the profiles after 24 hours of simulation. The generated spread for potential temperature reaches values up to 2 C ° (Fig. 4.11 left). Notice the general warm bias below 800 m which will be shortly treated in the next section. The vertical profile of the wind speed shows a larger spread between the simulations. The run started first shows an individual tendency and the largest difference compared to the observations. The run started on October 23 at 01 UTC shows the best match with the radiosounding. The spread covered by all the four simulations is larger than 5 m/s. For the wind direction a spread up to 60 ° is observed. In the lower part of the boundary layer the simulation started first yields the worst match with the observations.

The experiment introducing three additional initialisations clearly shows that the initialization time has a significant impact on the single column simulation results. Overall, the simulation started on October 23 at 01 UTC shows the best performance. This initialisation time will be used in the additional experiments presented in the next sections.

For the simulation started on October 23 at 01 UTC we performed a detailed comparison with the available turbulence observations. The results for the momentum fluxes at 10 m height have already been presented in Figure 4.9 (blue line). The performance picture at other heights

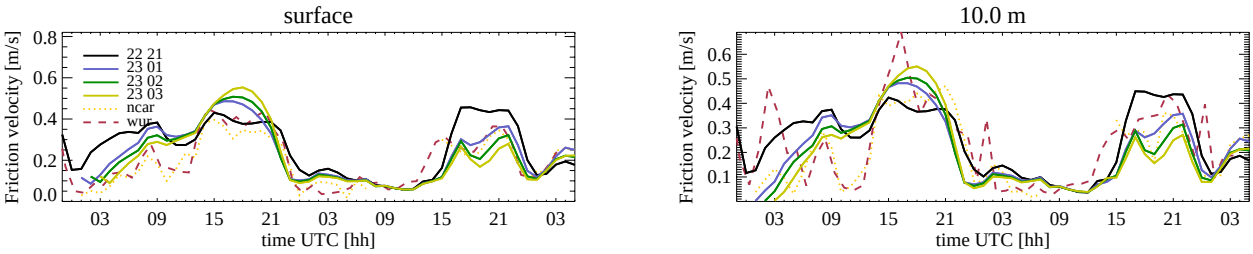


Figure 4.9: COSMO single column model results for the friction velocity at the surface (left) and at 10 m given as local property (right) for the simulations with different initialisation times as indicated in the legend.

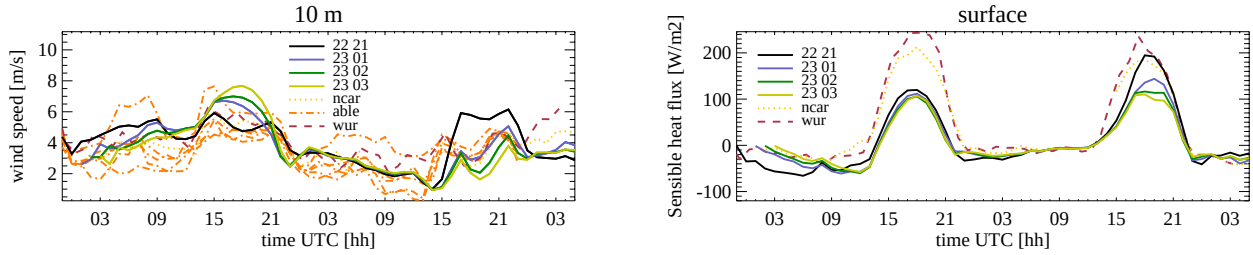


Figure 4.10: COSMO single column model results for the 10m wind (left) and for the sensible heat flux at the surface (right) for the simulations with different initialisation times as indicated in the legend.

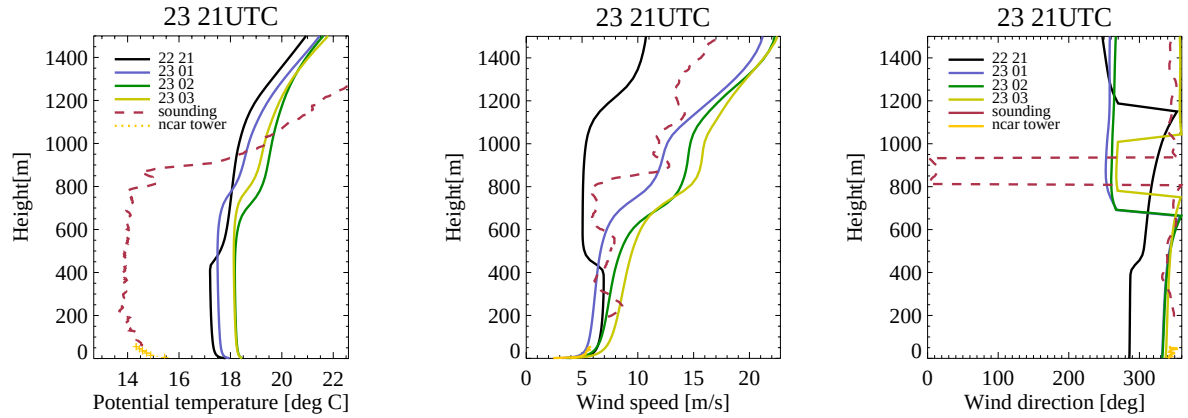


Figure 4.11: Profile for potential temperature (left), wind speed (middle) and wind direction (right) on October 23 at 21 UTC for the simulation started at different times as indicated in the legend.

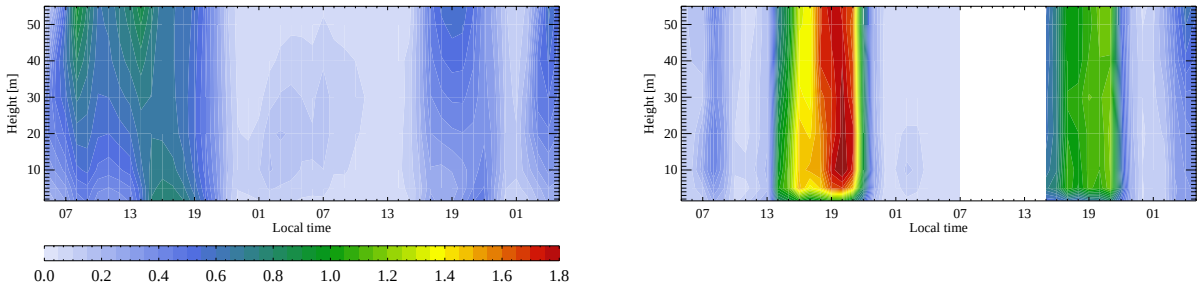


Figure 4.12: Turbulent kinetic energy (TKE) simulated (left) and observed with a tower at one site (right) for the simulation started on October 23 at 01 UTC. The TKE values corresponding to the contour colours are indicated in the legend.

is similar. We want to focus here the attention on the turbulent kinetic energy (TKE). Figure 4.12 presents the time evolution of the TKE in the first 55 m above the surface simulated by the model (left) and observed at one site (right). The TKE is overestimated during the first night and massively underestimated during the day-time of the first day and partially during the day-time of the second day. The overestimation during the first night confirms the already mentioned overestimation in the turbulent fluxes associated with the vertical wind gradients, which are the main source of turbulence in the SBL. The strong underestimation during day-time in the CBL has to be interpreted as a correspondence to the strong underestimation observed in the sensible heat fluxes. During the second night the simulated values are in agreement with the observations. The sharp morning and evening transitions are poorly simulated in terms of quantitative change, because the daily amplitude change is significantly underestimated.

### 4.2.4 Sensitivity to model parameters

#### Sensitivity to minimum turbulent diffusion coefficient

The minimum turbulent diffusion coefficient is an important parameter controlling the minimal vertical diffusion in stable situations (see previous chapter and its sections 3.2.2 and 3.2.4). For operational forecasts at MeteoSwiss, a minimum of 1 $m^2/s$ is used in order to increase the heat flux and avoid too cold near surface temperatures during the winter time and to dissolve maritime boundary layer clouds (Raschendorfer, personal communication). All the simulations presented above had 0.01 $m^2/s$.

Fig. 4.13 presents the effects on the surface turbulent momentum fluxes obtained increasing the minimum from 0.01 to 1.0 $m^2/s$. During night-time they are significantly increased with larger minimum coefficients leading to an additional overestimation during the first night and to a clear overestimation in the second night. During the day the momentum fluxes are only marginally increased and the differences between the simulations are only the consequence of the changes in the previous night. The sensible heat fluxes presented in Fig. 4.14 are also clearly increased during night-time, enlarging the difference to the observations. The impact during night reaches peaks up to 100 $W/m^2$. The effect induced by the larger minimal diffusion coefficient is increased by the shear driven situation with moderately high wind speeds. During daytime the impact of a larger diffusion coefficient is smaller but still significant: differences up to to 30 $W/m^2$ are observed. These are the consequence of the differences introduced during the night before, because the coefficients are during day-time significantly larger than one and the limitation does not act.

The impact on the 2 m temperature is not larger than 1°C because the surface forcing is active (not shown). On the contrary, the effect on the vertical profile of temperature is very important as shown in Figure 4.15. The lower part of the boundary layer up to 400 m is much warmer and the transition from the surface layer into the residual layer is smoothed. Notice the strong warm bias, which starts to grow at the beginning of the night and reaches its maximum extension on October 23 at 21 UTC (after 24 h of simulation), when the boundary layer is well-mixed. Considering that the model has been forced with the observed surface temperature and initialised with the observations, this warm bias can only be explained by a cold air advection in the residual layer during the first night with a maximum intensity just above the surface layer (200 m) and with decreasing intensity above (at about 1000 m the cold air advection vanishes), as can be deduced by the difference between observed and simulated potential temperature in Fig. 4.15. The intensity of the cold air advection has been estimated to be about $-2.0 \cdot 10^{-4} K/s$. This special feature of the boundary layer cannot be captured by the single column model, because advective tendencies have to be externally added to the model.

Larger minimum diffusion coefficients also increase the values of the turbulent kinetic energy slightly reducing the underestimation during day and increasing the overestimation during the first night (not shown).

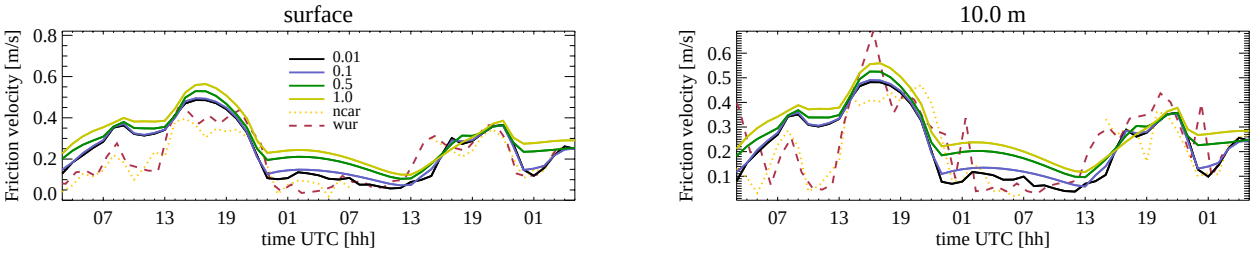


Figure 4.13: COSMO single column model results for the friction velocity at the surface (left) and at 10 m given as local property (right) using different minimum diffusion coefficients as indicated in the legend.

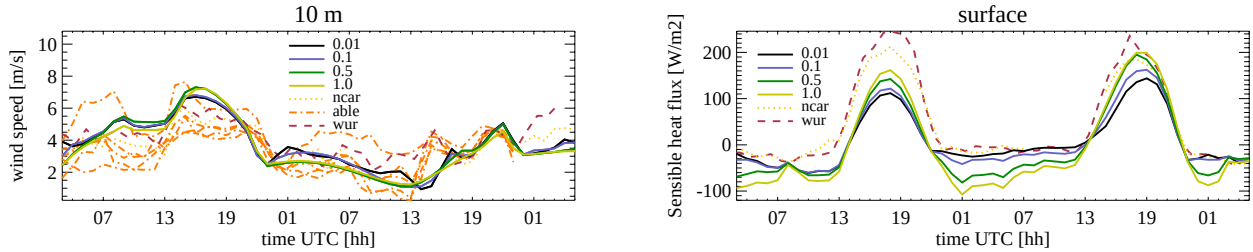


Figure 4.14: COSMO single column model results for the 10m wind (left) and for the sensible heat flux at the surface (right) using different minimum diffusion coefficients as indicated in the legend.

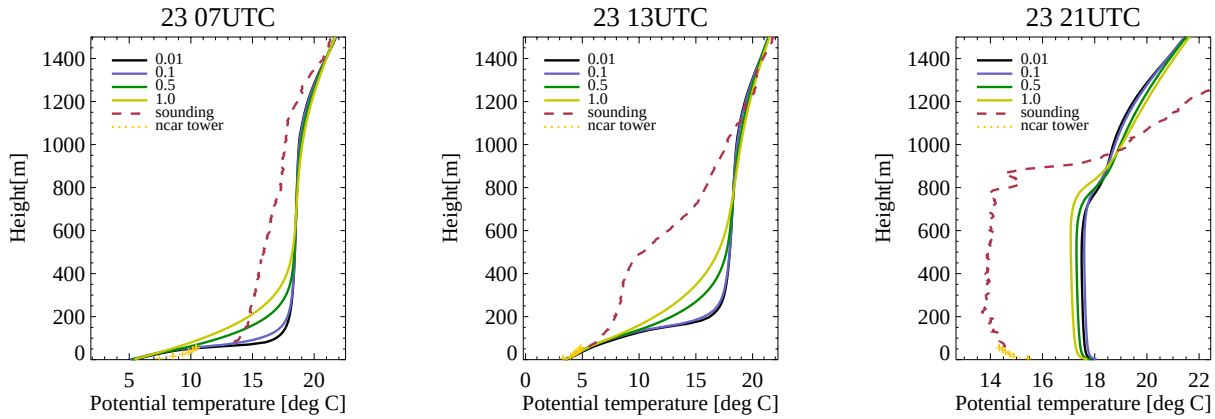


Figure 4.15: COSMO single column model results for the vertical profile of the potential temperature using different minimum diffusion coefficients as indicated in the legend. The title of each picture indicates the time.

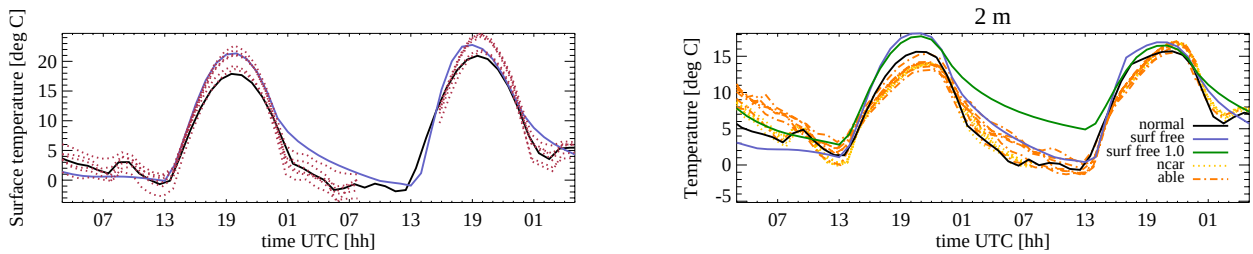


Figure 4.16: COSMO single column model results for the surface temperature (left) and 2 m temperature (right) in case of forced surface temperature (black line) and with coupled soil model (blue line). The green line illustrates the same situation as the blue line but using an higher minimum turbulent diffusion coefficient.

The experiment with the increased minimum diffusion coefficient indicates that the model is very sensitive to this parameter in stable situations. This confirms the conclusions of the previous chapter. Because of the surface forcing the reduction of the minimum diffusivities does not have any significant impact on the temperature near the surface. If the boundary condition of the surface temperature is correctly reproduced, as used in our simulations due to the applied observed forcing, the increase of the minimum is not necessary, because it leads even to an overestimation of the turbulent fluxes and a consequent deterioration of the results.

The minimum diffusion coefficient has a significant effect on the coupling with the surface and on the near surface temperature during stable conditions. This important feature of the COSMO model boundary layer parameterization has partially been reproduced with the COSMO single column model coupling with a land-surface coupling, combining the soil model (multi layers soil model developed by Schrodin and Heise (2001)), the radiation parameterizations of Ritter and Geleyn (1992), as previously used in this study, and the turbulence scheme, and leaving the surface temperature and humidity free. Fig. 4.16 shows the results for surface and 2 m temperature compared to the forced simulation. Even if the maximum temperature during the first day is clearly larger than the observed temperature (by about 4 °C), the results at the end of the second night are much closer to the observations indicating a stronger relative cooling in the coupled simulation at the surface (Fig. 4.16 left) and at 2 m (Fig. 4.16 right). The stronger cooling can be quantified to about 3 °C. In this special case the coupled simulation does not exhibit an underestimation during the night time due to the overestimated temperature maximum during day. In other words, imaging that the maximum temperature on the first day would be correctly simulated, the stronger cooling would inevitably lead to a colder bias during night time. An increase of the minimum diffusion coefficient from 0.01 to 1 $m^2/s$ (illustrated by the green line in Fig. 4.16) has significant consequences on the night temperature: 3 °C in the first night and even 5 °C in the second night. The downward heat flux and the ground flux coming from the soil are not able to compensate the strong radiative cooling of this cloud-free night, leading to a stronger cooling. This seems to be in contradiction with the simulated sensible heat fluxes which are closer to the observations during night for the case with low minimum diffusivities. The coupling effects on the momentum fluxes and on the wind speed are, as expected, smaller than on temperature. An additional effect of the coupling can be seen in the amplitude of the sensible heat flux during day-time, which is larger and closer to the observations (not shown). This is partially due to higher surface wind speeds. The coupling land-surface with the use of a soil parameterization plays in this case an important role and confirms the conclusions of Steeneveld et al. (2006b) and Holtslag et al. (2007). The different behaviour compared to forced simulations should always be taken into account, in order to avoid "wrong" generalisations.

**Sensitivity to other model parameters**

The model sensitivity has also been tested with three additional parameters: the asymptotic mixing length (used in the parameterisation of the master length scale) and the two control parameters for the laminar resistance for heat or momentum transfer in the transfer scheme. All these three parameters do not show a really significant impact (not shown). This result contrasts with the COSMO single column simulations of the first GABLS case (see previous chapter), where at least the parameter influencing the laminar resistance for momentum has shown a significant impact. In case of a diurnal cycle not only aspects related to shear produced turbulence play an important role. In addition, the relatively small roughness length used in this study experiment (3 cm) reduces the influence of the first two layers in the transfer scheme and for this reason the control parameters for the laminar resistance of momentum and heat are less important. The impact of the changes in the leaf area index and the plant coverage (external parameters which go into the surface transfer parameterizations) is relatively small. With larger roughness lengths

the effect is expected to be larger.

## 4.3 Summary and conclusions

The double diurnal cycle of the second GABLS intercomparison project (CASES 99 22-25 of October 1999) has been simulated with the COSMO single column model with slightly modified forcings and initializations. The case presented here is a radiation forced diurnal cycle, it shows a moderate complexity due to the change in the dynamical situation (geostrophic wind) and the presence of cold air advection during the first night and warm air advection in the second day. The wide availability of observations has permitted an interesting validation of the model results.

The following main aspects allow to combine the findings presented in this chapter with those of the previous dedicated to the first GABLS case:

1. When the surface temperature is forced towards the observations, the boundary condition for the atmosphere is correct and the turbulence scheme works properly. A larger minimum diffusion coefficient for allowing a minimal downward heat flux during night-time is not necessary. A minimum larger than 0.1 $m^2/s$ leads to a clear overestimation of the momentum fluxes and should be avoided. In addition, typical structures of the stable boundary layer could be filtered out and disappear in the simulation results. Similarly to the findings in the first GABLS case, the model is sensitive to changes in the minimum diffusion coefficient during stable conditions. The consequences of changes in the minimum introduced in the SBL can also be observed later during the CBL, mainly in the morning.

2. This study has additionally shown that the reduction of the minimum diffusion coefficient has to be strictly related to the ability of the turbulence scheme together with the land-surface parameterization to reproduce the surface temperature. For this reason a reduction of this parameter (set to 1.0 $m^2/s$ for operational NWP forecasts) should be evaluated considering the land-surface coupling. In fact, a simulation with coupled atmosphere and soil indicates that in such situations the model tends to produce an overestimation of the surface cooling probably due to an underestimation of the downward fluxes or an underestimation of the ground heat flux.

3. The TKE values produced by the model and used in the diffusivity parameterizations are overestimated in the night (stable boundary layer) as observed in the first GABLS case and massively underestimated during day-time (unstable boundary layer). The morning and the evening transitions in the TKE evolution are poorly simulated in terms of intensity change. As long as the TKE values go only into the diffusivity parameterizations the problem is not relevant. On the contrary, this aspect should be taken seriously into account if the TKE values are externally used for other purposes such as dispersion calculations.

4. The choice of two different reference data for evaluating the model performance (LES in the previous chapter and observations in this one) makes a direct qualitative comparison of the two cases relatively difficult. Unfortunately no LES data were available for this study in order to perform a similar validation as used in the first GABLS case. The LES performance in the special conditions of the second GABLS case would give an important information in order to distinguish errors generated by a sub-optimal dynamical forcing (geostrophic wind and advection have to be given to the model) and turbulence model deficiencies. In fact, the dynamical aspects probably play the same important role in a LES simulation as observed in the COSMO model.

The following four additional main findings can be summarised as specific to this study:

1. The simulated 2 m temperatures are well in the range of the observations. This is not surprising considering the fact that the surface temperature has been forced with observations. The overall performance for the wind speed is only moderately satisfying. The first night shows an overestimation, while the evening transition as well as the the wind speed reduction during the second night are well simulated. The morning transition during the second day is poorly captured in terms of amplitude. The performance for the momentum fluxes is similar to the results of the wind speed: overestimation in the first night (mainly due to dynamical reasons), good results for the evening transition and the second night, and underestimation of the morning transition during the second day.

2. During the two daily cycles the geostrophic wind undergoes a change in the intensity and in the direction. The COSMO single column model is very sensitive to changes in the geostrophic forcing. The use of a time dependent geostrophic forcing estimated from a mesoscale model analysis has a globally positive effect mainly during day-time and in the second night. This contrasts with the results of the first night, when an overestimation of the turbulent fluxes is observed, that is probably due to a height dependence of the geostrophic forcing, which cannot be considered by our model. The height and time dependence of the geostrophic wind is the major problem for a one-dimensional simulation of these two daily cycles. The variability of the geostrophic wind either in time or in space should seriously be taken into account in single column modelling. Cases with observed significant changes in time and space of the dynamical forcing should be avoided or evaluated with an additional external prescription of the geostrophic wind.
   Recently, the developer of the COSMO single column model has extended it independently of this study (newest version 1.7) in order to use a time and height dependent geostrophic forcing derived or calculated from a COSMO model 3D simulation.

3. The initialisation time has a large impact on the simulations results. The initiatisation on October 23 at 01 UTC shows the best results compared to the observations. The run with initialisation time October 22 at 21 UTC has the worst performance. The effect seems to some extent to be related to the combination between the time dependent geostrophic forcing and the initialisation profile for wind speed and direction. The spread in the temperature profile after 24 hours of simulation reaches a maximum value of 2 °C for temperature and more than 10 $m/s$ for wind speed. This aspect, well known in numerical weather prediction and related to the uncertainty of the initialisation fields (Ensemble Prediction Systems), should always be checked also for one-dimensional modelling.

4. The advection tendencies play an important role during the first night explaining about 4°C of the observed cooling above the surface layer in the residual layer. The cold air advection seems to be generated by small hills located in the region.
   The COSMO single column model should be extended in order to integrate and use externally computed advection tendencies in case they are available, e.g. from a 3D NWP model.

This case, simulated in the framework of the second GABLS intercomparison project, besides the important advantages of the single column modelling (fast calculation and large flexibility for tests) has identified some limits related to the dynamical forcing (geotrophic wind) and the horizontal advection (non-homogeneity of the surroundings), which have to be considered for the choice of case studies.

## Acknowledgements

The author thanks Matthias Raschendorfer (German Weather Service, DWD) for providing us with the code of the COSMO single column model code and the related introductory information.

We also appreciate the collaboration with Gunilla Svennsson (University of Stockolm), who leads the second intercomparison project and gave us the observation data.

# Chapter 5

# On the 2 m temperature and dew point diagnostics in the COSMO model

## 5.1 Introduction

### 5.1.1 The surface layer: the inertial sublayer and the roughness sublayer

The atmospheric boundary layer (ABL) governs the lower boundary of the atmosphere toward the Earth surface. The lower region of the ABL is defined as the surface layer, which can extend up to some 10% of the ABL height (Stull, 1988). The upper part of the ABL, the so-called Ekman layer, shows, on the one hand, little dependence on the nature of the surface, a significant rotation with height of the shear stress and a negligible effect of friction. In the surface layer, on the other hand, a strong dependence on the surface characteristics is observed, friction is an important source of turbulence and stress exhibits negligible rotation with height (Garratt, 1992). Here, turbulence processes significantly influence the local meteorological situation. Two main sublayers can be identified in the surface layer: (i) the inertial sublayer (ISL) at the top and (ii) the roughness sublayer (RSL) at the bottom (Garratt, 1992; Raupach et al., 1991). In the ISL, the turbulent fluxes vary less than 10% and for this reason it is also known as the constant flux layer. Here the wind velocity profile in neutrally buoyant conditions is logarithmic and the Monin-Obukhov similarity theory (surface layer scaling) can be applied to describe the turbulence processes. In contrast, the RSL is directly influenced by the three-dimensional distribution of roughness elements at the surface (e.g. vegetation, buildings, small topography structures). As a result, the constant flux assumption is no more valid and deviations from the logarithmic profile are observed (Garratt, 1992; Raupach et al., 1980; Garratt, 1980). During very stable conditions and in case of very tall roughness elements, the ABL height can be very shallow and the vertical extension of the ISL can become very small or even vanish (Rotach, 1999, 2001).

The boundary between ISL and RSL can be determined by the concept of the blending height, at witch the surface and local roughness disturbances have been blended out (Wieringa, 1986; Bou-Zeid et al., 2004). A similar approach has been proposed by Raupach et al. (1991) and used by Rotach (2001) for urban canopies defining the vertical extention of the RSL up to a height $z_*$, above which the flow can be considered in equilibrium and the influence of the roughness elements can be neglected. $z_*$ is often estimated as a multiple of the mean canopy height $H$ or of the roughness length $z_0$. Raupach et al. (1991) show that $z_* = 2H - 5H$ covers the range of the estimations made for vegetated surfaces. Rotach (2001, 1993) and Roth and Oke (1993) showed the similarity of the RSL range over urban areas with those estimated over vegetation surfaces excluding a significant divergence on the estimation of $z_*$.

Canopy structures in the RSL significantly influence the turbulence processes, often leading to the failure of the simple first order closure assumptions (Kaimal and Finnigan, 1994; Finnigan,

2000) and in extreme cases even to counter-gradient fluxes of momentum and scalars (Shaw, 1977; Raupach, 1987). In such situations, the turbulent flow inside the canopy can be described in terms of ejections, sweeps and outward and inward interactions depending on the sign of the horizontal and vertical turbulent fluctuations (Antonia, 1981; Katul et al., 2006). Raupach et al. (1996) suggest that at the top of the vegetation canopy the turbulent processes can be treated with the mixing layer theory (the mixing layer analogy).
The presence of a canopy leads to additional sinks for momentum (absorption) in form of additional drag on the roughness elements that can vary horizontally and vertically (Raupach and Thom, 1981; Denmead and Bradley, 1987). Similarly, additional sources or sinks for scalars (e.g. moisture and temperature) are observed either in vegetation canopies (Raupach, 1995; Raupach and Thom, 1981) or in urban canopies (Roth, 2000; Martilli et al., 2002). These RSL features influence the temperature and humidity distribution inside and above the canopy leading to a significant temperature and humidity variability (Jacobs et al., 1995; Graser et al., 1987).

The simulation and the forecast of the temperature and humidity profiles inside the surface layer with numerical weather prediction models has to account for these aspects of the surface layer and, in particular, the special features observed in its lower part, the RSL.

### 5.1.2 The 2 m temperature diagnose in NWP models: the description of the surface layer

In most numerical weather prediction (NWP) models, the surface layer is defined as the region between the rigid surface and the first atmospheric layer. Processes in the surface layer determining the lower boundary conditions of NWP models are mainly parameterised as surface and mass energy fluxes using ISL theory. In most NWP models the RSL is neglected and the transfer of momentum and scalars (temperature and humidity) is computed with approaches derived for the ISL using the original or modifications of Monin-Obukhov surface layer theory (Monin and Obukhov, 1954).

Typically, the surface fluxes are determined by surface exchange coefficients and the surface gradients. In general, they are computed for momentum and for (sensible and latent) heat, with different formulations for stable and unstable conditions (depending on the sign of a stability parameter, either the Obukhov length or the bulk Richardson number in the surface layer). For each stability condition, different flux-profile formulations are used (e.g. Businger et al., 1971; Dyer, 1974). A comprehensive review of the flux-profile relationships and its deviations found in the literature is given by Högström (1996). The transfer coefficients are often expressed using areodynamic resistances (Garratt, 1992). They are determined by special iterative procedures or with analytical procedures like those proposed by Louis (1979). The resistance approach allows to consider additional aspects of the canopy effects in the surface layer, which have not been treated in the original work of (Monin and Obukhov, 1954). However, NWP models hardly ever have vertically resolved canopies.

In order to apply the surface layer theory, NWP models should have the first atmospheric level in height ranges, which are within the surface layer under the majority of possible flow conditions. The height of the first atmospheric level in NWP models generally varies between 5 and 50 m. Models having the first atmospheric layer down to elevations reached by canopies should explicitly take into account the direct effect of vegetation or buildings on the model equations.

The height "2 m" is the WMO (World Meteorological Organisation) standard height for measuring the near surface temperature. This location is clearly inside the surface layer, sometimes in the ISL sometimes in the RSL depending on the coverage of the surface by roughness elements. The surface roughness is generally expressed in terms of a roughness length. The roughness length is defined for wind speed as the height above the surface in neutral conditions, where the extrapolation of the logarithmic wind profile is equal to zero (Garratt, 1992). The diagnostics of

temperature and humidity at the level of 2 m is often formulated as interpolation formula derived from the above mentioned surface layer profiles, e.g. as in the IFS model (ECMWF, 2007). In the past such interpolation formulas have been simplified, as reflected in an older diagnostics scheme of the German global model GME (Geleyn, 1988).

Most of the NWP forecast performance is judged using temperature and dew point measured at 2 m. For this reason, it is important to implement a correct formulation of the 2 m temperature, which responds to the typical model deficiencies and does not introduce any additional source of error. The coarse vertical resolution of most NWP models does not permit to compute this temperature and humidity values prognostically. For this reason a 2 m temperature and a 2 m dew point diagnostics is necessary, which combines the surface temperature and humidity on the one hand and the prognostic temperature and humidity at the first atmospheric level on the other hand within a surface layer framework.

The surface layer (ISL and RSL) is highly determined by the characteristics of the surface (Ament and Simmer, 2006). For this reason the first step in the simulation of the surface layer in NWP models is to assemble a possibly good description of the surface properties. This is done in the COSMO model (Steppeler et al., 2003) using external parameters, shortly described in the next section.

## 5.2 The COSMO model external parameters

The COSMO model and its parameterizations (description of unresolved processes) require additional parameters, which are not derived by data assimilation or by interpolation from the driving model. The default parameter database currently used is derived from international freely available datasets and can be applied for a grid up to 1-2 km mesh size. For very high resolution runs, however, it is advisable to refine these datasets with information of higher resolution. The external parameters (roughness length, root depth, plant cover and leaf area index) related to the vegetation coverage and the land use are extracted from the dominant land cover classes of three data sets (DWD, 2004): the Global Land Cover Characteristics (GLCC[1]) provided by the U.S. Geological Service (24 classes, see appendix B1) and the CORINE data-set based on an European Union initiative (44 classes, see again appendix B2) and the GLC2000[2] provided by the European Commission. The characteristic parameters of plants have to be determined from the dominant land cover using look-up-tables, which associate a surface type to the corresponding values of the different external parameters. The parameters required by the soil model in COSMO are (i) the fractional area covered by plants, (ii) the leaf area index and (iii) the root depth. Obviously, these parameters are time dependent. In order to roughly simulate an annual cycle of the data, maximum and minimum values for the plant coverage and leaf area index are used and a simple analytical annual cycle depending on latitude and height is prescribed to interpolate between maximum and minimum values. This has to be carried out during the model pre-processing depending on the actual initial Julian day of the forecast.

In the following, the needed external parameters are briefly presented, particularly focussing on the roughness length, which is the main external parameter, that influences the surface layer parameterizations in the COSMO model.

#### Mean orography

The mean orography is derived from the GTOPO30[3] data set (resolution $30'' \approx 1$km) and interpolated to the desired horizontal resolution. Typically, the effective numerical resolution needed for

[1] http://edc,usgs.gov/products/landcover/glcc.html
[2] http://www-gvm.jrc.it/glc2000/
[3] http://www.edc.usgs.gov/elevation/gtopo30/gtopo30.htm

resolving atmopheric phenomena is much coarser than the grid scale. Forcings below the scale of effective numerical resolution are not only without any sense, they even cause errors by translating the response to larger scales (Gassmann, 2001). Therefore, a filter is applied to the interpolated orography that smoothes small scale structures at a grid size of $4\Delta x$ ($\Delta x$ denotes the model mesh size). This filtering avoids for example unrealistic precipitation fields.

**Prevailing soil type**

The prevailing soil type is taken from the Digital Soil Map of the World, which is based on the FAO/UNESCO soil Map of the World. The data-set has a resolution of 5 arc minutes in a geographic projection and has been adapted for COSMO. COSMO differenciates 9 soil types (ice, rock, sand, sandy loam, loam, clay loam, peat, sea ice). Each soil class is characterised by 19 parameters such as pore volume, field capacity, minimum infiltration rate, air dryness point, minimum infiltration, hydraulic diffusivity, hydraulic conductivity, heat capacity and heat conductivity.

**Land fraction**

The land fraction can take values from 0 (100% sea) to 1 (100% land) and corresponds to the percentage in the land-see-mask of each COSMO grid element, which is covered by land.

**Percentage of vegetation coverage**

The percentage of the grid box that is covered by vegetation is extracted from the above mentioned land cover data-sets.

**Root depth**

The root depth mainly depends on the plant types, soil factor texture, compaction, underlying bedrock, clefts, and further physical and chemical properties of the soil. It determines the maximum depth of water and nutrient uptake from the soil profile (Breuer et al., 2003). This external parameter is extracted from the mentioned land cover data-sets.

**Leaf area index**

The leaf area index is defined as the one-sided green leaf area per unit ground area in broad-leaf canopies, or as the projected needle-leaf area per unit ground area in coniferous canopies. It depends on the soil and vegetation type (Breuer et al., 2003) and has an important saisonal variability.

**Roughness length**

The aerodynamic roughness length is based on the observed wind shear in the surface layer and is defined as the height where the wind speed becomes zero (in neutral conditions). The roughness length over land in COSMO depends on two contributions, namely the subgrid-scale variance of orography ($z_{0,oro}$) and the land use ($z_{0,loc}$). The orographic component is necessary in order to account for the additional drag that is caused by unresolved small-scale orography (Majewski and Ritter, 2006) (or orographic stress) and partially the gravity wave drag.

The concept of orographic roughness was initially developed by Fiedler and Panowsky (1972) and Mason (1985). Later, the orographic roughness has been introduced in NWP modelling as a convenient tuning parameter even for represented processes having a larger scale than it was initially developed for, as showed by the comparisons of Georgelin et al. (2000). The weakness of

this approach is related to the missing knowledge about the basic digital elevation model that has to be used in order to include all the effects of subgrid scale orography. In order to circumvent the use of an orographic roughness length different alternative approaches have been developed (e.g. by Wood et al., 2001; Brown and Wood, 2001), generally based on an additional drag term in the model equations. The ECMWF model (Beljaars et al., 2004), for example, uses a practical application of the alternative procedure proposed by Wilson (2003), which directly influences the momentum equations. Some of these alternative approaches have been implemented and tested in HIRLAM by Rontu (2006).

In COSMO the orographic roughness length $z_{0,oro}$ is related to the the subgrid-scale variance of orography $\sigma^2$ and computed in connection with the mean orography of the grid element. The roughness length contribution is parameterized according to

$$z_{0,oro} = a_0 \sigma^2 \arctan\left(\Delta x / b_0\right)$$

with $a_0 = 10^{-5} m$ and $b_0 = 2.5m$, $\Delta x$ is the average grid length. The roughness length $z_{0,i}$ of the different land cover classes is extracted from the mentioned land cover data sets. All the available values inside an COSMO grid element of area F are logarithmically averaged and weighted by their respective areas $F_i$ according to

$$z_{0,loc} = h \cdot \exp\left[-\frac{F}{\sum_{i=1}^{I} F_i / (\ln(h) - ln(z_{0,i}))}\right]$$

obtaining $z_{0,loc}$, which is the "land use" contribution for the total roughness length. Here, h=30m is an assumed average height of the surface layer (oder Prandtl layer). The two contributions are added to obtain the total value of the roughness length $z_0 = z_{0,oro} + z_{0,loc}$. As mentioned, an open point is the definition of the basic topography horizontal resolution used for this computation. The basic horizontal resolution can significantly influence the variance of the topography inside a model grid-box. Currently, a basic topography at about 1 km horizontal resolution is used and seems to give satisfactory results. However, the parameterization of the orographic roughness should further be evaluated with available higher resolved digital elevation models, in order to assess the sensitivity of this parameterization.

Over sea points, the roughness length is not an external parameter but rather a variable computed on the basis of a modificated Charnock-formula (Charnock, 1955; Raschendorfer, 2001). Over ice-covered sea points the roughness length is assigned a constant value of 0.001 m.

The orographic component of the roughness length is substantial in mountainous regions: in the Alps it reaches values of up to 8 m at 7 km horizontal resolution, compared to the maximum of the local component, which is always smaller than 1 m. Figure 5.1 presents the two main components of the roughness length and their sum, which is used for the parameterization of the surface transfer and the turbulence parameterizations at 7 km horizontal resolution. Notice the smaller ogrographic component for high-resolution simulations (2.2 km) compared to the traditional 7 km resolution, as shown in Fig. 5.1 (d).

## 5.3 The COSMO model transfer scheme

Once the surface characteristics are described the transfer between the surface and the atmosphere needs to be pameterized. Therefore, the surface transfer scheme calculates the fluxes from the rigid surface of the lower boundary of the Earth into the atmosphere and the corresponding profiles of the transported variables. The COSMO model surface layer scheme is not based on Monin-Obukhov similarity theory for the surface layer, but is formulated in the framework of the TKE based turbulence closure scheme, as used in the atmosphere part of the model (Raschendorfer, 2001; Doms et al., 2001; Raschendorfer, 2007a).

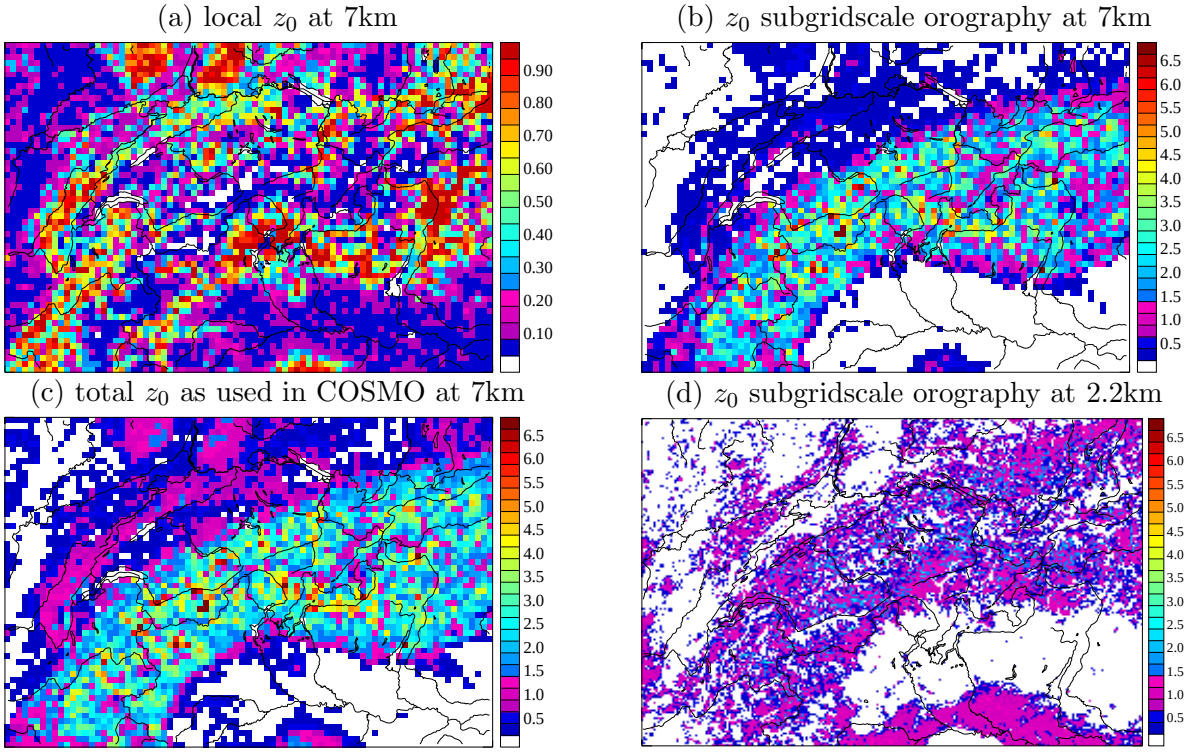


Figure 5.1: The roughness length used in COSMO region over Switzerland and surroundings: (a) local roughness length (surface coverage, land use), (b) orographic component of the roughness length and (c) the sum of both at 7 km horizontal resolution. (d) is the corresponding picture to (b) but at 2.2 km horizontal resolution.

The transfer layer is defined to extend from the rigid surface of the Earth up to the lowest main level, where all the first atmospheric variables are defined. The central step of the scheme is the computation of the transfer coefficients. The region between the solid surface and the lowest main model surface is divided into three sub-layers: a Prandtl layer or surface layer, a turbulent roughness layer and a laminar layer. The latter 2 layers are treated as mere "skin" layers without a real vertical extension (or having an combined extension equal to $z_0$, see Fig. 5.2) . The surface layer is assumed to begin at the height corresponding to the height $z_0$ or at the turbulence distance $z_0\kappa$, where $z_0$ is the roughness length and $\kappa$ is the von Karman constant. The surface layer extends up to the first atmospheric main level. The vertical description of the transfer layer is illustrated in Fig. 5.2.

As first step the transport resistances are computed for each layer, which depend on the turbulent diffusion coefficients $K_M$ and $K_H$ at the model levels with indices ke and ke1, the roughness length $z_0$ (no distinction between momentum and heat is made), the leaf area index (LAI) and the plant coverage. The transfer resistances are expressed by simplified integrals of the reciprocal diffusion coefficients along the transfer layer, in which different interpolation formulae for the turbulent velocity scale are used. Further details about some theoretical aspects of the resistances and the computation of the required diffusion coefficients can be found in Appendix B-2. In the following, the definition of each resistance is given.

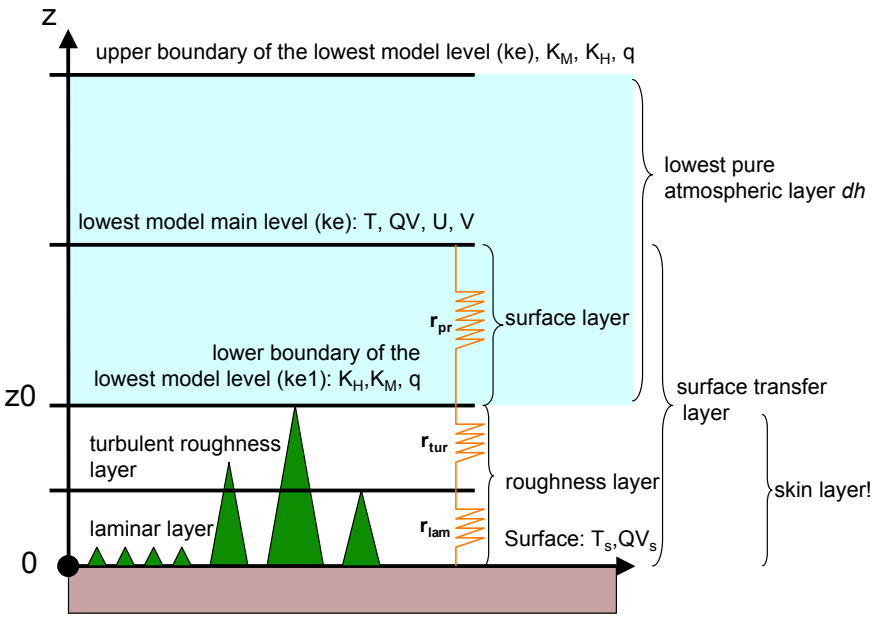


Figure 5.2: The surface transfer layer and its sub-layers: the surface layer (or Prandtl layer), the turbulent roughness layer and the laminar layer. For each sub-layer, transport resistances for vector and scalar quantities are computed. The surface layer extends from the height corresponding to the roughness length $z_0$ (level with the index ke1) to the lowest atmospheric main level (level with index ke), where all the model prognostic variables (except TKE or q defined on half levels) are known. At the bottom of the surface layer only the turbulence related variables as the diffusion coefficients are known. The roughness layer is placed below the height equal to the roughness length and is treated as a skin layer.

### Laminar layer

The resistances along the entire laminar layer are defined as follows:

$$r_{lam}^{M} = C_M \frac{z_0}{SAI} \tag{5.1}$$

$$r_{lam}^{H} = F \cdot C_H \frac{z_0}{SAI} \frac{\frac{K_H^{ke1}}{D_H}}{\frac{K_M^{ke1}}{D_M}} \tag{5.2}$$

Here, $C_M$ and $C_H$ are the scaling factors of the laminar layer for momentum and heat (or moisture). $C_M$ is normally assumed to be zero and $C_H$ to be one. Due to this assumption the resistance for momentum in the laminar layer vanishes. F is equal to one over land and influences the laminar resistance over grid-cells fully or partially covered by water ($F = 1 + (1 - FR_{LAND}(20 - 1))$, whereas $FR_{LAND}$ is the fraction of land having values form 0 to 1) . $K_H^{ke1}$ and $K_M^{ke1}$ are the turbulent diffusion coefficients computed at the lowest boundary of the first atmospheric layer. $D_H = k_H$ is the kinematic viscosity and $D_M = k_M$ the scalar conductivity of dry air, respectively. "$SAI$" is the surface area index: it depends on the "plant coverage index" ($PL_{cov}$), the leaf area index ($LAI$) and the surface area density of the roughness elements at the surface ($C_{lnd} = 2$).

$$SAI = PL_{cov} \cdot LAI + C_{lnd} \tag{5.3}$$

### Turbulent roughness layer

In the turbulent roughness layer the resistances are expressed as a function of the surface area index, the roughness length and the turbulent diffusion coefficient at the bottom of the surface

layer (level with index ke1).

$$r_{tur}^{M} = \sqrt{(\frac{1}{2}r_{lam}^{M})^2 + h_{can} \cdot r_{lam}^{M}} - \frac{1}{2} \cdot r_{lam}^{M} \tag{5.4}$$

$$r_{tur}^{H} = \frac{z_0}{SAI} \log \frac{K_{ke1}^{M}}{D_M} \tag{5.5}$$

Here, $h_{can}$ is the effective canopy height, calculated as follows:

$$h_{can} = \begin{cases} RC \cdot z_0 & r_{tur}^{H} = 0 \\ RC(r_{lam}^{H} + r_{tur}^{H}) \log(\frac{r_{lam}^{H} + r_{tur}^{H}}{r_{tur}^{H}}) & r_{tur}^{H} > 0 \end{cases} \tag{5.6}$$

RC represents the ratio of canopy height to the roughness length $z_0$ (operationally set to one).

**Surface layer**

In the surface layer the transfer resistance is calculated using a linear interpolation factor of the turbulent diffusion coefficients $K_M$ und $K_H$ calculated before in the turbulence scheme between the values at first atmospheric model level (level with index ke) and at the bottom of the surface layer (level with index ke1). Given $F_M$ and $F_H$, the factors 'facm' and fach' can be calculated as follows:

$$F_M = \min \begin{cases} 2 \\ \max \begin{cases} 0.5 \\ \frac{K_M^{ke} \cdot z_0}{K_M^{ke1} \cdot (dh + z_0)} \end{cases} \end{cases} \qquad F_H = \min \begin{cases} 2 \\ \max \begin{cases} 0.5 \\ \frac{K_H^{ke} \cdot z_0}{K_H^{ke1} \cdot (dh + z_0)} \end{cases} \end{cases}$$

$$facm = \frac{(F_M - 1) \cdot z_0}{dh} \qquad fach = \frac{(F_H - 1) z_0}{dh}$$

dh is the thickness of the lowest model layer and corresponds to the distance between the surface at index ke (upper boundary of the first model level) and ke1 (bottom of the surface layer or lower boundary of the first model layer). Once facm and fach are known the transport resistance can be computed according to:

$$r_{pr}^{M} = \begin{cases} \frac{z_0}{0.5 \cdot dh + z_0} \cdot \frac{1}{2} dh & \text{, if facm=1} \\ \frac{z_0}{1 - facm} \cdot \log\left(\frac{\frac{1}{2}dh + z_0}{z_0 + facm \cdot \frac{1}{2}dh}\right) & \text{, else} \end{cases} \tag{5.7}$$

$$r_{pr}^{H} = \begin{cases} \frac{z_0}{0.5 \cdot dh + z_0} \cdot \frac{1}{2} dh & \text{, if fach=1} \\ \frac{z_0}{1 - fach} \cdot \log\left(\frac{\frac{1}{2}dh + z_0}{z_0 + fach \cdot \frac{1}{2}dh}\right) & \text{, else} \end{cases} \tag{5.8}$$

**The total resistance and the transfer coefficients**

The total resistance from the surface to the top of the surface layer is given as the sum of the resistances of the single layers:

$$r_{tot}^{M} = r_{lam}^{M} + r_{tur}^{M} + r_{pr}^{M} \tag{5.9}$$

$$r_{tot}^{H} = r_{lam}^{H} + r_{tur}^{H} + r_{pr}^{H} \tag{5.10}$$

The laminar and roughness layer resistances are operationally set to zero. Only a resistance in the surface layer $r_{pr}$ is used and the free slip condition is applied at the height $z_0$. Given the

resistances it is now possible to compute the ratio of the resistance in the surface layer to the total resistance over all layers:

$$\mathrm{tfm} = \frac{r_{pr}^{M}}{r_{tot}^{M}} \tag{5.11}$$

$$\mathrm{tfh} = \frac{r_{pr}^{H}}{r_{tot}^{H}} \tag{5.12}$$

The transfer coefficients ($C_m$, $C_\Theta$ and $C_Q$) are then expressed as functions of the sum of the resistances of each sublayer ($r_{tot}^{M}, r_{tot}^{H}$), the horizontal velocity ($V_h$) and the turbulent diffusion coefficients at the bottom of the surface layer (at the height corresponding to $z_0$ or at the half level with index ke1).

$$C_m = \frac{K_M^{ke1} \cdot \mathrm{tfm}}{r_{pr}^{M} \cdot V_h} = \frac{K_M^{ke1}}{r_{tot}^{M} \cdot V_h} \tag{5.13}$$

$$C_\Theta = C_Q = \frac{K_H^{ke1} \cdot \mathrm{tfh}}{r_{pr}^{H} \cdot V_h} = \frac{K_H^{ke1}}{r_{tot}^{H} \cdot V_h} \tag{5.14}$$

Then determination of the surface fluxes for sensible heat ($H_0$) and latent heat ($(E \cdot L_v)_0$) at the surface is straightforward using the gradient between surface and first atmospheric layer:

$$H_0 = -\rho \cdot C_{pd} \cdot C_\Theta \cdot V_h \cdot \Delta T \tag{5.15}$$

$$(E \cdot L_v)_0 = -\rho \cdot C_Q \cdot V_h \cdot L_v \cdot \Delta QV \tag{5.16}$$

E is the total evaporation rate from the surface and from the soil. The momentum fluxes at the surface ($(Mo_U)_0$, $(Mo_V)_0$) are paremeterized by a drag-law formulation

$$(Mo_U)_0 = -\rho \cdot C_m \cdot V_h \cdot U_{ke} \tag{5.17}$$

$$(Mo_V)_0 = -\rho \cdot C_m \cdot V_h \cdot V_{ke} \tag{5.18}$$

where $V_h$ is the horizontal wind velocity and $U_{ke}$ and $V_{ke}$ are its eastward (zonal) and nordward (meridional) wind components at the lowest model level.

Finally, the diagnose of the 2 m temperature, the 2 m dew point and of the 10 m wind components is based on this transfer scheme, if the first atmospheric layer is above these levels. Different interpolation formulae are used depending on the vertical distribution of the model levels and on the characteristics of the surface.

## 5.4 Temperature and dew point diagnostics in the COSMO model

The COSMO 2 m temperature and 2 m dew point diagnostics is closely related to the transfer scheme presented in the previous section. Besides the surface temperature $T_s$ and the temperature at the first model level $T_{ke}$ (or only the atmospheric temperature at two atmospheric levels if the vertical resolution is extremely high) the transfer resistances for scalars are an important input component to the diagnostics.

Depending on the location of the 2 m level three cases are distinguished, as presented in Fig. 5.3 (location indicated with a yellow star): (i) the 2 m level is within the canopy layer (below an effective computed canopy height), (ii) the 2 m level is above the canopy and (iii) the 2 m level is located between two atmospheric levels. For each of the three cases different interpolation formulae are defined:

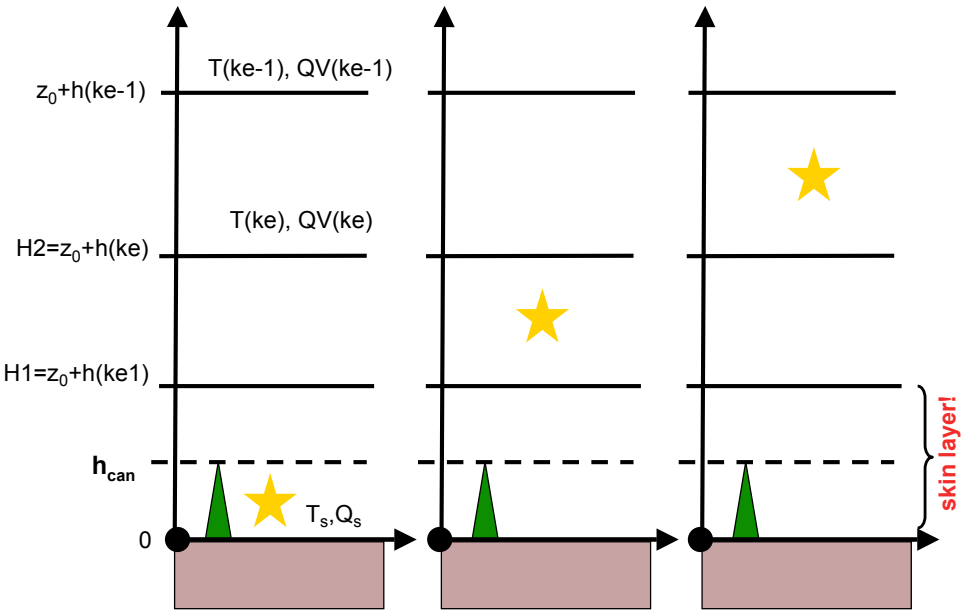


Figure 5.3: The three cases used for the diagnose of the 2 m temperature and 2 m specific humidity: (i) left panel when the 2 m level is below the effective canopy height, (ii) middle panel when the 2 m level is above the canopy and below the lowest atmospheric level, and (iii) right panel when the 2 m level is between the last and the last but one atmospheric level. H1 is the height above sea level of the surface and H2 is the height above sea level of the first atmospheric main level. $H2 - H1 = 0.5 \cdot dh$ is the half thickness of the first atmospheric layer.

i) The 2 m level is located below the canopy height, estimated dynamically using the transfer resistances. The canopy height varies in time depending on the transfer conditions at the single gridpoints and is determined with Eq. 5.6. The 2 m temperature and the 2 m specific humidity are computed at the level $z2 = 2m$ as function of the surface values ($T_s$ and $QV_s$) and the values at the first atmospheric level ($T_{ke}$ and $QV_{ke}$) with an exponential profile using the following interpolation formula:

$$T_{2m} = T_s + (T_{ke} - T_s) \cdot \text{fac} \tag{5.19}$$

$$QV_{2m} = QV_s + (QV_{ke} - QV_s) \cdot \text{fac} \tag{5.20}$$

where fac is

$$\text{fac} = \frac{r^H_{lam} + r^H_{tur}}{r^H_{tot}} \exp\left(\frac{z2 - h_{can}}{r^H_{lam} + r^H_{tur}}\right) \tag{5.21}$$

ii) If the 2 m level is above the canopy height a logarithmic profile is used for the temeperature and specific humidity interpolation. Equations 5.19 and 5.20 are used with the following factor fac:

$$\text{fac} = \frac{(r^H_{lam} + r^H_{tur}) + z_0 \cdot \frac{z2 - h_{can}}{(z2 - h_{can} + z_0)}}{r^H_{tot}} \tag{5.22}$$

$$\text{fac} = \frac{(r^H_{lam} + r^H_{tur}) + \frac{z_0}{1 - \text{fac}_h} \cdot \log\left(\frac{z2 - h_{can} + z_0}{z_0 + \text{fac}_h (z2 - h_{can})}\right)}{r^H_{tot}} \tag{5.23}$$

Equation 5.22 is used in extreme cases, when $1 - \text{fac}_h < 10^{-6}$, while Eq. 5.23 is applied in the other majority of the situations. $\text{fac}_h$ is defined as follows:

$$\text{fac}_h = (\text{rat}_h - 1)\frac{z_0}{dh} \tag{5.24}$$

where $dh$ is the thickness of the first atmospheric layer (twice the difference between H2 and H1 in Fig. 5.3) and $\mathrm{rat}_h$ is defined as

$$\mathrm{rat}_h = \frac{K_H^{ke} \cdot z_0}{K_H^{ke1}(dh + z_0)} \tag{5.25}$$

using the diffusion coefficients at the model level ke and ke1. The values of $\mathrm{rat}_h$ are restricted to the range of $0.5 < rat_h < 2$ in order to avoid undefined solutions, to assure the upward concavity of the interpolation and to limit the range of $\mathrm{fac}_h$.

iii) If the 2 m level is located between two model atmospheric levels a simple logarithmic interpolation between the two model levels is performed. The factor fac used in the Eq. 5.19 and 5.20 is defined as follows:

$$\mathrm{fac} = \frac{\log\left(\frac{z2-h_{can}+z_0}{0.5\cdot(h_{ke}-h_{ke1})+z_0}\right)}{\log\left(\frac{0.5\cdot(h_{ke}-h_{ke1-1})-h_{ke1}+z_0}{0.5\cdot(h_{ke}-h_{ke1})+z_0}\right)} \tag{5.26}$$

The heights are again defined in Fig. 5.3. This option is practically never used in any operational COSMO forecasts, because the first atmospheric level is generally above 10 m and the vertical resolution close to the surface never reaches values below 10 m.

From the computed specific humidity at 2 m, it is possible to calculate the 2 m dew point with the help of the estimated pressure at 2 m, $p_{2m}$, the 2 m temperature previously diagnosed and the water vapour pressure at 2 m, $e_{2m}$:

$$e_{2m} = \frac{p_{2m}}{\frac{R_d}{R_v QV_{2m}} - \frac{R_d}{R_v} + 1} \tag{5.27}$$

$$\mathrm{TD}_{2m} = \frac{b1 \cdot b3 - b4\frac{e_{2m}}{b1}}{b2 - \frac{e_{2m}}{b1}} \tag{5.28}$$

where b1=610.78, b2=17.27,b3=273.16 and b4=35.86. $R_d$ and $R_v$ are the gas constant for dry air and for water vapour, respectively.

## 5.5 The representativeness of point measurements compared to model grid box averages

The 2 m temperature and the 2 m dew point from NWP models are the main near-surface parameters, which are compared to observations for evaluation purposes. The verification or NWP model validation is actually one of the major challenges: the down-scaling problem has to be always kept in mind, even if often no alternatives are available. On the one hand, observations are recorded at exact point locations. On the other hand, NWP models are limited to their horizontal resolution and calculate the prognostic or diagnostic variables on a grid, where each grid point value is assumed to be representative for a whole grid box. For these reasons, a NWP model with limited horizontal and vertical resolution will never be able to take all the local conditions into account. Furthermore, the differences between real- and model-topography and their effects can be very substantial in particular in very complex terrain as in the Swiss Alps. In addition, the soil and surface descriptors (albedo, roughness length, leaf area index, root depth, soil type) in the model are assumed to be representative for the whole horizontal grid-box. Note that the same problem occurs in the opposite direction when observations are fed into NWP models during the initialisation and data assimilation. This is known as a typical up-scaling problem.

Generally, we are facing a problem of representativeness. Representativeness errors arise from the fact that there is a fundamental mismatch between the spatial and temporal scales represented by the models and the observations (Rife et al., 2004). This type of error can be large. Rife et al. (2004) describe a possible procedure for quantifying the representativeness error of a NWP mesoscale model grid-point value based on a very high resolution model, the so called Clark-Hall model (Clark and Hall, 1991). More accurate methods to explicitly consider the representativeness of both, observations and model data need to be designed. If such an explicit account of representativeness differences is not identified, differences between model and observations can be wrongly interpreted (Lalaurette, 2001).

If observation errors are neglected, the difference between a model grid-point and an observation point can be defined according to Rooy and Kok (2004, 2002) as a total error (model - observation). This can be decomposed to a small-scale representation mismatch or representativeness (RM) and a large scale error (ME) or model error (for instance due to erroneous parameterizations or synoptic errors). The RM error is caused by the difference between the grid-box mean conditions of the model and the locally valid conditions. The RM is often ignored in verification studies. Tuning efforts for example based on the roughness length of the model in order to get better wind speed for a local point are not correct, because the model simulates grid-box mean conditions (Rooy and Kok, 2004). In such cases, the variability inside the grid-box has to be considered.
Therefore, the key question to answer before any model validation exercise is: "What is the best way to compare point observations with grid-point values?". Different strategies or assumptions have been used and explored. Some of them have especially been developed for climate models, which generally have coarser horizontal resolution than mesoscale NWP models. In reading the subsequent section and in the presentation of the verification of the 2 m dew point and 2 m temperature this representativeness aspect has to be kept in mind for the interpretation of the results.

For the sake of intercomparability, the WMO (World Meteorological Organisation) has published standards for SYNOP meteorological stations which prescribe the surface properties of potential measurement stations. In particular, the station's area should be mainly covered by grass (roughness length $< 0.1$ m, e.g. 3 cm used in the ECMWF model for scalar transfer) and major roughness elements should be absent in the surroundings. Unfortunately, these prescriptions are often violated by some countries, making the definition of a typical SYNOP station roughness length difficult. Differences between local site roughness length and model roughness length (averaged on a model gridbox) can be a significant cause of mismatch between observed and forecasted surface values. Therefore, an adaptation to local conditions should be performed in a postprocessing step leaving the model in its own world also for diagnosed quantities. For this reason, this study will avoid to use the definition of a typical roughness length.

## 5.6 Observed deficiencies in the diagnostics: motivation

The direct model output of the diagnosed quantities at 2 m in the COSMO model (7 km horizontal resolution), generally shows quite large forecast errors, which considerably diminish the range of direct application of model data. In this section, a brief overview about the problems observed for the 2 m temperature is given. The errors in the 2 m dew point are correlated (the dew point depends directly on the temperature) and more complex, because they additionally depend on the moisture concentration.

The performance of the 2 m temperature diagnose is presented in Fig. 5.4 with scatter plots of the 2 m temperature: model diagnose versus SYNOP observations for all the seasons during 2006 are given (operational COSMO-7 runs, maximally 1172 SYNOP stations used, over the entire model domain). Here, only the forecast range from 0 to 24 hours has been considered. Only the stations with a maximum height difference of 100 m between model topography and reality have

been considered for this analysis so that height differences cannot be invoked as an explanation for observed differences. Although on average the mean error (ME) is on the order of 1 °C and the root mean square error (RMSE) is close to 2 °C for an entire season, many forecast points, mainly in complex alpine terrain exhibit errors larger than 4 °C .

During winter, a distinct cold bias is observed (Fig. 5.4 a). In spring and in summer it is interesting to note the pool of points, where the model temperature remains nearly constant at the melting or freezing point (Fig. 5.4 b and c). This indicates that in the model world, snow is melting at the surface and the temperature at the surface remains constant. This process is, on the one hand, physically consistent but, on the other hand, it indicates a mismatch of the modeled snow coverage and the true conditions or some deficiencies in the diagnostics being too close to the surface value (see the interpolation between surface and first model level as outlined in the Section 5.4). An increasingly tight coupling can again be observed for higher temperatures in summer and spring leading to an overestimation of the 2 m temperature. In summer and spring we observe an increased tendency to a temperature overestimation for higher temperatures, which indicates again that the diagnose is generally too close to the surface temperature. This aspect is probably partially related to the availability of soil moisture, which modulates the energy partition between latent and sensible heat flux at the surface. The forecast error for the autumn had the smallest variance and the mean error had the smallest value for that year.

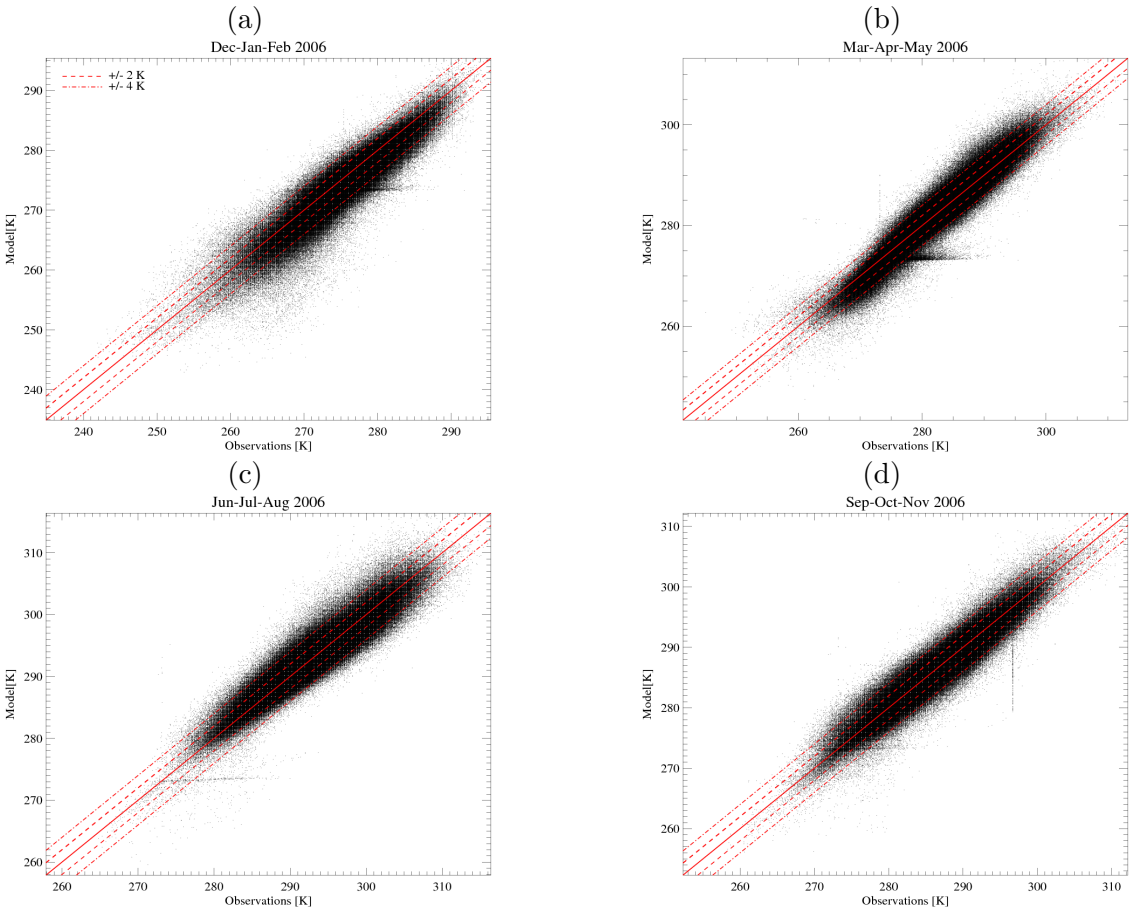


Figure 5.4: 2 m temperature performance of the COSMO-7 operational forecast (first 24 hours) in 2006 compared to the SYNOP observations. Only the stations with height difference between model grid and real topography smaller than 100 m have been considered. The meaning of the red lines is indicated in the legend. Here, all the SYNOP stations for the entire COSMO-7 domain have been considered. Note that the strange vertical line observed in (d) is probably due to a failure of measurement devices at one or more stations.

The diagnose for stations in the alpine region shows considerably larger errors than for stations located in flat terrain. Typically, the larger the height difference between model and reality, the larger is the RMSE error, even if the model temperature is corrected with a vertical temperature lapse rate just before comparing the model temperature with the observations (e.g. -0.65 °C/100m). The height reduction is the traditional way to account for height differences. Figure 5.5 presents the dependence of the RMSE on the height difference between model topography and reality. This aspect is expected to be improved by a higher resolution simulation (e.g. at 2.2 km), which reduces the height differences between the observations and the model (Kaufmann, personal communication).

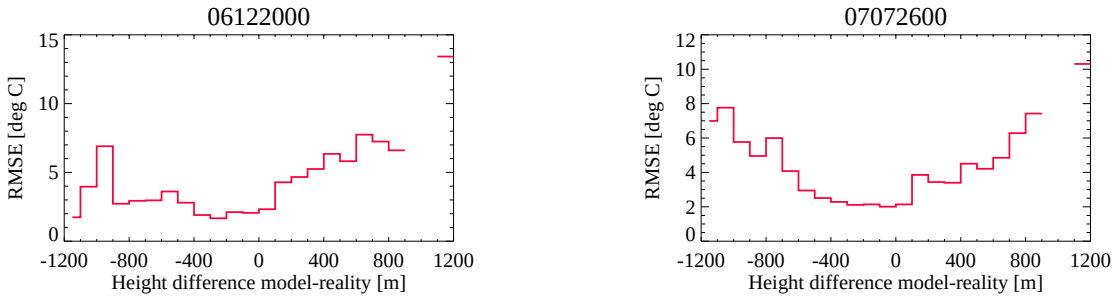


Figure 5.5: RMSE dependence on the height difference between model topography and stations height for a typical winter day (left, 20.12.2006) and summer day (right, 26.07.2007) over the entire COSMO 7 km domain. The height difference intervals without a value indicate that no stations are available for it. Note that the number of stations can be extremely small if the height difference gets large.

The poor topography description can be identified as an important source of error when looking at the RMSE dependence on the altitude of the gridpoints in the model as presented in Fig. 5.6. At high altitudes the the RMSE of the forecasts tends to be larger. An additional important factor at these altitudes is the snow coverage, which has to be very accurate in order to simulate a correct surface energy balance. The RMSE is larger the more snow is available at the ground in the model (not shown). Although these patterns of the 2 m temperature error are partially interdependent on each other (altitude, snow amount and height difference), it seems that the problems in the prediction of the 2 m temperature over snow covered surfaces in COSMO is particularly important.

In the alpine region the model often produces unrealistically high temperature gradients between the first atmospheric layer and the surface during winter time. In addition, the soil temperature is too often unrealistically low and the 2 m temperature daily cycle exhibits a significant phase error in winter.

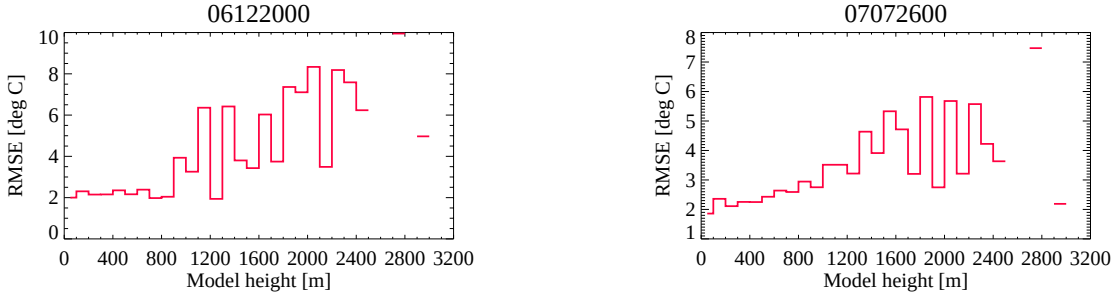


Figure 5.6: RMSE dependence on the grid point altitude for a winter day (left, 20.12.2006) and a summer day (right, 26.07.2007). The height intervals without a value indicate that no stations are available.

The maximum temperature is often reached 1.5-2h hours earlier than the observed values as

can be clearly seen in Fig. 5.7. This effect can be observed mainly during summer days. This timing of the temperature maximum is typical for the daily cycle of the shortwave radiation at the surface. Therefore, this is again an indication for a tight coupling between the diagnosed 2 m temperature and the surface temperature. Figure 5.7 also shows a lower temperature maximum and a more pronounced cooling in the afternoon and evening than in the observations. This is an additional confirmation of the typical cold bias in the model.

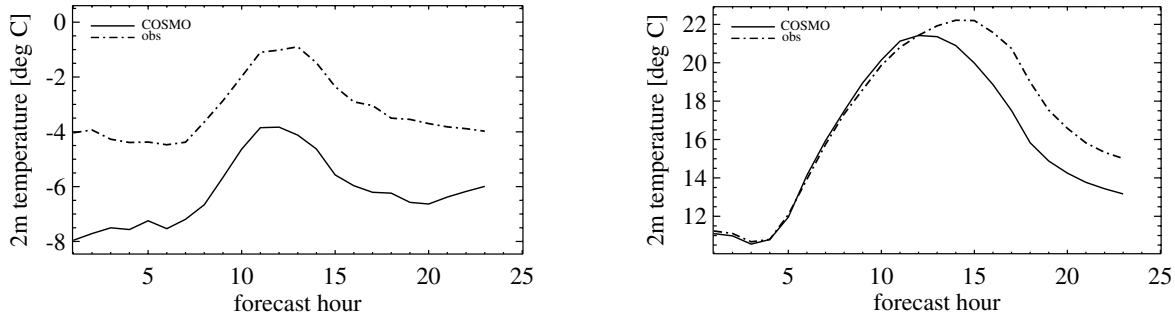


Figure 5.7: Mean 2 m temperature daily cycle for a typical winter day (left, 20.12.2006) and a summer day (right, 26.07.2007). The averaged daily cycle of the temperature is the mean of 66 stations over Switzerland. Notice the time shift of the maximum (1.5-2h) mainly in summer. The black continuous line represents the COSMO-7 model and the dashed-dotted line denotes the observations.

In summary, the 2 m temperature deficiencies in the COSMO model can be qualitatively condensed to 4 main problems :

- A cold bias mainly in winter (but also in spring and autumn in stable situations) leading to large and unrealistic temperature differences between the surface and the first atmospheric layer.
- A constant value of the temperature at 2 m in case of snow melting.
- A phase error of the maximum temperature value, reached 1.5-2 h too early (particularly in summer).
- Depending on the availability of soil moisture a tendency of overestimation in summer and spring has been observed.

The deficiencies can be associated with four possible sources of error:

1. Error in the surface temperature: the surface prognostic values for temperature is the most important input for the 2 m temperature determination.
2. Deficiencies in the atmospheric conditions strongly influence the surface fluxes and the temperature at the first atmospheric level.
3. Error in the description of the surface and different topography: a poor quality in the description of the surface properties (vegetation cover, leaf area index, roughness length, plant cover) has a direct impact on the surface temperature and hence on the 2 m diagnostics.
4. Error in the used physical interpolation for the diagnose: the interpolation formulae for temperature could contain physical errors, which leads to interpolated values too close to the surface temperature.

**Errors in the surface values**

Errors in the surface energy balance and its components (solar radiation, longwave radiation, ground flux and turbulent fluxes) have direct consequences on the surface temperature. A summary of the errors in the radiation parameterizations has been presented in Chapter 2. The observed negative bias in the shortwave radiation during clear sky days in winter probably has a small enhancing impact on the cold bias. A poor surface energy balance over snow surfaces is probably the main cause of the underestimation of the surface temperature also leading to large temperature differences between first atmospheric level and surface (up to 35 °C). The decoupling of the surface is probably caused and enhanced by the turbulence and transfer scheme, which seems to struggle in such very stable situations. The mechanical generation of turbulence in stable situations in not strong enough to prevent from the disappearance of turbulence and to maintain a substantial downward heat flux.

The surface temperature (also known as skin temperature or radiative temperature) is very rarely observed and monitored. Typically, it is computed from the observed upward longwave radiation using an appropriate value for the surface emissivity. A performance analysis of the deficiencies in the modeled surface temperature has been done for the meteorological station Payerne (single gridpoint). The observed 2 m temperature is highly correlated with the observed surface temperature as presented by the red dashed line in Fig. 5.8. The correlation between modelled and observed surface temperature for the single location of Payerne is generally close to 0.9 for spring and summer. During the winter months the correlation decreases, probably due to model's difficulties to detect fog situations over the Swiss Plateau. The correlation between observed and modeled 2 m temperature is slightly smaller mainly during the winter time, while in summer the correlation is nearly identical to that observed for the surface temperature. This indicates that during winter the error of the 2 m temperature diagnose cannot exclusively be explained by errors in the surface temperature. A correlation of the mean error in the surface temperature and the mean error in the 2 m temperature yields values between 0.6 and 0.8 with the smaller values in winter and spring. Therefore, additional error sources must contribute to the 2 m temperature error. Although it is inappropriate to generalise this point verification to the

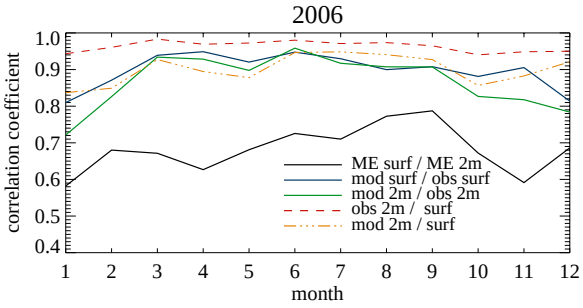


Figure 5.8: Monthly correlation analysis for the 2 m temperature and the surface temperature for the station of Payerne during 2006: the red dashed line shows correlation between observed values at 2 m and at the surface, orange dotted and dashed line denotes the correlation between modelled values at 2 m and at the surface, the blue line is correlation between observed and modelled surface temperature, the green line is the correlation between observed and modelled 2 m temperature and black line shows the correlation of the mean error (ME) at the surface and at 2 m.

entire COSMO domain, the common experience indicates that at least in the alpine region the surface temperature undergoes significant errors (Schubiger, personal communication). In winter an underestimation is often observed in clear sky situations and during summer an overestimation for high temperature has been mentioned.

The cold bias during the winter leads to large and unrealistic temperature differences between

the surface and the first atmospheric layer and, as consequence, to large negative bias in the surface temperature. The distribution of the temperature difference for a typical clear sky day in winter and in summer is given in Fig. 5.9. In summer the amount of gridpoints having a temperature difference larger than 10 °C is clearly smaller. The temperature difference is to some extent correlated with the amount of snow covering the surface as illustrated by Fig. 5.10.

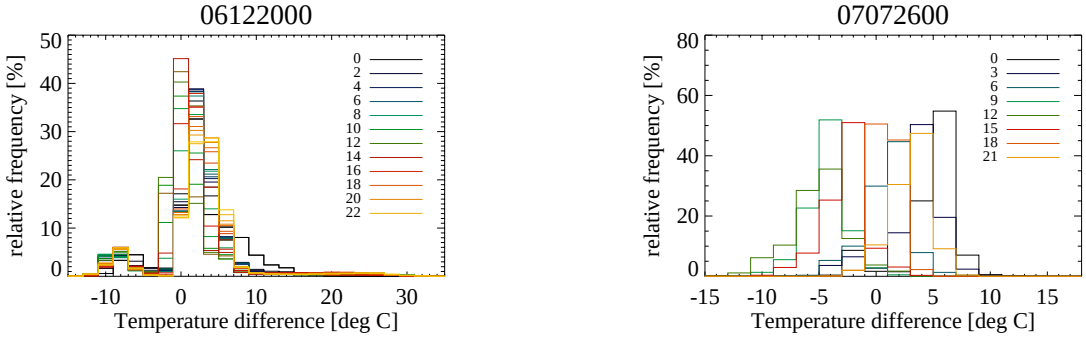


Figure 5.9: Distribution of the temperature difference between the first atmospheric layer at 10 m and the surface for a typical fair weather day in winter (left, 20.12.2006) and in summer (right, 26.07.2007). All the COSMO model gridpoints over land are considered. The colours indicate the distribution every 2 hours and 3 hours, respectively.

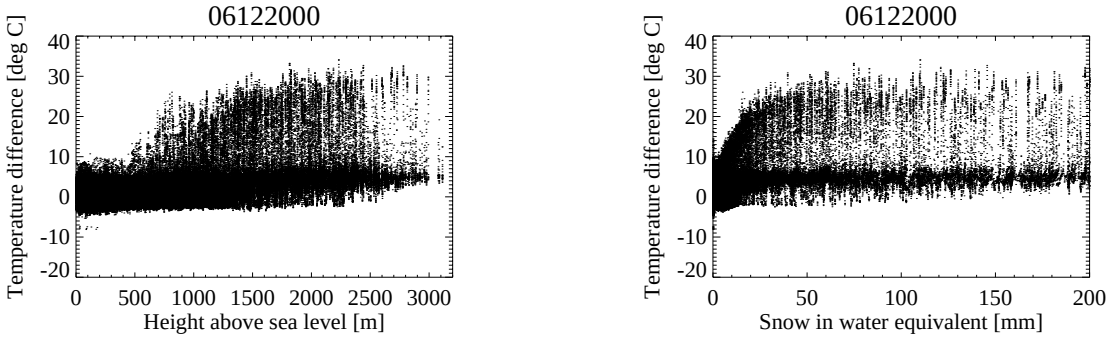


Figure 5.10: Dependence of the temperature difference between first atmospheric layer and the surface on the grid point altitude (left) and on the snow coverage (water equivalent of snow) for a winter day (20.12.2006) considering all model grid-points in the alpine region.

**Errors in the atmospheric values**

Errors in the atmospheric temperature and humidity have a direct impact on the 2 m diagnostics. The most obvious reason for the errors in the winter is the turbulence scheme that fails to simulate large enough downward turbulent fluxes, even if a minimum diffusion coefficient is used. The phase error in the temperature diagnose could partially be associated to the atmospheric values (i.e. wrong timing in the convection as observed in summer). The error in the first atmospheric layers may also be partially caused by the transfer scheme and through the vertical heat transport. A more detailed analysis and a subsequent correction is clearly beyond the scope of this study.

**Errors in the description of the surface**

Among the parameters which describe the surface in COSMO, particular attention should be put on the roughness length in the alpine region. As already mentioned in the description of

the external parameters (Section 5.2), the values can take up to 8 m, because in addition to the surface type the roughness length accounts for the subgridscale orography. The effect on the COSMO diagnose is expected to be substantial, because the effective canopy height computed by the transfer scheme indirectly depends on the total roughness length value. The canopy height in turn determines the choice between exponential and logarithmic profile.

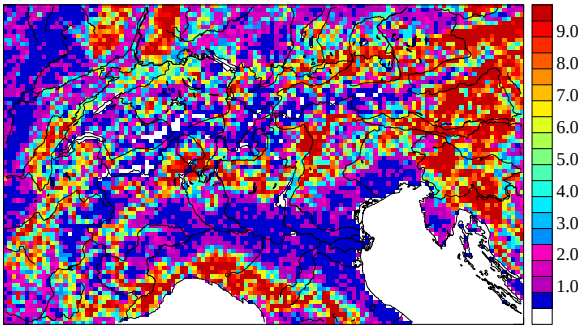


Figure 5.11: Canopy height estimated from the roughness length according to a similar expression as proposed by Raupach (1994) for a canopy area index equal to one and supported by Rotach (2001).

Figure 5.11 presents an estimation of the canopy height from the local roughness length ($z_{0,loc}$) using the simple relation

$$h_{can} = z_{0,loc}/0.1 \tag{5.29}$$

which corresponds to the expression proposed by Raupach (1994) for a canopy area index equal to one and supported by Rotach (2001). The maximum possible canopy height in the COSMO model at 7 km using this simple formulation is 10 m. The spatial distribution of the canopy height estimated with this constant method (the canopy height is time independent) has been compared to the canopy height used in the COSMO operational diagnostics. The results are presented in Fig. 5.12 for a winter case and in Fig. 5.13 for a summer case. The figures present the model values for two lead times (left column) and the corresponding difference to the static value given in Fig. 5.11 (right column). Due to the subgridscale roughness length the model canopy height over the alpine region is predominantly larger than the estimated value (see largely positive values in the difference). The modeled canopy height reaches in a few gridpoints maximum values up to 150 m. These very large canopy heights have very important consequences: for most of the grindpoints in the Alps the exponential profile is used in the 2 m temperature diagnose even if the local roughness is below 0.2 m (i.e. roughness which would correspond to a canopy height of some 2 m). According to Eq. 5.29, below this roughness length the 2 m level is supposed to be above the canopy layer. The exponential factor used in the interpolation profile (Eq. 5.19) presented in Eq. 5.21 produces temperatures which, compared to a logarithmic profile, more slowly depart from the surface value as mentioned earlier. For this reason the 2 m temperature is often in these situation with unrealistic canopy height too close to the surface value. Additionally, it may be also noticed that the dynamical computation of the canopy height can lead for the same gripoint during the same day to changes from the exponential to the logarithmic profile due to large changes in the effective canopy height. Significant differences in the canopy height are observed between summer and winter cases, confirming that a large portion of the variability in the canopy height is independent of the local roughness length.

**Errors in the diagnostics**

The phase error can partially be associated to the effect of the exponential profile in situations where the canopy height is unrealistic: in other words a wrong choice of the profile. However, it is also observed in situations, when the diagnostics uses a logarithmic profile. Additionally, an

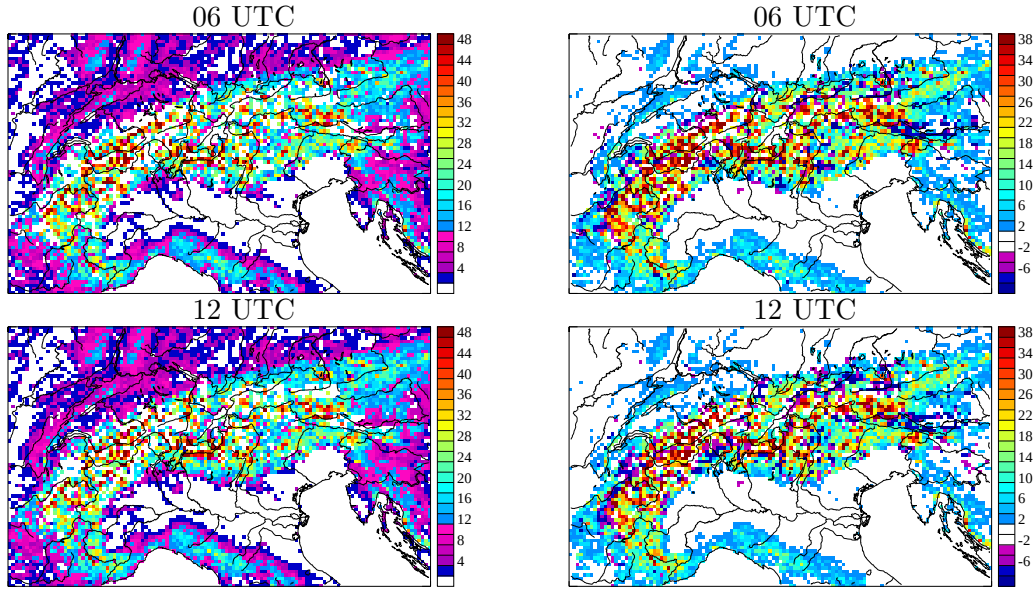


Figure 5.12: Left column: canopy height computed in the COSMO transfer scheme for a winter day (20.12.2006). Notice that values larger than 50 m have the colour corresponding to the maximum in the scale. Right column: difference (modelled-estimated) to the canopy height estimated from the roughness length (Fig. 5.11).

extended use of the interpolation formulae for temperature starting close to the surface and ending close to the first atmospheric level has shown that a match between the two boundary values is not properly achieved (see section 5.9).

## 5.7 Alternative diagnostics: theory

The deficiencies in the 2 m diagnostics as highlighted above suggest further development related to the diagnostics formulation and the description of the surface. In this study the following variants or modifications have been tested:

1. Introduction of the local roughness length in the actual diagnostics.
2. Elimination of the exponential profile and use of a simple logarithmic interpolation (as used in COSMO for the wind speed) with the introduction of the local roughness length (experiment indicated with "newlog").
3. Diagnostics used in the ECMWF model using a logarithmic interpolation combined with the introduction of the local roughness length (ecmwf).
4. A new diagnostics approach: introduction of the local roughness length, formulation for the profiles in the RSL and diagnostics independent of the surface value for high roughness lengths.

### 5.7.1 Introduction of the local roughness length in the actual diagnostics

Considering the unrealistic dynamically computed canopy height (discriminating between the use of the exponential and the logarithmic profile), one can try to substitute it in the diagnostics with a statically computed canopy height derived from the local roughness length, as presented in the previous section (Eq. 5.29). However, this estimation of $h_{can}$ makes it inconsistent with the resistances, the derivation of witch is based on the sum of the local and orographic roughness

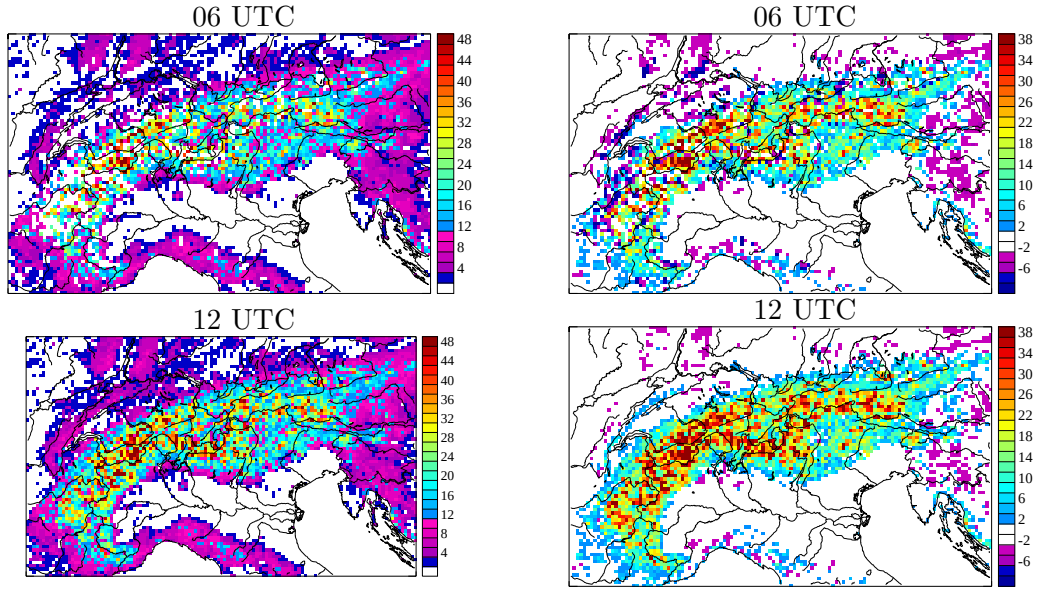


Figure 5.13: Left column: canopy height in the COSMO transfer scheme for a summer day (26.07.2007). Notice that values larger than 50 m are all coloured with the colour corresponding to this value. Right column: difference to the canopy height estimated from the roughness length as presented in Fig. 5.11 (modelled-estimated).

length. The resistances are in fact an input parameter in the diagnostics formula (Eq. 5.23). For this reason, this option cannot be pursued. The inconsistency could be circumvented if resistances only accounting for the local roughness length would be computed. This would mean a double call of both the transfer and turbulence scheme (at least for the lowest model levels ke and ke1). However, this introduces significant additional complexity and has therefore not been further explored.

### 5.7.2 Only a logarithmic profile (newlog)

The basic interpolation formula is identical to the one used in COSMO but only a logarithmic profile is used for the computation of the factor fac. The parameterization follows the same interpolation profile used for the surface layer part of the transfer scheme.

$$T_{2m} = T_s + (T_{ke} - T_s) \cdot \text{fac} \tag{5.30}$$

$$QV_{2m} = QV_s + (QV_{ke} - QV_s) \cdot \text{fac} \tag{5.31}$$

where fac is

$$\text{fac} = \frac{\log\left(\frac{z2+z_{0T}}{z_{0T}+f_h \cdot z2}\right)}{\log\left(\frac{0.5 \cdot dh+z_{0T}}{z_{0T}+f_h \cdot 0.5 \cdot dh}\right)} \tag{5.32}$$

z2 indicates the height at 2 m and the factor $f_h$ considers the turbulence conditions within the transfer scheme and is defined as follows:

$$f_h = \frac{(rat_h - 1)z_0}{dh} \tag{5.33}$$

$z_0$ is the complete roughness length (including orographic component) used in the transfer scheme, $0.5 \cdot dh$ is equal to the difference $H_2 - H_1$ (heights explained in Fig. 5.3), $rat_h$ is computed following

Eq. 5.25 and limited in its numerical extension using the following the relation.

$$0.5 < rat_h < \frac{dh + z_0}{z_0}$$

The lower limit assures that the logarithmic function remains concave upward and excludes inflection points. The upper limit avoids undefined solutions in the calculations of the resistance in the surface layer and has been modified compared to the one used for the wind speed (Eq. 5.25). $z_{0T}$ is the roughness length for temperature, which is not a strictly a physical quantity but rather an empirical one and generally takes lower values than the roughness length for momentum $z_0$ (Verhoef et al., 1997). It is defined in an indirect way: it is the height in the surface layer above the surface at which the extrapolation of the logarithmic semiempirical Monin-Obuchov theory in neutral conditions reaches the surface temperature value (Malhi, 1996).

The relation between roughness length for momentum and roughness length for heat is an unresolved and frequently discussed aspect in the boundary layer literature and several formulations have been proposed (e.g. Sheppard, 1958; Owen and Thomson, 1963; Calanca, 2001; Brutsaert, 1982; Kohsiek et al., 1993; Kustas et al., 1989; Sugita and Brutsaert, 1990; Stewart, 1995; Thom, 1972; Zilitinkevich, 1970). So far, no consensual accepted solution and widely applicable solutions has been identified. Brutsaert and Sugita (1996) suggest that the dimensionless number $kB^{-1} = ln(z_{0,loc}/z_{0T})$ is not a kind of surface property but rather depends on some environmental variables. Different dependencies from environment variables have been proposed. Owen and Thomson (1963) have suggested a dependency from the friction velocity $u_*$, an approach that has been tested for different surfaces by Garratt and Hicks (1973), obtaining values of $kB^{-1}$ from 0 (for low roughness Reynolds number $Re = u_* z_0/\nu$, where $\nu$ is the kinematic viscosity) to 10. For natural surfaces covered with grass Garratt and Hicks (1973) found a relatively constant value of $kB^{-1}$ close to 2. Other studies show that much larger values are possible, especially for sparse canopies (e.g. Garratt, 1980; Stewart et al., 1994; Blyth and Dolman, 1995). Kustas et al. (1989) suggested a dependence on the surface temperature introducing a diurnal variation of $kB^{-1}$. An extended comparison of some determination methods for vegetated surfaces starting from observations is given by Verhoef et al. (1997).

Due to the uncertainty found in the literature and the need of a formulation applicable over all the surfaces ($z_{0,loc}$ ranging from 0 to 1 m) in this study we use, in terms of a sensitivity experiment, an average between two dynamical formulations (Eq. 5.34, 5.35), a simple relation ($z_{0T} = z_0/100$, (Garratt and Francey, 1978)) and the equivalence between the two $z_{0T} = z_{0,loc}$ (Moelder and Lindroth, 1999), which gives reasonable results over all the meteorological situations and surfaces in the COSMO model.
According to Zilitinkevich (1970):

$$z_{0T} = \frac{z_{0,loc}}{\exp\left(0.13(u_* \cdot z_{0,loc} \cdot \nu^{-1})^{0.45}\right)} \tag{5.34}$$

According to Thom (1972):

$$z_{0T} = \frac{z_{0,loc}}{\exp\left(1.35 \cdot \kappa(100 \cdot u_*)^{1/3}\right)} \tag{5.35}$$

### 5.7.3 The ECMWF model 2 m diagnostics (ecmwf)

The 2 m temperature and humidity diagnostics in the ECMWF model is formulated as gradient functions for the dry static energy S

$$S = gz + C_p d \tag{5.36}$$

and the specific humidity QV following the Monin-Obuchov similarity theory (ECMWF, 2007).

$$\frac{\kappa z}{S_*}\frac{\partial S}{\partial z} = \phi_H(\frac{z}{L}) \tag{5.37}$$

$$\frac{\kappa z}{QV_*}\frac{\partial QV}{\partial z} = \phi_H(\frac{z}{L}) \tag{5.38}$$

Here, $S_* = J_s/u_*\rho$ and $QV_* = J_{qv}/u_*\rho$ are the scaling variables for the two scalar quantities, where $J_s$ and $J_q$ are the respective turbulent fluxes. $u_*$ is the friction velocity and $L$ is the Obuchov length.

$$u_* = (\overline{u'w'}^2 + \overline{v'w'}^2)^{1/4} \tag{5.39}$$

$$L = \frac{\theta_v u_*^3}{\kappa g(\overline{w'\theta'} + \overline{w'q'}(\frac{R_d}{R_v} - 1))} \tag{5.40}$$

For the unstable case the dimensionless functions proposed by Dyer (1974) are used (Eq. 5.41), while in stable situations the formulation documented by Högström (1988) is applied (Eq. 5.42).

$$\phi_H = (1 - 16\frac{z}{L})^{-1/2} \qquad unstable \tag{5.41}$$

$$\phi_H = (1 + 4\frac{z}{L})^2 \qquad stable \tag{5.42}$$

Integrating the gradient functions we obtain the following profiles functions.

$$S - S_s = \frac{J_s}{\kappa\rho u_*}\left(\log(\frac{0.5\cdot dh + z0,loc}{z_{0T}}) - \Psi_H(\frac{0.5\cdot dh + z_{0,loc}}{L}) + \Psi_H(\frac{z_{0T}}{L})\right) \tag{5.43}$$

$$QV - QV_s = \frac{J_q}{\kappa\rho u_*}\left(\log(\frac{0.5\cdot dh + z0,loc}{z_{0T}}) - \Psi_H(\frac{0.5\cdot dh + z_{0,loc}}{L}) + \Psi_H(\frac{z_{0T}}{L})\right) \tag{5.44}$$

$\Psi_H$ are the universal stability functions for unstable (Eq. 5.45) and stable situations (Eq. 5.46).

$$\Psi_H = 2\log(\frac{1+x^2}{2}) \tag{5.45}$$

$$\Psi_H = -b(\zeta - \frac{c}{d}\exp(-d\zeta) - (1 + \frac{2}{3}a\zeta)^{1.5} - \frac{bc}{d} + 1 \tag{5.46}$$

with $x = (1 - 16\zeta)^{1/4}$, $\zeta = \frac{z}{L}$, $a = 1$, $b = 2/3$, $c = 5$ and $d = 0.35$. With the combination of the profile functions at two elevations (2 m and first atmospheric level) it is possible to derive the interpolation formulae for the 2 m dry static energy and the 2 m specific humidity.

$$S_{2m} = S_s + (S - S_s)\frac{\left(\log(\frac{z2+z_{0,loc}}{z_{0T}}) - \Psi_H(\frac{z2+z_{0,loc}}{L}) + \Psi_H(\frac{z_{0T}}{L})\right)}{\left(\log(\frac{0.5\cdot dh+z_{0,loc}}{z_{0T}}) - \Psi_H(\frac{0.5\cdot dh+z_{0,loc}}{L}) + \Psi_H(\frac{z_{0T}}{L})\right)} \tag{5.47}$$

$$QV_{2m} = QV_s + (QV - QV_s)\frac{\left(\log(\frac{z2+z_{0,loc}}{z_{0T}}) - \Psi_H(\frac{z2+z_{0,loc}}{L}) + \Psi_H(\frac{z_{0T}}{L})\right)}{\left(\log(\frac{0.5\cdot dh+z_{0,loc}}{z_{0T}}) - \Psi_H(\frac{0.5\cdot dh+z_{0,loc}}{L}) + \Psi_H(\frac{z_{0T}}{L})\right)} \tag{5.48}$$

With Eq. 5.36 the temperature can be computed from the dry static energy. $z2$ is the 2 m height and $z_{0T}$ is computed with the same procedure as presented in previous section and used without any limitation (in the ECMWF model $z_{0T}$ is limited maximally to 3 cm).

In summary, the ECMWF diagnose uses a logarithmic interpolation based on the Monin-Obuchov similarity theory.

### 5.7.4 New approach considering the RSL and independent from the surface value (new)

Given the observed problems of the surface temperature (mainly during the winter time) it would be interesting to develop a diagnostics, which does not depend on the surface temperature. Additionally, in case of high local roughness lengths it would be very useful to have a diagnostic tool, which considers the impact of the RSL on the vertical profiles of temperature and humidity. Inside and above canopy structures the logarithmic profile is not adequate to reproduce the observations and different profile functions should be used. The 2 m level is significantly influenced by the canopy for roughness lengths larger than 0.1 m. The COSMO transfer scheme considers the roughness sublayer as a skin layer. As a result, the effective height of the first atmospheric level should be larger than the physical height of the layer.

In the following, a diagnostics tool is presented, which considers the main characteristics of the ISL and the RSL, their differences and their vertical extension. This new approach is used only in cases over land, when the 2 m level is lower than the level $z_* = 2h_{can}$ corresponding to the upper boundary of the RSL (e.g. Rotach, 2001). It starts with the atmospheric values of temperature, humidity and turbulent fluxes at the level $z_*$, where the canopy effects on the surface layer flow are supposed to be negligible and typical surface layer theory can be applied without constraints.

The canopy height is estimated from the local roughness length for momentum using the expression proposed by Raupach (1994) for a canopy area index equal to one and supported by Rotach (2001). This has been presented in Eq. 5.29. Over the COMSO 7 km domain the canopy height computed with this formulation varies between $10^{-2}$ m and 10 m. The canopy height defines the vertical range $[0, z_*]$ where the effect of the canopy on the flow is supposed to be significant. The upper boundary of the RSL and the transition in the ISL is located at $z_*$. $z_*$ can be estimated from the canopy height following the formulation of Rotach (2001):

$$z_* = 2h_{can} \tag{5.49}$$

The skin layer (roughness and laminar layer) in the transfer scheme is a problem in the diagnostics because it has no vertical extension. It is useful to give this layer a vertical extension and to define an effective height of the first atmospheric level. The effective height of the first atmospheric layer is estimated using the concept of the displacement height d (Malhi, 1996; Garratt, 1992; Raupach, 1994):

$$H2 = d + z_{0,loc} + h_{ke} \tag{5.50}$$

where d is estimated with the formulation proposed by Allen et al. (1989), which is very similar to the recommendation of Wieringa (1993).

$$d = \frac{2}{3} h_{can} \tag{5.51}$$

Assuming that the typical height of the first atmospheric layer varies from 10 to 30m, H2 and $z_*$ define the three possible cases for the diagnostics at 2 m, sketched in Fig. 5.14: (a) the $z_*$ level is below the 2 m level, (b) the $z_*$ level is located between the 2 m level and the first atmospheric level H2 and (c) the $z_*$ level is above the first atmospheric level. (a) is characterised by low roughness and the 2 mtemperature is computed using the logarithmic interpolation presented in Subsection 5.7.2. Here, instead of the roughness length for temperature the normal local roughness length is used in order to avoid inconsistencies with the other two cases. For cases (b) and (c) a new formulation explained in the following is used.

There exists no analytical formulation for the RSL profiles of a scalar in the literature. Kastner-Klein and Rotach (2004) have presented one for the mean wind speed, which is based on the local

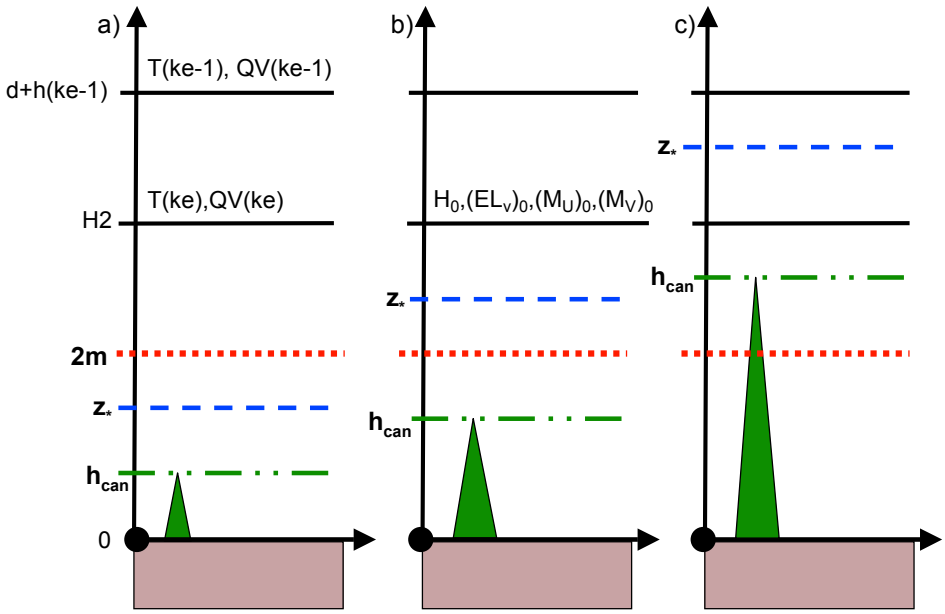


Figure 5.14: The three cases used for the new diagnostics of the 2 m temperature and 2 m dew point (derived from the 2 mspecific humidity)

profile of the momentum flux. In analogy, the vertical gradient of the potential temperature below $z_*$ can be formulated with a local temperature scaling (Eq. 5.52). The corresponding vertical gradient of the specific humidity follows a local humidity scale (Eq. 5.53). With this step we assume that no counter gradient effects take place in the RSL.

$$\frac{\partial \Theta}{\partial z} = \frac{\Theta_*(z)}{\alpha_\theta (z - z_{0,loc})} \tag{5.52}$$

$$\frac{\partial QV}{\partial z} = \frac{QV_*(z)}{\alpha_{qv} (z - z_{0,loc})} \tag{5.53}$$

$\alpha_\theta$ and $\alpha_{qv}$ are constant length scales, $\Theta_*(z)$ and $QV_*(z)$ are the local temperature scale and the local humidity scale, respectively, which depend on the vertical profiles of the turbulent fluxes in the RSL.

$$\Theta_*(z) = \frac{\overline{w'\theta'(z)}}{u_*(z)} = \frac{\overline{w'\theta'(z)}}{(\overline{u'w'(z)}^2 + \overline{v'w'(z)}^2)^{1/4}} \tag{5.54}$$

$$QV_*(z) = \frac{\overline{w'qv'(z)}}{u_*(z)} = \frac{\overline{w'qv'(z)}}{(\overline{u'w'(z)}^2 + \overline{v'w'(z)}^2)^{1/4}} \tag{5.55}$$

The vertical profiles for the momentum fluxes are defined following the work of Kastner-Klein and Rotach (2004) assuming that the relative ratio between the two components (meridional and zonal) remains constant from $z_*$ to the surface and no turning effects take place. The momentum flux decreases exponentially and vanishes at $z = z_{0,loc}$. $z_{0,loc}$ is the local roughness length.

$$\overline{u'w'(z)} = c \cdot \overline{u'w'}_{ISL} \left( \frac{z - z_{0,loc}}{z_s - z_{0,loc}} \right)^2 \exp\left( a(1 - \left( \frac{z - z_{0,loc}}{z_s - z_{0,loc}} \right)) \right) \tag{5.56}$$

$$\overline{v'w'(z)} = c \cdot \overline{v'w'}_{ISL} \left( \frac{z - z_{0,loc}}{z_s - z_{0,loc}} \right)^2 \exp\left( a(1 - \left( \frac{z - z_{0,loc}}{z_s - z_{0,loc}} \right)) \right) \tag{5.57}$$

In Equations 5.56 and 5.57 $z_s$ is the height above surface at which the maximum of momentum flux is reached. $a$ is a constant having the same value ($a = 2$) as proposed by Kastner-Klein and Rotach (2004), while c is a constant which permits to match the ISL value $\overline{u'w'}_{ISL}$ at $z_*$

$$c = \left(\frac{z_* - z_0}{z_s - z_0}\right) \exp\left(a(1 - \left(\frac{z_* - z_0}{z_s - z_0}\right)\right) \tag{5.58}$$

The momentum fluxes in the ISL ($\overline{u'w'}_{ISL}$ and $\overline{v'w'}_{ISL}$) are taken from the transfer scheme and determined from the surface fluxes dividing the expressions Eq. 5.17 and 5.18 by the air density ($\overline{u'w'}_{ISL} = (M_U)_0/\rho$; $\overline{v'w'}_{ISL} = (M_V)_0/\rho$). The same surface fluxes are taken in the third case of the diagnostics, when the $z_*$ level is above the effective height of the first atmospheric level. In case (c) the ISL fluxes are assumed to remain approximately constant in proximity of the first atmospheric layer. Depending on the physical height of the first atmospheric level, the possible error of this assumption has an effect only on a minority of gridpoints: for a first model level physically at 10 m (but effectively higher according to Eq. 5.50), the situation with $z_*$ larger than $H2$ occurs only for a local roughness length larger than 0.75 m.

The maximum momentum flux is generally close to the canopy height for vegetated surfaces (Denmead and Bradley, 1987; Raupach, 1987; Raupach and Thom, 1981) for moderately small canopy heights below 5 m and close to $z_*$ for large roughness lengths as in cities (Rotach, 2001). This observed discrepancy depends on the type of surface and has been parameterized with a linear approach as function of the roughness length:

$$z_s = \begin{cases} z_0 \frac{h_{can} - z_*}{-0.5} & z_{0,loc} > 0.5 \\ h_{can} & z_{0,loc} < 0.5 \end{cases} \tag{5.59}$$

An example for the vertical profiles of the momentum fluxes is presented in Fig. 5.15.

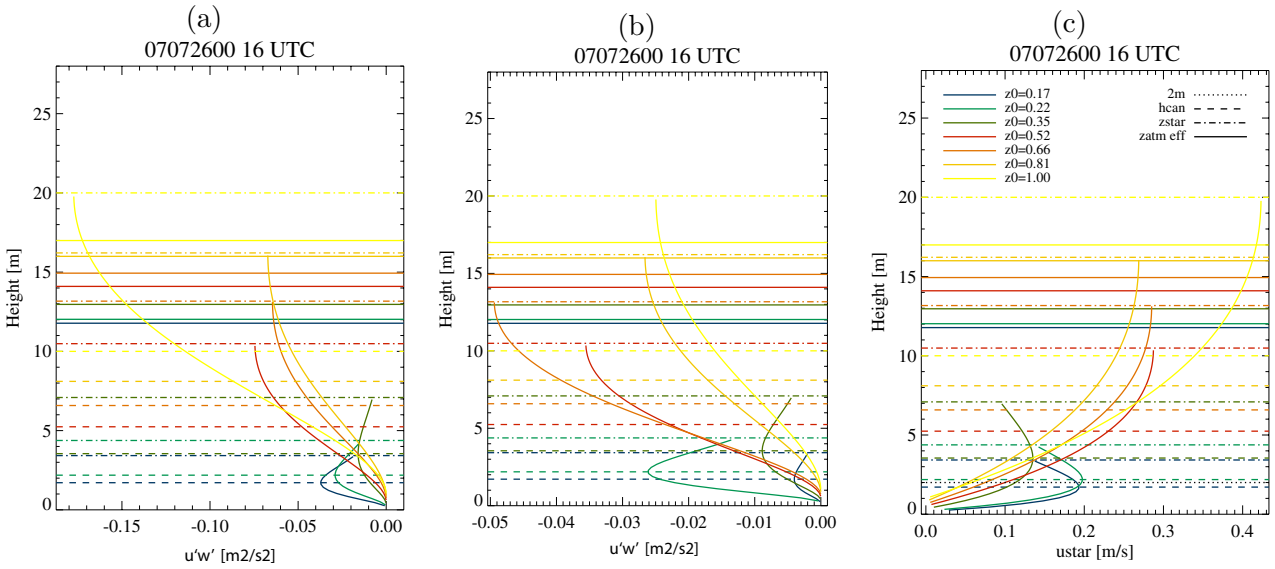


Figure 5.15: Example of the vertical profiles of the turbulent fluxes for momentum and friction velocity in the RSL for gridpoints with different roughness lengths as indicated in the legend. The key levels are given in the legend as well.

The vertical profiles of the sensible and latent heat flux are determined according to a modified exponential function as proposed by Christen (2005) for the urban canopy tempertaure: above the canopy height $z_s = h_{can}$ the flux is assumed to be constant (equal to the ISL value at $z_*$),

below the canopy height an exponential decrease is observed.

$$\overline{w'\theta'(z)} = \begin{cases} \overline{w'\theta'}_{ISL} \left(\frac{z-z_{0,loc}}{z_s-z_{0,loc}}\right)^2 \exp\left(-ch\frac{h_{can}-z}{h_{can}}\right) & z < h_{can} \\ \overline{w'\theta'}_{ISL} & z > h_{can} \end{cases} \tag{5.60}$$

$$\overline{w'qv'(z)} = \begin{cases} \overline{w'qv'}_{ISL} \left(\frac{z-z_{0,loc}}{z_s-z_{0,loc}}\right)^2 \exp\left(-ch\frac{h_{can}-z}{h_{can}}\right) & z < h_{can} \\ \overline{w'qv'}_{ISL} & z > h_{can} \end{cases} \tag{5.61}$$

ch=1.2 is a parameter estimated by Christen (2005) from tower measurements and $h_{can}$ is the canopy height. The introduced modification results to a faster convergence of the sensible heat flux to zero close to the surface and into a faster vanishing of the local vertical derivative for temperature (Eq. 5.52). The differences between this formulation and the profile derived from measurement (Christen, 2005) are presented in Fig. 5.16. The ISL values are computed from the

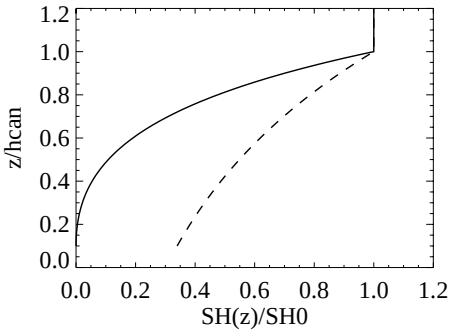


Figure 5.16: The difference between the vertical profile of the normalised sensible heat flux ($SH/SH0 = \overline{w'\theta'}/\overline{w'\theta'}_{ISL}$) used in this study (continuous line) and the parameterization proposed by Christen (2005) based on urban observations (dashed line).

modeled "surface fluxes" in analogy to what was done with the momentum fluxes. An example for the vertical profile of the sensible heat flux, the temperature scale and the vertical gradient of the potential temperature is given in Fig. 5.17. Similarly, the latent heat flux profile, the humidity scale and the vertical gradient of specific humidity are given in Fig. 5.18.

The parameter values $\alpha_\theta$ and $\alpha_{qv}$ in Eq. 5.52 and Eq. 5.53 are determined by matching the temperature gradient with the ISL gradient at $z_*$. The temperature gradient in the ISL can be computed with the Monin-Obuchov similarity theory using Eq. 5.37 written for the potential temperature and Eq. 5.38 substituting z with $z' = z - d$, where d is the displacement height. The matching with Eq. 5.52 gives

$$\alpha_\theta = \alpha_{qv} = \frac{\kappa(z_* - z_{0,loc})}{\phi_H(z_* - d)} \tag{5.62}$$

$\phi_H$ are the dimensionless gradients for the stable and unstable case defined as follows according to Högström (1996) and Garratt (1992), respectively:

$$\phi_H = 0.95\left(1 + 4\left(\frac{z-d}{L}\right)\right) \qquad \text{stable stratification} \tag{5.63}$$

$$\phi_H = 0.95\left(1 - 9\left(\frac{z-d}{L}\right)\right)^{-1/2} \qquad \text{unstable stratification} \tag{5.64}$$

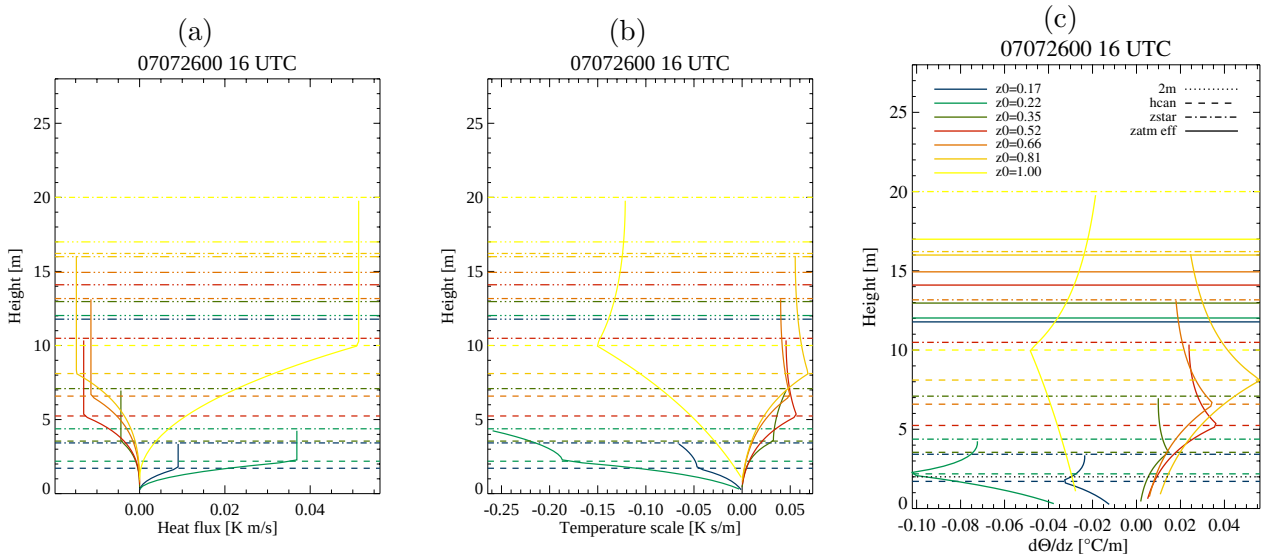


Figure 5.17: Example of the vertical profiles of the sensible heat flux, temperature scale and vertical temperature derivative in the RSL for gridpoints with different roughness length as indicated in the legend. The key levels are indicated in the legend as well.

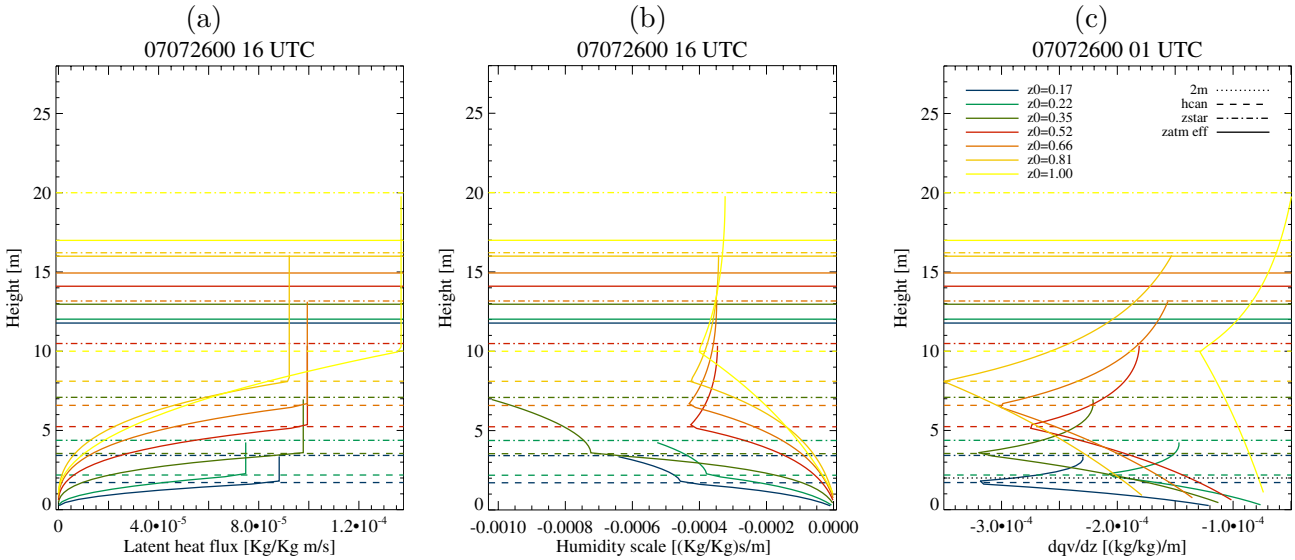


Figure 5.18: Example for the vertical profiles of the latent heat flux, humidity scale and vertical specific humity derivative in the RSL for gridpoints with different roughness length as indicated in the legend. The key levels are indicated in the legend as well.

In this implementation the Obuchov length L has been limited in its range of values in order to avoid too strong gradients in very stable conditions: in the stable cases $L > 2H2$ and in unstable cases $L < -1$.

Once the vertical profiles of the turbulent fluxes are determined it is possible to compute $\Theta_*(z)$ and the vertical derivative of the temperature according to Eq. 5.52. This equation can be numerically integrated (e.g. with the QROMB procedure suggested by Press et al., 1989) obtaining the vertical profile of the temperature and specific humidity:

$$\Theta(z) = \Theta(z_*) - \int_{z_{0,loc}}^{z} \frac{\Theta_*(z)}{\alpha_\theta(z - z_{0,loc})} \tag{5.65}$$

$$QV(z) = QV(z_*) - \int_{z_{0,loc}}^{z} \frac{QV_*(z)}{\alpha_{qv}(z - z_{0,loc})} \tag{5.66}$$

The temperature and specific humidity at $z_*$ are determined depending on the position of this level in comparison to the effective height of the first atmospheric layer $H2$. If $z_*$ is below the first atmospheric layer then the Monin-Obuchov theory is used to find the $T_*$ and $QV_*$ value (integration of Eq. 5.37 and 5.38). Otherwise an interpolation between two atmospheric layers is performed.

Figure 5.19 presents the vertical profile of temperature and specific humidity obtained by integrating the temperature (Eq. 5.52) and humidity gradient profiles (5.53). Finally, the 2 m dew point is computed from the 2 m temperature, surface pressure and 2 m humidity as presented in Eq. 5.28.

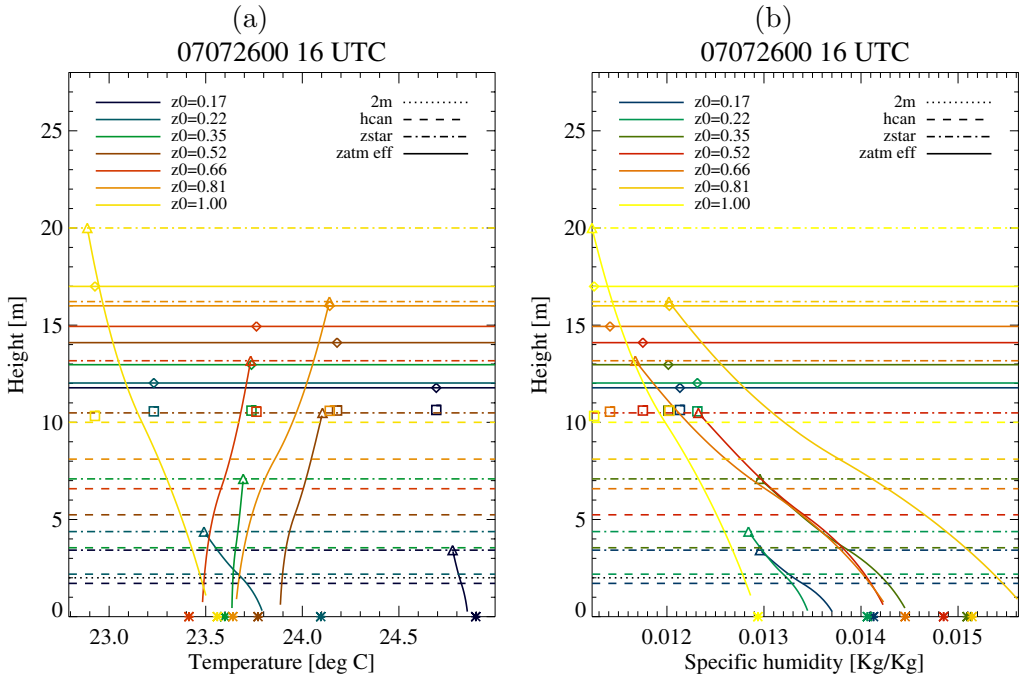


Figure 5.19: (a) Example for a vertical profile of the temperature and (b) the vertical specific humidity profile obtained with the integration of the gradient profiles Eq. 5.52 and 5.53. The squares (□) indicate the temperature or specific humidity value at the first atmospheric level, triangles (△) at $z_*$ , diamonds (◊) at the effective first level height $H2$ and stars (∗) at the surface. The horizontal lines give the different important levels: 2 m level, canopy height (hcan), $z_*$ (zstar) and effective first layer height (zatm eff). The colours are associated to different gridpoints having different roughness lengths.

The new RSL profiles are independent from the surface values computed prognostically by the model. This means that near the surface a difference between model and new diagnostics can

occur. This problem could be nearly completely resolved if the dimensionless gradient function in the ISL were tuned, in order to reach at the elevation $d + z_{0,loc}$ with a downward logarithmic extrapolation profile in the RSL the same value as at the surface. However, this option has not been followed in order to maintain realistic dimensionless functions, as found in the ISL literature. Optionally, a safety check can be switched on, which filters out all the values of the profile which are not between modeled surface value and value at $z_*$.

In this section three alternative 2 m diagnostics based on the local roughness length have been presented. The first two (newlog and ecmwf) are exclusively based on a logarithmic interpolation profile and are, therefore, physically not completely consistent with the typical RSL characteristics. On the contrary, the new approach based on RSL profiles should better account for the conditions over and within large canopy elements.

## 5.8 Case studies, observations and model settings

In order to obtain some preliminary indications about the performance of the new diagnostics, the operational 2 m diagnostics (Section 5.4) is compared with the three variants presented in the previous section (from Subsection 5.7.2 to Subsection 5.7.4) along a verification against SYNOP observations. 5 case studies have been chosen: one day for winter, one for spring, one for autumn and two for summer (18.06.2006, 20.12.2006, 15.04.2007, 26.07.2007 and 15.10.2007). The synoptic situation of these 5 cases is presented in Fig. 5.20: general characteristics of the chosen days are fair weather conditions over most of central and western Europe covered by the COSMO model. For the summer cases a fair weather day with (18.06.2006) and without (26.07.2006) convective precipitation over Switzerland during the afternoon have been selected.

For each chosen day, a forecast starting from the European Centre for Medium Range Weather Forecast (ECMWF) analysis has been performed with two necessary steps. First, a COSMO 7 km analysis has been produced and used as initial condition. Second, a 24 hours 7 km forecast, nested directly into the ECMWF analysis (boundary conditions) has been produced. The initialisation with a high-resolution analysis and the use of ECMWF analysis as boundary conditions is expected to have forced the runs at least to a synoptically correct state. The model domain at 7 km extends over western and central Europe with a grid of 385x325 grid points. For all the model integrations the COSMO version 3.20 has been used.

Despite the mentioned risks in associating model gridbox averages with specific locations (point observations) a traditional verification of the 2 m temperature and 2 m dew point with SYNOP observations has been performed. Given that no spacial verification alternatives are available (e.g. satellite data) this is assumed to be the best possible way to estimate the performance quality of the model in general and the diagnostics in particular. The specific locations of the meteorological stations are associated with gridpoints by always choosing the nearest gridpoint over land. If no land gridpoints are available in the surroundings the nearest sea point is taken. All the available stations are used independently from the height difference between the model and real topography.

However, the height difference has been taken into account by applying a simple vertical constant lapse rate of -0.65 $°C/100m$. This constant gradient is not the optimal choice: for example Kunz et al. (2007) have used regionally and seasonally differentiated climatological values. For an optimal height correction this aspect should be considered. This height correction has a significant impact considering the huge height differences between model topography and real topography at some locations (up to 1200 m) . Obviously, this critical step could have some potential risks. However, the comparison of the different diagnostics options is globally insensitive to this aspect because the correction is applied to all four versions of the diagnostics (operational and 3 alternatives).

For each case study 3 different domains have been verified: (i) the entire COSMO model

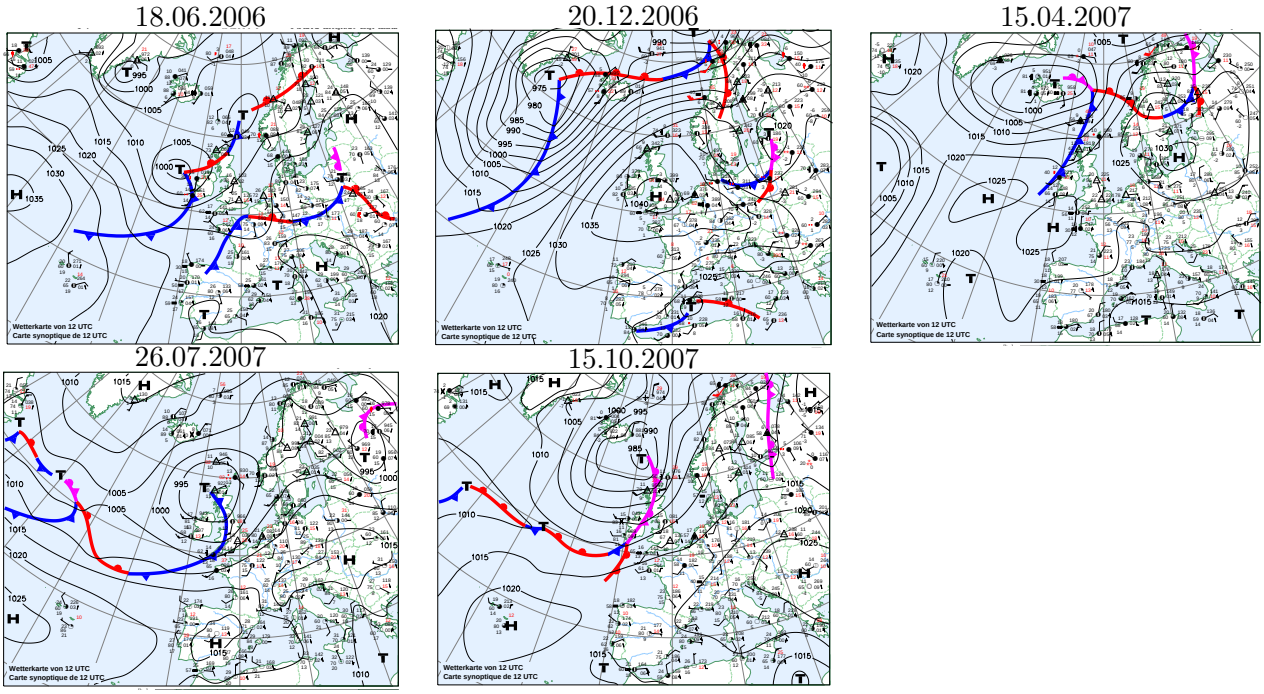


Figure 5.20: Synoptic situation of the five chosen test cases for the new diagnostics: all typical good weather situations in the corresponding season.

domain (a maximum of 1172 SYNOP stations), (ii) a domain covering the alpine region (more or less the operational COSMO 2.2 km domain, about 380 stations) and (iii) the domain over Switzerland (about 66 stations). Swiss stations data are available every hour, while data from stations outside Switzerland are available with variable frequency: hourly, every 3 hours or every 6 hours. This aspect can clearly be observed in the verification results.

Table 5.1 presents the distribution of the roughness lengths for the gridpoints associated with the different SYNOP stations. Most of them are located over surfaces having a local roughness lower than 0.2 m and an orographic component smaller than 0.5 m.

## 5.9 Results and discussion

This section focuses on the results obtained with the three variants of 2 m temperature and 2 m dew point diagnostics compared to the operational setting. First, some special aspects related to the new RSL profiles will be presented. Then, the spacial impact compared to the original diagnostics is highlighted and commented. Finally, with the SYNOP verification the quantitative performance of each variant as derived from the SYNOP verification will be illustrated and discussed. For this last step, also an additional conditional verification will be performed, depending on the distribution of the roughness length at the SYNOP station associated gridpoints. Note that the verification is based on only five days. To confirm the results a longer verification test suite should be performed.

#### The vertical profiles in the surface layer

Figure 5.21 presents a time series of the vertical profiles of temperature for a summer day as obtained from the new formulation presented in Subsection 5.7.4. Seven gridpoints with different roughness lengths from 0.17 m to 1 m are presented for 6 validation times over the day. The typical transition between stable (06, 16, 18 UTC) and unstable (10, 12, 14 UTC) conditions can easily be identified.

| $z_{0,loc}/z_{0,oro}$ | **0.0-0.5 m** | **0.5-2.0 m** | **2.0-3.0 m** | **3.0-6.0 m** | **total** |
|---|---|---|---|---|---|
| **0.0-0.05** | 21 | 13 | 3 | 1 | 38 |
| **0.05-0.1** | 75 | 9 | 6 | 1 | 91 |
| **0.1-0.2** | 63 | 9 | 3 | 3 | 78 |
| **0.2-0.3** | 23 | 5 | 4 | 2 | 34 |
| **0.3-0.4** | 22 | 3 | 2 | 2 | 29 |
| **0.4-0.5** | 12 | 2 | 1 | 2 | 17 |
| **0.5-0.6** | 9 | 4 | 4 | 0 | 17 |
| **0.6-0.7** | 13 | 4 | 2 | 2 | 21 |
| **0.7-0.8** | 10 | 7 | 2 | 1 | 20 |
| **0.8-0.9** | 8 | 12 | 2 | 0 | 22 |
| **0.9-1.0** | 9 | 3 | 2 | 1 | 15 |
| **total** | 265 | 71 | 31 | 15 | 382 |

Table 5.1: Distribution of the model roughness lengths for 382 SYNOP stations for the domain ALPS: the columns indicate the orographic component $z_{0,oro}$ and the rows show the local component $z_{0,loc}$. Each cell gives the number of SYNOP stations assigned to the corresponding class.

Assuming the profile value at the lowest possible elevation (just above $z_{0,loc}$) as pseudo surface temperature (surface specific humidity) it can be compared with the modeled surface temperature (modeled surface specific humidity) as computed prognostically by the model. The majority of grindpoints show a diagnosed near-surface temperature that is smaller than the surface temperature under unstable conditions, and larger under stable conditions. Therefore, the absolute difference between the first model level at $H2$ and the profile just above $z_{0,loc}$ is predominantly smaller than that between first model level and surface temperature. In other words, for the majority of gridpoints, where the new profiles are used ($z_{0,loc} > 0.1m$), all the values along the temperature profile up to $H2$ are between the surface temperature and the temperature at the first model level (at $H2$). This result is very promising, given that the formulation is independent of the surface value. Recalling the problems that have been observed in the operational COSMO model (underestimation of the surface value in winter and overestimation in summer), it follows that this aspect will have a positive effect on the diagnostics quality. There are a few gridpoints which show a larger absolute temperature or specific humidity difference than the difference between surface and first atmospheric level. However, for each time step maximally 100 land gridpoints (over more than 65'000) exhibit this characteristic.

The specific humidity profiles exhibit a similar behaviour depending on the direction of the latent heat flux. Figure 5.22 shows a underestimation of the profile in case of upward flux and an overestimation in case of downward flux. The humidity gradients do not necessarily have the same sign as the temperature gradients. Due to the more pronounced shape of the profile caused by a larger initial negative vertical gradient at $z_*$, more gridpoints exhibit an overestimation of the specific humidity near the surface compared to the model values in case of larger specific humidities at the surface than at the first atmospheric level. For example, this can be seen in the right panel of Fig. 5.22 (orange and green profile). For this reason, the filtering mechanism that has been implemented as security check and can be used optionally to avoid unrealistic temperature and humidity jumps near the surface, has a larger impact than for temperature. However, still less than 200 land gridpoints (over more than 65'000) are involved.

As expected, the model deficiency observed in spring and summer over melting snow surfaces is significantly reduced in the implemented RSL profiles, because the new profile value at 2 m is predominantly closer to the atmospheric value compared to the operational diagnostics (not shown).

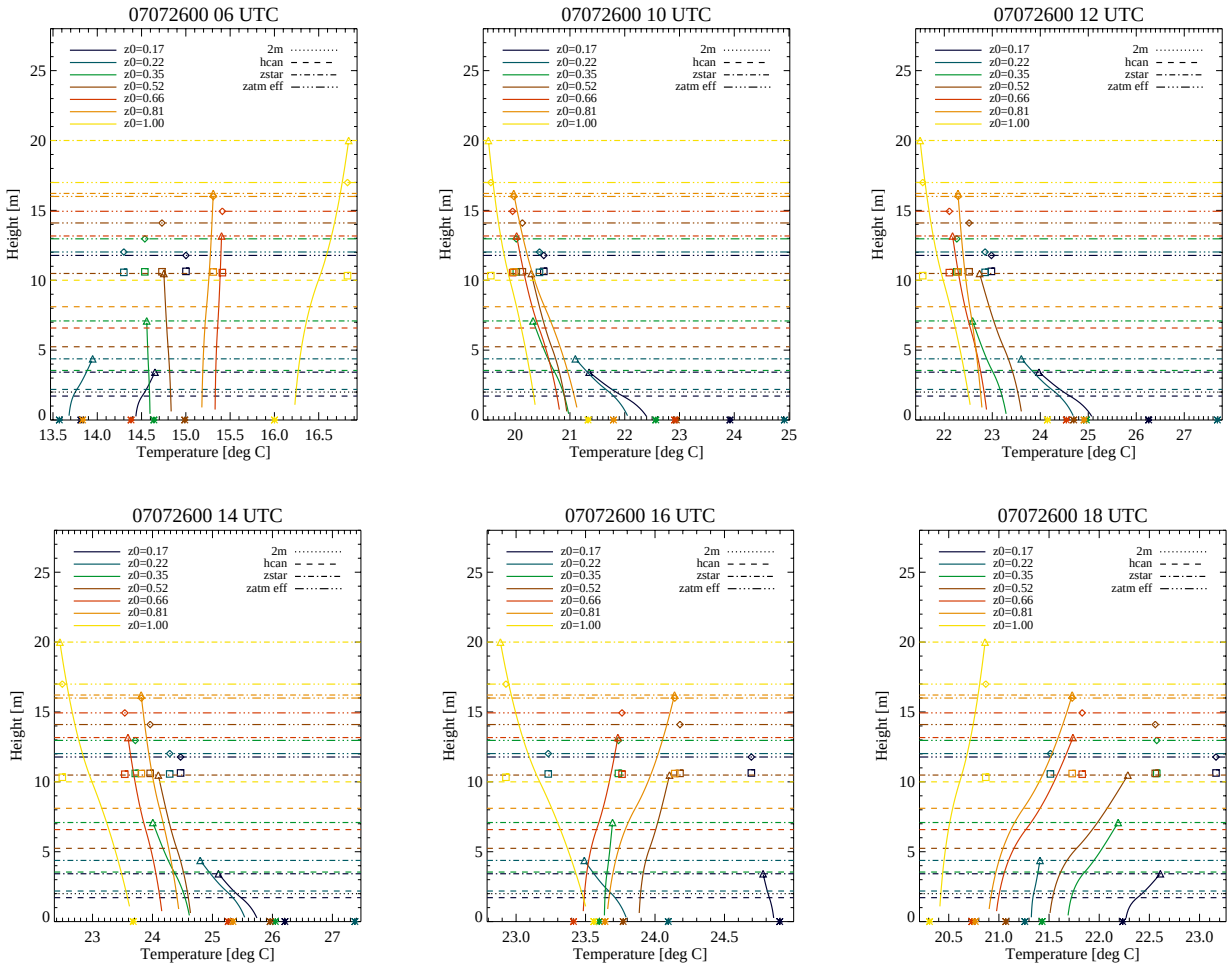


Figure 5.21: Vertical profiles of the temperature for six validation times during a summer day (26.07.2007) as indicated in each panel title: seven gridpoints with different roughness lengths are plotted, as indicated in the legend. The colours refer to the different gridpoints. Additionally, also the key vertical levels are given: the 2 m level (dotted line), the $z_*$ level (dash-dotted line), the canopy height (dashed line) and the effective height of the first atmospheric level (dashed and double dotted line). The squares ($\square$) indicate the values at the first atmospheric level, triangles ($\triangle$) at $z_*$ , diamonds ($\Diamond$) at the effective first level height $H2$ and stars ($*$) at the surface.

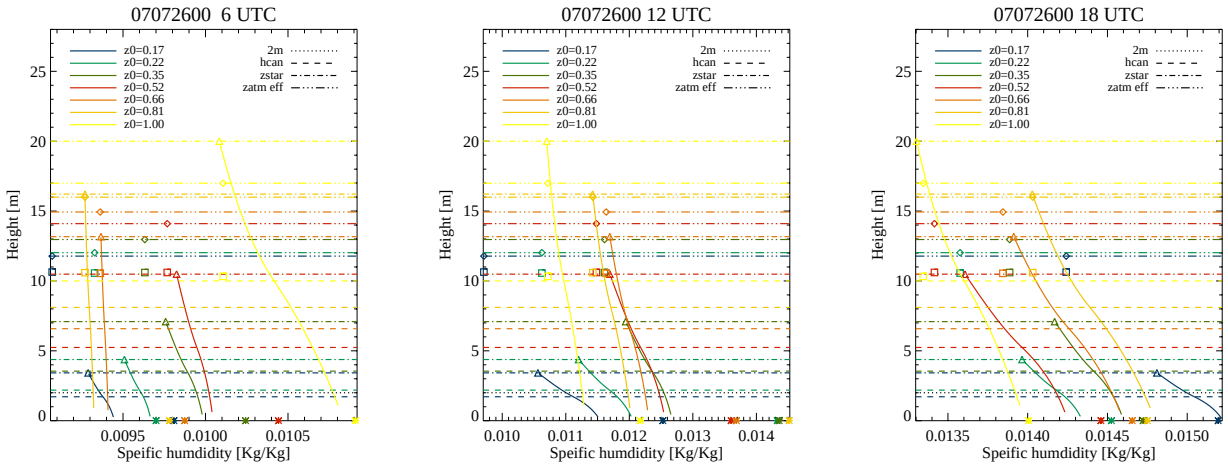


Figure 5.22: Vertical profiles of the specific humidity for three validation times during a summer day (26.07.2007) as indicated in each panel title. The colours and the lines have the same meaning as in Fig. 5.21

**Sensitivities of the new vertical profiles**

In this subsection some important sensitivities of the new profiles are highlighted and qualitatively commented.

The difference between the surface value and the profile value at the lowest possible elevation strongly depends on the the surface layer fluxes at $z_*$ and on in the temperature ($\Theta_*$) or humidity scale ($QV_*$). The gradient at the elevation $z_*$ is a function of the temperature scale (or humidity scale), of the dimensionless gradient and the elevation above the displacement height ($z-d$). The gradient at $z_*$ is the key parameter influencing the amount of differentiation of the vertical profile values from the atmospheric values, because at exactly this location the matching between the gradient calculated with the new formulation and the gradient derived from the traditional surface layer theory are synchronised. Therefore, the profile is reasonably sensitive to the value of $d$ and very sensitive to the dimensionless gradient at $z_*$. Larger $d$ generally means higher gradients and vice-versa. A diverse range of surface layer functions can be found in the literature and those with better results in the COMSO model have been chosen (see Eq. 5.63 and 5.64 in Subsection 5.7.4).

In unstable conditions better results are generally obtained with large surface layer dimensionless gradients. In unstable situations (Obuchov length $L$ is negative) only a soft limitation of $L$ to maximally -1 m is used, leading to satisfactory results with only a few overestimations of the near surface temperature compared to the model prognostically predicted surface temperature. On the contrary, in very stable situations (L is positive and small) the Monin-Obuchov formulation for the surface layer often results in to too strong gradients at $z_*$, presumably due to the absence of wind shear (very small friction velocity) and the vanishing turbulence. In such situations the model is entering a kind of decoupling mode and the turbulent fluxes become unrealistic for a derivation of the temperature profile in the RSL. Therefore, a limitation of L is necessary to avoid a too strong gradient leading to a large underestimation of the near-surface values of the computed RSL profiles. Similar problems of the ISL profiles in very stable situations have been found in the ECMWF diagnostics, for witch also a limitation of L is necessary in order to avoid even colder temperatures than the operational diagnostics (ECMWF, 2007).

The higher the matching point $z_*$ the more pronounced is the tendency of producing small temperature differences: a large roughness length often means large transfer scheme resistances and lower surface fluxes. For this reason, the typical shape of the RSL profile resembling a transition between a logarithmic and an exponential profile, can often be seen fully developed for moderately small roughness lengths. The shape of the profile also depends strongly on the above mentioned gradient at the matching point.

If the first atmospheric layer is shifted higher, the performance in terms of difference between the extrapolated values near the surface taken from the generated RSL profile and the surface temperature is slightly smaller (larger differences mean a worse performance), because the interpolation region is longer.

**The temperature daily cycle**

Figure 5.23 presents the daily cycle for the 2 m temperature using the three diagnostics options for the same summer day as in Fig. 5.21. The left panel shows the temperature daily cycle for one model gridpoint as an illustration ($z_0 = 0.66$, same point as the red line in Fig. 5.21). Two diagnostics variants are compared with the operational diagnostics: the new formulation (new) and the new logarithmic profile (lognew). The middle and the right panel present the corresponding vertical profiles in the RSL for a single validation time (4 and 16 UTC). The main difference between the two new formulations (logarithmic and new RSL profiles) and the operational diagnostics is the phase of the maximum temperature, which is much closer to the atmospheric value for the new options. During the late morning, the afternoon and the evening the operational diagnostics is closer to the surface value, while in stable situations in the morning

the coldest temperatures are obtained with the new logarithmic profile. This is not generally valid (in fact the logarithmic profile is in the majority of the cases warmer), but it permits to illustrate an interesting feature of the operational diagnostics. The vertical profiles indicate the reason of the apparent contradiction: the exponential profile in the operational diagnostics is used in this gridpoint situation only in unstable situations during the day and in stable situations during the evening. This is possible because the effective and dynamically computed canopy height changes during the day, which is somewhat unrealistic (see changes in the profile of the "opr" line between middle and right panel of Fig. 5.23). In stable situations, mainly in the morning hours, the new RSL profiles are significantly warmer than the other two options. Notice also the different canopy height (right panel). In a few limited cases as in this gridpoint the canopy height of the operational diagnostics is smaller than the estimated one.

The aspect of the phase shift observed for a single gridpoint and commented above is confirmed by the averaged daily cycles presented separately for three classes of subgridscale roughness lengths components over land in Fig. 5.24. The larger the subgridscale component of the roughness length the closer is the phase of the operational temperature diagnostics to the phase of the surface value. This is not the case for the other three options. In winter the operational diagnostics (first row) gives clearly the coldest mean daily cycle. The warmest temperatures are obtained with the new logarithmic profile for the class of small orographic roughness and for the new formulation for larger roughness classes. Notice that the orographic component of the roughness length only in the operational scheme directly influences the diagnosed temperature (choice of the exponential or logarithmic profile). Also in winter, a small phase difference is observed between the two new formulations. The ECMWF diagnostics during the winter time is much closer to the operational one and would be even closer if the limitation for the Obuchov length would not have been introduced. Interesting is the small daily change in the atmospheric temperature, which indicates that at many gridpoints the surface and atmosphere are partially or completely de-coupled. During the summer case study, the three additional diagnostics give similar results, while the operational diagnostics shows the strong dependence on the orographic roughness length component (second row in Fig. 5.24).

### 5.9.1 Observed spatial impact on the 2 m temperature field

Figure 5.25 presents the difference between the three alternative options ("new", "new log" and "ecmwf") and the operational diagnostics for the winter case (left column, 20.12.2006, 06 UTC) and the summer case (right column, 26.07.20067, 12 UTC) over a domain covering the alpine region. In winter the main differences are clearly observed in the Alps where for the new formulation (new) warmer temperature up to 7 degrees are observed. Colder temperatures are obtained only at a few gridpoints (see for example some points over Austria). For the regions located in flat terrain the difference is smaller than 0.5 °C but nearly always positive (warmer temperatures). Compared to the operational diagnostics the option "new log" gives nearly always a warm signal. The warmer temperature are less pronounced than in the RSL profiles. The "ecmwf" option shows a larger amount of gridpoints with colder temperatures (see for example in the south eastern Switzerland, Engadin). This diagnostic scheme has some problems in case of large temperature differences and very small turbulent fluxes, suggesting a possible mismatch and inconsistency between the COSMO transfer scheme and its surface fluxes and the Monin-Obuchov related diagnostics. Finally, notice that the new diagnostics have also a warm impact over the Mediterranean sea leading to temperature differences of between 0.5 and 1 °C, where both schemes use the new logarithmic profile.

During the summer case study colder temperatures at 2 m are obtained with the two new formulations (right column in Figure 5.25). Interesting are the 3-4 °C colder temperatures in the south western part of the Alps. On the contrary, the "ecmwf" option has similar values as

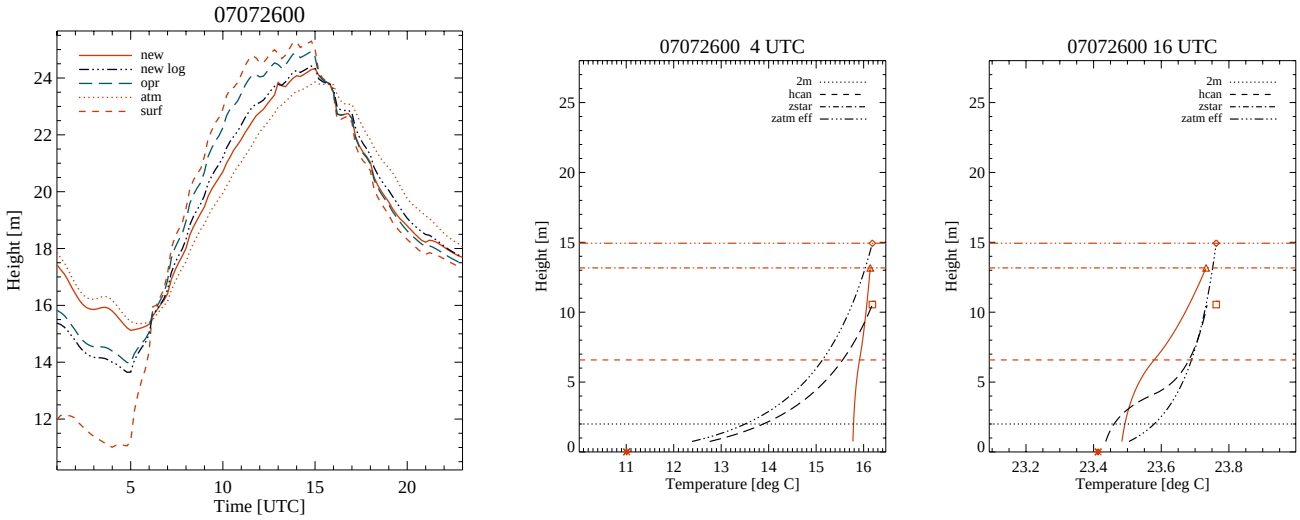


Figure 5.23: Left panel: the daily cycle of the 2 m temperature for the three diagnostics options as indicated in the legend (for the same gridpoint as the red line in Fig. 5.21). Additionally, the temperature at the surface (surf) and at the first atmospheric layer (atm) are shown. Right panels: the vertical profile for temperature on the 26.07.2007 at 4 and 16 UTC for the same diagnostics options. Additionally, the key vertical levels are indicated: the 2 m level (dotted line), the $z_*$ level (dash-dotted line), the canopy height (dashed line) and the effective height of the first atmospheric level (dashed and double dotted line). The squares ($\square$) indicate the values at the first atmospheric level, triangles ($\triangle$) at $z_*$ , diamonds ($\Diamond$) at the effective first level height $H2$ and stars ($*$) at the surface.

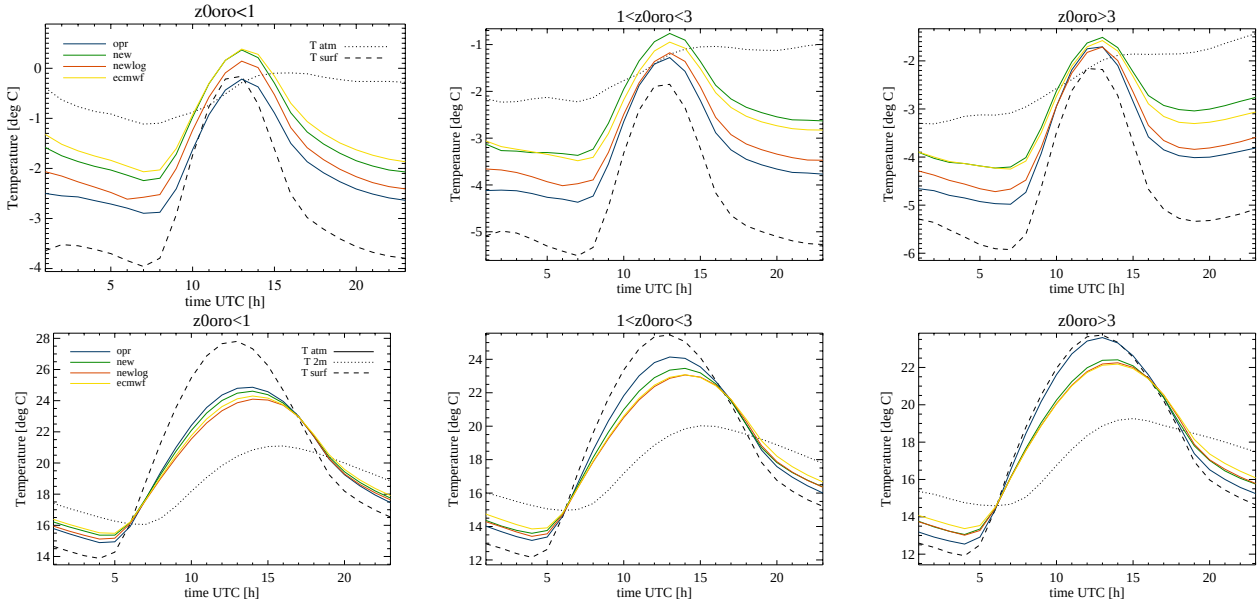


Figure 5.24: Averaged daily cycle over land for the 2 m temperature on a winter day (20.12.2007, first row) and a summer day (26.07.2007, second row). Three classes of orographic roughness lengths are distinguished (as indicated on the pictures) over a domain covering the entire Alps (as presented in Fig. 5.25). For each hour, class one (left panel) contains 2413, class two (middle panel) 2634 values and class three (right panel) 3250 values, respectively. The coloured lines are the compared options, the dotted line is the average temperature at the first atmospheric level and the dashed line the corresponding daily cycle for the surface temperature.

the operational diagnostics and a smaller general impact than the new RSL profiles and the new logarithmic option. In some regions slightly warmer temperatures are observed.

The documented problem observed in spring and in the beginning of the summer related to the snow melting (2m temperature remains nearly constant) is significantly reduced with all the three options introduced in this study (not shown). All the qualitative results presented indicate that the general cold bias during the winter time is probably significantly reduced with the new RSL profiles and the new log profile (see next section for quantitative details).

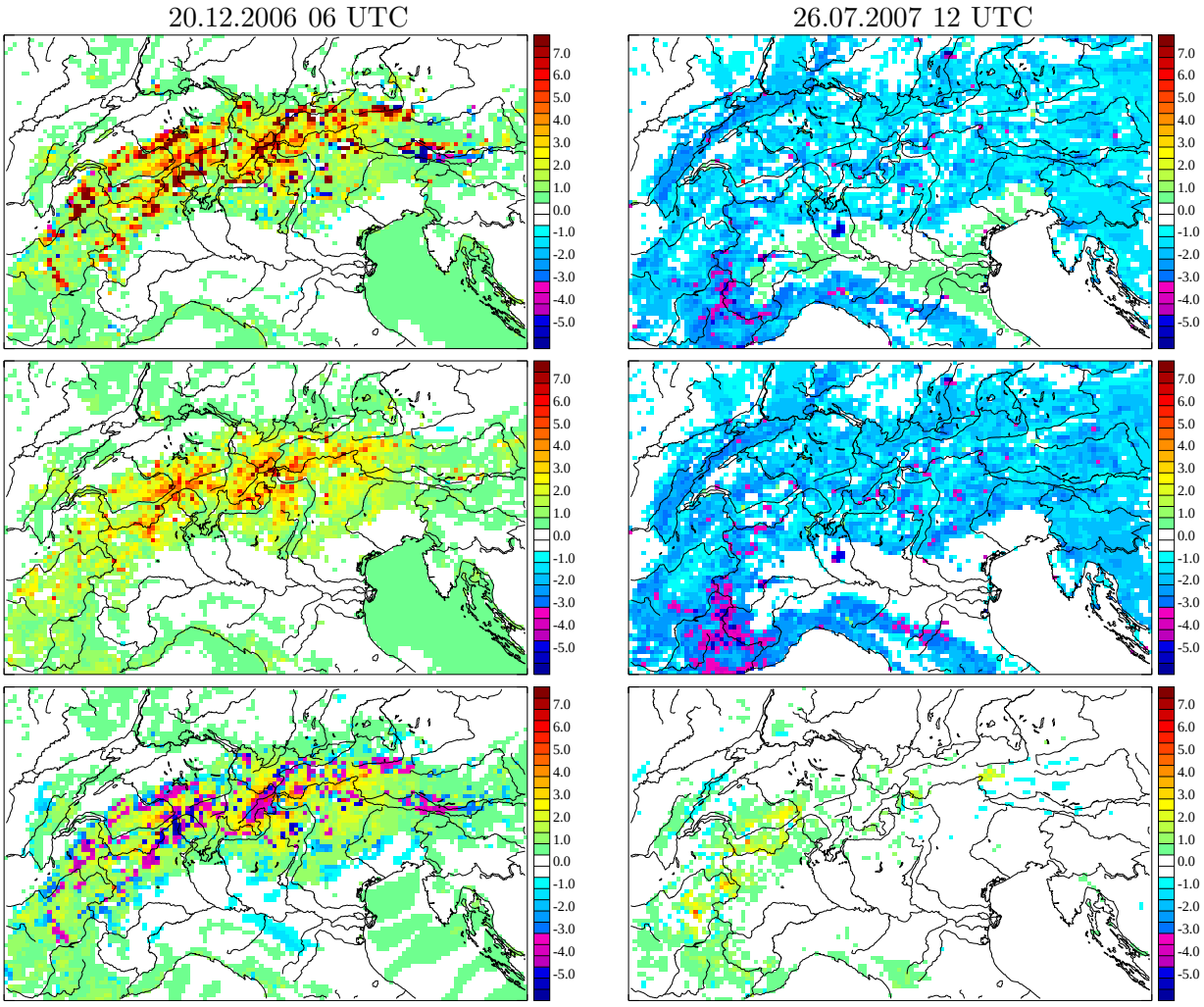


Figure 5.25: Observed impact of the three new diagnostics options on the 2 m temperature diagnostics in winter (20.12.2006, left column) and in summer (26.07.2007, right column) for COSMO 7km: difference between implemented alternatives and original diagnostics. First row new formulation (new), second row only logarithmic profile (newlog) and third row ecmwf diagnostics (ecmwf).

### 5.9.2 Verification results

In this section the verification results against SYNOP observations for 5 representative days will be presented particularly focussing on the Alps. In this domain up to 382 stations are available. The verification results of the other two domains (Switzerland and entire model domain) are given in Appendix C. Tables5.2 and 5.3 give the total performance scores for each of the 5 case studies: root mean square error (RMSE), mean error (ME), standard deviation (STDE) and correlation coefficient (CORR). Figures 5.26 and 5.27 illustrate the daily cycle of the RMSE and the ME

for the 2 m temperature and 2 m dew point, respectively. Additionally, the mean daily cycle of temperature and dew point are given in the same figure (right column).

The winter day shows a strong reduction of the RMSE and the ME for the options "newlog" and "new". The reduction of the negative bias is on the order of 0.5-0.6 °C. The improvement is even larger over the domain "Switzerland", where the RMSE is reduced up to 1.19 °C (Tab. C.1) and the ME up to 1.6 °C. On the contrary, the "ecmwf" option shows significantly smaller improvement in the RMSE and ME. All the new options, except the "ecmwf" variant, additionally have small positive effects on the standard deviation of the mean error (STDEV). The correlation is slightly reduced for the RSL profiles and the ECMWF diagnostics. The mean daily cycle of the 2 m temperature confirms the overall results (Fig. 5.26 a). The best performance is obtained with the new logarithmic profile (Fig. 5.26 a).

For the 2 m dewpoint the amelioration in terms of RMSE is smaller and the ME is even increased for all the compared options. This aspect has to be taken with particular caution (Fig. 5.27 a), as the dew point depends on the 2 m temperature and on the 2 m specific humidity. Given the 2 m temperature performance has been improved with the new schemes, the diagnostics of the 2 m specific humidity requires further investigation, because it is very likely that in the operational diagnostics the performance is better but for the wrong reason. In other words, a double error (in the temperature and in the humidity) gives as a result a better dew point. The best result for the RMSE daily cycle is given by the new logarithmic profile. Compared to the observations all the diagnostics overestimate the diurnal amplitude of the 2 m dew point. The standard deviation is slightly reduced with all new options and the correlation coefficient is slightly increased (mainly for the "newlog" profile). Notice that the winter case contrasts with the other case studies about the positive sign of the ME.

All three new diagnostics options give a positive signal in terms of RMSE for 2 m temperature during the spring case study. The RMSE reduction is largest for the new logarithmic diagnostics. The positive signal in the mean error is smaller and even absent in the ecmwf diagnostics (Table 5.2). A ME deterioration for all the three new options is observed during the morning and early afternoon (Fig. 5.26 c). All new options reach the maximum temperature about one hour later than the operational diagnostics, having a benefit on the phase error and contributing to a slightly larger correlation. The standard deviation is significantly reduced for all new options.

In spring, the 2 m dew point error is clearly reduced both in terms of RMSE and of ME. The positive ME is reduced by up to 0.5 °C. The standard deviation is slightly smaller, while the correlation is significantly larger for the new options. The better performance take place during the entire day and reaches its maximal amplitude in the late morning (Fig. 5.27 c).

The summer verification is represented by two case studies, because it gives partially contradictory results. The overall result for the new diagnostics options is positive for both cases, but in the July case the improvement is not significant (small improvement in RMSE and deterioration of the ME), while the positive impact on the RMSE in the convective case (June) is more pronounced (Table 5.2). The logarithmic diagnostics (new log and ecmwf) shows a small deterioration of the RMSE during the central part of the day and the new RSL diagnostics performance decreases in the early morning (Fig. 5.26 d). In the July case the daily cycle of the mean error gives similar results as in the spring case: deterioration in the morning and in the central part of the day for all new options. The June case shows a better performance throughout for all options during the entire day. The new options also show a reduced maximal temperature and a better timing of the maximum temperature. This aspect can better be seen for the verification over the Swiss domain where hourly data are available for each station. For the June day (Fig. C.4 b) the phase shift is about one hour, while for the July day (Fig. C.4 d) a phase shift of up to 2 hours can be observed. The standard deviation is significantly increased and the correlation is slightly larger for the new

options.

The 2 m dew point has been clearly improved for both the days either for the RMSE or for the ME. The distinct overestimation is significantly reduced in the central part of the day (Fig. **??** b and d). The improvement can be observed also in the standard deviation and in the correlation.

In the autumn case study again a significant overall improvement on the 2 m temperature achieved with the new options as can be seen in the RMSE and in the ME values. The positive impact is obtained mainly in the central part of the day (Fig. 5.26 e). However, the mean error reduction shows an exception in the first few hours of the day. The standard deviation is significantly reduced and the correlation increased with the new options. For the 2 m dew point a clear improvement in both the RMSE and ME for every part of the day is achieved with all the new options leading to a positive effect also in the standard deviation and in the correlation.

2 m temperature

| **ALPS** | **case** | **RMSE** | **ΔRMSE** | **ME** | **STDEV** | **CORR** |
|---|---|---|---|---|---|---|
| 20.12.2007 | opr | 3.40 | | -1.84 | 2.86 | 0.820 |
| | new | 3.07 | -0.33 | -1.33 | 2.77 | 0.804 |
| | newlog | 2.85 | -0.55 | -1.24 | 2.57 | 0.828 |
| | ecmwf | 3.38 | -0.02 | -1.64 | 2.96 | 0.802 |
| 18.06.2006 | opr | 3.35 | | -1.18 | 3.13 | 0.879 |
| | new | 3.08 | -0.26 | -1.25 | 2.82 | 0.889 |
| | newlog | 3.00 | -0.34 | -1.14 | 2.78 | 0.888 |
| | ecmwf | 3.04 | -0.31 | -1.18 | 2.80 | 0.884 |
| 15.04.2007 | opr | 3.88 | | -1.63 | 3.52 | 0.868 |
| | new | 3.49 | -0.38 | -1.46 | 3.18 | 0.875 |
| | newlog | 3.36 | -0.52 | -1.34 | 3.08 | 0.879 |
| | ecmwf | 3.50 | -0.38 | -1.65 | 3.09 | 0.882 |
| 26.07.2007 | opr | 2.49 | | -0.82 | 2.36 | 0.926 |
| | new | 2.47 | -0.03 | -0.91 | 2.29 | 0.931 |
| | newlog | 2.42 | -0.08 | -0.86 | 2.26 | 0.935 |
| | ecmwf | 2.42 | -0.08 | -1.04 | 2.18 | 0.939 |
| 15.10.2006 | opr | 3.49 | | -0.81 | 3.39 | 0.803 |
| | new | 3.30 | -0.19 | -0.32 | 3.28 | 0.805 |
| | newlog | 3.17 | -0.32 | -0.36 | 3.15 | 0.821 |
| | ecmwf | 3.24 | -0.25 | -0.69 | 3.17 | 0.821 |

Table 5.2: Summary of the results for the 2 m temperature verification for the domains ALPS, covering the alpine region (about 382 SYNOP stations): five days and 4 options are compared. 4 performance scores are given as well as the reduction of the root mean square error (ΔRMSE) compared to the operational diagnose (opr).

In summary, the presented verification of the new RSL profile based diagnostics and the new logarithmic interpolation profile gives very good results and a clear improvement in winter, in spring and in autumn. In summer, the signal is positive but not really large and a verification of a longer period is probably necessary to confirm the positive tendency. The ECMWF diagnostics seems to have some problems in very stable situations. Under other atmospheric conditions it gives good results. The RMSE is significantly reduced for four case studies (except one summer case) and for each of the three options (exception the "ecmwf" diagnostics in the winter case). The performance over the alpine region is increased on average by up to 0.69 °C for temperature and 0.45 °C for the dew point. All the three options have a positive effect on the phase shift of the temperature maximum delaying the peak for up to two hours. The overall best performance is

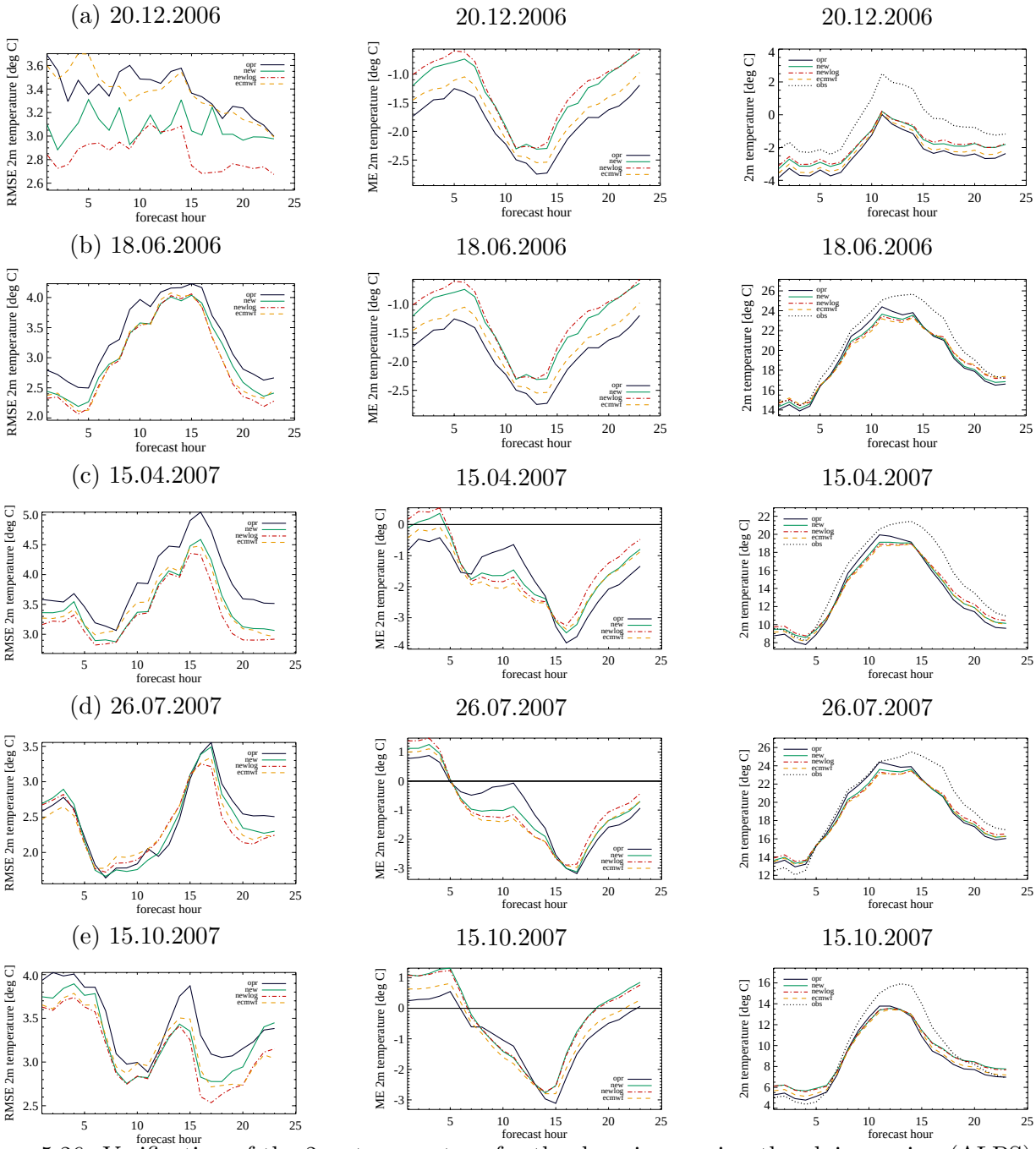


Figure 5.26: Verification of the 2 m temperature for the domain covering the alpine region (ALPS): left panel shows the daily cycle of the root mean square error (RMSE), the middle panel illustrates the daily cycle of the mean error (ME) and the right panel shows the averaged daily cycle. The plots for the others domain (Switzerland and Model domain) are presented in the appendix C.

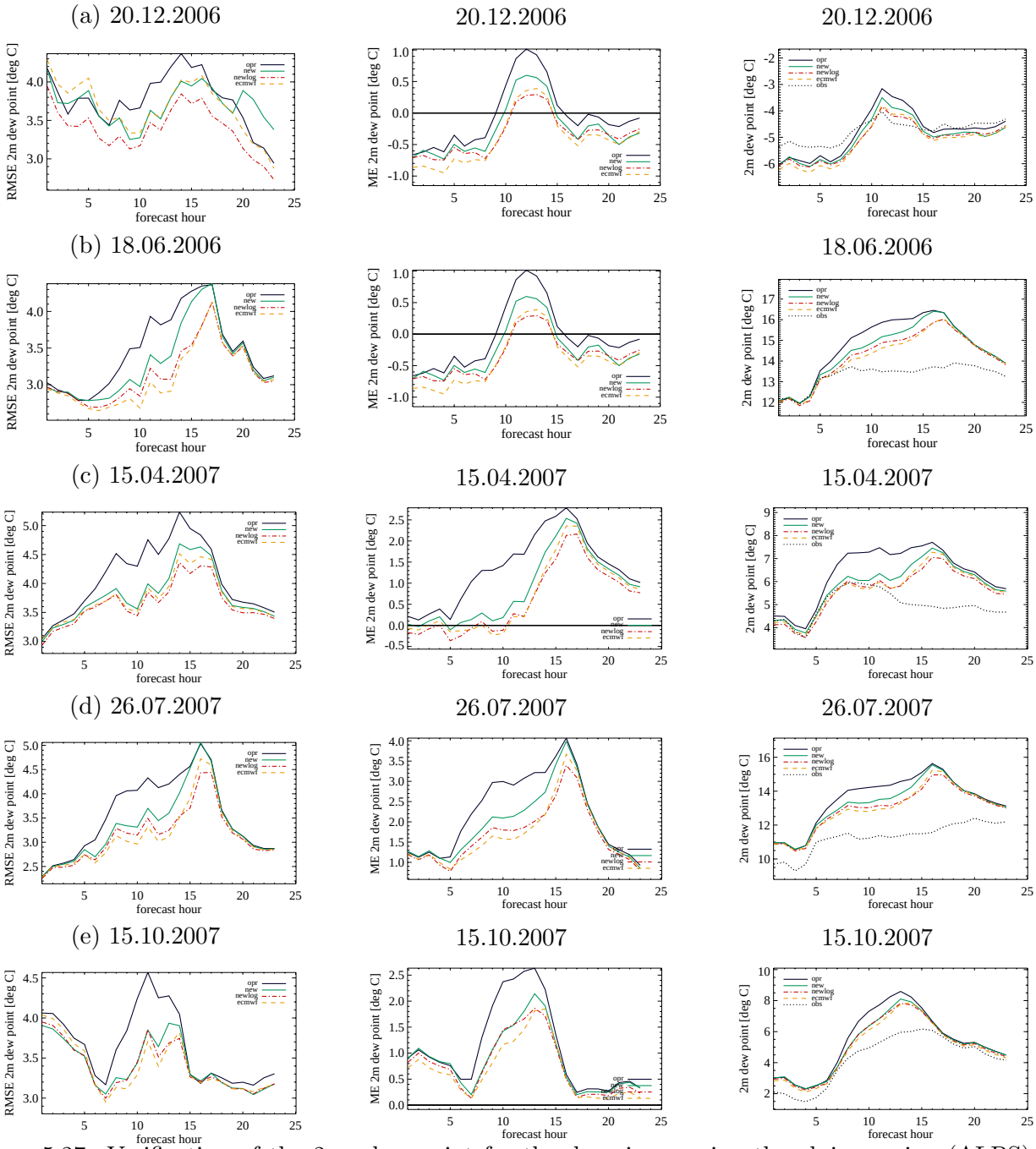


Figure 5.27: Verification of the 2 m dew point for the domain covering the alpine region (ALPS): left panel shows the daily cycle of the root mean square error (RMSE), the middle panel illustrates the daily cycle of the mean error (ME) and the right panel shows the averaged daily cycle. The plots for the others domain (Switzerland and Model domain) are presented in the appendix C.

2 m dew point

| ALPS | case | RMSE | ΔRMSE | ME | STDE | CORR |
|---|---|---|---|---|---|---|
| 20.12.2007 | opr | 3.79 | | -0.08 | 3.79 | 0.720 |
| | new | 3.73 | -0.07 | -0.27 | 3.72 | 0.738 |
| | newlog | 3.42 | -0.37 | -0.36 | 3.40 | 0.773 |
| | ecmwf | 3.70 | -0.09 | -0.43 | 3.68 | 0.749 |
| 18.08.2006 | opr | 3.48 | | 1.32 | 3.22 | 0.719 |
| | new | 3.31 | -0.17 | 1.07 | 3.13 | 0.724 |
| | newlog | 3.15 | -0.32 | 0.85 | 3.04 | 0.737 |
| | ecmwf | 3.10 | -0.37 | 0.80 | 3.00 | 0.738 |
| 15.04.2007 | opr | 4.10 | | 1.30 | 3.88 | 0.689 |
| | new | 3.78 | -0.31 | 0.82 | 3.69 | 0.724 |
| | newlog | 3.65 | -0.45 | 0.55 | 3.60 | 0.737 |
| | ecmwf | 3.72 | -0.37 | 0.63 | 3.67 | 0.726 |
| 26.07.2007 | opr | 3.60 | | 2.19 | 2.86 | 0.635 |
| | new | 3.35 | -0.25 | 1.90 | 2.76 | 0.660 |
| | newlog | 3.15 | -0.45 | 1.66 | 2.68 | 0.675 |
| | ecmwf | 3.15 | -0.45 | 1.65 | 2.68 | 0.675 |
| 15.10.2006 | opr | 3.69 | | 1.09 | 3.52 | 0.777 |
| | new | 3.45 | -0.24 | 0.86 | 3.34 | 0.801 |
| | newlog | 3.43 | -0.26 | 0.78 | 3.34 | 0.802 |
| | ecmwf | 3.43 | -0.26 | 0.68 | 3.36 | 0.800 |

Table 5.3: Summary of the results for the 2 m dew point verification for the domains ALPS, covering the alpine region (about 382 SYNOP stations): five days and four options are compared. Four performance scores are given as well as the reduction of the root mean square error (ΔRMSE) compared to the operational diagnose (opr).

given by the new logarithmic profile. The new RSL profiles are probably penalised by the generally smaller roughness lengths of most SYNOP stations, but are more realistic in the physical sense of the model world. For this reason they should be preferred.

All these positive and encouraging results should be confirmed by a verification considering a longer period in order to perform a more significant statistics.

### 5.9.3 Conditional verification considering the roughness length

The promising results of the verification motivate further analysis focussing on the performance for different roughness length classes. For the two best options (newlog and new) a verification of each roughness length class (previously presented in Tab. 5.1) has been performed. The total number of available stations in the different classes is also given in Tab. 5.1. The temperature RMSE reduction for each class with respect of the operational diagnostics is presented in Tab. 5.4 for the new RSL profiles and in Tab. 5.5 for the new logarithmic profile, respectively. The classes with local roughness length smaller than 0.1 m are treated with the same logarithmic profile for both cases, but there is a difference in the used roughness length (thermal roughness length for the version "newlog" and normal roughness length for "new"). In these two classes the improvement is similar, indicating that the impact of the thermal roughness length is not large.

The new RSL profiles perform equal or better than the new logarithmic profile for local roughness lengths of about up to 0.7-0.8 m. For larger roughnesses a small deterioration of the forecast quality is observed. These classes cover the gridpoints at which the $z_*$ level is above the effective height of the first atmospheric level. Therefore, the deterioration indicates either that this diagnostics performs worse in case of high $z_*$ (see for example the mentioned low gradient at the

| $z_{0,loc}/z_{0,oro}$ | **0.0-0.5** | **0.5-2.0** | **2.0-3.0** | **3.0-6.0** | **avg.** |
|---|---|---|---|---|---|
| **0.0-0.05** | -0.3 | -1.4 | -1.6 | -1.5 | -1.2 |
| **0.05-0.1** | 0.0 | -0.8 | -1.4 | -1.5 | -0.9 |
| **0.1-0.2** | 0.1 | -0.8 | -0.4 | -1.1 | -0.6 |
| **0.2-0.3** | 0.0 | -0.4 | -0.8 | -0.8 | -0.5 |
| **0.3-0.4** | -0.1 | -0.5 | -0.3 | -1.2 | -0.5 |
| **0.4-0.5** | -0.1 | -0.4 | -0.5 | -1.0 | -0.5 |
| **0.5-0.6** | 0.0 | 0.3 | -1.0 | -1.1 | -0.4 |
| **0.6-0.7** | 0.0 | -1.2 | -0.6 | -0.6 | -0.6 |
| **0.7-0.8** | -0.3 | 0.1 | -0.7 | -0.6 | -0.4 |
| **0.8-0.9** | 0.1 | 0.6 | 0.1 | - | 0.3 |
| **0.9-1.0** | -0.1 | -0.1 | 0.4 | 0.9 | 0.3 |
| **avg.** | -0.1 | -0.4 | -0.6 | -0.7 | -0.5 |

Table 5.4: Reduction of the temperature RMSE compared to the operational diagnostics for all the 5 case studies treated together for the new RSL profiles (new) depending on the local (rows) and orographic roughness length (columns) over the domain ALPS. A negative value indicates a RMSE reduction, while a positive one shows a deterioration. The roughness length classes are given in m. The number of stations considered for each class are given in Tab. 5.1.

matching point) or that the verification stations are not representative for such a rough model surface (see for example the SYNOP station at MeteoSwiss). In addition, the interpolation of the temperature combined with the use of the same turbulent surface flux could be inconsistent.

Excluded the two mentioned classes, the improvement is generally larger for classes with a large orographic roughness length confirming that the diagnostics error is related to this parameter. The performance of the new logarithmic profile (Tab. 5.4) is better especially in the two classes, where the new RSL profiles give a deterioration of the results. However, also with this diagnostics the improvement for these classes is smallest compared to the others. Given the fact that the "newlog" uses a "wrong" profile based only on surface layer type profile (ISL) and performs well for large $z_{0,loc}$ (deep RSL) the better performance does presumably not result from particularly well represented physics but rather from good "tuning".

## 5.10 Summary and conclusions

The 2 m temperature diagnostics in the COSMO model has been analysed and three important deficiencies have been identified: (i) a strong cold bias in winter and during stable situations in spring and autumn mainly in the alpine region, (ii) a problem in spring in combination with snow melt in the alpine region, (iii) a phase shift of the maximum temperature in the afternoon (1.5 hours too early).

All three deficiencies are partially caused by the fact that the operationally diagnosed 2 m temperature is too close to the surface temperature value. Therefore, a too small differentiation of the 2 m value from the surface value is observed.

A positive mean error in the 2 m dew point (too humid) is often observed. The derivation of the dew point has two degrees of freedom, because it depends on both the diagnostics of the 2 m temperature and 2 m specific humidity. The wet bias is partially enhanced by the diagnostics of the 2 m specific humidity, which is also too close to the surface value.

This study has focussed the attention on this main problem to validate the 2 m temperature and dew point diagnostics, which compute the 2 m quantities from an interpolation between the surface values and the values at the first model atmospheric level. Obviously, an important portion of the identified model errors cannot be related to the diagnostics itself and were not subject of this study:

| $z_{0,loc}/z_{0,oro}$ | **0.0-0.5** | **0.5-2.0** | **2.0-3.0** | **3.0-6.0** | **avg.** |
|---|---|---|---|---|---|
| **0.0-0.05** | -0.3 | -1.2 | -1.2 | -1.4 | -1.0 |
| **0.05-0.1** | 0.0 | -1.1 | -1.4 | -1.5 | -1.0 |
| **0.1-0.2** | 0.1 | -0.9 | -0.3 | -1.4 | -0.6 |
| **0.2-0.3** | -0.1 | -0.5 | -0.7 | -0.9 | -0.5 |
| **0.3-0.4** | -0.1 | -0.2 | 0.0 | -1.1 | -0.4 |
| **0.4-0.5** | -0.1 | -0.8 | -0.5 | -0.9 | -0.6 |
| **0.5-0.6** | -0.1 | 0.3 | -0.9 | -0.8 | -0.2 |
| **0.6-0.7** | 0.0 | -0.6 | -0.5 | -1.0 | -0.5 |
| **0.7-0.8** | -0.4 | 0.0 | -1.2 | -0.7 | -0.6 |
| **0.8-0.9** | -0.2 | 0.0 | -0.3 | - | -0.2 |
| **0.9-1.0** | -0.3 | -0.4 | -0.6 | 0.1 | -0.3 |
| **avg.** | -0.1 | -0.5 | -0.7 | -1.0 | -0.5 |

Table 5.5: Reduction of the temperature RMSE compared to the operational diagnostics for all the 5 case studies treated together for the new logarithmic profiles (newlog) depending on the local (rows) and orographic roughness length (columns) over the domain ALPS. A negative value indicates a RMSE reduction, while a positive one shows a deterioration. The roughness length classes are given in m. The number of stations considered for each class are given in Tab. 5.1.

aspects related to the turbulence scheme (e.g., cold bias in cases of vanishing turbulence in very stable cases), aspects of the surface transfer scheme (e.g., extremely strong tempertaure differences between surface and first atmospheric level), aspects of the snow or soil parameterization (surface energy budget over snow, soil moisture) as well as aspects of the strong topography differences between the model at 7 km horizontal resolution and reality.

The problem in the diagnostic principally occurs at gridpoints having a large orographic roughness length, which strongly influences the choice between exponential (2 m level in the canopy) and logarithmic dominance ( 2 m level above the canopy) during the interpolation in the diagnostics. In fact, gridpoints with large orographic roughness lengths exhibit only a very small phase shift between 2 m maximum and surface maximum. The unrealistically high canopy heights (up to 150 m, caused by a large total roughness length) lead to a too often use of the exponential profile even if the local roughness length would exclude large canopy elements at the surface. The exponential profile is often erroneously used, leading to a small difference of the 2 m value from the surface value.

In order to overcome the mentioned problems three alternative diagnostics have been implemented in the COSMO model and compared to the operational diagnostics: (i) a new diagnostics that introduces a special consideration of the characteristics of the roughness sublayer and that for roughness lengths larger than 0.1 m is independent from the surface value, (ii) a new diagnostics with a simple logarithmic profile similarly to the diagnostics already used in COSMO for the wind speed and (iii) the diagnostics used in the ECMWF IFS model which is also based on a logarithmic interpolation. All 3 uses only the local part of the roughness length as input variable.

A verification based on only five days indicates that all three new variants go in the right direction. All three implemented variants perform significantly better than the operational diagnostics in winter, in spring and in autumn. During the winter and under very stable conditions the ECMWF 2 m temperature diagnostics seems to have some problems and yields at some gridpoints even colder values. In summer the positive signal is not that large. The new logarithmic profile and the new roughness sublayer (RSL) profiles show improvements in terms of RMSE error up to 0.69 °C over the alpine region. If only Swiss stations are considered the reduction of the negative bias is on the order of 1°C. The new logarithmic profile seems to give the overall best results although being not physically meaningful at many gridpoints, where according to the local

roughness length large canopy elements cover the surface. Both logarithm-based interpolations use a logarithmic diagnostics also within the RSL, where a vertical profile closer to an exponential one would be expected. The better performance of the logarithmic profile should also be partially associated with the generally smaller roughness length at SYNOP stations than in many model gridpoints and with the mentioned problems in the surface temperature and surface humidity.

The improvement obtained with the new diagnostics in the 2 m dew point is on the same order of magnitude and shows that this new formulation goes in the right direction.

The combination of the logarithm-based diagnostics for small roughness lengths and the new RSL profiles in cases of large canopy elements at the surface should seriously be evaluated also for operational NWP purposes. In this assessment the additional computational costs of the new RSL profile calculation and a generalisation of the procedure for different and lower first atmospheric layers should be included.

The aspects related to the roughness length should seriously be investigated, in order to arrive at a proper separation into its two components, namely the local roughness length and the orographic roughness length, in the near future. The introduction of the local roughness length proposed in this study should be extended also to the 10 m wind diagnostics in particular for cases, where the 10 m level is below the first atmospheric level. But also in case of a prognostic computation of the 10 m wind, the subgridscale orography does probably have a large impact on the first atmospheric layers causing an underestimation of the computed wind speed in mountainous terrain. For the dynamical aspects of the roughness length a drag parameterization approach as implemented in the NWP model HIRLAM by Rontu (2006) should be evaluated.

The discussion of the error in the 2 m temperature diagnostics have permitted to highlight some other aspects of the COSMO model physics witch should be addressed in the future, in order to improve the model forecasts. The introduction of a higher resolution model (COSMO at 2.2 km resolution) will at least improve the large topographic differences between model and reality and reduce the vertical temperature adaptation that is necessary for a "proper" model verification. The large cold bias during winter time in the Alpine region and especially above snow surfaces should be further studied. The focus should be put on the surface energy balance in mountainous regions over snow covered surfaces. The role of the downward turbulent sensible heat flux should be further evaluated, although in such alpine conditions not many turbulence measurements are available to validate the physical parameterizations. As a first step, measurements taken in the Artic or over Greenland could be used (such data have already been used by Zilitinkevich and Calanca (2000) and Forrer and Rotach (1997)). Theoretical concepts based on the potential turbulent energy (Mauritsen and Svensson, 2007; Schumann and Gerz, 1995; Zilitinkevich, 2006) could help in order to overcome the problems of vanishing turbulence. Additionally, the wet signal in the boundary layer observed in spring and summer and sometimes also in autumn should be tackled by the COSMO model community starting from a measurements driven soil moisture analysis (Ament and Simmer, 2006).

# Chapter 6

# Conclusion and outlook

## 6.1 Conclusions

This study has focused on some challenging aspects of NWP modeling at high resolution in complex terrain using the COSMO model. The thesis has explored the topographic effects on radiation, tested the performance of the turbulence scheme in a semi-idealized case using the single column version, evaluated the ability of the single column model to reproduce a real diurnal cycle and analysed the deficiencies of the COSMO 2 m temperature diagnostics in the alpine region. The following main findings and conclusions can be drawn:

1. The parameterization scheme for topographical effects on radiation proposed by Müller and Scherrer (2005) has been modified and introduced into the COSMO model. The modifications make the radiation correction scheme physically more consistent for shortwave and longwave radiation. Both the gridscale and the subgridscale correction scheme have been evaluated. For the first time the radiation results in complex terrain have been compared with radiation observations for spatially distributed data. The main findings of this study are:

   i) The introduction of a parameterization scheme considering topographical effects on radiation into the COSMO model at 2.2 km horizontal resolution has a large impact on the near surface variables, as expected from observations done in complex terrain. For both the subgridscale option and gridscale option of the radiation correction scheme temperature, humidity, wind and even convective precipitation are significantly influenced by the topographical effects.

   ii) The satellite-based verification for the global radiation and the verification based on ground stations for the longwave radiation show that the radiation distribution is much more realistic. The used satellite data are also related to the inclined surfaces, i.e. the considered radiation amounts represent the real available energy, in net radiation, at the oriented and inclined location of computation. This is a very important step in order to perform a fair verification of the corrected radiation components.

   iii) The better description of the surface radiation balance has a positive effect on the 2 m temperature forecast: an improvement up to 0.15°C has been observed in winter, where the correction amount of the new scheme is also supposed to be the largest. No significant deterioration in the forecast of other meteorological fields (e.g. dew point and wind speed) has been observed.

   iv) The subgridscale radiation correction scheme performs slightly better than the gridscale scheme, indicating that even at 2.2 km horizontal resolution the subgridscale topography plays an important role. However, the gridscale scheme is much simpler to be operated.

2. The first GABLS intercomparison case (Cuxart et al., 2006) based on a shear-driven boundary layer has been used as a benchmark for testing the COSMO-SC model. In a first stage, the performance of the COSMO-SC turbulence scheme with the operational NWP configuration has been evaluated. In a second step, a parameter optimisation has been performed by a sensitivity study. The main conclusions of this study are:

   i) The COSMO-SC model in the optimised configuration performs well compared to the LES reference and the other models participating to the intercomparison.

   ii) The tests reveal that the "unphysical" minimum diffusion coefficient (1 $m^2/s$) used for operational purposes has as unavoidable consequence the loss of important PBL structures as the low level jet and increased inversion gradients. If the model is forced with the "true" surface temperature, the limitation of the diffusion coefficients is no more justified.

   iii) At high vertical resolution the closure stability functions proposed by Mellor and Yamada (1982) in their 2.5 level model and used in the COSMO-SC model in the stable case lead to unrealistic oscillations in the parameterized diffusivities in a shear-driven SBL. This occurs in cases, when the minimum diffusion coefficient is reduced as compared to the operational settings. Similar to a higher order numerical treatment of advection in the horizontal, this study has shown that also the vertical gradients cannot be safely determined from neighbouring levels alone. Rather, information from more distant levels is necessary. This study has investigated this important deficiency of the COSMO turbulence scheme and has proposed several solutions. The vertical filtering of the dimensionless gradients before the evaluation of the stability functions has demonstrated to give the best results and should be introduced.

3. The second GABLS intercomparison case (Svensson and Holtslag, 2007), based on the diurnal cycle of two days within the target time window of CASES-99 (Poulos et al., 2002), has been used as additional evaluation about the performance of the COSMO-SC turbulence scheme. This study has shown the following:

   i) The morning transition is generally poorly captured by the model and a clear underestimation of the turbulent fluxes and of the turbulent kinetic energy during daytime has been observed.

   ii) The simulation of a real case with the COSMO-SC model has highlighted the limits of the single column modelling in cases when the geostrophic wind forcing is changing with time and horizontal advection is important.

   iii) If the atmospheric simulation is coupled with the land-surface, the model results are significantly different compared to a run forced with surface observations. This means that the coupling with the soil model needs particular attention.

4. The diagnostics of the 2 m temperature and dew point in the COSMO model at 7 km horizontal resolution has been evaluated and some important deficiencies have been identified. Additionally, the performance of a new diagnostic approach and two other interpolation formulae have been compared to the present operational one. These investigations suggest the following conclusions:

   i) The analysis of the 2 m temperature diagnostics indicates that a substantial part of the observed error in the diagnosed values is due to the erroneous effects of the subgridscale roughness length. The fact that the exponential part in the interpolation between the surface and the first atmospheric layer is too often used leads - due to the often unrealistically large effective canopy height - to 2 m temperatures, which are too close to the surface value. This is the source of a significant phase error.

ii) The introduction of a new diagnostics alternative based on the local roughness length and considering some special characteristics of the roughness sublayer shows a large improvement: the RMSE error is significantly smaller and the phase error is strongly reduced. The increased performance in the 2 m temperature and 2 m dew point are much larger than that obtained with the topographic radiation correction at 2.2 km.

iii) The use of a logarithm-based diagnostics gives comparable results, although it is physically not consistent with the roughness sublayer. For this reason, the new diagnostic procedure should be preferred to any logarithmic profile in model gridcells with moderate and large roughness lengths.

## 6.2 Outlook

This study has highlighted some interesting features of the COSMO model which should be kept in mind for future research. The following recommendations for future work can be outlined:

- The interesting impact on the convective precipitation of the implemented correction schemes should be further evaluated in order to highlight the strong influence of this new parameterization scheme.
- If the present treatment of turbulence in the COSMO model would allow simulations at even higher resolution (500-1000 m), the aspects related to the three-dimensional effects of clouds should be taken seriously into account. The vertical column approximation has probably some significant constraints at such high resolutions.
- The significant background errors in the radiation parameterization in clear sky situations mainly during winter should further be investigated in order to find the physical source of the problem. The absorption coefficients of water vapour are a possible source of error in situations with low sun elevation angles (Bozzo, personal communication).
- The cold bias observed in stable situations mainly in winter should be further studied in detail. The failure of the turbulence scheme in cases of vanishing wind shear and turbulence should be further evaluated in order to avoid the artificial limitation of the turbulent diffusion coefficients. New concepts like the turbulent potential energy or additional mixing due to gravity wave drag should be considered. Besides the conceptual aspects connected with the circulation term - already implemented in the turbulence scheme (Raschendorfer, 2001) - other conceptual approaches could help to better simulate the SBL avoiding the vanishing of turbulence below a certain critical Richardson number. The turbulent potential energy and turbulent total energy concept (Mauritsen and Svensson, 2007; Schumann and Gerz, 1995; Zilitinkevich, 2006) or the introduction of additional mixing due to gravity wave drag could contribute to overcome the problem. The decoupling of the surface in a very stable SBL could also be partially avoided by introducing a minimum transfer coefficient for scalars active only in the transfer scheme. This would avoid the introduction of a too strong mixing over all the vertical extension of the model, which can strongly influence PBL structures such as the low level jet.
- The concepts of the roughness sublayer introduced in this study should also be applied for the wind forecast or diagnostics at 10 m. Here the role of the subgrid scale orography should be seriously evaluated even at 2.2 km horizontal resolution.
- The introduction of a one or more vegetation layers should be seriously taken into account in order to better describe the radiation balance near the surface and the effects of the canopy in the surface layer (e.g. a two component or non-isothermal canopy model). This is probably

much more important for simulations with COSMO in climate mode. If the vertical model resolution will be substantially increased in the near future, the lowest atmospheric layers will be fully located in the canopy, which intersect them. In this situation an additional approach to the current resistances limited to the transfer layer (from the surface to the first atmospheric layer) has to be considered. In such situations the model equations or at least the subgridscale turbulence fluxes should be adapted by integrating and evaluating the concept of flow through a porous medium, as already partially implemented in the COSMO turbulence scheme but still not used. Additionally, also the typical effects of canopy such as moisture release and heat storage or absorption should be vertically distributed. This can only be done if additional information about the characteristics of the canopy at the surface are available (e.g., type, height, density).

- The parameterization of the surface drag should be separated from the local roughness length in order to avoid problems in the diagnostic. A surface drag parameterization as implemented in HIRLAM by Rontu (2006) should be evaluated. At least for diagnostic purposes the local roughness length should be operationally introduced.

- The introduction of the local roughness length and the observed significant impact on the diagnostics suggests that an accurate surface description is necessary. The used external parameters in the COSMO model show a moderately poor quality of the surface description. This aspect is even more important if in the near future the horizontal resolution will be further increased.

# Appendix A

# The non-hydrostatic limited-area NWP model COSMO

The COSMO model is a limited area numerical weather prediction model (formerly known as "Lokal-Modell" LM in Germany or "Alpine Model" aLMo in Switzerland) initially developed at the "Deutscher Wetterdienst" (DWD) (Steppeler et al., 2003) and thereafter in the framework of the COSMO consortium (Consortium for Small-scale Modelling). A 7 km (since 2001) and a 2.2 km version (since 2008) is operationally used by MeteoSwiss for numerical weather prediction (NWP). In the following sections a short model overview essentially based on the model documentation ((Doms and Schättler, 2003a, 2002, 2003b; Doms et al., 2005; Doms and Schättler, 2002; Doms and Förstner, 2003)) is presented.

## A-1 Dynamics and numerics

The COSMO model is a non-hydrostatic limited-area prediction model based on the primitive hydro-thermodynamical equations in advection form for a fully compressible moist atmosphere without any scale approximations. The COSMO model is designed for meso-$\beta$ and meso-$\gamma$ scales where hydrostatic effects begin to play an essential role in the evolution of atmospheric flows. A horizontally homogeneous, vertically stratified and in hydrostatic balance basic state in a time independent dry atmosphere at rest is defined. This is subtracted from the equations, in order to reduce numerical errors associated with the calculation of the pressure gradient force in case of sloping coordinate surfaces. The continuity equation is replaced by a prognostic equation for the perturbation pressure, i.e. the deviation of pressure from the reference state. The model equations are formulated with respect to a rotated lat/lon-grid with coordinates $(\lambda, \varphi)$. The rotated coordinate system results from the geographical $(\lambda_g, \varphi_g)$ tilting of the north pole. In the vertical a generalised height-based terrain following coordinate $\zeta$ is used (Gal-Ghen et al., 1975). Since $\zeta$ doesn't depend on time, the $(\lambda, \varphi, \zeta)$-system represents a non-deformable coordinate system, where the surfaces of constant $\zeta$ are fixed in space.

By transforming the primitive hydro-thermodynamical equations from the $(\lambda, \varphi$,z) to the $(\lambda, \varphi, \zeta)$ coordinate system and subtracting the basic state, a set of 7 prognostic model equations is achieved: the three components of the wind vector $(u,v,w)$, the perturbation pressure $p'$, the temperature $T$ and the humidity variables $q^{l,f}$ (liquid, frozen).

$$\frac{\partial u}{\partial t} + \vec{v}\nabla u - \frac{uv}{a}\tan\varphi - fv = -\frac{1}{\rho a cos\varphi}\left(\frac{\partial p'}{\partial \lambda} + \frac{J_\lambda}{\sqrt{G}}\frac{\partial p'}{\partial \zeta}\right) + M_u \tag{A.1}$$

$$\frac{\partial v}{\partial t} + \vec{v}\nabla v - \frac{u^2}{a}\tan\varphi + fu = -\frac{1}{\rho a}\left(\frac{\partial p'}{\partial \varphi} + \frac{J_\varphi}{\sqrt{G}}\frac{\partial p'}{\partial \zeta}\right) + M_v \tag{A.2}$$

$$\frac{\partial w}{\partial t} + \overrightarrow{v}\nabla w = \frac{1}{\rho\sqrt{G}}\frac{\partial p'}{\partial \zeta} + B + M_w \tag{A.3}$$

$$\frac{\partial p'}{\partial t} + \overrightarrow{v}\nabla p' - g\rho_0 w = -\left(\frac{C_{pd}}{C_{vd}}\right) pD + (\frac{C_{pd}}{C_{vd}} - 1)\rho C_{pd} Q_T \tag{A.4}$$

$$\frac{\partial T}{\partial t} + \overrightarrow{v}\nabla T = \frac{1}{\rho C_{pd}}\left(\frac{\partial p'}{\partial t} + \overrightarrow{v}\nabla p' - g\rho_0 w\right) + Q_T \tag{A.5}$$

$$\frac{\partial q^v}{\partial t} + \overrightarrow{v}\nabla q^v = -(S^l + S^f) + M_{q^v} \tag{A.6}$$

$$\frac{\partial q^{l,f}}{\partial t} + \overrightarrow{v}\nabla q^{l,f} = +\frac{1}{\rho\sqrt{G}}\frac{\partial P_{l,f}}{\partial \zeta} = S^{l,f} + M_{q^{l,f}} \tag{A.7}$$

$J_\lambda$,$J_\varphi$,$J_\zeta$ are the three elements of the inverse Jacobian matrix, which permits the coordinate transformation from the orthogonal $(\lambda, \varphi, z)$-system to the terrain following $(\lambda, \varphi, \zeta)$-system.

$$J_\lambda = \left(\frac{\partial z}{\partial \lambda}\right)_\zeta, J_\varphi = \left(\frac{\partial z}{\partial \varphi}\right)_\zeta, J_\zeta = \frac{\partial z}{\partial \zeta} = -\sqrt{G}. \tag{A.8}$$

$a$ is the radius of the earth, $C_{pd}$ and $C_{vd}$ are the specific heat of dry air at constant pressure and constant volume, $g$ is the gravity acceleration, $f$ is the Coriolis parameter, $\rho$ is the density of moist air, which is calculated as a diagnostic variable from the equation of state.

$$\rho = \frac{1}{p\left[R_d\left(1 + \left(\frac{R_v}{R_d} - 1\right)q^v - q^l - q^f\right)T\right]} \tag{A.9}$$

$\rho_0$ is the reference density and $p'$ the perturbation pressure. $q^v$ is the specific humidity, $q^l$ represents the specific water content of a category of liquid water (cloud or rain water) and $q^f$ represents the specific water content of a category of frozen water (cloud ice or snow). The corresponding fluxes are denoted by $P_l$ and $P_f$. The terms $M_u, M_v, M_w, M_{q^v}, M_{q^{l,f}}$ denote the subgrid-scale processes as e.g. turbulence and convection and $Q_T$ summarises the diabatic heating rate due to these processes. Clearly, the scale of these non-resolved processes depends on the domain for averaging, i.e. on the grid spacing that is used to solve the model equations by finite differencing. The larger the grid spacing the more organised non-turbulent processes are to be included. The M-terms are essentially splitted into two parts: small scale turbulent diffusion (driven by the turbulent diffusion coefficients $K_H$ and $K_M$) and organised subgid scale moist convection (if deep convection is supposed to be parameterized).

The various sources and sinks in the equations for the humidity variables due to microphysical processes of clouds and precipitation formation are denoted by $S^l$ and $S^f$. The calculation of all these terms related to the sub-grid-scale processes is done by the physical parameterization schemes. The term B in the equation for the vertical velocity is the buoyant acceleration given by

$$B = g\frac{\rho_0}{\rho}\left[\frac{T - T_0}{T} - \frac{p'T_0}{p_0 T} + \left(\frac{R_v}{R_d} - 1\right)q^v - q^l - q^f\right] \tag{A.10}$$

The advection operator in terrain-following coordinates is defined as

$$\overrightarrow{v}\nabla = \frac{1}{acos\varphi}\left(u\frac{\partial}{\partial \lambda} + vcos\varphi\frac{\partial}{\partial \varphi}\right) + \dot{\zeta}\frac{\partial}{\partial \zeta} \tag{A.11}$$

where $\dot{\zeta}$ is the contravariant vertical velocity in the $\zeta$-system:

$$\dot{\zeta} = \frac{1}{\sqrt{G}}\left(\frac{J_\lambda}{acos\varphi}u + \frac{J_\varphi}{a}v - w\right) \tag{A.12}$$

D is the three dimensional wind divergence, which is calculated from

$$D = \frac{1}{acos\varphi}\left[\frac{\partial u}{\partial \lambda} + \frac{J_\lambda}{\sqrt{G}}\frac{\partial u}{\partial \zeta} + \frac{\partial}{\partial \varphi}(vcos\varphi) + cos\varphi\frac{J_\varphi}{\sqrt{G}}\frac{\partial v}{\partial \zeta}\right] - \frac{1}{\sqrt{G}}\frac{\partial w}{\partial \zeta} \tag{A.13}$$

The traditional equations for terrain following coordinates in a rotated lat-lon system presented before (from Eq. A.1 to Eq. A.7) are applied in COSMO in a slightly modified form. Three main aspects are changed:

i) The metric terms of the $\zeta$-system, $\sqrt{G}$, $J_\lambda$ and $J_\varphi$ are formulated in terms of base-state variables $p_0$ and $\rho_0$.

ii) The terms of the horizontal advection in the equation for $u$ and $v$ are combined with the metric term involving $tan\varphi$ and with the Coriolis term, and formulated in terms of kinetic energy of horizontal motion. Additionally, the vertical components of the absolute vorticity are defined as mass specific quantities.

iii) In the equation for the pressure perturbation the source term due to diabatic heating is neglected.

The final set of the COSMO model equations with these introduced modifications can be found in Doms and Schättler (2003a).

The three-dimensional fully elastic and non-hydrostatic atmospheric equations are solved numerically with second order or third order finite difference methods on a Arakawa-C/Lorenz grid (Arakawa and Lamb, 1977) based on a rotated geographical (lat/lon) coordinate system. In the vertical a stretched terrain-following grid after Gal-Ghen et al. (1975) is used and an option for the SLEVE vertical grid is available (Schär et al., 2002). In the recent past the commonly used numerical solver was based on the Leapfrog time integration scheme (three-time-level scheme with centered differences, horizontally explicit, vertically implicit), which is a variant of the numerical scheme proposed by Klemp and Wilhelmson (1978) with the extensions proposed by Skamarock and Klemp (1992). Since 2004 a new numerical solver has been added as option and since 2007 it is used for operational purposes mainly for high-resolution simulations. The new numerical core is based on a Runge-Kutta time integration scheme (Wicker and Skamarock, 1998; Förstner and Doms, 2003), which uses a two time level. The original Runge-Kutta integration scheme has been modified to a third-order upwind formulation and a fifth-order horizontal advection formulation, as suggested by Wicker and Skamarock (2002). In the near future this new numerical solver will fully substitute the Leapfrog scheme. The 3-D precipitation transport is also considered by the introduction of advection for the mixing ratios (liquid water, snow and ice). The lateral boundaries are treated with a one-way nesting from a driving model using the lateral boundary formulation according to Davies (1976). At the boundaries and for initialisations purposes the global model IFS of the European Centre for Medium Range Forecast (ECMWF) is used.

## A-2 Physical parameterizations

The physics package of COSMO considers 6 main components: radiation, precipitation microphysics, convection, soil and surface processes, turbulence in the atmosphere and turbulent transport at the surface (Doms et al., 2001, 2005).

- Radiation: The radiation fluxes are parameterized with the $\delta$-two-stream radiation scheme after Ritter and Geleyn (1992). For short (direct and diffuse) and long-wave fluxes eight spectral intervals as well as a constant aerosol distributions subdivided in four classes are

employed. The radiation at the surface is calculated on a horizontal plane. The radiation parameterization can be optionally adapted to complex-terrain conditions with a correction scheme at the surface, which considers sky-view, slope angle, slope aspect and shadowing effects. In the operational suite at 7 km the radiation scheme is called only once a hour, while at 2.2 km the radiation calculation are performed each 15 minutes.

- Grid-scale clouds and precipitation microphysics: cloud water condensation and evaporation are calculated by saturation adjustment. Precipitation formation is modelled by a bulk microphysics parameterization including water vapour, cloud water, rain, snow, ice and optionally graupel (Reinhardt and Seifert, 2006; Kessler, 1969). The 3-D precipitation transport is also considered by the introduction of a prognostic equation for the mixing ratios considering advection.

- Moist convection: As default the Tiedke (1989) mass-flux convection scheme with equilibrium closure based on moisture convergence is used. As options the Kain-Fritsch (Kain and Fritsch, 1993) and the Bechtold convection scheme (Bechtold et al., 2001) are available. At 2.2 km horizontal resolution deep convection is supposed to be explicitly resolved and the deep convection scheme is switched off leaving running only the shallow convection part.

- Soil processes: two different soil models can optionally be used. A 2 layers model after Jacobsen and Heise (1982) and a multilayers model after Schrodin and Heise (2001) are available.

- Surface transfer: The surface transfer scheme is based on transfer resistances for three sublayers from the rigid surface to the first atmospheric model layer (Raschendorfer, 2001, 2007a; Raschendorfer and Mironov, 2001). The parameterization uses a TKE scheme with a 1.5-order turbulence closure as in the atmosphere (see section B-1).

- Turbulent transport: The vertical turbulent transport is formulated with a TKE scheme following the 1.5 order turbulence closure at the hierarchy level 2.5 proposed by Mellor and Yamada (1982) in the framework of their hierarchical model (Mellor and Yamada, 1974) and formulated considering subgridscale clouds and their interaction with turbulence (Doms et al., 2001; Raschendorfer, 2007a, 2001). The subgridscale humidity fluctuations are determined with a statistical cloud scheme after Someria and Deardoff (1976). The closure stability functions for unstable conditions are modified compared to the original work of Mellor and Yamada (1982). Optionally, the vertical turbulent diffusion coefficients can be used horizontally in a modified form if the three-dimensional turbulence framework is used. For more details see subsections B-2.

## A-3 Data assimilation

The COSMO model at MeteoSwiss uses a data assimilation system based on a nudging technique (Schraff, 1997) also known as Newtonian relaxation. This method consists of relaxing the model's prognostic variables toward prescribed values within a predetermined time window. A detailed description can be found in Athens (1974), Davies and Turner (1977) and Stauffer and Seeman (1990). The nudging is performed in the COSMO model towards direct observations. For high resolution simulations (e.g. at 2.2 km) also the assimilation of radar reflectivity is possible with the latent heat nudging technique, which has been revisited by Leuenberger and Rossa (2007).

## A-4 Single column model (COSMO-SC)

Since 2007 a single column version of the COSMO model is available. The single column COSMO-SC model works in a hydrostatic environment and uses terrain following hybrid pressure levels. The same physical parameterizations of the NWP model COSMO are available and several forcings such as the geostrophic forcing or large scale subsidence (vertical advection) can be applied (Raschendorfer, 2007b).

# Appendix B

# COSMO boundary layer parameterizations

The following description of the boundary layer parameterization is essentially based on the unpublished work of Matthias Raschendorfer of the Deutsche Wetterdienst (DWD), who developed the parameterization schemes for turbulence and surface transfer (Raschendorfer, 2007a, 2001; Raschendorfer and Mironov, 2001; Doms et al., 2001; Wacker et al., 2005). The COSMO turbulence scheme for vertical turbulent transport is based on a 1.5 order turbulence closure after Mellor and Yamada (1982) at the hierarchy level 2.5 (Mellor and Yamada, 1974), resulting from the combination between a traditional K-closure and a prognostic equation for turbulent kinetic energy (TKE). This Reynolds stress model and its modifications have been widely used in meteorological and oceanographic applications (Galperin et al., 1988; Galperin and Kantha, 1989; Galperin and Mellor, 1991; Kantha and Clayson, 1994; Kantha, 2003; Janjic, 2001, 1990, 1994; Burk and Thompson, 1989). The surface transfer scheme is formulated in the framework of this TKE-scheme. The turbulence scheme can optionally be extended beyond the (Mellor and Yamada, 1982) 2.5 level scheme in order to account for the effects of roughness elements on the turbulent flow in the lower part of the boundary layer. However, this option is not yet fully tested.

## B-1 Turbulence scheme

### B-1.1 General aspects

In order to numerically solve the prognostic budget equations of an atmospheric circulation model, differentiation operators have to be approximated on a discrete numerical grid by the use of interpolation formulae. As those approximations can only be realistic, if the variable fields are smooth with respect to the scale of grid resolution, equations of filtered variable fields have to be solved (a filter operator has to be added). When the equations of motion are averaged over a grid-cell volume within a numerical weather prediction model, turbulence terms appear such as those for divergence of turbulent fluxes (Stull, 1988, 1994). The filtered budget equations for a mass-specific quantity $(q, \theta, u, v, w)$ can be written with the corresponding locally unresolved (sub-grid) fluctuation from the grid-cell mean $\phi' = \phi - \Phi$ following the Mellor and Yamada (1982) notation. The equations for the conservation of mass (continuity equation), the ensemble mean

velocity U and the potential temperature $\Theta$ modified from Mellor and Yamada (1982) are:

$$\frac{\partial \rho}{\partial t} + \frac{\partial \rho U_i}{x_i} = 0 \tag{B.1}$$

$$\rho \frac{\partial U_j}{\partial t} + \rho U_k \frac{\partial U_j}{\partial x_i} + \rho \frac{\partial \overline{u_k' u_j'}}{\partial x_k} + \rho \epsilon_{jkl} f_k U_l + (R_{vol}^{U_j} + R_{mol}^{U_j}) = -\frac{\partial P}{\partial x_j} - g_j \rho + \rho \nu \frac{\partial^2 U_j}{\partial^2 x_k} \tag{B.2}$$

$$\rho \frac{\partial \Theta}{\partial t} + \rho U_k \frac{\partial \Theta}{\partial x_k} + \rho \frac{\partial \overline{u_k' \theta'}}{\partial x_k} + (R_{vol}^{\Theta} + R_{mol}^{\Theta}) = \rho \alpha \frac{\partial^2 \Theta}{\partial^2 x_k} \tag{B.3}$$

Uppercase letters represent ensemble mean variables, whereas lowercase letters with apostrophe are the turbulent fluctuation variables (notice the difference with the previous chapters). $g_j = (0, 0, -g)$ is the gravity vector, $f_j = (f_x, f_y, 0)$ the Coriolis parameter, $\nu$ the kinematic viscosity and $\alpha$ the kinematic heat conductivity (or thermal diffusivity). $R_{vol}^{\phi}$ and $R_{mol}^{\phi}$ are the body-air interaction related terms, which consider the effect of canopy elements (roughness elements) on the momentum and potential temperature equation. Due to the Bousinnessq approximation density fluctuations are neglected except in the buoyancy term. Density fluctuations are written in the following discussion as $\beta\theta$, where $\beta$ is the coefficient of thermal expansion. The inclusion of a moist atmosphere with phase changes will be postponed to a later step in this chapter. In a moist atmosphere an additional conservation equation for moisture is necessary. Note that in Eq. B.3 a radiative flux divergence term should appear. Here, radiative affects are not considered but are an important tendency in the COSMO model equations. For the second order moments, also known as turbulent fluxes, $\overline{u_k' u_j'}$ and $\overline{u_k' \theta'}$ appearing in Eq. B.2 and B.3, new budget equations have to be written. If no further equations are desired, these terms have to be parameterized. In a traditional framework of a first-order closure the second order moments are assumed to be equal to a constant factor K, called turbulent exchange coefficient or turbulent transfer coefficient, multiplied with the local gradient of the quantity. This closure approximation is often called gradient transport theory or K-theory. Due to its simplicity it often fails in presence of large eddies in the flow (Stull, 1988). The turbulent exchange coefficient is generally assumed to be different for vector (wind components, $K_M$) and scalar quantities (heat and moisture, $K_H$).

$$\overline{u_k' u_j'} = -K_M \left( \frac{\partial U_j}{\partial x_j} \right) \tag{B.4}$$

$$\overline{u_k' \theta'} = -K_H \left( \frac{\partial \Theta}{\partial x_j} \right) \tag{B.5}$$

$$\overline{u_k' q_v'} = -K_H \left( \frac{\partial Q_v}{\partial x_j} \right) \tag{B.6}$$

$$\tag{B.7}$$

In order to overcome the above mentioned limitations of the first-order closure, caused mainly by the constant values of K, more complicated parameterizations have been proposed. K is generally assumed to be directly or indirectly dependent from the air stability and the intensity of the turbulence in the boundary layer. In addition, also information about the length scale of the turbulent transfer process following the general concept of the mixing length are often included. The parameterization proposed by Mellor and Yamada (1982) in their 1.5-order closure model, defines K as dependent on a turbulence length scale $\lambda_l$ (or mixing length), the prognostic turbulent velocity scale $q = \sqrt{2 \cdot e}$ (where e is the turbulent kinetic energy TKE/$m$) and on the stability functions $S_M$ for vector and $S_H$ for scalar variables, respectively.

$$K_M = q \lambda_l S_M \tag{B.8}$$

$$K_H = q \lambda_l S_H \tag{B.9}$$

A prognostic equation for the turbulent kinetic energy (TKE), a formula for the turbulence length scale $\lambda_l$ as well as a definition for the stability functions $S_M$ and $S_H$ are now needed.

i) The TKE per mass unit is defined as:

$$e = \frac{\text{TKE}}{m} = 0.5 \cdot (\overline{u'^2} + \overline{v'^2} + \overline{w'^2})$$

$\frac{\text{TKE}}{m}$ can be rewritten with the summation notation as $e = 0.5 \cdot \overline{u_i'^2} = 0.5 \cdot q^2$. q is the so called turbulent velocity scale. The conservation equation for the turbulent kinetic energy, a special second order moment equation, modified from Stull (1988) has following form:

$$\underbrace{\frac{\partial e}{\partial t}}_{1} \underbrace{+U_k \frac{\partial e}{\partial x_k}}_{2} = \underbrace{-\beta g_i \overline{u_i' \theta_\nu'}}_{3} \underbrace{-\overline{u_i' u_k'} \frac{\partial U_i}{\partial x_k}}_{4} \underbrace{-\frac{\partial (\overline{u_k' e})}{\partial x_k}}_{5} \underbrace{-\frac{1}{\bar{\rho}} \frac{\partial (\overline{u_i' p'})}{\partial x_i}}_{6} \underbrace{+ (R^e_{vol} + R^e_{mol})}_{7} \underbrace{-\epsilon}_{8} \qquad \text{(B.10)}$$

Where:

1. local storage or tendency of TKE
2. advection of TKE by the mean wind
3. buoyant production or damping term
4. mechanical shear production term
5. turbulent transport of TKE
6. pressure correlation term
7. volume reduction term and molecular flux towards the body surfaces
8. dissipation

$\Theta_\nu = \Theta \left[1 + (\frac{R_d}{R_\nu}) Q_v - Q_l\right]$ is the virtual potential temperature and $R_d$, $R_\nu$ are the specific gas constants for dry air and water vapour, respectively. This equation can easily be transformed in a budget equation for $q = \sqrt{2e}$. The fifth term of TKE-equation B.10 contains the undesidered third order moment $\overline{u_k' e}$, which represents the subgrid-scale turbulent transport of turbulent kinetic energy. In a 1.5-order closure model, this term has to be parameterized.

ii) The simplest way to to prescribe the turbulent length scale is by an algebraic equation. In doing so, one makes use of the widely accepted fact that the turbulence macroscale in a boundary layer on a solid surface is simply proportional to the distance from the surface. Blackadar (1962) proposed following formula:

$$\lambda_l = \lambda_l^\infty \frac{\kappa z}{\kappa z + \lambda_l^\infty} \qquad \text{(B.11)}$$

$\kappa$ is the von Karman constant (set to 0.4), z is the distance from the surface and $\lambda_l^0$ is the asymptotic value of $\lambda_l$ for high altitudes in the boundary layer. An overview about the so far used equations for the length scale in turbulence models is given by Kantha (2004).

iii) The stability functions $S_M$ and $S_H$ are derived as closure functions from the simplification of second order moments equations. This procedure will be presented in the next section.

**The turbulent fluxes**

Once that the turbulent diffusion coefficients have been calculated, it is possible to calculate the turbulent fluxes at each model grid point for heat (sensible heat, H), moisture (latent heat, LH) and momentum ($Mo_U$ and $Mo_V$):

$$H = -\rho C_{pd} K_H \frac{\partial \Theta}{\partial z} \tag{B.12}$$

$$LH = -\rho L_v K_H \frac{\partial Q}{\partial z} \tag{B.13}$$

$$Mo_U = -\rho K_M \frac{\partial U}{\partial z} \tag{B.14}$$

$$Mo_V = -\rho K_M \frac{\partial V}{\partial z} \tag{B.15}$$

This definition of the turbulent fluxes is only valid for a Cartesian coordinate system. Nevertheless, the same turbulent diffusion coefficients are used to compute the turbulent diffusion components of the subgrid scale mixing terms (or gradients of the vertical turbulent fluxes in the COSMO coordinate system) in the main model set of equations. The COSMO model equation are written in geographic terrain following coordinates (Doms and Schättler, 2003a).

$$M_T = \frac{1}{\rho\sqrt{G}} \frac{\partial}{\partial \zeta} \left( \frac{\rho \pi K^H}{\sqrt{G}} \frac{\partial \Theta}{\partial \zeta} \right) \tag{B.16}$$

$$M_Q = \frac{1}{\rho\sqrt{G}} \frac{\partial}{\partial \zeta} \left( \frac{\rho K^H}{\sqrt{G}} \frac{\partial Q}{\partial \zeta} \right) \tag{B.17}$$

$$M_U = \frac{1}{\rho\sqrt{G}} \frac{\partial}{\partial \zeta} \left( \frac{\rho K^M}{\sqrt{G}} \frac{\partial U}{\partial \zeta} \right) \tag{B.18}$$

$$M_V = \frac{1}{\rho\sqrt{G}} \frac{\partial}{\partial \zeta} \left( \frac{\rho K^M}{\sqrt{G}} \frac{\partial V}{\partial \zeta} \right) \tag{B.19}$$

$$M_W = 0 \tag{B.20}$$

Here $\sqrt{G}$ is the contravariant vertical velocity $\frac{\partial \psi}{\partial z}$ or Jacobian (Eq. A.8). $\pi$ denotes the Exner pressure function.

### B-1.2 The turbulence closure and its assumptions

Start point for the solution of the closure problem are the second order moments, described by the following 2 equations:

$$\begin{aligned} &\frac{\partial \overline{u_i' u_j'}}{\partial t} + U_k \frac{\partial \overline{u_i' u_j'}}{\partial x_k} \\ &\quad + \frac{\partial \overline{u_k' u_i' u_j'}}{\partial x_k} - \nu \frac{\partial^2 \overline{u_i' u_j'}}{\partial^2 x_k} + \frac{\partial \overline{p' u_i'}}{\partial x_i} + \frac{\partial \overline{p' u_i'}}{\partial x_j} + f_k(\epsilon_j k l \overline{u_i' u_j'} + \epsilon_i k l \overline{u_l' u_j'}) + \left( R_{vol}^{\overline{u_i' u_j'}} + R_{mol}^{\overline{u_i' u_j'}} \right) \\ &\quad = \overline{u_k' u_i'} \frac{\partial U_j}{\partial x_k} - \overline{u_k' u_j'} \frac{\partial U_i}{\partial x_k} - \beta(g_j \overline{u_i' \theta'} + g_i \overline{u_j' \theta'}) + \overline{p' \left( \frac{\partial u_i}{\partial x_j} \frac{\partial u_j}{\partial x_i} \right)} - 2\nu \overline{\frac{\partial u_i}{\partial x_k} \frac{\partial u_j}{\partial xk}} \end{aligned} \tag{B.21}$$

$$\frac{\partial\overline{u_i'\theta'}}{\partial t} + U_k\frac{\partial\overline{\theta' u_j'}}{\partial x_k} + \frac{\partial\overline{u_k' u_j'\theta'}}{\partial x_k} - \alpha\frac{\partial}{\partial x_k}\overline{u_j'\frac{\partial\theta'}{\partial x_k}} - \nu\frac{\partial}{\partial x_k}\overline{\theta'\frac{\partial u_j'}{\partial x_k}} + \frac{\partial\overline{p'\theta'}}{\partial x_j} + \overline{p'\frac{\partial\theta'}{\partial x_j}} + \epsilon_j k l f_k\overline{u_l'\theta'} + \left(R_{vol}^{\overline{u_i'\theta'}} + R_{mol}^{\overline{u_i'\theta'}}\right) = \overline{u_j' u_k'}\frac{\partial\Theta}{\partial x_k} - \overline{\theta' u_k'}\frac{\partial U_j}{\partial x_k} - \beta g_j\overline{\theta'^2} - (\alpha+\nu)\overline{\frac{\partial u_j}{\partial x_k}\frac{\partial\theta'}{\partial x_k}} \quad \text{(B.22)}$$

Equation B.22 involves $\overline{\theta'^2}$, for which an equation has to be written.

$$\frac{\partial\overline{\theta'^2}}{\partial t} + U_k\frac{\partial\overline{\theta'^2}}{\partial x_k} + \frac{\partial\overline{u_k\theta'^2}}{\partial x_k} - \alpha\frac{\partial^2\overline{\theta'^2}}{\partial^2 x_k} + \left(R_{vol}^{\overline{\theta'^2}} + R_{mol}^{\overline{\theta'^2}}\right) = -2\overline{u_k\theta'^2}\frac{\partial\Theta}{\partial x_k} - 2\alpha\overline{\frac{\partial\theta'}{\partial x_k}\frac{\partial\theta'}{\partial x_k}} \quad \text{(B.23)}$$

When attempting to write equations for the second order moments, new turbulence unknowns lead to even more unknowns - a dilemma known as the closure problem. In fact, third order moments and additional volume and surface terms apper into the second order budget equations. These terms have to be parameterized.

For turbulent motions the COSMO turbulence scheme introduces the following simplifications or parameterizations, postulated with help of the turbulent length scale $\lambda_l$ (mixing length or master length scale) and a turbulent velocity scale $q = \sqrt{2e}$:

1. Local equilibrium applied to all second order moments:
   - Neglecting local time derivatives: first term in the equations B.21,B.22 and B.23
   - Neglecting advection: second term in the equations B.21,B.22 and B.23.
   - Neglecting turbulent transport: third term in the equations B.21,B.22 and B.23
   - Neglecting the body-air interaction terms (volume and molecular surface terms)
2. The return-to-isotropy term in the Eq. B.21 is parameterized according to the Rotta-Hypothesis (Rotta, 1951a,b):

   $$\overline{p'\left(\frac{\partial u_i}{\partial x_j}\frac{\partial u_j}{\partial x_i}\right)} = -\frac{q}{3\lambda_l}\left(\overline{u_i' u_j'} - \frac{\delta_{ij}}{3}q^2\right) + C_1 q^2\left(\frac{\partial U_i}{\partial x_j} + \frac{\partial U_j}{\partial x_i}\right) \quad \text{(B.24)}$$

   $C_1$ is a model parameter.
3. The respective term in Eq. B.22 (term 8) is parameterized in a similar way:

   $$\frac{\partial\overline{p'\theta'}}{\partial x_j} = \frac{q}{3A_2\lambda_l}\overline{u_j'\theta'} \quad \text{(B.25)}$$

   $A_2$ is also a model parameter.
4. The transport by the pressure correlation term (terms 5 and 6 in Eq. B.21 and term 6 in the Eq. B.22) are treated to be a part of turbulent transport and are neglected according to the local equilibrium hypothesis and considering their order of magnitude.
5. The dissipation in the covariance equations for momentum (last term in Eq. B.21) following Kolmogorov is assumed as follows:

   $$2\nu\overline{\frac{\partial u_i}{\partial x_k}\frac{\partial u_j}{\partial xk}} = \frac{2}{3}\frac{q^3}{\lambda_l B_1}\delta_{ij} \quad \text{(B.26)}$$

   $B_1$ is a model parameter as well.

6. The dissipation term in Eq. B.22 (last term) is neglected:

$$(\alpha+\nu)\overline{\frac{\partial u_j}{\partial x_k}\frac{\partial \theta'}{\partial x_k}} = 0 \tag{B.27}$$

7. However, the last term in Eq. B.23 is assumed to be:

$$-2\alpha\overline{\frac{\partial \theta'}{\partial x_k}\frac{\partial \theta'}{\partial x_k}} = 2\frac{q}{B_2\lambda_l}\overline{\theta'^2} \tag{B.28}$$

8. Blackadar's relation for the turbulent length scale is assumed:

$$\lambda_l(z) = l_{scal}\frac{\kappa(z+z_0)}{(z+z_0)+l_{scal}} \tag{B.29}$$

   Here $\kappa$ is the von Karman constant, z the geometric distance from the lower model boundary where $z = 0$ and $l_{scal} = min(l_{max}, L_g)$, which depends on the horizontal grid scale $L_g$ of the model and a maximum distance value $l_{max} = 500m$. $z_0$ is the roughness length. $l_{scal}$ is related to the $\lambda_l^\infty$ proposed by Blackadar (1962) by division of $\kappa$: $l_{scal} = \lambda_l^\infty/\kappa$. $\lambda_l^\infty$ is the maximal length scale that turbulent eddies can reach.

9. All the coriolis terms are neglected.

By Introducing all these simplifications and parameterizations into the second oder budget equations (Eq. B.21, B.22, B.23) we obtain a set of 10 algebraic equations in a diagnostic form.

$$\begin{aligned}\overline{u_i'u_j'} = \frac{\delta_{ij}}{3}q^2 &- \frac{3A_1\lambda_l}{q}\left[\overline{u_k'u_i'}\frac{\partial U_j}{\partial x_k} + \overline{u_k'u_i'}\frac{\partial U_i}{\partial x_k} + \frac{2}{3}\delta_{ij}P_s\right] \\ &- \frac{3A_1\lambda_l}{q}\left[-C_1q^2\left(\frac{\partial U_j}{\partial x_i}+\frac{\partial U_i}{\partial x_j}\right) + \beta g_j\overline{u_j'\theta_\nu'} + \beta g_i\overline{u_i'\theta_\nu'} + \frac{2}{3}\delta_{ij}P_b + \epsilon_{ikl}\overline{u_l'u_j'}\right]\end{aligned} \tag{B.30}$$

$$\overline{u_j'\theta'} = -\frac{3A_2\lambda_l}{q}\left[\overline{u_j'u_k'}\frac{\partial \Theta}{\partial x_k} + \overline{\theta'u_k'}\frac{\partial U_j}{\partial x_k} + \beta g_j\overline{\theta_\nu'\theta_\nu'}\right] \tag{B.31}$$

$$\overline{\theta'^2} = \frac{B_2\lambda_l}{q}\overline{u_k'\theta'}\frac{\partial \Theta}{\partial x_k} \tag{B.32}$$

where

$$P_s = -\overline{u_i'u_j'}\frac{\partial U_i}{\partial x_j} \quad P_b = -\beta g_i\overline{u_i'\theta_\nu'}$$

Neglecting horizontal derivatives, because the vertical turbulent scale height is much larger than the horizontal turbulent scale, leeds to following simplified diagnostic equations for the second

order moments:

$$\overline{u'u'} = \frac{q^2}{3} + \frac{A_1\lambda_l}{q}\left[-4\overline{w'u'}\frac{\partial U}{\partial z} + 2\overline{w'u'}\frac{\partial V}{\partial z} - 2P_b\right] \tag{B.33}$$

$$\overline{v'v'} = \frac{q^2}{3} + \frac{A_1\lambda_l}{q}\left[2\overline{w'u'}\frac{\partial U}{\partial z} - 4\overline{w'u'}\frac{\partial V}{\partial z} - 2P_b\right] \tag{B.34}$$

$$\overline{w'w'} = \frac{q^2}{3} + \frac{A_1\lambda_l}{q}\left[2\overline{w'u'}\frac{\partial U}{\partial z} + 2\overline{w'u'}\frac{\partial V}{\partial z} + 4P_b\right] \tag{B.35}$$

$$\overline{v'u'} = \frac{3A_1\lambda_l}{q}\left[\overline{u'w'}\frac{\partial V}{\partial z} - \overline{v'w'}\frac{\partial U}{\partial z}\right] \tag{B.36}$$

$$\overline{w'u'} = \frac{3A_1\lambda_l}{q}\left[-(\overline{w'w'} - C_1q^2)\frac{\partial U}{\partial z} + \beta g\overline{u'\theta'_\nu}\right] \tag{B.37}$$

$$\overline{w'v'} = \frac{3A_1\lambda_l}{q}\left[-(\overline{w'w'} - C_1q^2)\frac{\partial U}{\partial z} + \beta g\overline{v'\theta'_\nu}\right] \tag{B.38}$$

$$\overline{u'\theta'} = \frac{3A_2\lambda_l}{q}\left[-\overline{u'w'}\frac{\partial \Theta}{\partial z} - \overline{w'\theta'}\frac{\partial U}{\partial z}\right] \tag{B.39}$$

$$\overline{v'\theta'} = \frac{3A_2\lambda_l}{q}\left[-\overline{v'w'}\frac{\partial \Theta}{\partial z} - \overline{w'\theta'}\frac{\partial V}{\partial z}\right] \tag{B.40}$$

$$\overline{w'\theta'} = \frac{3A_2\lambda_l}{q}\left[-\overline{w'w'}\frac{\partial \Theta}{\partial z} + \beta g\overline{\theta'\theta'_\nu}\right] \tag{B.41}$$

$$\overline{\theta'\theta'} = -\frac{B_2\lambda_l}{q}\overline{w'\theta'}\frac{\partial \Theta}{\partial z} \tag{B.42}$$

The TKE equation B.10 is written as a prognostic equation for $q^2 = 2e$ and simplified introducing following assumptions:

- Neglecting the body-air interaction terms (volume and molecular surface terms).
- The pressure correlation term (term 6) of equation B.10 is assumed to be part of the turbulent transport.
- A flux gradient parameterization of the turbulent TKE-transport term :

$$\overline{u'_j e} = \frac{3}{5}\lambda_l q S_q\left(\frac{\partial \overline{u_i u_j}}{\partial x_k} + \frac{\partial \overline{u_i u_k}}{\partial x_j} + \frac{\partial \overline{u_j u_k}}{\partial x_i}\right) = \alpha_{TKE}\lambda_l q\left(\frac{\partial \overline{e}}{\partial x_k} + \frac{\partial \overline{e}}{\partial x_j} + \frac{\partial \overline{e}}{\partial x_i}\right) \tag{B.43}$$

- As in the general second order moments budget equations the Kolmogorov-Hypothesis is used for the parameterization of the TKE dissipation:

$$\epsilon = \frac{1}{3}\frac{q^3}{B_1\lambda_l}\delta_{ij} = \frac{q^3}{B_1\lambda_l} \tag{B.44}$$

The resulting TKE- or $q^2$-equation is:

$$\frac{\partial q^2}{\partial t} + U_j\frac{\partial q^2}{\partial x_k} + \frac{\partial}{\partial x_k}\left(\alpha_{TKE}\lambda_l q\frac{\partial q^2}{\partial x_k}\right) = 2(P_s + P_b - \epsilon) \tag{B.45}$$

$P_s$ and $P_b$ become:

$$P_s = -\overline{w'u'}\frac{\partial U}{\partial z} - \overline{w'v'}\frac{\partial V}{\partial z} \quad P_b = -\beta g\overline{w'\theta'_v}$$

$P_s$ is the mechanical production term (fourth term in Eq. B.10) and $P_b$ is the buoyant production or consumption term of TKE (third term in Eq. B.10). $\epsilon = \frac{q^3}{B_1 \lambda_l}$ represents the TKE dissipation term. The 10 diagnostic equations for the second order moments and the TKE-equation together build up the hierarchy model level 2.5 following Mellor and Yamada (1974, 1982). Exactly the same equations derived before are applicable for a moist atmosphere as long as no phase changes occur. In order to avoid as far as possible additional source terms in the second order moment equations it is convenient to use the liquid water potential temperature $\Theta_l$ and the total water content $Q_w$.

$$\Theta_l = \Theta - \frac{L_c}{C_{p_d}} Q_l \tag{B.46}$$

$$Q_w = Q_v + Q_l \tag{B.47}$$

$L_c$ and $C_{p_d}$ are the specific heat of water condensation and the specific heat capacity of dry air for constant pressure. $Q_v$ and $Q_l$ are the mixing ratio of water vapour and liquid water, respectively. If we neglect the ice phase, obviously $Q_w$ is conservative, where $\Theta_l$ at least during moist adiabatic processes can be treated as conservative, if we neglect radiative heating. In this idealisation those source terms can be neglected, if source terms of either $Q_w$ or $\Theta_l$ appear. The equations from B.33 to B.38 remain the same. Equations from B.39 to B.42 are the same except that $\theta'$ or $\Theta$ is replaced by $\theta'_l$ and $\Theta_l$. In addition, diagnostic equations for the fluxes and variances of the total water content may be derived.

In a 1.5-order turbulence closure framework we can write following relations:

$$\overline{u'w'} = -K_M \frac{\partial U}{\partial z} \tag{B.48}$$

$$\overline{v'w'} = -K_M \frac{\partial V}{\partial z} \tag{B.49}$$

$$\overline{q'_w w'} = -K_H \frac{\partial Q_w}{\partial z} \tag{B.50}$$

$$\overline{\theta'_l w'} = -K_H \frac{\partial \Theta_l}{\partial z} \tag{B.51}$$

$$K_M = q \lambda_l S_M \tag{B.52}$$

$$K_H = q \lambda_l S_H \tag{B.53}$$

$K_M$ and $K_H$ represent the turbulent diffusion coefficients, which are a function of two stability functions $S_M$ and $S_H$, respectively. Using $P_s$ and $P_b$, introducing the above defined turbulent fluxes (Eq. B.48-B.49), inserting the definition of $K_M$ and $K_H$ and multiplying by $\frac{l}{q^3 S_M}$ for momentum and by $\frac{l}{q^3 S_H}$ for scalars we can define two dimensionless gradients $G_M$ and $G_H$:

$$G_M =: \frac{\lambda_l^2}{q^2} \left[ \left( \frac{\partial U}{\partial z} \right)^2 + \left( \frac{\partial V}{\partial z} \right)^2 \right] \tag{B.54}$$

$$G_H =: -\frac{\lambda_l^2}{q^2} \beta g \frac{\partial \Theta_\nu}{\partial z} = \frac{\lambda_l^2}{q^2} (A_\Theta \frac{\partial \Theta_l}{\partial z} + A_{Q_w} \frac{\partial Q_w}{\partial z}) \tag{B.55}$$

The sensible heat flux appearing in the TKE equation ($P_b$) can be rewritten as function of the liquid water temperature and the total water content:

$$\overline{\theta'_v w'} = -K_H \frac{\partial \Theta_v}{\partial z} = -K_H \Gamma_v = -K_H (A_{\Theta_l} \frac{\partial \Theta_l}{\partial z} + A_{Q_w} \frac{\partial Q_w}{\partial z}) \tag{B.56}$$

where $A_{\Theta_l}$ and $A_{Q_w}$ depend on the saturation fraction $r_c$ and may be diagnosed by a statistical cloud scheme (Someria and Deardoff, 1976). This relation introduces in the TKE-equation also the sub-grid scale condensation, by the use of the quasi conservative variables $\Theta_l$ and $Q_w$. For dry conditions (cloud fraction $r_c = 0$) $\Gamma_v$ is given by the gradient of potential temperature, whereas for moist saturated conditions (cloud fraction $r_c = 1$) $\Gamma_v$ is given by the gradient of the equivalent potential temperature.

The equations from B.33 to B.42, using the above presented definitions of $G_M$ and $G_H$, can be reduced with considerable algebra to:

$$S_M[6A_1A_2G_M] + S_H[1 - 3A_2B_2G_H - 12A_1A_2G_H] = A_2 \tag{B.57}$$

$$S_M[1 + 6A_1^2G_M - 9A_1A_2G_H] - S_H[12A_1^2G_H + 9A_1A_2G_H] = A_1(1 - 3C_1) \tag{B.58}$$

Based on the formulations of the mechanical and thermal production rates of $q^2$ and the dissipation rate $\epsilon$, one finds the relation

$$\frac{P_s + P_b}{\epsilon} = B_1(S_MG_M + S_HG_H) \tag{B.59}$$

Inserting B.59 $G_M$ can be eliminated from B.57 and B.58 obtaining the following set of algebraic equations:

$$S_H[1 - (3A_2B_2 + 18A_1A_2)G_H] = A_2\left[1 - \frac{6A_1}{B_1}\frac{P_s + P_b}{\epsilon}\right] \tag{B.60}$$

$$S_M[1 - 9A_1A_2G_H] - S_H[(18A_1^2 + 9A_1A_2)G_H] = A1\left[1 - 3C_1 - \frac{6A_1}{B_1}\frac{P_s + P_b}{\epsilon}\right] \tag{B.61}$$

To solve B.57,B.58 or B.60, B.61 q or $\frac{P_s+P_b}{\epsilon}$ has to be known. This is an implicit set of equations. The ratio between $P_b$ and $P_s$ is known as flux Richardson number $R_f$, which is a dimensionless quantity describing how turbulent a flow is.

$$R_f = -\frac{P_b}{P_s} \tag{B.62}$$

Equation B.57 and Eq. B.58 can be solved for $S_M$ and $S_H$ obtaining following functions, which depend on $G_H$ and $G_M$.

$$S_M = \frac{be2 \cdot a11 - be1 \cdot a21}{a11 \cdot a22 - a12 \cdot a21} \tag{B.63}$$

$$S_H = \frac{be1 \cdot a22 - be2 \cdot a12}{a11 \cdot a22 - a12 \cdot a21} \tag{B.64}$$

where the variables have the following definition:

$$\begin{aligned}
be1 &= 1 \\
be2 &= 1 - 3C1 \\
a11 &= \frac{1}{A_2} - (3B_2 - 12A_1)G_H \\
a12 &= 6A_1G_M \\
a21 &= -(9A_2 + 12A_1)G_H \\
a22 &= \frac{1}{A_1} - 9A_2G_H + 6A_1G_M
\end{aligned}$$

These functions are used in COSMO only in stable conditions. The closure constant parameters $(A_1, A_2, B_1, B_2, C_1)$ have the same numerical values of the Mellor and Yamada (1982) scheme (Eq. B.65).

$$(A_1, A_2, B_1, B_2, C_1) = (0.92, 0.74, 16.6, 10.1, 0.08) \tag{B.65}$$

The particular dependence of $S_M$ and $S_H$ from $G_M$ and $G_H$ is presented in the Fig. B.1. The

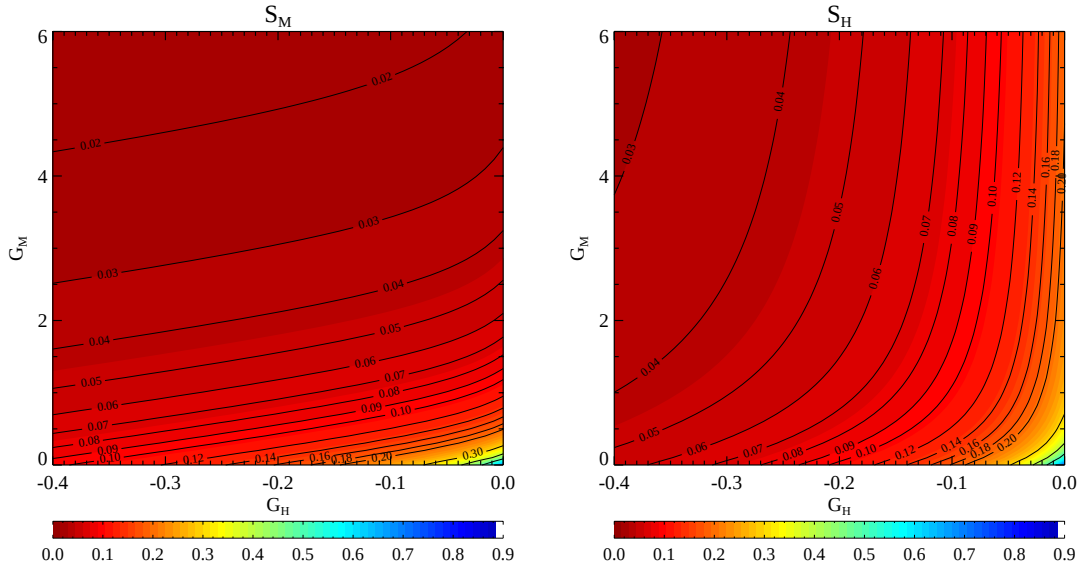


Figure B.1: Stability functions $S_M$ (left) and $S_H$ (right) as function of $G_M$ and $G_H$ following the Mellor and Yamada (1982) turbulence closure as used in the COSMO model for the stable case. Note that none limitation for $G_M$ is active.

gradient Richardson number $R_i$ is defined as follows:

$$R_i = R_f \frac{S_M}{S_H} = -\frac{G_H}{G_M} \tag{B.66}$$

In case of the level 2 model, Mellor and Yamada (1982) replace the prognostic $q^2$-equation by the diagnostic production-dissipation balance:

$$\frac{P_s + P_b}{\epsilon} = 1 \tag{B.67}$$

The Mellor and Yamada (1982) solution for the stability functions presented above is only used in stable situations, since the solution breaks down when $G_H$ exceeds a critical value in case of unstable stratification. To avoid this singularity, $S_M$ and $S_H$ are calculated for unstable situations in a modified way. The production and dissipation rates $P_s$, $P_b$ and $\epsilon$ are calculated as function of the predicted q and the previous value of $S_M$ and $S_H$ (previous time step). The resulting ratio between production and dissipation is denoted as $B_1\gamma$, which gives the definition of $\gamma$.

$$\frac{P_s + P_b}{\epsilon} = B_1\gamma \tag{B.68}$$

In case $B_1\gamma = 1$ the solution is equal to the level 2 model proposed by (Mellor and Yamada, 1982). Proceeding as in the 2 level model and using B.68 $S_M$ and $S_H$ follow as

$$S_H = 3A_2 \frac{\gamma_1 - (\gamma_1 + \gamma_2)R_f}{1 - R_f} \tag{B.69}$$

$$S_M = \frac{A_1}{A_2} \frac{B_1(\gamma_1 - C_1) - [B_1(\gamma_1 - C_1) + \gamma B_1(6A_1 + 3A_2)]R_f}{B_1\gamma_1 - [B_1(\gamma_1 + \gamma_2) - 3A_1\gamma B_1]R_f} S_H \tag{B.70}$$

with

$$\gamma_1 = \frac{1}{3} - 2\gamma B_1 \frac{A_1}{B_1}, \gamma_2 = \left(\frac{B_2}{B_1} + 6\frac{A_1}{B_1}\right)\gamma B_1$$

The equations B.69 and B.70 are implicit. Using $R_i$ instead of $R_f$ and solve for $S_M$ and $S_H$, results a quadratic equation for $y = \frac{S_M}{S_H}$:

$$y = \frac{p_1}{2}\sqrt{-p_0 + \frac{p_1^2}{4}} \tag{B.71}$$

where

$$p_0 = \frac{A_1}{A_2\gamma_1}[(\gamma_1 - C_1) + \gamma(6A_1 + 3_A 2)]R_i$$

$$p_1 = \frac{1}{\gamma_1}\left[(\gamma_1 + \gamma_2 - 3A_1\gamma)R_i + \frac{A_1}{A_2}(\gamma_1 - C_1)\right]$$

The stability functions follow as

$$S_H = 3A_2\frac{\gamma_1 y - (\gamma_1 + \gamma_2)R_i}{y - R_i} \tag{B.72}$$

$$S_M = yS_H \tag{B.73}$$

To prevent any singularity, $\gamma$ has to ensure the sufficient condition $\gamma \geq C_1$. The stability functions for the unstable case are presented for the special case $B_1\gamma = 1$ in Fig. B.2.

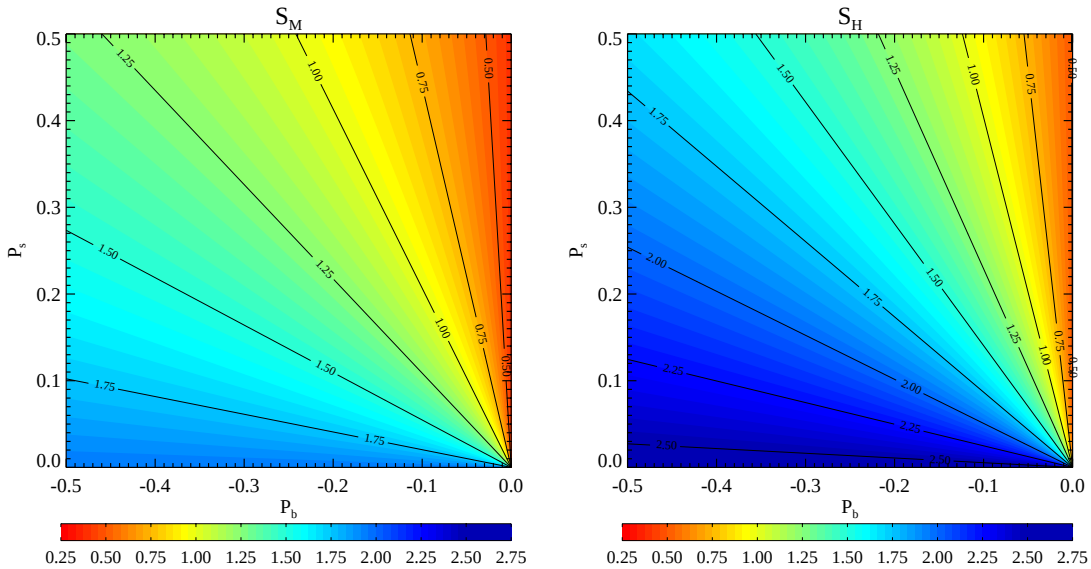


Figure B.2: Stability functions $S_M$ (left) and $S_H$ (right) for the unstable case as function of $P_b$ and $P_s$, here plotted for the special situation where $B_1\gamma = 1$ corresponding to the level 2 of the Mellor and Yamada (1982) hierarchy model.

Introducing the formulation for the forcing terms and for the dissipation, the TKE-or $q^2$-equation becomes:

$$\frac{\partial q^2}{\partial t} + U_j\frac{\partial q^2}{x_j} - \frac{1}{\bar{\rho}}\frac{\partial}{\partial z}\left(\alpha_{TKE}\bar{\rho}\lambda_l q\frac{\partial q^2}{\partial z}\right) =$$
$$2K_M\left[\left(\frac{\partial U}{\partial z}\right)^2 + \left(\frac{\partial V}{\partial z}\right)^2\right] - 2K_H(A_{\Theta_l}\frac{\partial \Theta_l}{\partial z} + A_{Q_w}\frac{\partial Q_w}{\partial z}) - 2\frac{q^3}{B_1\lambda_l} \tag{B.74}$$

Besides the inclusion of sub-grid scale condensation, there is one major extension compared to the traditional 2.5 level schemes: the inclusion of sub-grid thermal circulations. Inhomogeneities at the rigid surface will always give rise to differential heating and cooling resulting in direct thermal circulation patterns of a length scale being smaller than grid scale but larger than that of the small-scale turbulence. In such a situation, there will be a conversion of kinetic energy related to the circulation patterns (CKE) into TKE with a positive definite source term. This process will especially prevent that the solution of the TKE-equation tends to zero in case of very stable thermal stratification, where the well known but unrealistic decoupling of the atmosphere and the surface can be avoided. The covariance of the sensible heat flux may be decomposed in two parts: a large and a small-scale one.

$$\overline{\theta_v' w'} = (\overline{\theta_v' w'})_L + (\overline{\theta_v' w'})_S \tag{B.75}$$

Using this, it is possible to derive second order budget equations for the turbulent large scale and the circulating part separately. Formally, those band pass budgets differ from the total budgets only by conversion terms describing scale interactions of the circulation patterns. In the large scale transport equations stationarity is assumed. Advection and dissipation are neglected. The shear production by the mean wind treat the conversion term there like a dissipation term and consider the sub grid scale transport (third order moments), in which the related molecular transport from the rigid surfaces is not negligible. For this reason is not only responsible for pure redistribution but is describing a real source for the whole atmosphere. Due to the mentioned thermal inhomogeneities at the rigid surface, temperature variance will always be transported from that surface into the atmosphere. Applying the mentioned approximations for the large scale second order equation it can be shown that the conversion term is mainly formed by the large scale part of $\overline{\theta_v' w'}|_L$ of the sensible heat flux $\overline{\theta_v' w'}$. The simplified equation provides the relation:

$$(\overline{\theta_v' w'})_L \propto -\tau_L^2 \frac{g}{\theta_v \bar{\rho}} \frac{\partial (\bar{\rho} \overline{w' \theta_v'^2})_L}{\partial z} \tag{B.76}$$

In the present version of the scheme the large scale heat flux is parameterized as follow:

$$(\overline{\theta_v' w'})_L = -L_{pat} \left( \frac{\lambda_l^2}{q^2} \right) \frac{g}{\theta_v \bar{\rho}} \frac{\partial \left( \bar{\rho} K_H \Gamma_v^2 \right)}{\partial z} \tag{B.77}$$

Introducing this term into equation B.56 we obtain the final $q^2$-equation.

$$\begin{aligned} \frac{\partial q^2}{\partial t} - \frac{1}{\bar{\rho}} \frac{\partial}{\partial z} \left[ \alpha_{TKE} \bar{\rho} \lambda_l q \frac{\partial q^2}{\partial z} + 2 L_{pat} \bar{\rho} \left( \frac{\lambda_l g}{q \bar{\Theta}_v} \right)^2 K_H \left( A_\Theta \frac{\partial \Theta_l}{\partial z} + A_{Q_w} \frac{\partial Q_w}{\partial z} \right)^2 \right] = \\ 2 K_M \left[ \left( \frac{\partial U}{\partial z} \right)^2 + \left( \frac{\partial V}{\partial z} \right)^2 \right] - 2 K_H \frac{g}{\Theta_v} \left( A_\Theta \frac{\partial \Theta_l}{\partial z} + A_{Q_w} \frac{\partial Q_w}{\partial z} \right) - 2 \frac{q^3}{B_1 \lambda_l} \end{aligned} \tag{B.78}$$

This $q^2$ equation is solved in order to get the q value subsequently used for the calculation of the new the turbulent diffusion coefficients. Notice that the advection term has been neglected. So far no advection of q is considered in the COSMO model.

## B-2 Surface transfer scheme

### B-2.1 General aspects

The aim of the surface transfer scheme is to calculate the fluxes from the rigid surfaces of the lower boundary of the earth into the atmosphere and the corresponding profiles of the transported

variables. The COSMO model (Steppeler et al., 2003) surface layer scheme instead being based on the Monin-Obukhov similarity theory for the surface layer is formulated in the framework of the TKE based turbulence scheme, as used in the atmosphere (Raschendorfer, 2001; Doms et al., 2001; Raschendorfer, 2007a).

The transfer layer is defined to extend from the rigid surface of the earth up to the lowest main level, where all the first order model variables are defined. The central step of the scheme is the computation of the transfer coefficients. The region between the solid surface and the lowest model main surface is divided in three sub-layers: a Prandtl layer or surface layer, a turbulent roughness layer and a laminar layer. The last 2 layers are treated as only skin layers without real vertical extension (or having an extension equal to $z_0$). The surface layer is assumed to begin at the height corresponding to the height $z_0$ or at the turbulence distance $z_0 k$, where $z_0$ is the roughness length and k is the von Karman constant. The surface layer extends up to the first atmospheric main level. The vertical description of the transfer layer is illustrated in Fig. B.3.

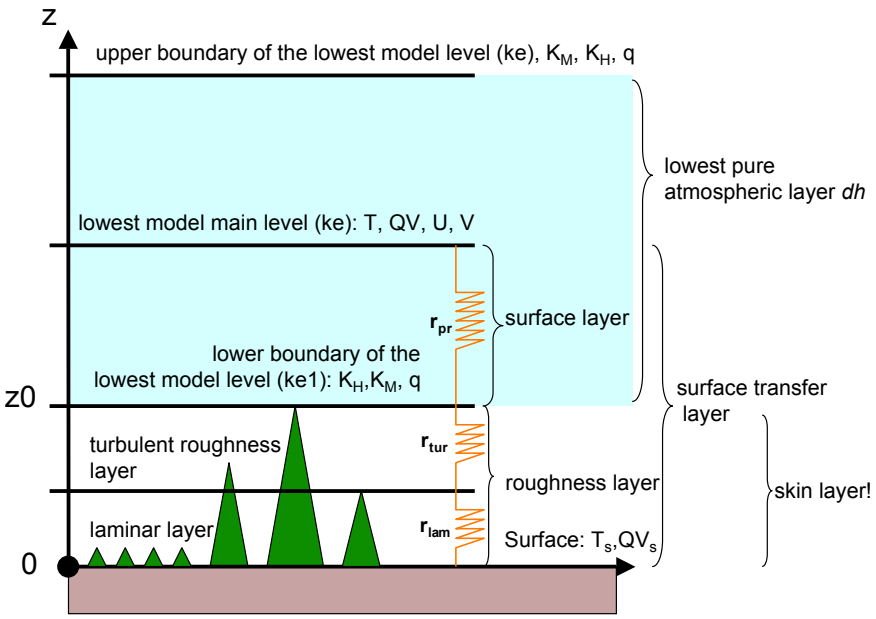


Figure B.3: The surface transfer layer and its sub-layers: the surface layer (or Prandtl layer), the turbulent roughness layer and the laminar layer. For each sub-layer transport resistances for vector and scalar quantities are computed. The surface layer extends from the height corresponding to the roughness length $z_0$ (level with the index ke1) to the lowest atmospheric main main level (level with index ke), where the turbulent diffusion coefficients and all the model variables are known. At the bottom of the surface layer only the turbulence related variables as the diffusion coefficients are known. The roughness layer is placed below the height equal to the roughness length and is treated as a skin layer.

As first step for each layer transport resistances are computed, which depend on the turbulent diffusion coefficients at the level with index ke and index ke1, on the roughness length $z_0$ (no direct distinction between momentum and heat is done), the leaf area index (LAI) and on the plant coverage. The roughness length contains two main components: the local roughness (surface coverage with roughness elements) and subgrid scale orography. The subgrid-scale orography intersects model levels, and consequently influences the momentum of the atmosphere. Because no special parameterization of the additional surface drag due to subgridscale orography is used in COSMO, this aspect is considered only using a larger roughness length containing also the subgridscale variance of the topography.

The computation of the turbulent diffusion coefficients at these two levels (index ke and index ke1) is done using the same TKE turbulence closure scheme as used in the atmosphere following the 1.5 order turbulence closure at the hierarchy level 2.5 and 2.0, respectively, proposed by Mellor

and Yamada (1982) in the framework of their hierarchical model (Mellor and Yamada, 1974). The turbulent diffusion coefficients are determined with Eq. B.52 and B.53. The master length scale $\lambda_l$ is computed at the level ke following Eq. B.29, while at the level ke1 it is defined as $\lambda_l = \kappa z_0$ ($\kappa = 0.4$ is the von Karman constant). The q value is produced at the level ke with a complete prognostic equation considering also its vertical turbulent transport (Eq. B.78), while at the level ke1 the q transport is not taken into account. A the level ke1 the following simplified q equation is solved:

$$\frac{\partial q^2}{\partial t} = 2K_M \left[ \left( \frac{\partial U}{\partial z} \right)^2 + \left( \frac{\partial V}{\partial z} \right)^2 \right] - 2K_H (A_{\Theta_l} \frac{\partial \Theta_l}{\partial z} + A_{Q_w} \frac{\partial Q_w}{\partial z}) - 2 \frac{q^3}{B_1 \lambda_l} \tag{B.79}$$

The necessary gradients for the forcing terms of the q-equation as well as for the computation of the stability functions at the level ke1, are determined with help of the ratio of resistance in the surface layer to the total resistance over all layers (tfm and fth, Eq. B.102 and B.103) and the resistance in the surface layer ($r^M_{pr}$, $r^H_{pr}$) as follows:

$$\frac{\partial U}{\partial z} = \frac{\text{tfm} \cdot U_{ke}}{r^M_{pr}} \tag{B.80}$$

$$\frac{\partial V}{\partial z} = \frac{\text{tfm} \cdot V_{ke}}{r^M_{pr}} \tag{B.81}$$

$$\frac{\partial Q_w}{\partial z} = \frac{QV_{ke} - (QV_{ke}(1 - \text{tfh}) + QV_s \cdot \text{tfh})}{r^H_{pr}} \tag{B.82}$$

$$\frac{\partial \Theta_l}{\partial z} = \frac{\Theta^{ke}_l - \left(\Theta^{ke}_l (1 - \text{tfh}) + \Theta^s_l \cdot \text{tfh}\right)}{r^H_{pr}} \tag{B.83}$$

$U_{ke}$ and $V_{ke}$ are the wind components at the lowest model level, $Q_w$ is the total water content (here, compared to Eq. B.47, the liquid water is not considered), $\Theta_l$ is the liquid water potential temperature (Eq. B.46) at ke and at the surface.

### B-2.2 The transfer resistances

The dimensionless resistance for momentum $r^M_{AB}$ and for scalars $r^H_{AB}$ within the transfer layer between two general heights A and B are defined as function of the transport velocity scale at the turbulence distance $z_0$ and of the transfer resistance $F^M_{AB}$ or $F^H_{AB}$:

$$r^M_{AB} = \kappa u^M_{z_0} F^M_{AB} \tag{B.84}$$

$$r^H_{AB} = \kappa u^H_{z_0} F^H_{AB} \tag{B.85}$$

$z_0$ refers to the start height of the surface layer (third layer in the transfer scheme). The transport velocity scale is a function of the diffusion coefficient at $z_0$:

$$u^M_{z_0} = q_{z_0} S^{z_0}_M + \frac{k_M}{\kappa z_0} \tag{B.86}$$

$$u^H_{z_0} = q_{z_0} S^{z_0}_H + \frac{k_H}{\kappa z_0} \tag{B.87}$$

where $k_M$ and $k_H$ are the constant laminar diffusion coefficient for scalars and momentum, respectively, while $q_{z_0}$ and $S^{z_0}$ are the turbulent velocity scale and the stability function. The transfer

resistance can be computed by evaluating a transport integral along the turbulent distance a:

$$F_{AB}^{M} = \int_{A}^{B} \frac{da}{s_0 \kappa u_a^M} \tag{B.88}$$

$$F_{AB}^{H} = \int_{A}^{B} \frac{da}{s_0 \kappa u_a^H} \tag{B.89}$$

$u_a^M$ and $u_a^H$ are the transport velocity for momentum and scalars at the turbulent distance a according to the turbulence scheme. $s_0$ is defined as the the relation between the roughness length and the surface area index ($s_0 = z_0/\mathrm{SAI}$).

$$u_a^M = q_a S_M^a + \frac{k_M}{\kappa a} = \nu_a^M + \frac{k_M}{\kappa a} \tag{B.90}$$

$$u_a^H = q_a S_H^a + \frac{k_H}{\kappa a} = \nu_a^M + \frac{k_H}{\kappa a} \tag{B.91}$$

$\nu_a^M$ and $\nu_a^M$ is a velocity scale according to the turbulence scheme. The turbulent velocity scale multiplied by the mixing length gives the turbulent diffusion coefficient. The transfer integral is resolved for each of the three sublayers with different interpolation formulae for the transport velocity scale and some additional special assumptions.

i) laminar layer: integration $0 \rightarrow dh_l$, $au_a^M$ and $au_a^H$ are set as constant, the velocity scale vanishes $\nu_a^M = 0$ and $\nu_a^M = 0$, $dh_l$ is defined as $dh = \frac{k_M}{u_{z_0}^M}$.

ii) roughness layer: integration $dh \rightarrow z_0$, a constant transport velocity scale is used $u_a^M = u_{z_0}^M$ and $u_a^H = u_{z_0}^H$.

iii) surface layer: integration $z_0 \rightarrow (0.5 \cdot dh) + z_0$, the transport velocity scale $u_a^M$ and $u_a^H$ is linearly interpolated between the turbulent distance $z_0$ (first half level ke1, where the turbulent velocity scale is defined) and $dh + z_0$ (second half level ke, where the turbulent velocity scale is defined). $dh$ is the thickness of the first atmospheric layer.

The resistance of the whole transfer layer is equal to the sum of all the single layer resistances. In the following each resistance will be presented in its final form, which has been obtained after the integration sketched above and some useful variable substitutions.

**Laminar layer**

The resistances along the entire laminar layer are defined as follows:

$$r_{lam}^M = E_M \frac{z_0}{SAI} \tag{B.92}$$

$$r_{lam}^H = F \cdot E_H \frac{z_0}{SAI} \frac{\frac{K_H^{ke1}}{D_H}}{\frac{K_M^{ke1}}{D_M}} \tag{B.93}$$

Here $E_M$ and $E_H$ are the scaling factors of the laminar layer for momentum and heat (or moisture). $E_M$ is normally assumed to be zero and $E_H$ to be one. Due to this assumption the resistance for momentum in the laminar layer vanishes. F is equal to one over land and influences the laminar resistance over gridcells fully or partially covered by water ($F = 1 + (1 - FR_{LAND}(20 - 1))$, whereas $FR_{LAND}$ is the fraction of land having values form 0 to 1). $K_H^{ke1}$ and $K_M^{ke1}$ are the turbulent diffusion coefficients computed at the lowest boundary of the first atmospheric layer. $D_H = k_H$ is the kinematic viscosity and $D_M = k_M$ the scalar conductivity of dry air, respectively. "$SAI$" is the surface area index, which depends on the "plant coverage index" ($PL_{cov}$), the leaf area index ($LAI$) and the surface area density of the roughness elements at the surface ($C_{lnd} = 2$).

$$SAI = PL_{cov} \cdot LAI + C_{lnd} \tag{B.94}$$

**Turbulent roughness layer**

In the turbulent roughness layer the resistances are expressed as function of the surface area index, the roughness length and the turbulent diffusion coefficient at the bottom of the surface layer (level with index ke1).

$$r_{tur}^{M} = \sqrt{(\frac{1}{2} r_{lam}^{M})^2 + h_{can} \cdot r_{lam}^{M}} - \frac{1}{2} \cdot r_{lam}^{M} \tag{B.95}$$

$$r_{tur}^{H} = \frac{z_0}{SAI} \log \frac{K_{ke1}^{M}}{D_M} \tag{B.96}$$

where $h_{can}$ is the effective canopy height calculated as follow:

$$h_{can} = RC \cdot (r_{lam}^{H} + r_{tur}^{H}) \log \frac{r_{lam}^{H} + r_{tur}^{H}}{r_{lam}^{H}} \tag{B.97}$$

RC represents the ratio of canopy height to the roughness length $z_0$ (operationally set to one).

**Surface layer**

In the surface layer the transfer resistance is calculated using a linear interpolation factor of the turbulent diffusion coefficients $K^M$ und $K^H$ calculated before in the turbulence scheme between the values at first atmospheric model level (level with index ke) and at the bottom of the surface layer (level with index ke1). Given $F_M$ and $F_H$, the factors 'facm' and fach' can be calculated as follows:

$$F_M = \min \begin{cases} 2 \\ \max \begin{cases} 0.5 \\ \frac{K_{ke}^{M} \cdot z_0}{K_{ke1}^{M} \cdot (dh + z_0)} \end{cases} \end{cases} \qquad F_H = \min \begin{cases} 2 \\ \max \begin{cases} 0.5 \\ \frac{K_{ke}^{H} \cdot z_0}{K_{ke1}^{H} \cdot (dh + z_0)} \end{cases} \end{cases}$$

$$facm = \frac{(F_M - 1) \cdot z_0}{dh} \qquad fach = \frac{(F_H - 1) z_0}{dh}$$

dh is the thickness of the lowest model layer and corresponds to the distance between the surface at index ke (upper boundary of the first model level) and ke1 (bottom of the surface layer or lower boundary of the first model layer). Once facm and fach are known the transport resistances can be computed according to:

$$r_{pr}^{M} = \begin{cases} \frac{z_0}{dh + z_0} \cdot \frac{1}{2} dh & \text{, if facm=1} \\ \frac{z_0}{1 - facm} \cdot \log \left( \frac{\frac{1}{2} dh + z_0}{z_0 + facm \cdot \frac{1}{2} dh} \right) & \text{, else} \end{cases} \tag{B.98}$$

$$r_{pr}^{H} = \begin{cases} \frac{z_0}{dh + z_0} \cdot \frac{1}{2} dh & \text{, if fach=1} \\ \frac{z_0}{1 - fach} \cdot \log \left( \frac{\frac{1}{2} dh + z_0}{z_0 + fach \cdot \frac{1}{2} dh} \right) & \text{, else} \end{cases} \tag{B.99}$$

### B-2.3 The total resistance and the transfer coefficients

The total resistance from the surface to the top of the boundary of the surface layer is given as the sum of the resistances of the single layers:

$$r_{tot}^{M} = r_{lam}^{M} + r_{tur}^{M} + r_{pr}^{M} \tag{B.100}$$

$$r_{tot}^{H} = r_{lam}^{H} + r_{tur}^{H} + r_{pr}^{H} \tag{B.101}$$

Operationally, the laminar and roughness layer resistances for momentum vanish because the parameter $E_M$ is set to zero. For this reason, only a resistance in the surface layer $r_{pr}$ is used

and the free slip condition is located at the height $z_0$. With the resistances it is now possible to compute the ratio of the resistance in the surface layer to the total resistance over all layers:

$$\text{tfm} = \frac{r_{pr}^M}{r_{tot}^M} \tag{B.102}$$

$$\text{tfh} = \frac{r_{pr}^H}{r_{tot}^H} \tag{B.103}$$

The transfer coefficients ($C_m$, $C_\Theta$ and $C_Q$) are then expressed as functions of the sum of the resistances of each sublayer ($r_{tot}^M, r_{tot}^H$), the horizontal velocity ($V_h$), the turbulent diffusion coefficients at the bottom of the surface layer (at the height corresponding to $z_0$ at the level with index ke1) and at the top of the first model level (level indicated with the index ke).

$$C_m = \frac{K_M^{ke1} \cdot \text{tfm}}{r_{pr}^M \cdot V_h} = \frac{K_M^{ke1}}{r_{tot}^M \cdot V_h} \tag{B.104}$$

$$C_\Theta = C_Q = \frac{K_H^{ke1} \cdot \text{tfh}}{r_{pr}^H \cdot V_h} = \frac{K_H^{ke1}}{r_{tot}^H \cdot V_h} \tag{B.105}$$

Then the surface fluxes for sensible heat ($H_0$) and latent heat ($E \cdot L_v$) at the surface can be determined straightforward using the gradient between surface and first atmospheric layer .

$$H_0 = -\rho \cdot C_{pd} \cdot C_\Theta \cdot V_h \cdot \Delta T \tag{B.106}$$

$$(E \cdot L_v)_0 = -\rho \cdot C_Q \cdot V_h \cdot L_v \cdot \Delta QV \tag{B.107}$$

E is the evaporation rate from the surface and from the soil. The momentum fluxes at the surface ($(M_U)_0$, $(M_V)_0$) are paremeterized by a drag-law formulation

$$(M_U)_0 = -\rho \cdot C_m \cdot V_h \cdot U_{ke} \tag{B.108}$$

$$(M_V)_0 = -\rho \cdot C_m \cdot V_h \cdot V_{ke} \tag{B.109}$$

where $V_h$ is the horizontal wind velocity, $U_{ke}$ and $V_{ke}$ its eastward (zonal) respectively nordward (meridional) wind component at the lowest model level.
In the framework of this transfer scheme the diagnostics of the 2 m temperature, the 2 m dew point and of the 10 m wind components takes place, if the first atmospheric layer is above these levels. Different interpolation formulae are used depending on the vertical distribution of the model levels and on the characteristics of the surface.

# Appendix C

# Additional material for Chapter 5

## C-1 External parameters: CLCC-data-set

| No. | Land use class | $z_o$ [m] | root depth [m] | plant cover | | leaf area index | |
|---|---|---|---|---|---|---|---|
| | | | | Max | Min | Max | Min |
| 1 | urban and built up land | 1.00 | 0.60 | 0.10 | 0.05 | 4.70 | 0.10 |
| 2 | dryland cropland and pasture | 0.10 | 1.00 | 0.90 | 0.45 | 5.00 | 0.20 |
| 3 | irrigated cropl. and pasture | 0.10 | 0.60 | 1.00 | 0.50 | 5.60 | 0.20 |
| 4 | mixed dryland/irrigated .... | 0.10 | 0.80 | 0.90 | 0.45 | 5.30 | 0.20 |
| 5 | cropland/grassland mosaic | 0.07 | 1.00 | 0.90 | 0.45 | 5.90 | 0.35 |
| 6 | cropland/woodland mosaic | 0.25 | 1.00 | 0.90 | 0.45 | 6.10 | 1.20 |
| 7 | grassland | 0.03 | 0.60 | 1.00 | 1.00 | 4.50 | 0.50 |
| 8 | shrubland | 0.20 | 1.00 | 0.40 | 0.10 | 4.00 | 0.10 |
| 9 | mixed shrubland/grassland | 0.15 | 1.00 | 0.60 | 0.10 | 4.00 | 0.10 |
| 10 | savannah | 0.15 | 2.00 | 0.80 | 0.20 | 3.00 | 1.00 |
| 11 | deciduous broadleaf forest | 1.00 | 1.00 | 1.00 | 0.00 | 6.00 | 0.00 |
| 12 | deciduous needleleaf forest | 1.00 | 0.60 | 1.00 | 0.00 | 6.00 | 0.00 |
| 13 | evergreen broadleaf forest | 1.00 | 1.00 | 1.00 | 1.00 | 9.00 | 9.00 |
| 14 | evergreen needleleaf forest | 1.00 | 0.60 | 1.00 | 1.00 | 8.00 | 8.00 |
| 15 | mixed forest | 1.00 | 0.80 | 1.00 | 0.50 | 7.00 | 2.25 |
| 16 | water bodies | 0.0002 | 0.00 | 0.00 | 0.00 | 0.00 | 0.00 |
| 17 | herbaceous wetland | 0.05 | 0.40 | 0.80 | 0.40 | 3.00 | 1.00 |
| 18 | wooded wetland | 0.20 | 0.40 | 0.90 | 0.10 | 4.00 | 1.00 |
| 19 | barren or sparsely vegetated | 0.05 | 0.30 | 0.05 | 0.02 | 1.00 | 0.50 |
| 20 | herbaceous tundra | 0.05 | 0.10 | 0.30 | 0.00 | 2.10 | 0.00 |
| 21 | wooded tundra | 0.20 | 0.10 | 0.40 | 0.20 | 3.20 | 0.50 |
| 22 | mixed tundra | 0.10 | 0.10 | 0.35 | 0.10 | 2.60 | 0.25 |
| 23 | bare ground tundra | 0.03 | 0.00 | 0.00 | 0.00 | 0.00 | 0.00 |
| 24 | snow or ice | 0.01 | 0.00 | 0.00 | 0.00 | 0.00 | 0.00 |

Figure C.1: Characteristic parameters for land use from CLCC-data-set.

## C-2 External parameters: CORINE data-set

| No. | Land use class | $z_o$ [m] | root depth [m] | plant cover Max | plant cover Min | leaf area index Max | leaf area index Min |
|---|---|---|---|---|---|---|---|
| 1 | continuous urban fabric | 1.00 | 0.60 | 0.05 | 0.05 | 4.70 | 0.10 |
| 2 | discontinuous urban fabric | 1.00 | 0.60 | 0.20 | 0.05 | 4.70 | 0.10 |
| 3 | industrial/commercial units | 1.00 | 0.60 | 0.05 | 0.05 | 4.70 | 0.10 |
| 4 | road and rail networks | 0.10 | 0.10 | 0.05 | 0.05 | 4.70 | 0.10 |
| 5 | port areas | 1.00 | 0.10 | 0.05 | 0.05 | 4.70 | 0.10 |
| 6 | airports | 0.10 | 0.10 | 0.30 | 0.10 | 4.50 | 0.50 |
| 7 | mineral extraction sites | 0.10 | 0.10 | 0.05 | 0.05 | 1.00 | 0.50 |
| 8 | dump sites | 0.10 | 0.10 | 0.05 | 0.05 | 1.00 | 0.50 |
| 9 | construction sites | 1.00 | 0.60 | 0.10 | 0.05 | 1.00 | 0.50 |
| 10 | green urban areas | 0.25 | 1.00 | 1.00 | 0.80 | 5.80 | 1.40 |
| 11 | sport and leisure facilities | 0.03 | 0.60 | 1.00 | 0.80 | 5.80 | 1.40 |
| 12 | non-irrigated arable land | 0.10 | 1.00 | 0.90 | 0.45 | 5.00 | 0.20 |
| 13 | permanently irrigated land | 0.10 | 0.60 | 1.00 | 0.50 | 5.60 | 0.20 |
| 14 | rice fileds | 0.10 | 0.60 | 1.00 | 0.00 | 4.50 | 0.00 |
| 15 | vineyards | 0.30 | 0.60 | 0.90 | 0.30 | 4.00 | 0.10 |
| 16 | fruit trees and berry plant. | 0.80 | 0.60 | 1.00 | 0.00 | 6.00 | 0.00 |
| 17 | olive groves | 1.00 | 0.60 | 1.00 | 0.50 | 5.00 | 3.00 |
| 18 | pastures | 0.10 | 0.60 | 1.00 | 0.50 | 4.50 | 0.50 |
| 19 | annual crops | 0.50 | 0.80 | 1.00 | 0.50 | 5.00 | 0.20 |
| 20 | complex cultivation patterns | 0.15 | 1.00 | 0.90 | 0.20 | 5.30 | 0.20 |
| 21 | agriculture (principally) | 0.15 | 1.00 | 0.90 | 0.30 | 5.30 | 0.20 |
| 22 | agro-forestry areas | 0.25 | 1.00 | 0.90 | 0.45 | 6.10 | 1.20 |
| 23 | broadleaf forest | 1.00 | 1.00 | 1.00 | 0.00 | 6.00 | 0.00 |
| 24 | coniferous forest | 1.00 | 0.60 | 1.00 | 1.00 | 8.00 | 8.00 |
| 25 | mixed forest | 1.00 | 0.80 | 1.00 | 0.50 | 7.00 | 4.00 |
| 26 | natural grassland | 0.03 | 0.60 | 1.00 | 1.00 | 4.50 | 0.50 |
| 27 | moors and heathlands | 0.05 | 0.40 | 0.80 | 0.40 | 3.00 | 1.00 |
| 28 | sclerophyllus vegetation | 0.50 | 0.60 | 0.80 | 0.65 | 4.30 | 3.00 |
| 29 | transitional woodland-shrub | 0.60 | 0.90 | 0.70 | 0.40 | 5.50 | 1.10 |
| 30 | beaches, dunes, sand | 0.02 | 0.30 | 0.10 | 0.05 | 1.00 | 0.50 |
| 31 | bare rocks | 0.10 | 0.00 | 0.00 | 0.00 | 0.00 | 0.00 |
| 32 | sparsely vegetated areas | 0.05 | 0.30 | 0.05 | 0.02 | 1.00 | 0.50 |
| 33 | burnt areas | 0.05 | 0.30 | 0.05 | 0.02 | 0.50 | 0.50 |
| 34 | glaciers and perpetual snow | 0.01 | 0.00 | 0.00 | 0.00 | 0.00 | 0.00 |
| 35 | inland marshes | 0.03 | 0.60 | 1.00 | 1.00 | 4.50 | 0.50 |
| 36 | peat bogs | 0.05 | 0.40 | 0.80 | 0.40 | 3.00 | 1.00 |
| 37 | salt marshes | 0.03 | 0.60 | 0.80 | 0.80 | 3.00 | 1.00 |
| 38 | salines | 0.02 | 0.00 | 0.00 | 0.00 | 0.00 | 0.00 |
| 39 | intertidal flats | 0.01 | 0.00 | 0.00 | 0.00 | 0.00 | 0.00 |
| 40 | water courses | 0.0002 | 0.00 | 0.00 | 0.00 | 0.00 | 0.00 |
| 41 | water bodies | 0.0002 | 0.00 | 0.00 | 0.00 | 0.00 | 0.00 |
| 42 | coastal lagoones | 0.0002 | 0.00 | 0.00 | 0.00 | 0.00 | 0.00 |
| 43 | estuaries | 0.0002 | 0.00 | 0.00 | 0.00 | 0.00 | 0.00 |
| 44 | sea and ocean | 0.0002 | 0.00 | 0.00 | 0.00 | 0.00 | 0.00 |

7

Figure C.2: Characteristic parameters for land use from the CORINE-data-set.

## C-3 External parameters: GLC 2000 data-set

| No. | Land use class | $z_o$ [m] | root depth [m] | plant cover | | leaf area index | |
|---|---|---|---|---|---|---|---|
| | | | | Max | Min | Max | Min |
| 1 | evergreen broadleaf forest | 1.00 | 1.00 | 0.80 | 0.80 | 2.40 | 1.40 |
| 2 | deciduous broad closed | 1.00 | 1.00 | 0.90 | 0.75 | 3.40 | 1.00 |
| 3 | deciduous broadleaf open | 0.15 | 2.00 | 0.80 | 0.70 | 2.00 | 1.00 |
| 4 | evergreen needleleaf forest | 1.00 | 0.60 | 0.80 | 0.80 | 3.80 | 1.30 |
| 5 | deciduous needleleaf forest | 1.00 | 0.60 | 0.90 | 0.75 | 3.80 | 1.00 |
| 6 | mixed leaf trees | 1.00 | 0.80 | 0.90 | 0.75 | 3.40 | 1.10 |
| 7 | fresh water flooded trees | 1.00 | 1.00 | 0.80 | 0.80 | 2.40 | 1.40 |
| 8 | saline water flooded trees | 1.00 | 1.00 | 0.80 | 0.80 | 2.40 | 1.40 |
| 9 | mosaic tree/natural veget. | 0.20 | 1.00 | 0.80 | 0.70 | 1.50 | 0.60 |
| 10 | burnt tree cover | 0.05 | 0.30 | 0.50 | 0.50 | 0.60 | 0.40 |
| 11 | evergreen shrubs closed/open | 0.20 | 1.00 | 0.80 | 0.70 | 1.50 | 0.60 |
| 12 | deciduous shrubs closed/open | 0.15 | 2.00 | 0.80 | 0.70 | 2.00 | 1.00 |
| 13 | herbaceous veget.closed/open | 0.03 | 0.60 | 0.90 | 0.75 | 3.10 | 1.00 |
| 14 | sparse herbaceous or grass | 0.05 | 0.30 | 0.50 | 0.50 | 0.60 | 0.40 |
| 15 | flooded shrubs or herbaceous | 0.05 | 0.40 | 0.80 | 0.70 | 2.00 | 1.00 |
| 16 | cultivated and managed | 0.07 | 1.00 | 0.90 | 0.50 | 3.30 | 0.70 |
| 17 | mosaic crop/tree/net veget. | 0.25 | 1.00 | 0.80 | 0.65 | 2.10 | 1.00 |
| 18 | mosaic crop/shrub/grass | 0.07 | 1.00 | 0.90 | 0.50 | 3.30 | 0.70 |
| 19 | bare areas | 0.05 | 0.30 | 0.50 | 0.20 | 0.60 | 0.40 |
| 20 | water | 0.0002 | 0.00 | 0.00 | 0.00 | 0.00 | 0.00 |
| 21 | snow and icea | 0.01 | 0.00 | 0.00 | 0.00 | 0.00 | 0.00 |
| 22 | artificial surface | 1.00 | 0.60 | 0.20 | 0.10 | 1.00 | 0.10 |
| 23 | undefined | - | - | - | - | - | - |

Figure C.3: Characteristic parameters for land use from the GLC2000-data-set.

## C-4 Additional verification results

| Switzerland temperature | case | RMSE | delta RMSE | ME | STDE | CORR |
|---|---|---|---|---|---|---|
| 20.12.2007 | opr | 5.15 | | -3.02 | 4.17 | 0.651 |
| 20.12.2007 | new | 4.09 | -1.06 | -1.37 | 3.86 | 0.581 |
| 20.12.2007 | newlog | 3.96 | -1.19 | -1.51 | 3.67 | 0.616 |
| 20.12.2007 | ecmwf | 5.13 | -0.02 | -2.55 | 4.45 | 0.587 |
| 18.08.2006 | opr | 4.90 | | -1.81 | 4.56 | 0.837 |
| 18.08.2006 | new | 4.26 | -0.65 | -1.57 | 3.96 | 0.840 |
| 18.08.2006 | newlog | 4.15 | -0.75 | -1.45 | 3.89 | 0.839 |
| 18.08.2006 | ecmwf | 4.15 | -0.75 | -1.38 | 3.91 | 0.833 |
| 15.04.2007 | opr | 5.60 | | -3.61 | 4.29 | 0.838 |
| 15.04.2007 | new | 4.80 | -0.80 | -2.93 | 3.81 | 0.840 |
| 15.04.2007 | newlog | 4.50 | -1.10 | -2.72 | 3.58 | 0.854 |
| 15.04.2007 | ecmwf | 4.88 | -0.73 | -3.21 | 3.67 | 0.853 |
| 26.07.2007 | opr | 2.57 | | -0.97 | 2.38 | 0.924 |
| 26.07.2007 | new | 2.47 | -0.10 | -0.87 | 2.31 | 0.925 |
| 26.07.2007 | newlog | 2.33 | -0.24 | -0.88 | 2.16 | 0.935 |
| 26.07.2007 | ecmwf | 2.31 | -0.26 | -1.08 | 2.05 | 0.941 |
| 15.10.2006 | opr | 4.19 | | -1.83 | 3.77 | 0.743 |
| 15.10.2006 | new | 3.59 | -0.60 | -0.63 | 3.54 | 0.696 |
| 15.10.2006 | newlog | 3.35 | -0.84 | -0.88 | 3.24 | 0.739 |
| 15.10.2006 | ecmwf | 3.57 | -0.63 | -1.43 | 3.27 | 0.761 |
| **Switzerland dew point** | **case** | **RMSE** | **delta RMSE** | **ME** | **STDE** | **CORR** |
| 20.12.2007 | opr | 5.63 | | -0.43 | 5.61 | 0.554 |
| 20.12.2007 | new | 5.33 | -0.30 | -0.70 | 5.29 | 0.597 |
| 20.12.2007 | newlog | 4.84 | -0.79 | -0.74 | 4.78 | 0.651 |
| 20.12.2007 | ecmwf | 5.35 | -0.28 | -1.06 | 5.25 | 0.613 |
| 18.08.2006 | opr | 4.11 | | 0.75 | 4.04 | 0.726 |
| 18.08.2006 | new | 3.76 | -0.35 | 0.44 | 3.74 | 0.725 |
| 18.08.2006 | newlog | 3.57 | -0.54 | 0.14 | 3.57 | 0.732 |
| 18.08.2006 | ecmwf | 3.55 | -0.56 | 0.17 | 3.54 | 0.730 |
| 15.04.2007 | opr | 4.85 | | 1.90 | 4.46 | 0.655 |
| 15.04.2007 | new | 4.29 | -0.55 | 1.07 | 4.16 | 0.693 |
| 15.04.2007 | newlog | 4.06 | -0.79 | 0.80 | 3.98 | 0.712 |
| 15.04.2007 | ecmwf | 4.17 | -0.67 | 0.89 | 4.08 | 0.698 |
| 26.07.2007 | opr | 3.81 | | 2.14 | 3.16 | 0.742 |
| 26.07.2007 | new | 3.36 | -0.45 | 1.56 | 2.98 | 0.766 |
| 26.07.2007 | newlog | 3.19 | -0.63 | 1.27 | 2.92 | 0.767 |
| 26.07.2007 | ecmwf | 3.20 | -0.62 | 1.28 | 2.93 | 0.766 |
| 15.10.2006 | opr | 4.52 | | 0.92 | 4.43 | 0.753 |
| 15.10.2006 | new | 4.05 | -0.47 | 0.58 | 4.01 | 0.797 |
| 15.10.2006 | newlog | 4.07 | -0.46 | 0.41 | 4.05 | 0.794 |
| 15.10.2006 | ecmwf | 4.18 | -0.34 | 0.27 | 4.18 | 0.782 |

Table C.1: Summary of the results for the 2 m temperature (upper part) and 2 m dew point (lower part) for the domain Switzerland (66 SYNOP stations): five days and 4 options are compared. Note the column with the reduction of the root mean square error ($\Delta$RMSE) compared to the operational version.

| Model domain | case | RMSE | delta RMSE | ME | STDE | CORR |
|---|---|---|---|---|---|---|
| 20.12.2007 | opr | 2.57 | | -1.13 | 2.30 | 0.878 |
| 20.12.2007 | new | 2.39 | -0.17 | -0.91 | 2.22 | 0.878 |
| 20.12.2007 | newlog | 2.27 | -0.29 | -0.81 | 2.13 | 0.887 |
| 20.12.2007 | ecmwf | 2.51 | -0.06 | -1.02 | 2.29 | 0.877 |
| 18.08.2006 | opr | 2.50 | | -0.38 | 2.47 | 0.895 |
| 18.08.2006 | new | 2.33 | -0.17 | -0.48 | 2.28 | 0.905 |
| 18.08.2006 | newlog | 2.29 | -0.21 | -0.44 | 2.25 | 0.907 |
| 18.08.2006 | ecmwf | 2.32 | -0.17 | -0.49 | 2.27 | 0.904 |
| 15.04.2007 | opr | 3.04 | | -0.53 | 3.00 | 0.867 |
| 15.04.2007 | new | 2.82 | -0.22 | -0.53 | 2.77 | 0.878 |
| 15.04.2007 | newlog | 2.76 | -0.29 | -0.44 | 2.72 | 0.880 |
| 15.04.2007 | ecmwf | 2.78 | -0.26 | -0.67 | 2.70 | 0.883 |
| 26.07.2007 | opr | 2.21 | | -0.61 | 2.12 | 0.923 |
| 26.07.2007 | new | 2.17 | -0.04 | -0.68 | 2.06 | 0.929 |
| 26.07.2007 | newlog | 2.15 | -0.05 | -0.66 | 2.05 | 0.931 |
| 26.07.2007 | ecmwf | 2.15 | -0.06 | -0.75 | 2.01 | 0.934 |
| 15.10.2006 | opr | 2.77 | | -0.73 | 2.68 | 0.866 |
| 15.10.2006 | new | 2.66 | -0.12 | -0.53 | 2.60 | 0.871 |
| 15.10.2006 | newlog | 2.60 | -0.18 | -0.51 | 2.55 | 0.877 |
| 15.10.2006 | ecmwf | 2.61 | -0.16 | -0.66 | 2.53 | 0.879 |
| **Model domain** | **case** | **RMSE** | **delta RMSE** | **ME** | **STDE** | **CORR** |
| 20.12.2007 | opr | 2.63 | | -0.08 | 2.63 | 0.863 |
| 20.12.2007 | new | 2.62 | -0.01 | -0.14 | 2.62 | 0.867 |
| 20.12.2007 | newlog | 2.44 | -0.19 | -0.21 | 2.43 | 0.884 |
| 20.12.2007 | ecmwf | 2.58 | -0.05 | -0.24 | 2.57 | 0.873 |
| 18.08.2006 | opr | 2.98 | | 1.10 | 2.77 | 0.687 |
| 18.08.2006 | new | 2.90 | -0.08 | 0.98 | 2.73 | 0.692 |
| 18.08.2006 | newlog | 2.78 | -0.20 | 0.80 | 2.67 | 0.705 |
| 18.08.2006 | ecmwf | 2.75 | -0.24 | 0.73 | 2.65 | 0.706 |
| 15.04.2007 | opr | 3.49 | | 1.18 | 3.29 | 0.732 |
| 15.04.2007 | new | 3.29 | -0.20 | 0.93 | 3.16 | 0.756 |
| 15.04.2007 | newlog | 3.17 | -0.33 | 0.72 | 3.08 | 0.768 |
| 15.04.2007 | ecmwf | 3.24 | -0.26 | 0.77 | 3.14 | 0.758 |
| 26.07.2007 | opr | 3.10 | | 1.57 | 2.67 | 0.668 |
| 26.07.2007 | new | 2.98 | -0.11 | 1.43 | 2.62 | 0.684 |
| 26.07.2007 | newlog | 2.83 | -0.26 | 1.25 | 2.54 | 0.701 |
| 26.07.2007 | ecmwf | 2.84 | -0.25 | 1.26 | 2.55 | 0.701 |
| 15.10.2006 | opr | 3.07 | | 1.00 | 2.91 | 0.844 |
| 15.10.2006 | new | 2.94 | -0.13 | 0.88 | 2.81 | 0.856 |
| 15.10.2006 | newlog | 2.92 | -0.15 | 0.83 | 2.80 | 0.856 |
| 15.10.2006 | ecmwf | 2.91 | -0.16 | 0.77 | 2.80 | 0.856 |

Table C.2: Summary of the results for the 2 m temperature (upper part) and 2 m dew point (lower part) for the entire COSMO 7 domain (about 1100 SYNOP stations): five days and 4 options are compared. Note the column with the reduction of the root mean square error ($\Delta$RMSE) compared to the operational version.

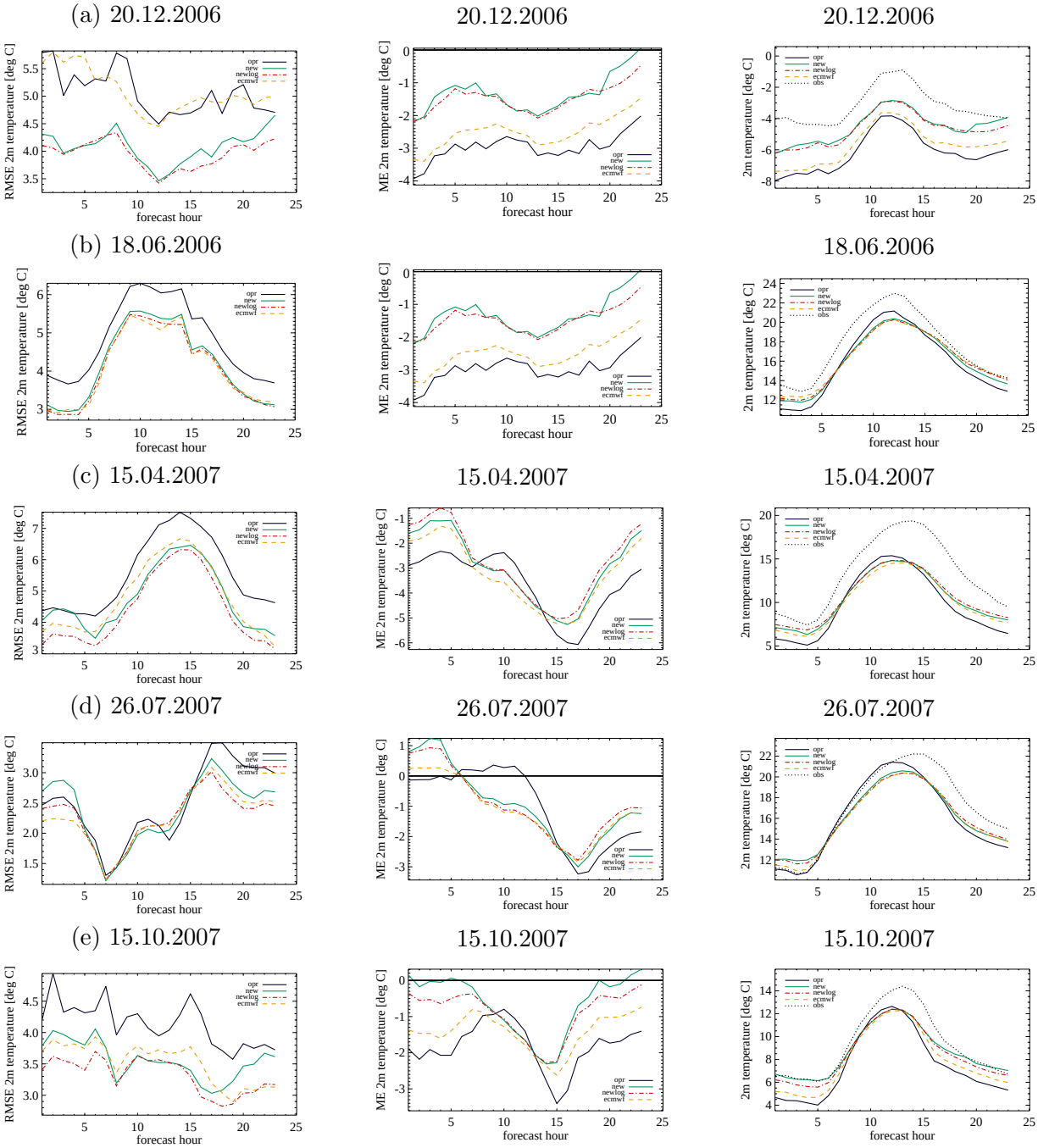


Figure C.4: Verification of the 2 m temperature for the domain covering Switzerland: left panel the daily cycle of the root mean square error (RMSE), right panel the daily cycle of the mean error (ME) and right panel the averaged daily cycle.

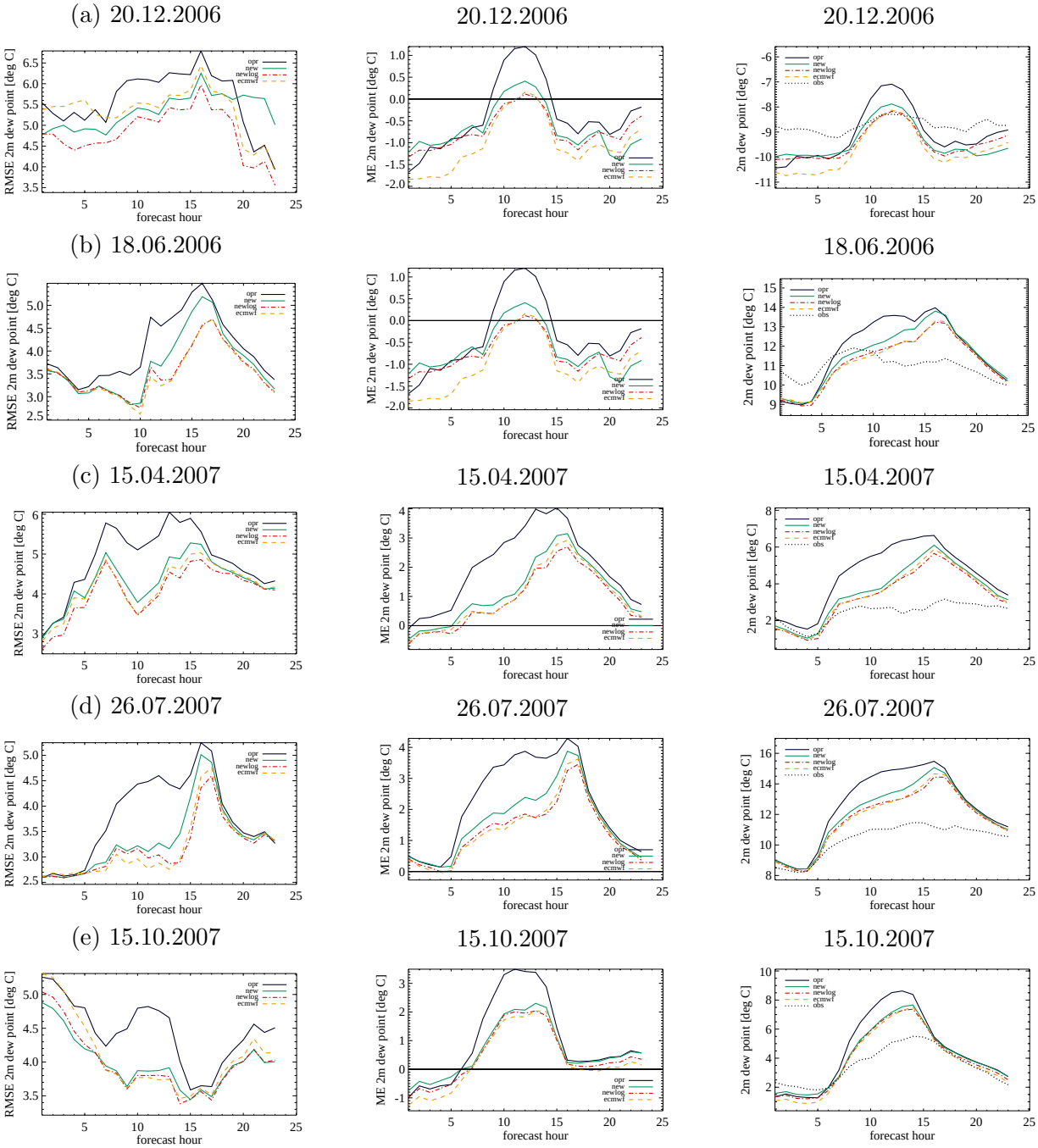


Figure C.5: Verification of the 2 m dew point for the domain covering Switzerland: left panel the daily cycle of the root mean square error (RMSE), right panel the daily cycle of the mean error (ME) and right panel the averaged daily cycle.

# Bibliography


Allen, R. G., M. Jensen, J. Wright, and R. Burman, 1989: Operational estimates of evapotranspiration. *Agron. J.*, pp. 650–662.

Ament, F., and C. Simmer, 2006: Improved representation of land-surface heterogeneity in a non-hydrostatic numerical weather prediction model. *Boundary-Layer Meteorol.*, **121**, 153–174.

Andre, J. C., and L. Mahrt, 1982: The nocturnal surface inversion and influence of clear-air radiation. *J. Atmos. Sci.*, **39**, 864–878.

Antonia, R. A., 1981: Conditional sampling in turbulence measurements. *Ann. Rev. Fluid Mech.*, **13**, 131–156.

Arakawa, A., and V. R. Lamb, 1977: Computational design of the basic dynamical processes of the UCLA general circulation model. *Methods in computational physics*, vol. 17, Academic Press, pp. 173–265.

Arpagaus, M., P. Kaufmann, G. D. Morsier, D. Ruffieux, F. Schubiger, and E. Zala, 2006: Verification of aLMo in the year 2005. *COSMO Newsletter No. 6*, Consortium for Small-Scale Modelling, available at: http://www.cosmo-model.org.

Athens, R. A., 1974: Data assimilation and initialisation of hurricane predictions models. *J. Atmos. Sci.*, **31**, 702–719.

Banta, R. M., Y. L. Pichugina, and R. K. Newson, 2003: Relationship between low-level jet properties and turbulence kinetik energy in the nocturnal stable boundary layer. *J. Atmos. Sci.*, **60**, 2549–2555.

Banta, R. M., Y. L. Pichugina, and W. A. Brewer, 2006: Turbulent velocity-variance profiles in the stable boundary layer generated by a nocturnal low-level jet. *J. Atmos. Sci.*, **63**, 2700–2719.

Barry, R. G., 1992: *Mountain Weather and Climate*. Routledge.

Beare, R. J., et al., 2006: An intercomparison of large-eddy simulations of the stable boundary layer. *Bound.-Layer Meteorol.*, **118**, 247–272.

Bechtold, P., E. Bazile, F. Guichard, P. Mascart, and E. Richard, 2001: A mass-flux convection scheme for regional and global models, part I. *Quart. J. Roy. Meteor. Soc.*, **127**, 869–886.

Beljaars, A. C., and A. A. Holtslag, 1991: Flux parameterization and land-surface in atmospheric models. *J. Appl. Meteor.*, **30**, 327–341.

Beljaars, A. C. M., A. R. Brown, and N. Wood, 2004: A new parameterization of turbulent orographic form drag. *Quart. J. Roy. Meteor. Soc.*, **130**, 1327–1347.

Benoit, R., M. Desgagne, P. Pellerin, Y. Chartier, and S. Desjardins, 1997: The canadian MC2: a semi-lagrancian, semi implicit wide-band atmosphere model suited for fine-scale process studies and simulations. *Monthly Weather Review*, **125**, 2382–2415.

Blackadar, A. K., 1957: Boundary layer wind maxima and their significance for the growth of nocturnal inversions. *Bull. Amer. Meteor. Soc.*, **83**, 283–290.

Blackadar, A. K., 1962: The vertical distribution of wind and turbulence exchange in a neutral atmosphere. *J. Geophys. Res.*, **67**, 3095–3102.

Blumen, W., 1990: Mountain meteorology. *Atmospheric Processes over Complex Terrain*, American Meteorological Society, Meteorological Monographs.

Blyth, E. M., and A. J. Dolman, 1995: The roughness length for heat of sparse vegetation. *J. Appl. Meteor.*, **34**, 327–341.

Bou-Zeid, E., C. Meneveau, and M. B. Parlange, 2004: Large-eddy simulation of neutral atmospheric boundary layer flow over heterogeneous surfaces: blending height and effective surface roughness. *Water Resources Research*, **40**(W02505), 1–18.

Bougeault, P., P. Binder, A. Buzzi, R. Dirks, R. Houze, J. Kuettner, R. B. Smith, R. Steinacker, and H. Volkert, 2001: The MAP special observing period. *Bull. Amer. Meteor. Soc.*, **82**, 433–462.

Breuer, L., K. Eckhard, and H.-G. Frede, 2003: Plant parameter values for models in temperate climates. *Ecol. Model.*, **169**, 237–293.

Brown, A. R., and N. Wood, 2001: Turbulent form drag on isotropic three-dimensional orography. *Bound.-Layer Meteorol.*, **101**, 229–241.

Brutsaert, W., 1982: *Evaporation in the Atmosphere*. D. Reidel.

Brutsaert, W., and M. Sugita, 1996: Sensible heat transfer parameterizations for surfaces with dense vegetation or similar permeable roughness. *Bound.-Layer Meteor.*, **53**, 209–216.

Burchard, H., and E. Deleersnijder, 2001: Stability of algebraic non-equilibrium second order closure models. *Ocean Modelling*, **3**, 33–50.

Burk, S. D., and W. T. Thompson, 1989: A vertically nested regional numerical weather prediction model with second-order closure physics. *Monthly Weather Review*, **117**, 2305–2324.

Businger, J. A., J. C. Wyngaard, Y. Izumi, and E. F. Bradley, 1971: Flux profile relationships in the atmospheric surface layer. *J. Atmos. Sci.*, **28**, 181–189.

Calanca, P., 2001: A note on the roughness length for temperature over melting snow and ice. *Quart. J. Roy. Meteor. Soc.*, **127**, 255–260.

Chapman, L., and J. E. Thornes, 2004: Real-time sky-view factor calculation and approximation. *Journal of Atmospheric and Oceanic Technology*, **21**, 730–741.

Charnock, H., 1955: Wind stress on a water surface. *Quart. J. Roy. Meteor. Soc.*, **81**, 639–640.

Chevallier, F., and J.-J. Morcrette, 2000: Comparison of model fluxes with surface and top-of-the atmosphere observations. *Monthly Weather Review*, **128**, 3839–3852.

Chow, F. K., 2004: Subfilter-scale turbulence modeling for large-eddy simulations of the atmospheric boundary layer over complex terrain, Ph.D. thesis, Standford University.

Chow, F. K., A. P. Weigel, R. L. Street, M. W. Rotach, and M. Xue, 2006: High-resolution large-eddy simulations of flow in a steep alpine valley. Part I: Methodology, verification and sensitivity studies. *J. App. Meteor.*, **45**, 63–86.

Christen, A., 2005: Atmospheric turbulence and surface energy exchange in urban environments: results from the Basel Urban Boundary Layer Experiment (BUBBLE), Ph.D. thesis, UNI Basel, ISBN 3-85977-266.

Clark, T. L., and W. D. Hall, 1991: Multi-domain simulations of the time dependent Navier Stokes equations: benchmark error analysis of some nesting procedures. *J. Comp. Phys.*, **92**, 456–481.

Colette, A., F. K. Chow, and R. L. Street, 2003: A numerical study of inversion-layer breakup and the effects of topographic shading in idealized valleys. *J. App. Meteor.*, **42**, 1255–1272.

Cuxart, J., et al., 2006: Single-column model intercomparisopn for a stably stratified atmospheric boundary layer. *Boundary-Layer Meteorol.*, **118**, 273–303.

Davies, H. C., 1976: A lateral boundary formulation for multi-level prediction models. *Quart. J. Roy. Meteor. Soc.*, **102**, 1002–1012.

Davies, H. C., and R. E. Turner, 1977: Updating prediction models by dynamical relaxation: an examination of the technique. *Quart. J. Roy. Meteor. Soc.*, **103**, 225–245.

Deardoff, J. W., 1972: Numerical investigation of neutral and unstable planetary boundary layers. *J. Atmos. Sci.*, **29**, 91–115.

Deardoff, J. W., 1980: Stratocumulus-capped mixed layers derived from a 3-dimensional model. *Bound.-Layer Meteorol.*, **18**, 495–527.

Deleersnijder, E., and H. Burchard, 2003: Reply to Mellor's comments on "Stability of algebraic non equilibrium second order closure models". *Ocean Modelling*, **5**, 291–293.

Denmead, O. T., and E. F. Bradley, 1987: On scalar transport in plant canopies. *Irrigation Science*, **8**, 131–149.

Derbyshire, S. H., 1999a: Boundary-layer decoupling over cold surfaces as physical boundary-instability. *Boundary-Layer Meteorol.*, **90**, 297–325.

Derbyshire, S. H., 1999b: Stable boundary layer modelling: established approaches and beyond. *Boundary-Layer Meteorol.*, **90**, 423–446.

DeWekker, S. F. J., D. G. Steyn, J. D. Fast, M. W. Rotach, and S. Zhong, 2005: The performance of RAMS in representing the convective boundary layer structure in a steep valley. *Environ. Fluid Mech.*, **5**, 35–62.

Doms, G., and J. Förstner, 2003: Developement of a kilometer-scale NWP-system: LMK. *COSMO Newsletter No. 4*, Consortium for Small-Scale Modelling, available at: http://www.cosmo-model.org.

Doms, G., and U. Schättler, 2002: *A description of the Nonhydrostatic Regional Model LM. Part 4: Implementation and documentation*, Deutscher Wetterdienst (DWD), Offenbach.

Doms, G., and U. Schättler, 2003a: *A description of the Nonhydrostatic Regional Model LM. Part 1: Dynamics and numerics*, Deutscher Wetterdienst (DWD), Offenbach.

Doms, G., and U. Schättler, 2003b: *A description of the Nonhydrostatic Regional Model LM. Part 3: Data assimilation*, Deutscher Wetterdienst (DWD), Offenbach.

Doms, G., and U. Schättler, 2005: *A description of the Nonhydrostatic Regional Model LM. Part 7: User Guide*, Deutscher Wetterdienst (DWD), Offenbach.

Doms, G., A. Gassmann, E. Heise, M. Raschendorfer, C. Schraff, and R. Schrodin, 2001: Parameterization issues in the non-hydrostatic NWP-model LM. *Key issues in the parameterization of subgrid physical processes*, European Centre for Medium-Range Weather Forecast, Proceedings of a seminar held at ECMWF.

Doms, G., J. Förster, E. Heise, H.-J. Herzog, M. Raschendorfer, R. Schrodin, T. Reinhardt, and G. Vogel, 2005: *A description of the Nonhydrostatic Regional Model LM. Part 2: Physical parameterizations*, Deutscher Wetterdienst (DWD), Offenbach.

Dubayah, C. R., and S. Loechel, 1997: Modelling topographic solar radiation using GOES data. *J. App. Meteor.*, **36**, 141–154.

Dudhia, J., 1993: A non-hydrostatic version of the Penn-State/NCAR mesoscale model: validation tests and simulation of an atlantic cyclone and cold front. *Monthly Weather Review*, **121**, 1493–1513.

Dürr, B., 2004: The greenhouse effect in the Alps - by models and observations, Ph.D. thesis, ETH Zürich.

Dürr, B., and A. Zelenka, 2007: Stallite derived surface global irradiance over the Alpine region from METEOSAT Second Generation data. *submitted Int. J. of Remote Sensing*.

DWD, 2004: LM external parameters, available at: Deutsche Wetterdienst (DWD), Offenbach.

Dyer, A. J., 1974: A review of flux-profile relationships. *Bound.-Layer Meteorol.*, **7**, 363–372.

ECMWF, 2007: *IFS documentation - Cy31r1, Operational implementation 12 September 2006, PART IV: physical processes*, available at: www.ecmwf.int.

Estourel, C., R. Vehil, and D. Guedalia, 1986: An observational study of radiative and turbulent cooling in the nocturnal boundary layer (ECLATS experiment). *Bound.-Layer Meteor.*, **34**, 55–62.

Fiedler, F., and H. A. Panowsky, 1972: The geostrophic drag coefficient and the effective roughness length. *Quart. J. Roy. Meteor. Soc.*, **98**, 213–220.

Finnigan, J., 2000: Turbulence in plant canopies. *Ann. Rev. Fluid Mech.*, **32**, 519–571.

Forrer, J., and M. W. Rotach, 1997: On the turbulence structure in the stable boundary layer over the Greenland ice sheet. *Bound.-Layer Meteor.*, **85**, 111–136.

Förstner, J., and G. Doms, 2003: Runge-Kutta time integration and high-order spatial discretization of advection - a new dynamical core for the LMK. *COSMO Newsletter No. 4*, Consortium for Small-Scale Modelling, available at: http://www.cosmo-model.org.

Gal-Ghen, G. A., , and C. J. Sommerville, 1975: On the use of a coordinate transform for the solution of the Navier-Stokes equations. *J. Comput. Phys.*.

Gall, P., 1998: Strahlungsbilanz am Boden - Vergleich von SM-Prognosen mit BSRN-Messungen, Master's thesis, ETH Zürich.

Galperin, B., and L. H. Kantha, 1989: Turbulence model for rotating flows. *AIAA J.*, **27**, 750–757.

Galperin, B., and G. L. Mellor, 1991: The effects of streamline curvature and spanwise rotation on near-surface, turbulent boundary layers. *J. App. Math. Physics (ZAMP)*, **42**, 565–583.

Galperin, B., L. K. Kantha, S. Hassid, and A. Rosati, 1988: A quasi-equilibrium turbulent energy model for geophysical flows. *J. Atmos. Sci.*, **45**, 55–62.

Garnier, B. J., and A. Ohmura, 1968: A method of calculating the direct shorwave radiation income of slopes. *J. App. Meteor.*, **7**, 796–800.

Garnier, B. J., and A. Ohmura, 1969: The evaluation of surface variations in solar radiation income. *Solar Energy*, **13**, 21–33.

Garratt, J. R., 1980: Surface influence upon vertical profiles in the atmospheric near-surface layer. *Quart. J. Roy. Meteor. Soc.*, **106**, 803–819.

Garratt, J. R., 1992: *The atmospheric boundary layer*. Cambridge University Press, Cambridge New York Melbourne, pp. 316.

Garratt, J. R., and R. A. Brost, 1981: Radiative cooling effects within and above the nocturnal boundary layer. *J. Atmos. Sci.*, **38**.

Garratt, J. R., and R. J. Francey, 1978: Bulk characteristics of heat transfer in the unstable, baroclinic atmospheric boundary layer. *Bound.-Layer Meteor.*, **15**, 399–421.

Garratt, J. R., and B. B. Hicks, 1973: Momentum,heat and water vapour transfer to and from natural and artificial surfaces. *Quart. J. Roy. Meteor. Soc.*, **99**, 680–687.

Gassmann, A., 2001: Filtering of LM-topography. *COSMO Newsletter No. 1*, Consortium for Small-Scale Modelling, http://www.cosmo-model.org.

Geleyn, J. F., 1988: Interpolation of, wind, temperature and humidity values from model levels to the height of measurements. *Tellus*, **40A**, 347–351.

Georgelin, M., P. Bougeault, M. Dèquè, V. Invanovici, and coauthors, 2000: The second COMPARE exercice: A model intercomparison using a case of a typical mesoscale orographic flow the PYREX IOP3. *Quart. J. Roy. Meteor. Soc.*, **126**, 991–1029.

Gohm, A., G. Zängl, and G. J. Mayr, 2004: South foehn in the Wipp Valley on 24 october 1999 (MAP IOP 10): verification of high-resolution numerical simulations with observations. *Monthly Weather Review*, **132**, 78–102.

Graser, E. A., S. B. Verma, and N. J. Rosenberg, 1987: Within-canopy temperature patterns of sorghum at two row spacings. *Agricoltural and Forest Meteorology*, **41**, 187–205.

Grell, G. A., J. Dudhia, and D. R. Stauffer, 1995: A description of the fifth-generation Penn State/NCAR mesoscale model MM5. NCAR, Tech. rep., NCAR/TN 398, STR.

Ha, K.-J., and L. Mahrt, 2003: Radiative and turbulent fluxes in the nocturnal boundary layer. *Tellus*, **55A**, 317–327.

Haugen, D., J. C. Kaimal, and E. Bradley, 1971: An experimental study of an experimental study of Reynolds stress and heat flux in the atmospheric surface layer. *Quart. J. Roy. Meteor. Soc.*, **97**, 168–180.

Högström, U., 1988: Non-dimensional wind and temperature profiles in the atmospheric surface layer: A re-evaluation. *Bound.-Layer Meteor.*, **42**, 55–78.

Högström, U., 1996: Review of some basic characteristics of the atmospheric surface layer. *Bound.-Layer Meteorol.*, **78**, 215–246.

Hohenegger, C., and C. Schär, 2007: Atmospheric predictability at synoptic versus cloud-resolving scales. *Bull. Amer. Meteor. Soc.*, **88**(11), 1783–1793.

Holtslag, A. A., and F. T. M. Nieuwstadt, 1986: Scaling the atmospheric boundary layer. *Bound.-Layer Meteor.*, **36**, 201–209.

Holtslag, A. A. M., 2006: Gewex atmospheric-boundary layer study (gabls) on stable boundary layers. *Bound.-Layer Meteor.*, **118**, 243–246.

Holtslag, A. A. M., and B. A. Boville, 1993: Local versus nonlocal boundary-layer diffusion in a global climate model. *J. Climate*, **6**, 1825–1842.

Holtslag, A. A. M., R. J. Beare, and J. C. Rodamillans, 2003: GABLS workshop on stable boundary layers. *GEWEX News, GEWEX newsletter*, **13**(4), 11–13.

Holtslag, A. A. M., G. J. Steeneveld, and B. J. H. V. de Wiel, 2007: Role of land-surface temperature feedback on model performance for the stable boundary layer. *Bound.-Layer Meteor.*, **125**, 361–376.

Hong, S.-H., and H.-L. Pan, 1996: Nonlocal boundary layer vertical diffusion in a medium range forecast model. *Monthly Weather Review*, **124**, 2322–2339.

Jacobs, A. F. G., J. H. Boxel, and R. M. M. El-Kilani, 1995: Vertical and horizontal distribution of wind speed and air temperature in a dense vegetation canopy. *Journal of Hydrology*, **166**, 313–326.

Jacobsen, I., and E. Heise, 1982: A new economic method for the computation of the surface temperature in numerical models. *Contr. Atmos. Phys.*, **55**, 128–141.

Janjic, Z. I., 1990: The step mountain coordinate: physical package. *Monthly Weather Review*, **118**, 1429–1443.

Janjic, Z. I., 1994: The step-mountain eta coordinate model: further development of the convection, viscous sublayer and turbulence closure schemes. *Monthly Weather Review*, **122**, 927–945.

Janjic, Z. I., 2001: Nonsingular implementation of the Mellor-Yamada level 2.5 scheme in the NCEP Meso model. National Centers For Environmental Prediction, Office Note 437.

Janjic, Z. I., 2003: A non-hydrostatic model based on a new approach. *Meteorol. Atmos. Phys.*, **82**, 271–285.

Jarvis, A., J. Rubiano, A. Nelson, A. Farrow, and M. Mulligan, 2004: Practical use of SRTM data in the tropics - comparisons from cartographic data. Centro International de Agricoltura Tropical, Colombia, Working Document 198.

Johnson, G. T., and I. D. Watson, 1984: The determination of viewfactors in urban canyons. *J. Appl. Climate Meteor.*, **23**, 329–335.

Kaimal, J., J. C. Wyngaard, Y. Izumi, and O. R. Coté, 1972: Spectral characteristics of surface layer turbulence. *Quart. J. Roy. Meteor. Soc.*, **98**, 563–589.

Kaimal, J. C., and J. J. Finnigan, 1994: *Atmospheric Boundary layer Flows: their structure and measurements*. Oxford University Press, New York, 289pp.

Kain, J. S., and J. M. Fritsch, 1993: Convective parameterization of mesoscale models: The Kain-Fritsch-Scheme. *Meteor. Mongr.*, Amer. Meter. Soc.

Kantha, L., 2003: On an improved model for the turbulent PBL. *J. Atmos. Sci.*, **60**, 2239–2246.

Kantha, L. H., 2004: The length scale equation in turbulence models. *Nonlinear Processes in Geophysics*, **11**, 83–97.

Kantha, L. H., and C. A. Clayson, 1994: An improved mixed layer model for geophysical applications. *J. Geophys. Res.*, **99**, 235–266.

Karlsson, M., 2000: Nocturnal air temperature variation between forest and open areas. *J. Appl. Meteor.*, **39**, 851–862.

Kastner-Klein, P., and M. W. Rotach, 2004: Mean flow and turbulence characteristics in an urban roughness sublayer. *Bound.-Layer Meteorol.*, **111**, 55–84.

Katul, G., D. Poggi, and D. Cava, 2006: The relative importance of ejection and sweeps to momentum transfer in the atmospsheric boundary layer. *Bound.-Layer Meteorol.*, **120**, 367–375.

Kessler, E., 1969: On the distribution and continuity of water substance in the atmospheric circulations. *Meteor. Mongr. Vol 24 No. 32*, Amer. Meter. Soc.

Klemp, J. B., and R. Wilhelmson, 1978: The simulation of three-dimensional convective storm dynamics. *J. Atmos. Sci.*, **35**, 1070–1096.

Kohsiek, W., H. A. R. D. Bruin, and B. J. J. M. Van den Hurk, 1993: Estimation of the sensible heat flux of a semi-arid area using surface radiative temperature measurements. *Bound.-Layer Meteor.*, **63**, 213–230.

Kolmogorov, A. N., 1941: The local structure of turbulence in incompressible viscous fluid for very large Reynolds numbers. *Doklady ANSSSR*, **30**, 301–304.

Kondratiev, K. J., Pivovavora, and M. P. Fedorova, 1978: The radiation regime of sloping surfaces. *Hydrometeoizdat*, p. 216.

Kondratiev, K. Y., 1977: Radiation regime of inclined surfaces. *WMO Tech. Note*, **152**. 82 pp.

Kumar, C., J. Kleissl, C. Meneveau, and M. B. Parlange, 2006: Large-eddy simulation of a dieunal cycle of the atmospheric boundary layer: atmospheric stability and scaling issues. *Water Resources Research*, **42**, W06D09 1–18.

Kunz, H., S. C. Scherrer, M. A. Liniger, and A. Christof, 2007: The evolution of ERA-40 surface temperatures and total ozone compared to observed Swiss time series. *Meteorologische Zeitschrift*, **16**(2), 171–181.

Kustas, W. P., B. J. Choudhurry, M. S. Moran, R. J. Reginato, R. D. Jackson, L. W. Gay, and H. L. Weaver, 1989: Determination of sensible heat flux over sparse canopy using thermal infrared data. *Agricoltural and Forest Meteorology*, **44**, 197–216.

Lalaurette, F., 2001: Verification of physical parameters: upscaling or downscaling? *Key issues in the parameterization of subgrid physical processes*, European Centre for Medium-Range Weather Forecast, pp. 339–349, Proceedings of a seminar held at ECMWF.

Leuenberger, D., and A. Rossa, 2007: Revisiting the latent heat nudging scheme for the rainfall assimilation of a simulated convective storm. *Meteor. Atmos. Phys.*, **98**, 195–215.

Louis, J. F., 1979: A parametric model of vertical eddy fluxes in the atmosphere. *Bound.-Layer Meteor.*, **17**, 187–202.

Mahrt, L., 1999: Stratified atmospheric boundary layers. *Boundary-Layer Meteorol.*, **90**, 375–396.

Mahrt, L., and D. Vickers, 2006: Extremely weak mixing in stable conditions. *Boundary-Layer Meteorol.*, **119**, 19–39.

Majewski, D., and B. Ritter, 2006: Gebirgeinflüsse in operationellen numerischen Wettervohersagemodellen. *Promet - DWD*, **32**, 68–64.

Malhi, Y., 1996: The behaviour of the roughness length for tempertaure over heterogenous surfaces. *Quart. J. Roy. Meteor. Soc.*, **122**, 1095–1125.

Marshall, C. H., K. C. Crawford, K. E. Mitchell, and D. J. Stensrud, 2003: The impact of the land surface physics in the operational NCEP Eta model on simulating the diurnal cycle: evaluation and testing using Oklaoma mesonet data. *Weather Forecasting*, **18**, 748–768.

Martilli, A., A. Clappier, and M. W. Rotach, 2002: An urban surface exchange parameterisation for mesoscale models. *Bound.-Layer Meteor.*, **104**, 262–304.

Marty, C., R. Philipona, C. Fröhlich, and A. Ohmura, 2002: Altitude dependence of surface radiation fluxes and cloud forcing in the Alps: results from the alpine surface radiation budget network. *Theor. and App. Clim*, **72**(3-4), 137–155.

Mason, P. J., 1985: On the parameterization of the orographic drag. *Proc. Seminar on Physical parameterization for numerical Models of the atmosphere*, ECMWF, Ed., pp. 139–165.

Matzinger, N., M. Andretta, E. V. Gorsel, R. Vogt, A. Ohmura, and M. W. Rotach, 2003: Surface radiation budget in an alpine valley. *Quart. J. Roy. Meteor. Soc.*, **129**, 877–895.

Mauritsen, T., and G. Svensson, 2007: Observations of stably stratified shear-driven atmospheric turbulence at low and high Richardson numbers. *J. Atmos. Sci.*, **64**, 645–655.

Mellor, G. L., 2003: Comments on "stability of algebraic non-equilibrium second-order closure models" by H. Burchard and E. Deleersnijder". *Ocean Modelling*, **5**(193-194).

Mellor, G. L., and T. Yamada, 1974: A hierarchy of turbulence closure models for planetary boundary layers. *J. Atmos. Sci.*, **31**, 1791–1806.

Mellor, G. L., and T. Yamada, 1982: Developement of a turbulence closure model for geophysical fluid problems. *Reviews of Geophysics and Space Physics*, **20**, 851–875.

Moelder, M., and A. Lindroth, 1999: Thermal rougness length of a boreal forest. *Agricoltural and Forest Meteorology*, **98-99**, 659–670.

Moeng, C.-H., 1984: A large-eddy simulation model for the study of planetary boundary layer turbulence. *J. Atmos. Sci.*, **41**, 2052–2062.

Mölders, N., and A. Raabe, 1996: A comparison of two strategies on land surface heterogeneity used in a mesoscale $\beta$ meteorological model. *Tellus*, **48A**(733-749).

Molod, A., H. Salmun, and S. W. Waugh, 2003: A new look at modeling surface heterogenety. *Journal of Hydrometeorology*, **4**, 810–825.

Monin, A. S., and A. M. Obukhov, 1954: Basic laws of turbulent mixing in the ground layer of the atmosphere. *Tr. Geofiz. Inst. Akad. Nauk. SSSR*, **24**, 163–187.

Müller, M. D., and D. Scherrer, 2005: A grid and subgrid scale radiation parameterization of topographic effects for mesoscale weather forecast models. *Monthly Weather Review*, **133**, 1431–1442.

Nakamura, R., and L. Mahrt, 2005: A study of intermittend turbulence with CASES-99 tower measurements. *Bound.-Layer Meteor.*, **114**, 367–387.

Nieuwstadt, F. T. M., 1984a: The turbulent structure of the stable, nocturnal boundary layer. *J. Atmos. Sci.*, **41**, 2202.

Nieuwstadt, F. T. M., 1984b: Some aspects of the turbulent stable boundary layer. *Bound.-Layer Meteor.*, **30**, 31–55.

Nieuwstadt, F. T. M., P. J. Mason, C.-H. Moeng, and U. Schumann, 1993: Large eddy simulation of the convective boundary layer: A comparison of four computer codes. *Turbulent Shear Flows*, Springer-Verlag: Berlin.

Nunez, M., 1980: The calculation of solar and net radiation in montainous terrain. *Journal of Biogeography*, **7**(2), 173–186.

Oke, T. R., 1978: *Boundary Layer Climates*. Methuen, New York.

Oliphant, A., R. A. Spronken-Smith, A. P. Sturman, and I. F. Owens, 2003: Spatial variability of surface radiation fluxes in montainous terrain. *J. App. Meteor.*, **42**, 113–128.

Owen, P. R., and W. R. Thomson, 1963: Heat transfer across rough surfaces. *J. Fluid Mech.*, **15**, 321–334.

Pflüger, U., 2003: Operational verification of vertical profiles at DWD. *COSMO Newsletter No. 3*, Consortium for Small-Scale Modelling, available at: http://www.cosmo-model.org, pp. 93–100.

Pflüger, U., 2004: Operational verification of vertical profiles at DWD. *COSMO Newsletter No. 4*, Consortium for Small-Scale Modelling, available at: http://www.cosmo-model.org, pp. 95–103.

Pielke, R. A., W. R. Cotton, R. L. Walko, C. J. Tremback, W. A. L. L. D. Grasso, M. E. Nicholls, M. D. Moran, D. A. W. T. J. Lee, and J. H. Copeland, 1992: A comprehensive meteorological modeling system - RAMS. *Meteor. Atmos. Phys.*, **49**, 69–91.

Pinard, J. D. J.-P., and J. D. Wilson, 2001: First- and secon-order closure models for wind in a plant canopy. *J. Appl. Meteor.*, **40**, 1762–1768.

Plüss, C., and A. Ohmura, 1996: Longwave radiation on snow-covered montainous surfaces. *J. App. Meteor.*, **36**, 818–824.

Poulos, G. S., et al., 2002: CASES-99: A comprehensive investigation of the stable nocturnal boundary layer. *Bulletin of American Meteorological Society*, **83**, 555–581.

Press, W. H., B. P. Flannery, S. a Teukolsky, and W. T. Vetterlig, 1989: *Numerical Recipies : FORTRAN version*. Cambridge University Press, Cambridge, New York, Melbourne, Sydney, Port Chester, pp. 702.

Raschendorfer, M., 2001: The new turbulence Paramterization of LM. *COSMO Newsletter No. 1*, Consortium for Small-Scale Modelling, available at: http://www.cosmo-model.org.

Raschendorfer, M., 2007a: A new TKE-based scheme for vertical diffusion and surface-layer transfer, available at Deutscher Wetterdienst (DWD), Offenbach.

Raschendorfer, M., 2007b: A single column (SC) framework applied to the COSMO local model (SCLM), available at Deutscher Wetterdienst (DWD), Offenbach.

Raschendorfer, M., and D. Mironov, 2001: Evaluation of empirical parameters of the new LM surface-layer parameterization scheme. Results from numerical experiments including the soil moisture analysis. Consortium for Small-Scale Modelling (COSMO), available at www.cosmo-model.org, Tech. rep.

Raupach, M. R., 1987: A lagrancian analysis of scalar transfer in vegetation canopies. *Quart. J. Roy. Meteorol. Soc.*, **113**, 107–120.

Raupach, M. R., 1994: Simplified expressions for the vegetation roughness length and zero-plane displacement as function of canopy height and area index. *Boundary-Layer Meteorol.*, **71**, 211–216.

Raupach, M. R., 1995: Vegetation-atmosphere interaction and surface conductance at leaf, canopy and regional scales. *Agricoltural and Forest Meteorology*, **73**, 151–179.

Raupach, M. R., and A. S. Thom, 1981: Turbulence in and above plant canopies. *Ann. Rev. Fluid Mech.*, **13**, 97–129.

Raupach, M. R., A. S. Thom, and I. Edwards, 1980: A wind-tunnel study of turbulent flow close to regularly arrayed rough surfaces. *Bound.-Layer Meteor.*, **18**, 373–397.

Raupach, M. R., R. A. Antonia, and S. Rajagopalan, 1991: Rough-wall turbulent boundary layers. *Appl. Mech. Rev.*, **44**, 1–25.

Raupach, M. R., J. J. Finnigan, and Y. Brunet, 1996: Coherent eddies and turbulence in vegetation canopies: the mixing-layer analogy. *Bound.-Layer Meteor.*, **78**, 351–382.

Reinhardt, T., and A. Seifert, 2006: A three-category ice scheme for LMK. *COMSO Newsletter No. 6*, vol. 6, Consortium for Small-Scale Modelling, available at: http://www.cosmo-model.org, pp. 115–120.

Rife, D. L., A. Davis, and Y. Liu, 2004: Predictability of low-level winds by mesoscale meteorological models. *Monthly Weather Review*, **132**, 2553–2569.

Ritter, B., and J.-F. Geleyn, 1992: A comprehensive radiation scheme for numerical weather prediction models with potential applications in climate simulations. *Monthly Weather Review*, **120**, 303–325.

Rontu, L., 2006: A study on parameterization of orography-related momentum fluxes in a synoptic-scale NWP model. *Tellus*, **58A**, 69–81.

Rooy, W. C., and K. Kok, 2002: On the use of statistical downscaling techniques for NWP model output, available: http://www.knmi.nl/onderzk/index.html.

Rooy, W. C., and K. Kok, 2004: A combined physical-statistical approach for the downscaling of model wind speed. *Weather forecasting*, **19**, 485–495.

Rotach, M. W., 1993: Turbulence close to a rough urban surface Part I: Reynolds stress. *Bound.-Layer Meteor.*, **65**, 1–28.

Rotach, M. W., 1995: On the boundary layer over montainous terrain - a frog's perspective. *MAP-Newsletter*, **3**, 31–32.

Rotach, M. W., 1999: On the influence of the urban roughness sublayer on turbulence and dispersion. *Atmospheric Environment*, **33**, 24–25.

Rotach, M. W., 2001: Simulation of urban-scale dispersion using a lagrancian stochastic dispersion model. *Bound.-Layer Meteor.*, **99**, 379–410.

Rotach, M. W., and D. Zardi, 2007: On the boundary-layer structure over highly complex terrain: Key findings from MAP. *Quart. J. Roy. Meteor. Soc.*, **133**, 937–948.

Rotach, M. W., et al., 2004: Turbulence structure and exchange processes in an alpine valley, The Riviera Project. *Bull. Amer. Meteor. Soc.*, **85**, 1367–1384.

Roth, M., 2000: Review of atmospheric turbulence over cities. *Quart. J. Roy. Meteor. Soc.*, **126**, 1941–1990.

Roth, M., and T. R. Oke, 1993: Turbulent transfer relationships over an urban surface: I spectral caracteristics. *Quart. J. Roy. Meteor. Soc.*, **126**, 1941–1990.

Rotta, J. C., 1951a: Statistische Theorie nichthomogener Turbulenz. *Z. Phys.*, **129**, 547–572.

Rotta, J. C., 1951b: Statistische Theorie nichthomogener Turbulenz. *Z. Phys.*, **131**, 51–77.

Schär, C., D. Leuenberger, O. Fuhrer, D. Lüthi, and C. Girard, 2002: A new terrain-following vertical coordinate formulation for atmospheric prediction models. *Monthly Weather Review*, **130**, 2459–2480.

Scherer, D., and E. Parlow, 1994: Terrain as an important controlling factor for climatological meteorological and hydrological processes in NW-Spitsbergen. *Zeitschrift für Geomorphologie*, **97**, 175–193.

Schraff, C. H., 1997: Mesoscale data assimilation and prediction of low stratus in the alpine region. *Meteor. Atmos. Phys.*, pp. 21–50.

Schrodin, R., and E. Heise, 2001: The multi-layer version of the soil model TERRA_LM. Consortium for Small-Scale Modelling (COSMO), available at http://www.cosmo-model.cscs.ch, Technical Report 2.

Schubiger, F., 2002: Verification results of aLMo with and without new TKE-scheme: 14 august - 6 november 2001. *COSMO Newsletter No. 2*, Consortium for Small-Scale Modelling, available at: http://www.cosmo-model.org, pp. 197–202.

Schubiger, F., 2003: High resolution verification of daily cycle over Switzerland. *COSMO Newsletter No. 4*, Consortium for Small-Scale Modelling, available at: http://www.cosmo-model.org, pp. 63–66.

Schulz, J. P., L. Dùmenil, and J. Polcher, 2001: On the land surface-atmosphere coupling and its impact in a single-column atmospheric model. *J. App. Meteor.*, **40**, 642–662.

Schumann, U., and T. Gerz, 1995: Turbulent mixing in stably stratified shear flows. *J. Appl. Meteor.*, **34**, 33–48.

Senkova, A. V., L. Rontu, and H. Savijärvi, 2007: Parameterization of orographic effects on surface radiation in HIRLAM. *Tellus*, **59A**, 279–291.

Sharan, M., T. V. B. P. S. R. Krishna, and Aditi, 2003: Surface-layer characterisctics on the stable boundary layer with strong and weak winds. *Bound.-Layer Meteor.*, **108**, 1573–1472.

Shaw, R. H., 1977: Secondary wind speed maxima inside plant canopies. *J. Appl. Meteor.*, **16**, 514–521.

Sheppard, P. A., 1958: Transfer across the Earth's surface and through the air above. *Quart. J. Roy. Meteor. Soc.*, **84**, 205–224.

Skamarock, W. C., and J. B. Klemp, 1992: The stability of time-split numerical methods for the hydrostatic and the non-hydrostatic elastic equations. *Monthly Weather Review*, **120**, 2109–2117.

Smagorinsky, J., 1963: General circulation experiments with the primitive equations. *Monthly Weather Review*, **91**, 99–164.

Someria, G., and J. W. Deardoff, 1976: Subgrid-scale condensation in models of non-precipitating clouds. *J. Atmos. Sci.*, **34**, 344–355.

Stauffer, D. R., and J.-W. Seeman, 1990: Use of four-dimensional data assimilation in a limited-area mesoscale model. Part I: Experiments with synoptic scale data. *Monthly Weather Review*, **118**, 1250–1277.

Steeneveld, G. J., B. J. H. V. de Wiel, and A. A. M. Holtslag, 2006a: Modelling the evolution of the atmospheric boundary layer coupled to the land surface for three contrasting nights in CASES-99. *J. Atmos. Sci.*, **63**, 920–935.

Steeneveld, G. J., B. J. V. de Wiel, and A. A. M. Holtslag, 2006b: Modelling the arctic stable boundary layer and its coupling to the surface. *Bound.-Layer Meteor.*, **118**, 357–378.

Steppeler, J., G. Doms, U. Schättler, H. Bitzer, A. Gassmann, U. Darmrath, and G. Gregoric, 2003: Meso-gamma scale forecast using the non-hydrostatic model LM. *Meteorol. Atmos. Phys.*, **82**, 75–96.

Stewart, J. B., 1995: Turbulent surface fluxes derived from radiometric surface temperature of sparse prairie grass. *J. Geophys. Res.*, **100**(D12), 429–25.

Stewart, J. B., W. P. Kustas, K. S. Humes, W. D. Nichols, M. S. Moran, and H. A. R. D. Bruin, 1994: Sensible heat flux-radiometric surface temperature relationship for height semi arid areas. *J. App. Meteor.*, **33**, 1110–1117.

Stökli, R., 2004: Modeling and observations of seasonal land-surface heat and water exchanges at local and catchement scales over Europe, Ph.D. thesis, ETH Zürich, diss. ETH No. 15742.

Stull, R. B., 1988: *An Introduction to Boundary Layer Meteorology*. Atmospheric Sciences Library, Kluwer Academic Publishers, Dordrecht, Boston,London, pp. 666.

Stull, R. B., 1994: A review of parameterizations schemes for turbulent boundary-layer processes. *Parameterization of sub-grid scale physical processes*, European Centre for Medium-Range Weather Forecast, Proceedings of a seminar held at ECMWF.

Sturman, A. P., et al., 2003: The Lake Tekapo experiment (LTEX): an investigation of atmospheric boundary layer processes in complex terrain. *Bulletin of American Meteorological Society*, **84**, 371–380.

Sugita, M., and W. Brutsaert, 1990: Regional fluxes from remotely sensed skin temperature and lower boundary layer measurements. *Water Resources Research*, **26**(12), 2937–2944.

Sukoriansky, S., B. Galperin, and V. Perov, 2005: Application of a new spectral theory of stably stratified turbulence to the atmospheric boundary layer over sea ice. *Bound.-Layer Meteorol.*, **117**, 231–257.

Sukoriansky, S., B. Galperin, and V. Perov, 2006: A quasi-normal scale elimination model of turbulence and its application to stably stratified flows. *Processes in Geophysics*, **13**, 9–22.

Sun, J., P. Burns, T. W. H. A C. Delany, S P Oncley, and D. H. Lenschow, 2003: Heat balance in the nocturnal boundary layer during CASES-99. *J. Appl. Meteor.*, **42**, 1649–1666.

Svensson, G., and A. A. M. Holtslag, 2007: The diurnal cycle - GABLS second Intercomparison Project. *GEWEX News, GEWEX newsletter*, **17**(1), 9–10.

Taylor, P. A., and H. W. Teunissen, 1987: The Askervein hill project: Overview and background data. *Bound.-Layer Meteor.*, **39**, 15–39.

Thom, A. S., 1972: Momentum, mass, and heat exchange of vegetation. *Quart. J. Roy. Meteor. Soc.*, **98**, 124–134.

Tiedke, M., 1989: A comprehensive mass flux scheme for cumulus parameterization in large-scale models. *Monthly Weather Review*, pp. 3040–3061.

Van de Wiel, B. J. H., A. F. Moene, O. K. Hartogensis, H. A. R. D. Bruin, and A. A. M. Holtslag, 2002a: Intermittent turbulence and oscillations in the stable boundary layer over land. Part 3: A classification for observations during CASES-99. *J. Atmos. Sci.*, **59**, 2567–1581.

Van de Wiel, B. J. H., A. F. Moene, R. J. Ronda, H. A. R. D. Bruin, and A. A. M. Holtslag, 2002b: Intermittent turbulence and oscillations in the stable boundary layer over land. Part 2: A system dynamics approach. *J. Atmos. Sci.*, **59**, 2567–1581.

Van de Wiel, B. J. H., R. J. Ronda, A. F. Moene, H. A. R. D. Bruin, and A. A. M. Holtslag, 2002c: Intermittent turbulence and oscillations in the stable boundary layer over land. Part 1: A bulk model. *J. Atmos. Sci.*, **59**, 942–958.

Verhoef, A., H. A. A. D. Bruin, and B. J. J. M. V. D. Hurk, 1997: Some practical notes on the parameter $kB^{-1}$ for sparse vegetation. *J. Appl. Meteor.*, **36**, 560–561.

Viterbo, P., A. C. Beljaars, J. Mahfouf, and J. Teixeira, 1999: The representation of soil moisture freezing and ist impact on the stable boundary layer. *Quart. J. Roy. Meteorol. Soc.*, **125**(2401-2426).

Vosper, S. B., and S. D. Mobbs, 1997: Measurement of pressure field on a mountain. *Quart. J. Roy. Meteor. Soc.*, **123**, 129–144.

Vosper, S. B., and S. D. Mobbs, 2002: Measurements of the near-surface flow over a hill. *Quart. J. Roy. Meteor. Soc.*, **128**(2257-2280).

Wacker, U., K. V. J. Potty, C. Lüpkes, J. Hartmann, J, and M. Raschendorfer, 2005: A case study on a polar cold air outbreak over fram strait using a mesoscale weather prediction model. *Bound.-Layer Meteor.*, **117**, 301–336.

Walker, D., 2005: aLMo-verification in the complex terain of the Swiss Alps, Master's thesis, ETH Zürich.

Walser, A., and C. Schär, 2003: Predictability mysteries in MAP IOP 2 and IOP 3. *International Conference on Apline Meteorology and MAP-meeteing 2003*, Meteoswiss, Ed., Brig, Extended Abstracts, Volume A.

Walser, A., D. Lüthi, and C. Schär, 2004: Predictability of precipitation in a cloud-resolving model. *Monthly Weather Review*, **132**, 560–577.

Weigel, A. P., 2005: On the atmospheric boundary layer over highly complex topography, Ph.D. thesis, ETH Zürich, 143 pp.

Weigel, A. P., and M. Rotach, 2004: Flow structure and turbulence characteristics of the daytime atmosphere in a steep and narrow valley. *Quart. J. Roy. Meteor. Soc.*, **130**, 2605–2627.

Weigel, A. P., F. K. Chow, M. W. Rotach, R. L. Street, and M. Xue, 2006: High-resolution large eddy simulations of flow in a steep alpine valley. Part II: Flow structure and heat-budgets. *J. App. Meteor.*, **45**, 87–107.

Weigel, A. P., F. K. Chow, and M. W. Rotach, 2007a: On the nature of turbulent kinetic energy in a steep and narrow alpine valley. *Bound.-Layer Meteor.*, **124**, 269–290.

Weigel, A. P., F. K. Chow, and M. W. Rotach, 2007b: The effect of mountainous topography on moisture exchange between the "surface" and the free atmosphere. *Bound.-Layer Meteor.*, **125**, 227–244.

Whiteman, C. D., 1982: Breakup of temperature inversions in deep mountain valleys: Part I. observations. *J. App. Meteor.*, **21**, 270–289.

Whiteman, C. D., 1990: Observations of thermally developed wind systems in mountainous terrain. *Atmospheric Processes over Complex Terrain*, American Meteorological Society, Meteorological Monographs.

Whiteman, C. D., 2000: *Mountain Meteorology: fundamentals and applications*. Oxford University Press.

Whiteman, C. D., and J. C. Doran, 1993: The relationship between overlying synoptic-scale flows and winds within a valley. *J. App. Meteor.*, **32**, 1669–1682.

Whiteman, C. D., K. J. Allwine, L. J. Fritschen, M. M. Orgill, and J. R. Simpson, 1989: Deep valley radiation and surface energy budget microclimates. part 1: Radiation. *J. App. Meteor.*, **28**, 414–437.

Whiteman, C. D., X. Bian, and J. L. Sutherland, 1999a: Wintertime surface wind patterns in the Colorado River valley. *J. App. Meteor.*, **38**, 1118–1130.

Whiteman, C. D., S. Zhong, and X. Bian, 1999b: Wintertime boundary layer structure in grand canyon. *J. App. Meteor.*, **38**, 1084–1102.

Whiteman, C. D., B. Podpichal, S. Eisenbach, R. Steinacker, M. Dorninger, E. Mursch-Radlgruber, and C. B. Clements, 2003: Temperature inversion breakup in the Gstettneralp sinkhole. *International Conference on Apline Meteorology and MAP-meeteing 2003*, Meteoswiss, Ed., Brig, Extended Abstracts, Volume A.

Whiteman, C. D., T. Haiden, B. Pospichal, S. Eisenbach, and R. Steinacker, 2004: Minimum temperatures, diurnal temperature ranges and temperature inversions in Limestone sinkholes of different shapes and sizes. *J. Appl. Meteor.*, **43**(8), 1224–1236.

Wicker, L., and W. Skamarock, 1998: A time-splitting scheme for elastic equations incorporating second -order kunge-kutta time differencing. *Monthly Weather Review*, **126**, 1992–1999.

Wicker, L., and W. Skamarock, 2002: Time-splitting methods for elastic models using forward time schemes. *Monthly Weather Review*, **130**, 1857–1875.

Wieringa, J., 1986: Roughness-dependent geographical interpolation of surface wind speed averages. *Quart. J. Roy. Meteorol. Soc.*, **112**, 867–889.

Wieringa, J., 1993: Representative roughness parameters for homogenous terrain. *Bound.-Layer Meteor.*, **63**, 323–363.

Wild, M., 2005: Solar radiation budgets in atmospheric model intercomparisons from a surface perspective. *Geophysical Research Letter*, **32**(L07704).

Willis, G. E., and J. W. Deardoff, 1974: A laboratory model of the unstable planetary boundary layer. *J. Atmos. Sci.*, **31**, 1297–1307.

Wilson, J. D., 1988: A second-order closure model for flow through vegetation. *Bound.-Layer Meteor.*, **42**, 371–392.

Wilson, J. D., 2003: Representing drag on unresolved terrain as a distributed momentum sink. *J. Atmos. Sci.*.

Wilson, N. R., and R. H. Shaw, 1977: A higher order closure model for canopy flow. *J. Appl. Meteor.*, **16**, 1197–1205.

Wood, N., A. R. Brown, and F. E. Hewer, 2001: Parametrizing the effects of orography on the boundary layer: An alternative to effective roughness length. *Quart. J. Roy. Meteor. Soc.*, **127**, 759–777.

Xue, M., K. K. Droegemeier, and V. Wong, 2000: The advanced regional prediction system (ARPS) - a multi-scale non-hydrostatic atmospheric and prediction tool - Part I: Model dynamics and verificatiob. *Meteor. Atmos. Phys.*, **75**, 161–193.

Xue, M., K. K. Droegemeier, V. Wong, A. Shapiro, K. Brewster, F. Carr, and D. Weber, 2001: The advanced regional prediction system (ARPS) - a multi-scale non-hydrostatic atmospheric and prediction tool - Part II: Model physics and applications. *Meteor. Atmos. Phys.*, **76**, 143–165.

Yamada, T., 1982: A numerical study of turbulent airflow in and above a forest canopy. *Meteorol. Soc. Japan*, **60**, 439–454.

Zängl, G., B. Chimani, and C. Häberli, 2004a: Numerical simulations of the foehn in the Rhin Valley on 24 oktober 1999 (MAP IOP10). *Monthly Weather Review*, **132**, 368–389.

Zängl, G., A. Gohm, and G. Geiger, 2004b: South foehn in the Wipp Valley - Innsbruck region: Numerical simulations of the 24 oktober 1999 (MAP IOP10). *Meteor. and Atmos. Phys.*, **86**, 213–243.

Zgraggen, L., 2001: Strahlungsbilanz der Schweiz, Ph.D. thesis, ETH Zürich, diss. ETH Nr. 14158.

Zhang, D.-L., and W.-Z. Zheng, 2004: Diurnal cycles of surface winds and tempertaures as simulated by five boundary layer parameterizations. *J. App. Meteor.*, **43**, 157–169.

Zilitinkevich, S., 2006: Turbulent energies and richardson numbers in stably stratified sheared flows. *NATO Advanced Research Workshop Dubrovnik 18-22 April 2006*.

Zilitinkevich, S., and P. Calanca, 2000: An extended similarity theory for the stable stratified atmospheric surface layer. *Quart. J. Roy. Meteor. Soc.*, **126**, 1913–1923.

Zilitinkevich, S. S., 1970: Dynamics of the atmospheric boundary layer. *Leningrad Gidrometeor.*, p. 291.

# Aknowledgements

Im most grateful to my supervisor Mathias Rotach, who guided my PhD thesis and accepted me as his first PhD student in his "new career" at MeteoSwiss. During the work with him I have greatly appreciated the many inspiring discussions, his broad scientific background, his excellent knowledge in the boundary layer meteorology and last but not least his precious social skills. I am in depth to him for the time he spent in reviewing, correcting, discussing and guiding my work. I am grateful to him for many things I have learned in this 3 years. Thank you very much Mathias!

I am also indebted with Prof. Atsumu Ohmura, which accecpted to be my doctor father and gave me the honour to be one of his last PhD students of his long and successful professor career. A special thank goes also to Prof. Christoph Schär and Bert Holtslag, who accepted to be my coreferents.

A very huge thank is dedicated to the model group at MeteoSwiss and all his members during my three and half years as PhD student (Philippe, Guy, Pirmin, Francis, Dani L., Marco A., Christophe, Silke, Felix F., Vanessa, Oliver, Marco S., Donat, Felix A., Marcel, Dani W., Anne, Martin, Balász, Fabian, Ronny, Daniela), which have provided an excellent work atmosphere and were always available to answer my questions. In particular I would mention the "osm" crew (Emanuele, Andre and Dani) for the many technical hints referring to the LM-package and the answers to all my technical questions, the verification team formed by Pirmin and Francis for the important hints about their verification experience and software, Jean-Marie for answering my questions about the "all-making" software Fieldextra, Vanessa for having improved my English in some parts of this work, Guy and Felix A. for the aspects related with the external parameters, Marco A. for the interesting discussions about model Physics, and Philippe for all the administrative aspects at MeteoSwiss.

I would like also to mention Matthias Raschendorfer (turbulence parameterizations and single column model), Bodo Ritter (radiation parameterizations), Juergen Helmert (single column model) and Uli Schättler (technical coding aspects of the COSMO model) at the DWD for having always time to answers my questions about the COSMO model.

I would like to especially thank Antoine Zelenka and Bruno Duerr from the "KD team" at MeteoSwiss for providing me the adapted satellite data, the algorithm for the skyview factor and for interesting discussions about radiation in the alpine region.

A special mention is also dedicated to my container mates Dani W., Donat and Balász, which contributed to an excellent work atmosphere in my "special office in the garden". Additionally I would mention the "NAZ NCCR and MO" connection group for the joined lunch breaks, most of them on the inspiring MeteoSwiss roof.

I would also like to thank flatmates at the "WG in Ahornstrasse 22" which have contributed for longer or shorter periods to a great living atmosphere (Dania, Johannes, Ulf, This, Katrin, Simone, Olaf, Andrea, Marcel and Sharmistha).

My deepest gratitude goes to my girlfried Silvia for her love, support and comprehension (mainly in the last months of this study when I have sacrificed lot of free time). You are the miracle.

Finally and most importantly, I feel indebted to my parents Luca and Silvana, my brother Simone and my sister Sara, for their love and support during all these years.

# List of acronyms and abreviations

| Acronym | Description |
|---|---|
| ABL | Atmospheric boundary layer |
| aLMo | Alpine model |
| AROME | Non-hydrostatic and convection resolving model of Meteofrance |
| ARPS | Advanced Regional Prediction System |
| CASES 99 | US boundary layer field experiment in 1999 |
| CBL | Convective boundary layer |
| COAMPS | Coupled Ocean/Atmosphere mesoscale prediction system |
| CORR | Correlation coefficient |
| COSMO | Consortium for small scale modelling |
| COSMO-2 | COSMO model with 2.2 km horizontal resolution |
| COSMO-7 | COSMO model with 7 km horizontal resolution |
| COSMO-SC | COSMO single column model |
| DWD | Deutscher Wetterdienst |
| ECMWF | European Center for medium range forecast |
| ETH | Swiss Federal Institute of Technology |
| GABLS | GEWEX Atmospheric Boundary layer Study |
| GEWEX | Global Energy and Water Cycle Experiment |
| HIRLAM | High resolution limited area model |
| IAC | Institute for atmospheric and climate science |
| ISL | Inertial sublayer |
| LES | Large eddy simulation |
| LM | Lokal Modell |
| MAP | Mesoscale Alpine Programm |
| MC2 | Mesoscale Compressible Community NWP Model |
| ME | Mean errror |
| Meso-NH | Non-hydrostatic mesoscale model of the French research comunity |
| NBL | Nocturnal boundary layer |
| MM5 | Fifth generation mesoscale model from NCAR |
| NCAR | National Center for Atmospheric Research |
| NCEP | National Center for Environmental Prediction |
| NMM | Non-hydrostatic mesoscale Model |
| NWP | Numerical weather prediction |
| PBL | Planetary boundary layer |
| RAMS | Regional Atmospheric Modelling System |
| RANS | Reynolds-averaged Navier-Stokes equations |

| Acronym | Description |
|---|---|
| RM | Representation mismatch or representativeness error |
| RMSE | Root mean square error |
| RSL | Roughness sublayer |
| SBL | Stable boundary layer |
| STDEV | Standard deviation |
| TKE | Turbulent kinetic energy |
| WRF | Weather Research Forecasting Model |
| 3-D | Three-dimensional |
| 1-D | One-dimensional |

# List of symbols

| Symbol | Description |
|---|---|
| $\theta_N$ | slope angle |
| $\theta_S$ | sun elevation angle |
| $\phi_N$ | slope aspect |
| $\phi_S$ | sun azimuth angle |
| $\alpha$ | angle between the direction of the solar beam and the normal of the surface |
| $mask_{\text{shawow}}$ | shadow mask |
| $\theta_{h,\phi_S}$ | horizon angle towards the sun azimuth angle $\phi_S$ |
| $\downarrow SW_{\perp\text{dir}}$ | direct short wave downward radiation on a surface perpendicular to the sun rays |
| $\downarrow SW_{\text{dir}}$ | direct short wave downward radiation on a horizontal surface |
| $\downarrow SW^*_{\text{dir}}$ | effective short wave downward radiation |
| $\downarrow SW_{\text{diff}}$ | diffuse short wave downward radiation on a horizontal surface |
| $\downarrow SW^*_{\text{diff}}$ | effective diffuse short wave downward radiation |
| $\downarrow SW_{\text{diff}}$ | direct short wave downward radiation on a horizontal surface |
| $\uparrow SW^*_{\text{diff}}$ | effective diffuse short wave upward radiation |
| $\downarrow LW$ | direct longwave downward radiation on a horizontal surface |
| $\downarrow LW^*$ | effective long wave downward radiation |
| $f_{cor}$ | correction factor for direct solar radiation |
| $\psi_i$ | temporary azimuth angle for integration |
| $h_i$ | horizon angle for the sector i |
| $\Delta\psi$ | angle of the n discrete sectors for computing the horizon |
| $hpl_i$ | height of the tilted plane |
| $\epsilon_i$ | sign for the Coriolis parameter (+ U,-V) |
| $U_i$,$u_i$, $u_i'$ | horizontal wind speed component and turbulent part |
| $U_{ig}$ | geostrophic wind |
| $f_c$ | coriolis parameter |
| $T$ | air temperature |
| $\Theta$, $\theta'$ | potential temperature and its turbulent part |
| $\Theta_l$ | liquid water potential temperature |
| $\Theta_\nu$ | virtual potential temperature |
| $Q$,$q'$ | specific humidity and its turbulent part |
| $Q_w$ | total water content |
| $\overline{u_i'w'}$ | vertical momentum covariances |
| $\overline{\theta'w'}$ | vertical temperature covariance |
| $\overline{q'w'}$ | vertical specific humidity covariance |
| $K_M$,$K_H$ | turbulent diffusion coefficient for momentum and heat |
| $S_M$,$S_H$ | stability functions for momentum and heat transport |

| Symbol | Description |
|---|---|
| $z$ | height above surface |
| $W/w$,$w'$ | vertical velocity and its turbulent part |
| $\lambda_l$ | turbulent length scale or mixing length |
| $\lambda_l^\infty$ | asymptotic mixing length |
| $q^2$ | $0.5 \cdot$ TKE |
| $\rho$ | air density |
| $\alpha$ | constant for the parameterization of the turbulent diffusion of TKE |
| $L_{pat}$ | horizontal length scale for surface heterogeneities |
| $A_{\Theta_l}$, $A_{Q_w}$ | coefficients computed with the subgridscale cloud scheme |
| $A_1, A_2, B_1, B_2, C_1$ | closure constants |
| $G_M$,$G_H$ | dimensionless gradients for momentum and heat |
| $be2, be1, a11, a21, ...$ | auxiliary variables for the stability functions |
| $\kappa$ | von Karman constant |
| $z_0$ | roughness length |
| $\sigma^2$ | variance of the subgrid scale orography |
| $H_0$ | sensible heat flux at the surface |
| $(M_U)_0, (M_V)_0$ | components of the momentum flux at the surface |
| $V_h$ | horizontal wind speed |
| $C_m, C_Q, C_\Theta$ | transfer coefficients between surface and atmosphere for momentum, humidity and heat |
| $L_v$ | latent heat of vaporisation |
| $C_{pd}$ | specific heat of dry air at constant pressure |
| $U_{ke}, V_{ke}$ | horizontal wind components at the model level ke |
| $H, h_{can}$ | canopy height |
| $z_*$ | maximum vertical extension of the RSL |
| $z_{0,oro}$ | orographic component of the roughness length |
| $z_{0,loc}$ | local component of the roughness length |
| $r_{lam}^M, r_{lam}^H$ | laminar transfer resistance for momentum and heat |
| $r_{tur}^M, r_{tur}^H$ | turbulent transfer resistance for momentum and heat in the roughness layer |
| $r_{pr}^M, r_{pr}^H$ | transfer resistance for momentum and heat in the surface or Prandtl layer |
| $r_{tot}^M, r_{tot}^H$ | total transfer resistance |
| tfm, tfh | ratio of resistance in the laminar layer to the total resistance |
| $SAI$ | surface area index |
| $LAI$ | leaf area index |
| $C_H, C_M$ | scaling factors of the laminar layer for momentum and heat (or moisture) |
| $FR_{LAND}$ | fraction of land |
| $D_H = k_H$ | kinematic viscosity of air |
| $D_M = k_M$ | scalar conductivity of dry air |
| $C_{lnd}$ | surface area density of the roughness elements at the surface |
| $PL_{cov}$ | plant coverage |
| $RC$ | ratio of canopy height to the roughness length $z_0$ |
| $dh$ | thickness of the lowest model layer |
| $T_{ke}$ | temperature at the lowest model layer |
| $QV_{ke}$ | specific humidity at the lowest model layer |
| $T_s$ | surface temperature |
| $QV_s$ | surface specific humidity |
| $z2$ | 2 m height |
| $T_{2m}$ | 2 m temperature |
| $QV_{2m}$ | 2 m specific humidity |

| Symbol | Description |
|---|---|
| $h_{ke}, h_{ke1}$ | height above sea level of the first atmospheric level and of the surface |
| $H1$ | effective height above sea level of the surface |
| $H2$ | effective height above sea level of the first atmospheric main level |
| $H2 - H1 = 0.5 \cdot dh$ | half thickness of the first atmospheric layer. |
| $R_d$, $R_v$ | gas constant for dry air and for water vapour |
| z2 | height at 2 m |
| $z_{0T}$ | roughness length for temperature |
| $u_*$ | friction velocity |
| $S$ | dry static energy |
| $S_s$ | dry static energy at the surface |
| $S_2m$ | dry static energy at 2 m |
| $L$ | Obuchov length |
| $g$ | gravity constant |
| $QV_*$ | surface layer scaling variable for specific humidity |
| $S_*$ | surface layer scaling variable for dry static energy |
| $J_s, J_{qv}$ | turbulent fluxes at the surface for the dry static energy and the specific humidity |
| $\Psi_H$ | universal stability function |
| $\zeta$ | $\frac{z}{L}$ |
| $d$ | displacement height |
| $\alpha_\theta$, $\alpha_{qv}$ | constant length scale for temperature and specific humidity |
| $e_{2m}$ | water vapour pressure at 2 m |
| $p_{2m}$ | estimated pressure at 2 m |

# Curriculum Vitae

Matteo Buzzi, Via Vela 21, 6500 Bellinzona, Switzerland
born on 22 May 1975 in Lima, Perù, Swiss citizen.

EDUCATION AND PROFESSIONAL TRAINING

| | |
|---|---|
| 09/04 - 01/08 | PhD student at MeteoSwiss in the modeling groop (COSMO model) under the surververision of PD Dr. M. W. Rotach and Prof. Dr. A. Ohmura. PhD defence on 2 April 2008. |
| 06.03 - 07.03 | Community service at Greenpeace Switzerland in Zürich: Solar energy campaign and virgin forests campaign. |
| 01/01 - 05/03 | Scientific collaborator at METEOTEST in Bern: wind energy potential studies (modeling and measurements) and numerical weather prediction. |
| 06/00 - 12/00 | Community service at the WSL in Bellinzona: forestry research and dendrochronological study. |
| 10/99 - 05/00 | Community service at WWF Switzerland in Zürich: climate campaign. |
| 04/99 - 09/99 | Diploma thesis at the Swiss Federal Institute of Technology in the dynamical meteorology group of Prof. Dr. Huw Davies (supervision: Alexia Massacand and Cornelia Schwierz): "Influences of Greenland on the atmospheric flow patterns in the Northern Atlantic". |
| 09/97 - 01/98 | Practical course at the AWEL (Amt für Wasser Energie und Luft, Office for air water energy and air) of the canton Zürich: monitoring of the indoor air quality in public buildings. |
| 10/94 - 10/99 | Studies of the environmental sciences at the ETH of Zürich: these studies are based on the integral consideration of all aspects of the environment an its systems and the application of the different subjects (the systems: water, air, soil, human; the subjects: biology, chemistry and physics, environmental hygiene and social sciences). The second part of the studies were focussed on the study of the system atmosphere with the help of physics and chemistry. |
| 09/90 - 06/94 | Cantonal high school of Bellinzona (Switzerland), type C (scientific). |